



**HAL**  
open science

# Beads-on-a-string and transfer ratio for viscoelastic solutions

Hrishikesh Pingulkar

► **To cite this version:**

Hrishikesh Pingulkar. Beads-on-a-string and transfer ratio for viscoelastic solutions. Fluids mechanics [physics.class-ph]. Normandie Université, 2021. English. NNT : 2021NORMLH07 . tel-03567493

**HAL Id: tel-03567493**

**<https://theses.hal.science/tel-03567493>**

Submitted on 12 Feb 2022

**HAL** is a multi-disciplinary open access archive for the deposit and dissemination of scientific research documents, whether they are published or not. The documents may come from teaching and research institutions in France or abroad, or from public or private research centers.

L'archive ouverte pluridisciplinaire **HAL**, est destinée au dépôt et à la diffusion de documents scientifiques de niveau recherche, publiés ou non, émanant des établissements d'enseignement et de recherche français ou étrangers, des laboratoires publics ou privés.



Normandie Université

## Pour obtenir le diplôme de doctorat

**Spécialité** (Mécanique)

Préparée au sein de LOMC, CNRS - Université Le Havre Normandie

## Beads on a string and transfer ratio for viscoelastic solutions

Présentée et soutenue par  
**Hrishikesh PINGULKAR**

Thèse soutenue publiquement le 11 février 2021  
devant le jury composé de

Dr. Günter BRENN	Professeur, Graz University of Technology, Autriche	Rapporteur
Dr. Sandra LEROUGE	Professeur, MSC, Université Paris-Diderot	Rapporteur
Dr. Michel GRISEL	Professeur, URCOM, Université Le Havre Normandie	Président
Dr. Fabio SANTOS	Adjunct Professor, Federal University of Rio de Janeiro (UFRJ), Brazil	Examineur
Dr. Marie-Charlotte RENOULT	Maître de Conférences, CORIA, INSA Rouen	Invitée
Dr. Olivier CRUMEYROLLE	Maître de Conférences, LOMC, CNRS et Université Le Havre Normandie	Co-superviseur
Dr. Jorge PEIXINHO	Chargé de recherche HDR, LOMC, CNRS, Université Le Havre Normandie et PIMM, Arts et Métiers Institute of Technologie	Directeur de thèse

Thèse dirigée par Jorge PEIXINHO, LOMC, CNRS – Université Le Havre Normandie et PIMM, CNRS, Arts et Métiers Institute of Technologie et co-supervisée par Olivier CRUMEYROLLE, LOMC, CNRS - Université Le Havre Normandie



**Abstract:** This thesis deals with uniaxial stretching of capillary bridges of polymer solutions. It consists of two experimental parts investigating drop dynamics and liquid transfer. The stretching of viscoelastic polymer solutions can create the beads on a string. Solutions are prepared with a wide range of mass fractions. The stretching is quantified using diameter-space-time diagrams, which demonstrate hierarchy, asymmetry, migration, oscillation, and merging of drops. Also, position of minimum diameter on the filament is determined, along with number, positions and diameters of the drops. The maximum number of drops can be predicted using the characteristic relaxation time. The extracted minimum diameter is used to calculate extensional viscosity. Then, the viscoelastic liquid transfer for cylindrical-shaped capillary bridges, pinned on circular parallel plates is studied. Specifically, the effects of polymer mass fraction, solvent viscosity, plate diameter, initial and final height, stretching speed, and contact angle are investigated. With the increase in polymer mass fraction and solvent viscosity, the liquid transfer to the top plate significantly reduces. The increase in the initial and final height of the capillary bridge decreases the final liquid transfer to the top plate. The shape of the initial capillary bridge is studied by varying the liquid volume introduced, and for the Newtonian and viscoelastic solutions, an opposite liquid transfer behaviour is noticed. Finally, numerical simulations for a liquid capillary bridge are reported and show formation of filament and a big central drop having size similar to the experimental value.

**Keywords:** Viscoelastic solutions, beads on a string pattern, liquid transfer

**Résumé:** Cette thèse traite de l'étirement uniaxial de ponts capillaires de solutions de polymères. Celle-ci se compose de deux parties expérimentales étudiant la dynamique des gouttes et le transfert du liquide. L'étirement des solutions de polymères viscoélastiques peut créer le motif de perle-sur-ficelle. Les solutions sont préparées pour une large gamme de concentrations. L'étirement est quantifié à l'aide de diagrammes diamètre-espace-temps, qui démontrent la hiérarchie, l'asymétrie, la migration, l'oscillation et la coalescence des gouttes. La position du diamètre minimum sur le filament est déterminée, ainsi que le nombre, les positions et les diamètres des gouttes. Le nombre maximum de gouttes peut être prédit en utilisant le temps caractéristique de relaxation. Le diamètre minimum est utilisé pour calculer la viscosité élongationnelle. Puis, le transfert de liquide viscoélastique pour des ponts capillaires de forme cylindrique, entre deux plaques circulaires parallèles, est étudié. En particulier, les effets de la concentration, de la viscosité du solvant, du diamètre des plateaux, des hauteurs initiale et finale, de la vitesse et de l'angle de contact sont présentés. Avec l'augmentation de la concentration et de la viscosité du solvant, le transfert vers la plaque supérieure diminue. L'augmentation des hauteurs initiale et finale du pont capillaire diminue le transfert de liquide. La forme du pont capillaire initial est modifiée, et on constate un comportement opposé du transfert pour les solutions newtonienne et viscoélastique. Enfin, des simulations numériques sont présentées et montrent la formation d'un filament avec une grosse goutte centrale de taille similaire aux expériences.

**Mots-clés :** Solutions viscoélastique, motif perle-sur-ficelle

## Acknowledgements

This work has been done during my stay as a PhD student at Laboratoire Ondes et Milieux Complexes (LOMC) and Université Le Havre Normandie, with the support of a PhD fellowship (allocation établissement) from Université Le Havre Normandie.

First and foremost, I am grateful to Dr. Jorge Peixinho and Dr. Olivier Crumeyrolle for accepting me as a PhD candidate, for their support, guidance and patience from the start to the end of my PhD study. I would also like to thank Olivier for helping me in settling down in France.

I am thankful to Prof. Gunter Brenn for the invitation and excellent monitoring during my stay at Graz University of Technology, Austria, for the retardation time measurements. Furthermore, I appreciate the time invested by him and Prof. Sandra Lerouge for the critical reading, enriching comments and suggestions that helped me to improve and finalise the present thesis.

For the downward stretching liquid transfer experiments, I would like to thank Dr. Marie-Charlotte Renoult for allowing me to use their experimental setup at CORIA, Rouen. The rheological properties of the polymer test liquids were measured at the URCOM, Université Le Havre Normandie. Hereby, I would like to thank Prof. Michel Grisel for kindly allowing us to use their equipment, and Mr. Vincent Loisel for his assistance during the experiments. I am grateful to Prof. Michel Grisel for being my CSI advisor and member of my thesis committee. I also thank Dr. Pierre Marechal for being my CSI advisor. I would like to acknowledge Dr. Fabio Santos for his help and guidance for OpenFOAM simulations.

Moreover, I am grateful to Dr. Benoit Duchemin for helping me with the surface tension measurements and insightful discussions. I would like to appreciate Prof. François Marin for helping me with a PhD contract extension. Also, I am thankful to Prof. Innocent Mutabazi for meaningful discussions and his encouraging words. Dr. Mandar Tendolkar, I am grateful for helping me with proofreading on short notice. Furthermore, I would like to thank Prof. S V. Prabhu, Prof. Sudarshan Kumar and Prof. Kannan Iyer for giving me opportunities at IIT-Bombay and for being an inspiration to me in the field of research.

Finally, I am thankful to all my colleagues and friends at LOMC for your friendship, support and numerous creative diversions. I am grateful to Ragav, Abdessamad, Ahmad,

Abdillah, Sixtine, Changwoo, Hassan, Harmindar, Ellyn, Elhadj and Victoria for helping me in every possible way during my stay in Le Havre. I am also thankful to Marc for his assistance to initialise OpenFOAM and helping me to resolve issues. I also appreciate Siddhesh for proofreading and meaningful discussions. Finally, I would also like to thank my parents for their support and motivation throughout my education.

Without you all, this journey would not be possible.

# Table of contents

<b>General introduction</b>	<b>ix</b>
<b>1 Basic principles of rheology, beads on a string, liquid transfer, and numerical modelling</b>	<b>1</b>
1.1 Elastic solid and viscous fluid . . . . .	2
1.1.1 Elastic solids . . . . .	2
1.1.2 Viscous fluid . . . . .	3
1.2 Governing equations . . . . .	4
1.3 Shear and extensional flows . . . . .	5
1.4 Constitutive equations and viscoelastic models . . . . .	8
1.4.1 Maxwell model and Kelvin-Voigt model . . . . .	9
1.4.2 Jeffreys and Oldroyd-B models . . . . .	10
1.4.3 FENE-P model . . . . .	12
1.5 Extensional rheology . . . . .	14
1.6 Review on beads on a string . . . . .	23
1.7 Review on liquid transfer . . . . .	33
1.7.1 Contact lines and angles . . . . .	35
1.7.2 Effect of parameters . . . . .	38
1.7.3 Viscoelastic inks . . . . .	41
1.8 Numerical modelling . . . . .	45
1.9 Summary of objectives of the present work . . . . .	48
<b>2 Test fluids, their properties, and numerical setup</b>	<b>49</b>
2.1 Test fluids and their properties . . . . .	50
2.1.1 Polymers and solution preparation . . . . .	50
2.1.2 Solution properties . . . . .	52
2.1.2.1 Density measurements . . . . .	52
2.1.2.2 Surface tension measurements . . . . .	53

2.1.2.3	Shear rheometry . . . . .	54
2.2	Extensional rheology of polymer solutions . . . . .	56
2.2.1	Experimental setup and instrumentation . . . . .	57
2.2.2	Experimental method and image analysis . . . . .	58
2.2.2.1	Filament thinning and BOAS . . . . .	59
2.2.2.2	Relaxation time . . . . .	62
2.2.2.3	Apparent extensional viscosity . . . . .	65
2.2.3	Experimental details for liquid transfer . . . . .	68
2.3	Solution property table . . . . .	70
2.4	Numerical setup . . . . .	70
2.4.1	Newtonian solution: PEG20 . . . . .	72
2.4.2	Viscoelastic solution: PEG20PEO1000 . . . . .	76
<b>3</b>	<b>Beads on a string</b>	<b>85</b>
3.1	Diameter-space-time (DST) and Hencky strain-space-time (HSST) diagrams	86
3.1.1	Analysis of space-time diagrams . . . . .	88
3.1.2	Drop dynamics . . . . .	96
3.2	Effect of different parameters on the beads on a string . . . . .	98
3.2.1	Plate diameter . . . . .	98
3.2.2	Initial aspect ratio . . . . .	101
3.2.3	Final aspect ratio . . . . .	103
3.2.4	Stretching speed . . . . .	109
3.3	Partial conclusion . . . . .	111
<b>4</b>	<b>Liquid transfer</b>	<b>113</b>
4.1	Experimental results and discussion . . . . .	115
4.1.1	Polymer mass fraction . . . . .	115
4.1.2	Geometrical parameters . . . . .	118
4.1.2.1	Plate diameter . . . . .	118
4.1.2.2	Initial aspect ratio . . . . .	120
4.1.2.3	Final aspect ratio . . . . .	123
4.1.3	Stretching speed . . . . .	125
4.1.4	Initial bridge shape . . . . .	127
4.2	Partial conclusion . . . . .	130
<b>5</b>	<b>Conclusions and future work</b>	<b>133</b>
5.1	Conclusions . . . . .	134

---

5.2	Future work . . . . .	137
<b>References</b>		<b>139</b>
<b>Appendix A</b>	<b>Published article</b>	<b>149</b>
<b>Appendix B</b>	<b>OpenFOAM <i>rheoTool</i> scripts</b>	<b>151</b>
B.1	Newtonian solution: PEG20 . . . . .	152
B.1.1	Initial conditions . . . . .	152
B.1.1.1	alpha.water . . . . .	152
B.1.1.2	Pressure, p . . . . .	153
B.1.1.3	Velocity, U . . . . .	154
B.1.1.4	Constitutive properties . . . . .	155
B.1.1.5	Gravity, g . . . . .	155
B.1.2	Mesh generation: blockMeshDict . . . . .	156
B.1.3	Time step control: controlDict . . . . .	157
B.1.4	Convection schemes settings: fvSchemes . . . . .	158
B.1.5	Solver control: fvsolution . . . . .	160
B.1.6	Setting initial field: setFieldsDict . . . . .	162
B.2	Viscoelastic solution: PEG20PEO1000 . . . . .	163
B.2.1	Initial conditions . . . . .	163
B.2.1.1	alpha.water . . . . .	163
B.2.1.2	Constitutive properties . . . . .	165
B.2.1.3	Polymeric extra-stress: Tau . . . . .	166
B.2.2	Setting initial field: setFieldsDict . . . . .	167
<b>Appendix C</b>	<b>Measurements of the retardation time</b>	<b>169</b>
<b>Appendix D</b>	<b>Polarised Light Microscopy</b>	<b>173</b>
<b>Appendix E</b>	<b>Effect of stretching direction on liquid transfer</b>	<b>175</b>
<b>Appendix F</b>	<b>Résumé en langue française</b>	<b>177</b>



# General introduction

Take a drop of saliva between your thumb and forefinger, and then pull your fingers apart to a distance. Often, you can see a thread of saliva that starts thinning and instead of breaking rapidly, it evolves into a quasi-periodic pattern of drops formed on the thread (filament), as shown in Fig. 1. This pattern is commonly known as beads on a string (BOAS) [1–3] and recently as drops on a filament [4]. The formation of BOAS pattern is not observed for the Newtonian fluids, e.g. water, alcohol. However, this process of formation of filaments and BOAS is widely observed in nature, e.g. stringiness of cheese and sliced okra. In some spider webs (see Fig. 2), BOAS appears due to a solution of low molecular mass compound from the spider, “distributed throughout the aqueous material” [5], where water comes from humidity of the environment. The process of formation of BOAS is still not well understood and specifically occurs in non-Newtonian and viscoelastic fluids, e.g. saliva, paint, polymer solutions, etc.

Classical linear stability analysis shows that a viscoelastic liquid filament is, in fact, more unstable than a Newtonian liquid of the same viscosity and inertia [6–9]. Instead of breaking off by a Rayleigh-Plateau instability to form a detached drop as a Newtonian fluid does [10, 11], viscoelastic fluids form filaments that delay its breakup. The breakup process is driven by the action of capillarity, which seeks to minimise interfacial energy of the free surface of a liquid filament. This dynamical process can be rapid, depending on the composition of the fluid. Viscous, elastic and inertial forces play an important role in resisting the action of capillarity. In case of Newtonian liquids, the filament thinning undergoes *visco-capillary* or *inertio-capillary* thinning depending on the influence of inertial or viscous forces [12]. In case of viscoelastic liquids, after undergoing initial *visco-capillary* or *inertio-capillary* thinning, the filament experiences *elasto-capillary* thinning due to presence of elastic polymer chains [12]. The balance of elastic and capillary forces in the axially uniform filament leads to an apparent extensional viscosity. The uniaxial extensional viscosity is a fundamental material property of fluids which characterises the resistance of a material to stretching deformations. One of the most common demonstrations of extensional viscosity effects in complex fluids is its influence on the lifetime of a liquid filament undergoing a

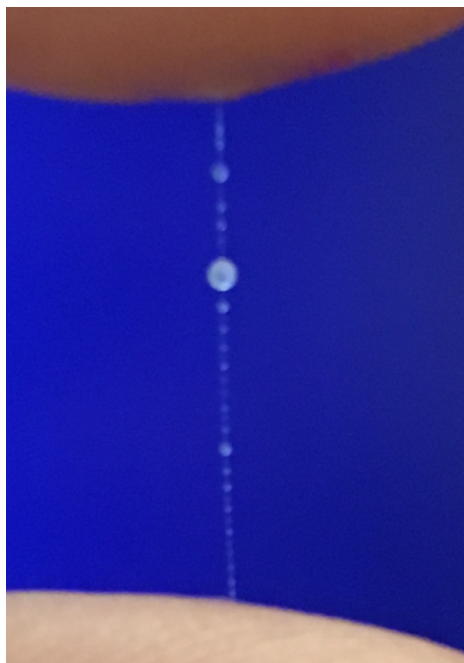


Fig. 1 Filament and beads on a string (BOAS), for saliva, formed between forefinger and thumb. Size of the big central drop is approximately  $150 \mu\text{m}$ .

capillary break-up. When a liquid jet of high molecular weight polymer undergoes a capillary driven thinning, a BOAS instability that appears, delaying breakup, is a well-known example of this phenomenon [7].

The formation of a BOAS structure is a nonlinear dynamic process [13]. In a BOAS structure, spherical fluid drops are interconnected by long thin fluid filaments of random lengths. In the spherical drops, the polymer molecules are relaxed and surface tension dominates; whereas in the thin filament, the molecules are highly stretched and viscoelastic stresses dominate. Experimental studies [9, 14, 15] and numerical simulations [2, 16] have demonstrated the evolution and the interaction of multiple drops on a viscoelastic filament. Multiple generations of drops are developed in a BOAS structure due to iterated instabilities caused by capillary and elastic forces. However, sometimes in the final stages of thinning, another secondary instability called blistering is also observed which is apparently similar to a BOAS structure [17, 18]. Recently, Deblais et al. [18] demonstrated that the blistering instability is due to a dynamical phase separation (caused by temperature) and inhomogeneities of polymer concentration in a filament. Even though multiples generations of drops have been reported [9, 14, 17, 18], the role of viscoelasticity and liquid bridge geometry in the formation of multiple generations of drops and drop dynamics are yet to be explored thoroughly. In a BOAS structure, drops migrate along the filament due to gravity or differences in capillary forces and coalescence occurs. Eventually, when the structure

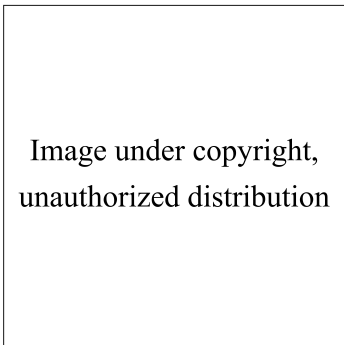


Image under copyright,  
unauthorized distribution

Fig. 2 Formation of beads on a string in spider web that contains solution of low molecular mass compounds from the spider in humidity attracted from the environment. (A) A web formed by a female *Argiope aurantia* consisting of threads. (B) Scanning electron microscope image of the spinning spigots that are responsible for a production of a thread. Aggregate gland spigots (AG); flagelliform gland spigot (FL). (C) A thread showing the formation of droplets due to increased humidity content in the solution, that initially enlarged the diameter. (D) The same thread 30 seconds after the formation of droplets is completed. Figures adapted from Opell et al. [5].

has coarsened to a few large drops, the extensibility limit of the polymer is reached and the filament breaks. To study the formation of the BOAS structure, various methods have been used, notably, the capillary jets [6, 7, 19], dripping-onto-substrate [20], stretched liquid bridge [1, 9], as shown in Fig. 3. In recent years, interest in the BOAS structure has grown, because of their numerous applications in printing [21], see Fig. 4, lab-on-a-chip [22], optics [23], bio-engineering [24] and electro-spraying [25].

In nature, liquid bridges are ubiquitous. In various medical problems such as respiratory diseases or body joints, small capillary bridges appear [28–30]. Liquid bridge configuration also exists in many industrial applications such as food processing, material engineering, adhesion processes, powder granulation, oil recovery, flow in porous media and microfluidics [20, 30]. Liquid bridge configuration can also be used to measure rheological and interfacial properties of liquids as an extensional rheometer, tensiometer and surfactometer [30]. The present study was inspired by the variety of natural phenomena and technical applications in which liquid bridges play a relevant and significant role.

Non-Newtonian fluids have many applications, but only a few applications are listed here: printing, atomisation of sprays [31–33], agricultural [34] or cosmetic (sunscreens) liquids, fuels stabilised with polymers, and drag reduction effect with coatings of fire hoses [35, 36]. Printing is often a more accurate and cost-friendly method than other conventional manufacturing processes due to its simplicity and versatility. Nowadays, a printing process is not only limited to books, magazines and newspapers but has also expanded to various areas

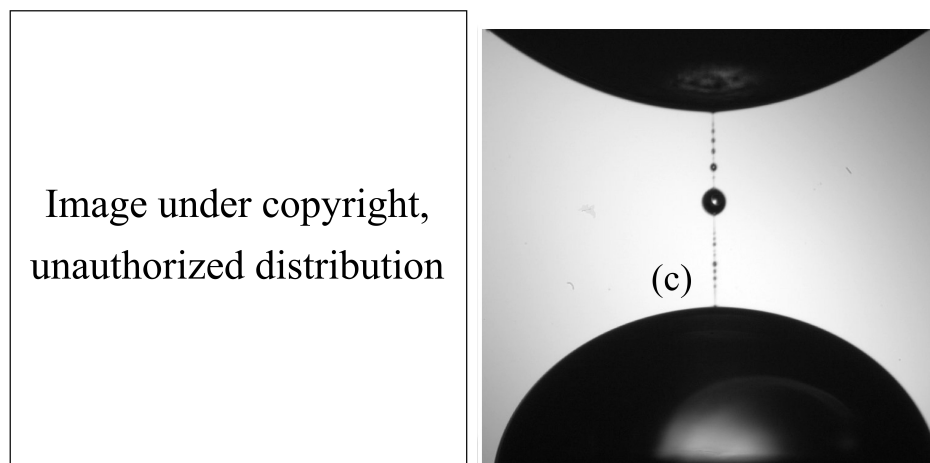


Fig. 3 Formation of beads on a string structures for polymer solutions using different methods, (a) Continuous capillary jet (from Tirel et al. [26]), (b) Dripping-from-nozzle (from Dinic et al. [27]) and (c) Stretched capillary bridge (from the present work).

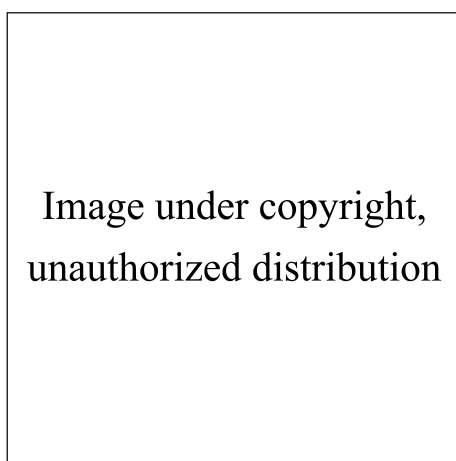


Fig. 4 A portrait printed with dots (diameter = 490 nm) using a polyurethane ink and a 500 nm internal-diameter nozzle. The inset shows a magnified image of the printed dots. Adapted from Park et al. [21].

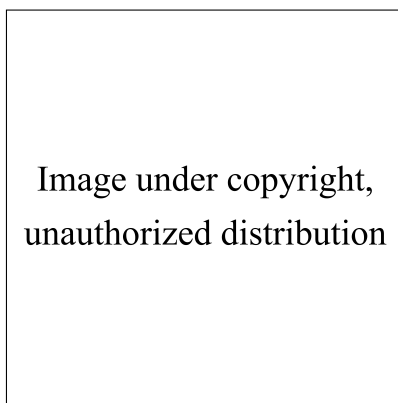


Fig. 5 Printing of electronics. (a) A roll-to-roll printing process, (b) A temperature sensor, (c) An electronic circuit with zoomed view of the transistor. Reprinted from Kumar [20].

like manufacturing of electric circuits and electronics [20], see Fig. 5, screen displays, lab-on-a-chip [21], solar cells [37] and 3D microstructures (polymer wires, needles, pillars, cones, or microspheres) [23]. There are many methods of printing, for example roll-to-roll printing, see Fig. 5(a), inkjet printing and gravure printing, see Fig. 6. One of the key motivations for the study of stretched liquid bridges is its close association with these printing processes. The printing industry deals with inks having non-Newtonian rheological properties. The advanced printing methods, like inkjet printing [38], flexographic printing [37], 3D printing [39] and gravure printing, use inks containing polymers. In printing, the liquid from one surface is transferred to another surface. The main issue is to calculate the volume of liquid transferred from one surface to another as the two surfaces are separated. In practice, successful printing involves both the transfer of a sufficiently large volume of liquid from one surface (a printing plate) to another (a substrate) and the preservation of the desired liquid shape, e.g., elongated shapes that could form wires [23]. In case of a stretched liquid bridge, solution pools are created on the end plates for Newtonian fluids, and a filament appears along with these solution pools for a viscoelastic liquid bridge. The transfer of the desired volume of liquid is a major challenge in the printing industry, due to complexities involving surface and liquid properties, along with the formation of filaments. Furthermore, capillary, viscous, inertial, elastic and gravitational forces play important role in this liquid transfer. Existing works have mostly focused on the impact of capillarity and liquid contact angles on a volume of Newtonian [40, 41] and viscoelastic [42, 43] liquid transferred to a substrate. However, no systematic studies on the influence of a polymer mass fraction (in viscoelastic fluids) and geometric properties (of a liquid bridge) on a liquid transfer are reported.

The present thesis mainly addresses the formation of drops on a filament and liquid transfer. We investigate the role of viscoelasticity and liquid bridge geometry in drop

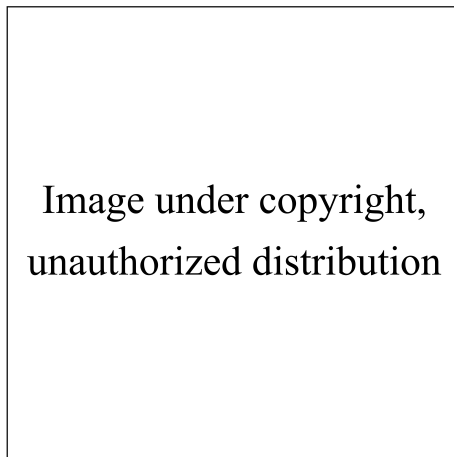


Fig. 6 A typical gravure printing process, showing the gravure roll with ink directed from doctor blade. Reprinted from Cen et al. [44].

dynamics of a BOAS structure and liquid transfer. This manuscript is organised in five chapters whose details are as follows:

- Chapter 1: This chapter gives a brief introduction about basic principles of rheology and viscoelastic fluids. Governing equations along with theoretical models describing the filament thinning are also discussed. Then, the present state of knowledge regarding the beads on a string and liquid transfer is documented. This chapter will establish a foundation for the thesis and will be useful in interpreting the experimental results.
- Chapter 2: The sample solutions tested, protocols for their preparation, and their rheological characterisation, both in shear and extensional flows are explained. The experimental setup used in the present study, along with the details of the instruments employed are given in this chapter. Details of experimental methods and image analysis to investigate both drops on a filament and liquid transfer are also provided. Finally, for numerical investigation, details of the geometry and meshes used, numerical schemes to solve the fundamental equations are described, together with preliminary numerical results.
- Chapter 3: This chapter deals with the experimental results obtained for the drops on a filament phenomenon. We present new space-time diagrams called 'diameter-space-time diagrams' and 'Hencky strain-space-time diagrams'. We further analyse these diagrams to investigate characteristic behaviours of BOAS instability and drop dynamics. Then, effect of different geometrical and stretching parameters on the formation of BOAS structure and drop dynamics are reported, together with preliminary numerical results.

- Chapter 4: This chapter focuses on the study of liquid transfer. The role of viscoelasticity in liquid transfer is investigated by varying polymer mass fractions in viscoelastic liquids, along with preliminary numerical results. We then explore the influences of geometrical and stretching properties, such as plate diameter, initial liquid bridge height, final stretching height and stretching speed, on liquid transfer for both viscoelastic and Newtonian fluids. In addition, the role of the initial liquid volume introduced in the liquid bridge is investigated.
- Chapter 5: Finally, the major conclusions drawn from the present study, along with the detailed observations, are presented in this chapter.



# Chapter 1

## Basic principles of rheology, beads on a string, liquid transfer, and numerical modelling

### Contents

---

<b>1.1</b>	<b>Elastic solid and viscous fluid</b> . . . . .	<b>2</b>
1.1.1	Elastic solids . . . . .	2
1.1.2	Viscous fluid . . . . .	3
<b>1.2</b>	<b>Governing equations</b> . . . . .	<b>4</b>
<b>1.3</b>	<b>Shear and extensional flows</b> . . . . .	<b>5</b>
<b>1.4</b>	<b>Constitutive equations and viscoelastic models</b> . . . . .	<b>8</b>
1.4.1	Maxwell model and Kelvin-Voigt model . . . . .	9
1.4.2	Jeffreys and Oldroyd-B models . . . . .	10
1.4.3	FENE-P model . . . . .	12
<b>1.5</b>	<b>Extensional rheology</b> . . . . .	<b>14</b>
<b>1.6</b>	<b>Review on beads on a string</b> . . . . .	<b>23</b>
<b>1.7</b>	<b>Review on liquid transfer</b> . . . . .	<b>33</b>
1.7.1	Contact lines and angles . . . . .	35
1.7.2	Effect of parameters . . . . .	38
1.7.3	Viscoelastic inks . . . . .	41
<b>1.8</b>	<b>Numerical modelling</b> . . . . .	<b>45</b>
<b>1.9</b>	<b>Summary of objectives of the present work</b> . . . . .	<b>48</b>

---

## 2 Basic principles of rheology, beads on a string, liquid transfer, and numerical modelling

---

Rheology is the study of the deformation of matter resulting from the application of a force [45]. Type of deformation response depends on the state of matter; for example, gases and liquids will flow when a force is applied, while solids will deform by a fixed amount and are expected to regain their shape when the force is removed. The term rheology was coined by Eugene C. Bingham, along with Markus Reiner [46]. Rheology generally deals with the behaviour of non-Newtonian fluids. Fluids are characterised as Newtonian and non-Newtonian fluids, based on the response of their viscosity with change in a rate of deformation. Newtonian fluids are named after Sir Isaac Newton, who first used an equation to establish the relation between the rate of deformation and shear stress for such fluids.

In this chapter, general definitions of non-Newtonian and viscoelastic fluids are described. After a general overview, extensional flows along with the capillary bridge thinning, formation of a filament, and extensional viscosity are discussed. Then, a current state of knowledge for drops on a filament and liquid transfer is presented, in addition to the numerical study of both phenomena. This analysis will be a useful guide for the interpretation of experimental results concerning drops on a filament and liquid transfer. Finally, the chapter is concluded with objectives of the thesis.

### 1.1 Elastic solid and viscous fluid

In this section, classical descriptions of solids and liquids in their simplest (non-tensorial) form are presented.

#### 1.1.1 Elastic solids

**Hooke's law** Hooke's law describes the behaviour of an ideal elastic solid (called Hookean solid). Hooke's law states that the applied stress (force per unit surface area),  $\tau$ , is proportional to the deformation,  $\gamma$ , by a factor  $G$  called shear modulus:

$$\tau = G\gamma. \quad (1.1)$$

Here, the example of a shear deformation is presented (see Fig. 1.1), where  $\tau$  is the shear stress and  $\gamma = \delta/L$  is the shear deformation or shear strain. However, for an extensional deformation, a strain,  $\kappa$ , is defined as a change in length divided by the original length. For the extensional deformation, a ratio of the stress to strain is called Young's modulus,  $E$ . Both  $G$  and  $E$  measure the stiffness of the solid in shear and extension, respectively; and are related

by  $E = 2G(1 + \bar{\nu})$ . Here,  $\bar{\nu}$  is the Poisson ratio defined as a ratio of transverse to axial strain in the direction of a stretching force.

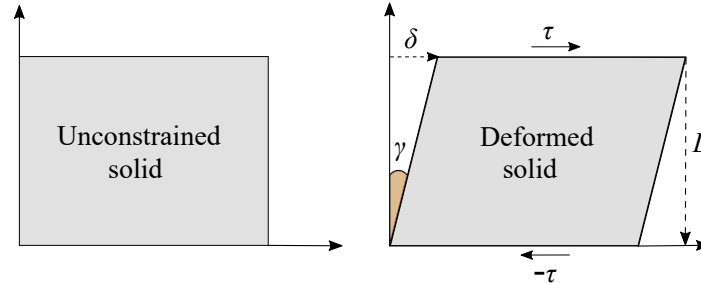


Fig. 1.1 An applied shear stress,  $\tau$ , on a solid leads to a deformation,  $\delta$ . The shear strain,  $\gamma$ , is given as:  $\gamma = \delta/L$ .

Hooke's law suggests that the material responds instantaneously to any mechanical deformation since it does not have any internal relaxation time. After a sudden deformation, the stress instantaneously switches from 0 to  $G\gamma$ . In addition, once the source of stress is removed, the Hookean body will always recover its original shape. Since the internal structure of the material is not affected by the deformation at all, it can be said that the Hookean body does not "flow," even if the stress is applied for a long time. The elastic deformations in the body are reversible and elasticity is in fact closely related to the idea of memory. Hence, a Hookean elastic solid is a limiting case of a material with infinite memory. Hooke's law is generally valid in the regime of small deformations. Above these deformations, the material starts creeping and it enters from the elastic regime into the plastic regime. In the plastic regime, the internal structure of the material is modified permanently.

### 1.1.2 Viscous fluid

**Newton's law** Newton's law of viscosity says the shear stress,  $\tau$ , in a fluid is directly proportional to the rate of deformation,  $\dot{\gamma}$ , by the factor  $\eta$ , which is defined as its shear viscosity, as shown in Eq. 1.2. Contrary to Hookean elastic solids, any stress  $\tau$  applied during a short time  $t$  causes a permanent and irreversible deformation i.e. the fluid will never spontaneously recover its previous internal structure once the stress is removed. Newton's law describes the behaviour of an ideal viscous fluid (called Newtonian fluid).

$$\tau = \eta \dot{\gamma} \quad ; \quad \eta = \frac{\tau}{\dot{\gamma}} \quad (1.2)$$

## 4 Basic principles of rheology, beads on a string, liquid transfer, and numerical modelling

Newton's law of viscosity is valid for both liquids with small molar mass and gases. Fluid viscosity is associated with the energy dissipation within the fluid and is due to internal friction between the molecules. At a macroscopic level, viscosity can be viewed as the resistance to deformation at a given shear rate. As shown in Fig. 1.2, a velocity gradient is created along  $y$  direction within the fluid as the bottom plate is fixed and the top plate moves with velocity,  $u$ . Hence, a shear flow is developed, and along the  $y$  direction, each fluid layer moves with a different average velocity. In the shear flow, viscosity describes the transfer of momentum due to molecular collisions between the different layers of the fluid. These collisions are affected by temperatures. Hence, it is important to carry out the shear viscosity measurements at a constant temperature.

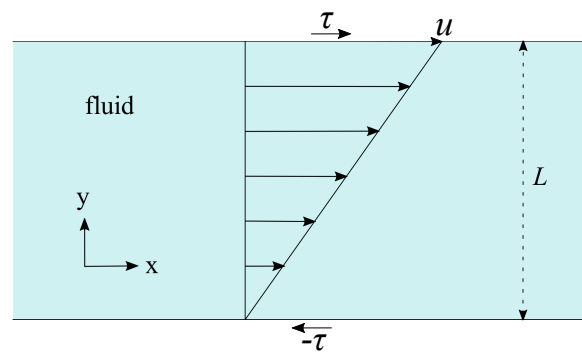


Fig. 1.2 Shear flow of a viscous fluid in-between two parallel plates separated by a distance  $L$ . The top plate is moved at a speed of  $u$  and the bottom plate is fixed.

## 1.2 Governing equations

The branch of physics dealing with the motion of continuous materials (rather than modelled as discrete particles), such as fluids and solids, is called continuum mechanics. The french mathematician Augustin-Louis Cauchy was the first to formulate the fundamental equations in 19<sup>th</sup> century. These equations include the conservation of mass and conservation of momentum. For isothermal, single-phase, unsteady flows and incompressible fluids, the basic governing equations are the mass conservation:

$$\nabla \cdot \underline{u} = 0 \quad (1.3)$$

and the momentum balance:

$$\rho \left( \frac{\partial \underline{u}}{\partial t} + (\underline{u} \cdot \nabla) \underline{u} \right) = -\nabla p + \nabla \cdot \underline{\underline{\tau}} + \underline{g}. \quad (1.4)$$

Here  $\underline{u}$  is the local velocity field,  $t$  is time,  $\rho$  is the material density (which is constant for isothermal and incompressible flow),  $p$  is the pressure within the fluid and  $\underline{\underline{\tau}}$  is the local stress tensor describing the internal forces arising at any position in the material during deformations. The conservation of momentum equation is also known as the Cauchy equation. In the present study, we only consider incompressible flows and symmetric stress tensors, i.e.  $\tau_{xy} = \tau_{yx}$ .

### 1.3 Shear and extensional flows

For the investigation of the mathematical structure of constitutive equations, two types of flows have been of particular interest: pure shear flows and pure extensional flows. These two flows will be discussed now.

**Shear flow** The velocity field and the associated strain rate tensor for a pure shear flow are

$$\underline{u} = \begin{cases} u_x = \dot{\gamma}y \\ u_y = 0 \\ u_z = 0 \end{cases} \quad \text{and} \quad \underline{\underline{D}} = \dot{\gamma} \begin{bmatrix} 0 & 1/2 & 0 \\ 1/2 & 0 & 0 \\ 0 & 0 & 0 \end{bmatrix} \quad (1.5)$$

where  $x$  and  $y$  are the direction of the flow and the direction of the velocity gradient, respectively, (see Fig. 1.2), and  $\dot{\gamma}$  is the shear rate. Here,  $\underline{\underline{D}}$  is the rate of deformation tensor, defined as:

$$\underline{\underline{D}} = \frac{1}{2} [(\underline{\underline{\nabla u}})^T + \underline{\underline{\nabla u}}] \quad \Rightarrow \quad D_{xy} = \frac{1}{2} \left( \frac{\partial u_x}{\partial y} + \frac{\partial u_y}{\partial x} \right) \quad (1.6)$$

where  $(\underline{\underline{\nabla u}})^T$  is the transpose of  $(\underline{\underline{\nabla u}})$  and  $\underline{\underline{\nabla u}}$  is the velocity gradient tensor. By symmetry, we can show that some components of the stress tensor are 0. The most general form of the stress tensor is then

$$\underline{\underline{\tau}} = \begin{bmatrix} \tau_{xx} & \tau_{xy} & 0 \\ \tau_{yx} & \tau_{yy} & 0 \\ 0 & 0 & \tau_{zz} \end{bmatrix} \quad (1.7)$$

The three important physical quantities are

- the shear stress,  $\tau_{xy} = \tau_{yx}$
- the first normal stress difference,  $N_1 = \tau_{xx} - \tau_{yy}$
- the second normal stress difference,  $N_2 = \tau_{yy} - \tau_{zz}$ .

The shear viscosity, also called apparent shear viscosity, is defined as

$$\eta \equiv \tau_{xy} / \dot{\gamma}. \quad (1.8)$$

**Extensional flow** The velocity field and the associated strain rate tensor for a pure extensional flow are

$$\underline{u} = \begin{cases} u_x = e_x \dot{\epsilon} x \\ u_y = e_y \dot{\epsilon} y \\ u_z = e_z \dot{\epsilon} z \end{cases} \quad \text{and} \quad \underline{\underline{D}} = \dot{\epsilon} \begin{bmatrix} e_x & 0 & 0 \\ 0 & e_y & 0 \\ 0 & 0 & e_z \end{bmatrix} \quad (1.9)$$

where,  $\dot{\epsilon}$  is called the extension rate. For incompressibility,  $e_x + e_y + e_z = 0$ . Two types of extensional flows are considered:

- for a three-dimensional extensional flow along  $x$ :  $e_x = 1$  and  $e_y = e_z = -1/2$
- for a planar extensional flow along  $x$ :  $e_x = -e_y = 1$  and  $e_z = 0$ .

The associated form of the stress tensor is

$$\underline{\underline{\tau}} = \begin{bmatrix} \tau_{xx} & 0 & 0 \\ 0 & \tau_{yy} & 0 \\ 0 & 0 & \tau_{zz} \end{bmatrix} \quad (1.10)$$

In the case of a three-dimensional extensional flow, since directions  $y$  and  $z$  are equivalent, there is only one normal stress difference  $\tau_{xx} - \tau_{yy}$  and the extensional viscosity is defined as

$$\eta_e \equiv \frac{\tau_{xx} - \tau_{yy}}{\dot{\epsilon}}. \quad (1.11)$$

The same definition of extensional viscosity applies to the planar case.

**Newtonian fluids** The constitutive equation in tensor form for incompressible Newtonian fluids is written as

$$\underline{\underline{\tau}} = 2\eta\underline{\underline{D}} \quad \Rightarrow \quad \tau_{xy} = \eta \left( \frac{\partial u_x}{\partial y} + \frac{\partial u_y}{\partial x} \right) \quad (1.12)$$

where  $\eta$  is the shear viscosity defined by Eq. 1.8. It is a constant parameter of the fluid, independent of the shear rate. Eq. 1.12 is the tensorial form of Newton's law of viscosity (Eq. 1.2). The normal components of the stress tensor,  $\underline{\underline{\tau}}$ , are 0 in a pure shear flow, i.e.  $N_1 = N_2 = 0$ , and the extensional viscosity is  $\eta_e = 3\eta$  for a three-dimensional pure extensional flow. Fluids which follow Eq. 1.12 are called Newtonian fluids. The main examples of Newtonian fluids are water, air and alcohol.

**Non-Newtonian fluids** Many complex fluids do not obey the Newton's law of viscosity (Eq. 1.2 and Eq. 1.12). There are many examples of so-called non-Newtonian fluids in nature (saliva, blood, egg-white, mud, magma, etc.), food (ketchup, sauces, soups, yoghurts, jams, mayonnaise), cosmetics (shampoo, cremes, toothpaste, gels, foams), civil engineering (concretes, paints) and industry (polymer melts, molten metals). Many models have been developed to predict behaviour of non-Newtonian fluids. For instance, an equation for power-law fluid is shown in Eq. 1.13, also known as Ostwald–de Waele relationship [47], where  $K$  is the flow consistency and  $n$  is the flow index. Values of  $n$  can be greater or less than one. If  $n = 1$ , then the fluid is a Newtonian fluid, recovering Eq. 1.2. The different behaviours of Eq. 1.13 are represented in Fig. 1.3.

$$\tau = K\dot{\gamma}^n \quad ; \quad \eta = K\dot{\gamma}^{n-1} \quad (1.13)$$

Moreover, non-Newtonian fluids are often categorised based on the change in their viscosity with respect to time and rate of deformation. Viscosity of time-dependent non-Newtonian fluids changes with the time duration of applied stress: viscosity of thixotropic fluids decreases with the time duration of applied shear stress and for rheopexy fluids, viscosity of fluid increases with the time duration of applied shear stress. Rheopexy fluids are also known as anti-thixotropic fluids because of their exact opposite behaviour, compared to thixotropic fluids. Additionally, the viscosity of non-Newtonian fluids may increase or decrease with the rate of deformation, as shown in Fig. 1.3(b), and, fluids are categorised as shear-thinning or shear-thickening. Shear-thinning fluids are also called pseudo-plastic fluids. For shear-thinning fluids,  $n < 1$  and for shear-thickening fluids,  $n > 1$ .

**Viscoelastic fluids** Viscoelastic fluids are special types of non-Newtonian fluids which exhibit both viscous, as well as elastic properties under an applied rate of deformation.

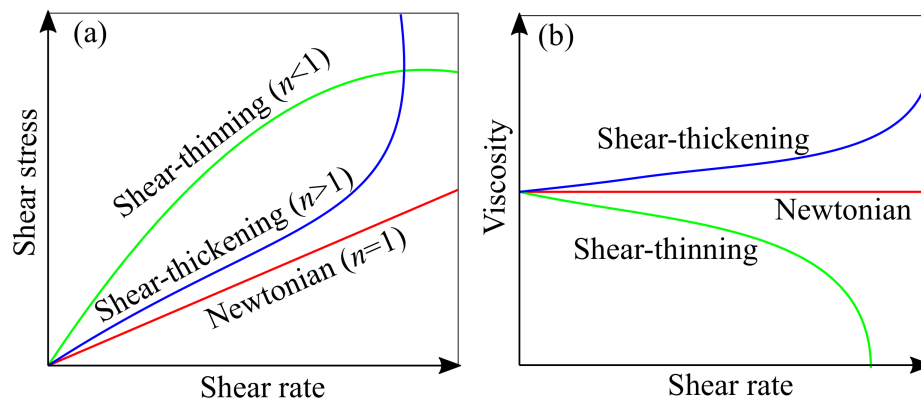


Fig. 1.3 Different types of responses, as a function of applied rate of deformation, for (a) shear stress and (b) viscosity, distinguishing the Newtonian and non-Newtonian behaviour of fluids, adapted from Plohl [48].

Additionally, their behaviour can be time-dependent, i.e. rheopectic or thixotropic. The main examples of viscoelastic fluids are saliva, egg white, polymer melts and solutions.

A polymer is a large molecule composed of chains or rings, of linked repeated small molecules, which are known as monomers. Polymers can be divided into two categories: natural polymers and synthetic polymers. Natural polymers are the polymers found in nature, such as silk, wool, proteins and deoxyribonucleic acid (DNA). Synthetic polymers are man-made polymers, obtained by chemical reactions in industries. Examples of synthetic polymers are polyvinyl chloride (PVC), polystyrene (PS), polyamide (PA or nylon), polyethylene oxide (PEO) and polyethylene glycol (PEG). Based on the structure of monomer chains, polymers are categorised as linear, branched-chain and cross-linked polymers. The polymers used in this study are linear.

## 1.4 Constitutive equations and viscoelastic models

The purpose of measuring rheological properties of materials is to provide parameters which enable a description of the fluid flow behaviour. Viscoelastic models are used to represent viscoelastic fluid flow behaviours. Behaviour of viscoelastic solutions resembles closely to different combinations of dampers (viscous elements) and springs (elastic elements). Different models have been developed, using these elements, to relate the stress tensor to the material deformation by establishing constitutive equations. Some of the important models related to this study are described below:

### 1.4.1 Maxwell model and Kelvin-Voigt model

Simplest forms of linear constitutive models used for viscoelastic fluids are the Maxwell model and the Kelvin-Voigt model, as shown in Fig. 1.4. In the Maxwell model, a dashpot and a spring are in a serial connection, while, in the Kelvin-Voigt model, a dashpot and a spring are in a parallel connection. The total deformation for both models is denoted as  $\gamma$  and the total stress for both models is denoted as  $\tau$ . The corresponding deformation and stress of the spring are denoted by  $\gamma_s$  and  $\tau_s$ , respectively. For the dashpot, the corresponding deformation and stress are shown by  $\gamma_d$  and  $\tau_d$ , respectively.

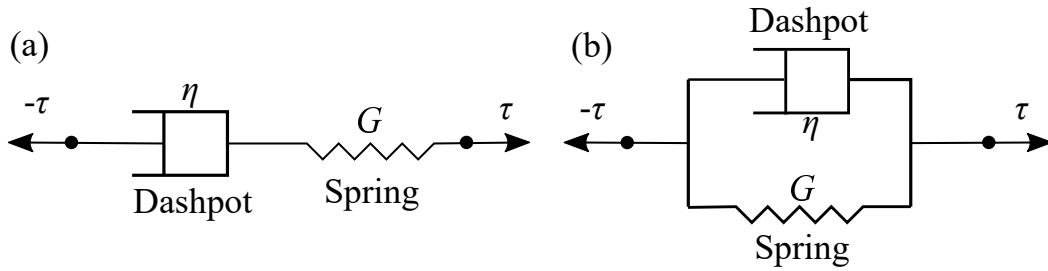


Fig. 1.4 (a) Maxwell model with a purely viscous damper of viscosity  $\eta$ , and purely elastic spring of elastic modulus  $G$ , in serial connection, (b) Kelvin-Voigt model with a purely viscous damper of viscosity,  $\eta$ , and purely elastic spring of elastic modulus,  $G$ , in parallel connection.

Hence, under the application of  $\tau$ , for Maxwell model, we can observe that  $\gamma = \gamma_s + \gamma_d$  and  $\tau = \tau_s = \tau_d$ . For Kelvin-Voigt model, we can observe that,  $\tau = \tau_s + \tau_d$  and  $\gamma = \gamma_s = \gamma_d$ . Then, the linearised Maxwell model is represented by

$$\tau + \frac{\eta}{G} \dot{\tau} = \eta \dot{\gamma} \quad (1.14)$$

and the general equation for the Kelvin-Voigt Model is given as:

$$\tau = G\gamma + \eta \dot{\gamma} \quad (1.15)$$

Here,  $G$  is the elastic constant of the material or shear modulus. The differential equation of the Maxwell model, Eq. 1.14, can be solved for step excitation of stress or deformation. The response represents the creep and relaxation functions, respectively [49, 50]. The Maxwell model can be further modified by introducing the Maxwell stress relaxation time,  $\lambda = \eta/G$ . Hence, Eq. 1.14 will become,

$$\tau + \lambda \dot{\tau} = \eta \dot{\gamma} \quad (1.16)$$

## 10 Basic principles of rheology, beads on a string, liquid transfer, and numerical modelling

The above linear models can be turned into convected models. Scalar stress and strain rate are replaced by stress and rate of deformation tensors,  $\underline{\underline{\tau}}$  and  $\underline{\underline{D}}$ , respectively. For convected models to be independent of the frame of reference, time derivatives of tensors are introduced. The Oldroyd convected derivative is a time derivative in a local coordinate system along the fluid flow [51]. The upper convected derivative of stress,  $\overset{\nabla}{\underline{\underline{\tau}}}$ , is given as,

$$\overset{\nabla}{\underline{\underline{\tau}}} \equiv \frac{\partial \underline{\underline{\tau}}}{\partial t} + \underline{\underline{u}} \cdot \underline{\underline{\nabla}} \underline{\underline{\tau}} - (\underline{\underline{\nabla}} \underline{\underline{u}})^T \cdot \underline{\underline{\tau}} - \underline{\underline{\tau}} \cdot \underline{\underline{\nabla}} \underline{\underline{u}}. \quad (1.17)$$

The Maxwell model in the upper convected form can be written as:

$$\underline{\underline{\tau}} + \lambda \overset{\nabla}{\underline{\underline{\tau}}} = 2\eta_0 \underline{\underline{D}}, \quad (1.18)$$

where  $\eta_0$  is the zero-shear-rate viscosity, i.e. the viscosity at low shear rates. The upper convected Maxwell model among other things is limited by its shear-rate independent viscosity [47].

### 1.4.2 Jeffreys and Oldroyd-B models

**Jeffreys model** Jeffreys model is a linear viscoelastic fluid model with two-time constants that was introduced in 1929 for the study of wave propagation in the Earth's mantle [47]:

$$\tau + \lambda \dot{\tau} = \eta_0 (\dot{\gamma} + \lambda_2 \ddot{\gamma}). \quad (1.19)$$

This model contains three independent parameters; the zero-shear-rate viscosity,  $\eta_0$ , and two material time constants: the stress relaxation time,  $\lambda$ , and the deformation retardation time,  $\lambda_2$ . These two polymeric time scales describe the rheological behaviour of viscoelastic liquids upon small deformations. For small deformations of a liquid element, the polymeric time scales  $\lambda$  and  $\lambda_2$  describe the stress relaxation after removal of strain and strain rate relaxation after removal of stresses, respectively.

**Oldroyd-B model** The upper convected equivalent of the Jeffreys model is identical to the Oldroyd-B model, introduced by Oldroyd in 1950 [51]. The Oldroyd-B model is given as:

$$\underline{\underline{\tau}} + \lambda \overset{\nabla}{\underline{\underline{\tau}}} = 2\eta_0 (\underline{\underline{D}} + \lambda_2 \overset{\nabla}{\underline{\underline{D}}}) \quad (1.20)$$

The Oldroyd-B model contains several other as special cases:

- If  $\lambda_2 = 0$ , the Oldroyd-B model reduces to the Maxwell model in the upper convected form (Eq. 1.18).
- If  $\lambda = \lambda_2$ , the Oldroyd-B model reduces to a Newtonian fluid with viscosity  $\eta_0$ .

There are different forms of the Oldroyd-B model and they are used depending upon the applications. Some of the important forms are listed below:

- Solvent-polymer stress splitting (SPSS)

This form was introduced by Bird et al. [47]. The Oldroyd-B equation is formulated in terms of the polymeric stress,  $\underline{\underline{\tau}}_p$ , and solvent stress,  $\underline{\underline{\tau}}_s$ , contributions to the stress:

$$\begin{aligned}\underline{\underline{\tau}} &= \underline{\underline{\tau}}_p + \underline{\underline{\tau}}_s, \\ \underline{\underline{\tau}}_s &= 2\eta_s \underline{\underline{D}}, \\ \underline{\underline{\tau}}_p + \lambda \frac{\nabla}{\nabla} \underline{\underline{\tau}}_p &= 2\eta_p \underline{\underline{D}}.\end{aligned}\tag{1.21}$$

After substitution of  $\underline{\underline{\tau}}_p = \underline{\underline{\tau}} - \underline{\underline{\tau}}_s$  in the last equation, one recovers Eq. (1.20) provided that  $\eta_0 = \eta_s + \eta_p$ , where  $\eta_p$  is polymer viscosity,  $\eta_s$  is solvent viscosity, and  $\lambda_2 = \lambda[\eta_s/(\eta_p + \eta_s)] = \lambda\eta_s/\eta_0$ . The ratio,  $\eta_s/\eta_0$ , is called viscosity ratio,  $S$ .

- Elasto-viscous stress splitting (EVSS)

This form was introduced by Perera and Walters [52] for stable numerical simulation. The Oldroyd-B equations are formulated in terms of Newtonian stress,  $\underline{\underline{\tau}}_n$ , and elastic stress,  $\underline{\underline{\tau}}_e$ , contributions to the stress:

$$\begin{aligned}\underline{\underline{\tau}} &= \underline{\underline{\tau}}_n + \underline{\underline{\tau}}_e, \\ \underline{\underline{\tau}}_n &= 2\eta_0 \underline{\underline{D}}, \\ \underline{\underline{\tau}}_e + \lambda \frac{\nabla}{\nabla} \underline{\underline{\tau}}_e &= -2\lambda \eta_{el} \underline{\underline{D}}\end{aligned}\tag{1.22}$$

After substitution of  $\underline{\underline{\tau}}_e = \underline{\underline{\tau}} - \underline{\underline{\tau}}_n$  in the last equation, one recovers Eq. 1.20 provided that  $\eta_{el} = [1 - (\lambda_2/\lambda)]\eta_0$ . The EVSS model does not use the solvent viscosity nor

the polymeric viscosity. Furthermore, calculations with this model require either the retardation time,  $\lambda_2$ , or the elastic viscosity,  $\eta_{el}$ , to be provided.

However, SPSS is the most popular form in numerical simulations compared to the EVSS method [53–56]. In the work by Amoreira and Oliveira [57], SPSS was more efficient than EVSS as the latter requires longer iterative cycles to converge. Also, in our numerical simulations, *rheoTool* only allows us to implement the SPSS form.

Polymer solutions may exhibit both stress relaxation and deformation retardation times [58]. These two material time constants, along with the zero-shear-rate viscosity are captured by the Oldroyd-B model and can be determined by rheological methods. The relaxation time can be measured experimentally using the Capillary Breakup Extensional Rheometer (discussed later in details in section 1.5) and retardation time can be measured experimentally using the oscillating drop method (discussed in appendix C). Even though the Oldroyd-B model provides satisfactory results in a simple steady shear flow, yet the model is limited by its shear-rate independent viscosity [47]. Moreover, the model fails to predict breakup of a filament seen in the experiments, and does not include the finite extensibility of polymers.

### 1.4.3 FENE-P model

The FENE-P model is one of the most commonly used constitutive equations that takes intrinsic nonlinearities into account. The model has been derived by Bird, Curtiss, Armstrong and Hassager [47] from the kinetic theory of dilute polymer solution where polymer molecules are modelled as “finitely extensible nonlinear elastic” (FENE) dumbbells. The Oldroyd-B model is also derived from this theory, however the polymer molecules are modelled as Hookean dumbbells, with a linear intrinsic stress-strain relationship. The FENE-P model and its key predictions for pure extensional flows are simply discussed here (see Bird et al. [47, 59], Herrchen and Öttinger [60] and Gaillard [61] for more detailed discussions).

The polymer contribution to the stress tensor can be written as

$$\underline{\underline{\tau}}_P = G(f\underline{\underline{A}} - \underline{\underline{I}}) \quad (1.23)$$

where

$$\lambda \overset{\nabla}{\underline{\underline{A}}} + f\underline{\underline{A}} = \underline{\underline{I}} \quad (1.24)$$

and

$$f = \left(1 - \frac{\text{tr}(\underline{\underline{A}})}{b}\right)^{-1} = 1 + \frac{3}{b} \left(1 + \frac{\text{tr}(\underline{\underline{\tau}}_P)}{3G}\right) \quad (1.25)$$

where  $\underline{\underline{A}}$  is a conformation tensor (defined in section 1.8),  $\underline{\underline{I}}$  is the unit tensor,  $G$  is the elastic modulus,  $\lambda$  is the relaxation time and  $\text{tr}$  is the trace of a tensor.  $f$  is a correction term accounting for non-linearity and finite extensibility,  $b$ , of the dumbbell.  $b$  is defined as a ratio of the polymer size at full extension to its size in the coiled state at equilibrium. Thus,  $b$  is a positive dimensionless parameter, usually greater than ten, which accounts for the finite extensibility of the polymer chains. For semi-dilute solutions,  $b$  is an effective value as FENE models do not take into consideration any chain-chain interaction. The Oldroyd-B model can be recovered for infinitely extensible polymers, i.e. for  $f_{b \rightarrow \infty} = 1$ .

**Extensional flow** For an extensional flow, the asymptotic values ( $t \rightarrow \infty$ ) of the stress components are given as:

$$\tau_{P,ii} = \frac{2e_i G \lambda \dot{\epsilon}}{f - 2e_i \lambda \dot{\epsilon}} \quad \text{where } i = x, y, z \quad (1.26)$$

and

$$f = 1 + \frac{3}{b} \left( 1 + \frac{\tau_{P,xx} + \tau_{P,yy} + \tau_{P,zz}}{3G} \right) \quad (1.27)$$

In the case of a three-dimensional extensional flow, the extensional viscosity,  $\eta_e \equiv (\tau_{xx} - \tau_{yy})/\dot{\epsilon}$  is given as

$$\begin{cases} (\eta_e - 3\eta_s)/G\lambda = 2/(f - 2\lambda\dot{\epsilon}) + 1/(f + \lambda\dot{\epsilon}) \\ f^3 - [\lambda\dot{\epsilon} + 1 + 3/b]f^2 + [\lambda\dot{\epsilon}(1 + 3/b) - 2(\lambda\dot{\epsilon}^2)]f + 2(\lambda\dot{\epsilon})^2 = 0 \end{cases} \quad (1.28)$$

for which there is no simple analytical expression. The two limiting scalings are

$$\eta_e - 3\eta_s = \begin{cases} 3G\lambda b/(b+3) & \text{for } \lambda\dot{\epsilon} \rightarrow 0 \\ 2G\lambda b & \text{for } \lambda\dot{\epsilon} \rightarrow +\infty \end{cases} \quad (1.29)$$

Considering the polymer contribution to the zero-shear viscosity, i.e.  $\eta_P = \eta_0 - \eta_s$ , we obtain

$$\frac{\eta_e - 3\eta_s}{\eta_0 - \eta_s} = \begin{cases} 3 & \text{for } \lambda\dot{\epsilon} \rightarrow 0 \\ 2(b+3) & \text{for } \lambda\dot{\epsilon} \rightarrow +\infty \end{cases} \quad (1.30)$$

The FENE-P model is more realistic than the Oldroyd-B model since shear thinning behaviour is allowed. It has been successfully used to describe, at least qualitatively, many physical phenomena including the breakup stage of thinning filaments [12, 15].

### 1.5 Extensional rheology

Industrial processing of viscoelastic polymer solutions is usually a combination of shear and extensional flows. Therefore, rheological characterisation of solutions in both shear and extensional flows is necessary to optimise the properties of the final products. We now explain how to experimentally measure the relaxation time and the extensional viscosity of a viscoelastic liquid. There are different types of extensional rheometers available depending upon the applications. Details of extensional rheometers along with their applications can be found in a handbook by Tropea and Yarin [49]. One of the most popular devices to measure these extensional properties of polymer solutions is the Capillary Breakup Extensional Rheometer (CaBER). In order to produce an extensional flow, we use the well-documented filament thinning technique, using CaBER, described by Anna and McKinley [1]. It is a standard technique and is now used by many authors [9, 14, 62, 63]. CaBER is a filament stretching extensional rheometer, as it monitors thinning of a liquid filament, formed after stretching of a liquid bridge, connecting two circular end plates. A typical protocol is the following one. A droplet of liquid is placed between two horizontal plates with diameter  $D_P$  or radius  $R_P$ , see Fig. 1.5, like a drop of saliva between a thumb and index finger. Hence, a liquid bridge is formed with an initial diameter,  $D_0$ , or radius,  $R_0$ , and an initial height,  $L_0$ . At this point, the liquid bridge diameter and the plate diameter are the same  $D_0 = D_P$ . Then, the bottom plate is kept fixed and the upper plate is moved upwards to a final stretching height,  $L$ . The liquid bridge starts necking and a filament connecting the two solution pools undergoes a succession of thinning regimes until the final breakup. The filament thinning process is recorded in order to measure the filament diameter,  $D(t)$ , as a function of time,  $t$  (experimental details are given in the next chapter). The stretching of the liquid bridge can be defined using dimensionless quantities called the aspect ratio. The initial aspect ratio,  $IAR$ , can be defined as  $IAR = L_0/R_P$ , and the final aspect ratio,  $FAR$ , can be defined as  $FAR = L/R_P$ .

A global picture of the filament thinning process of complex fluids can be found in the review article published by McKinley [12]. Capillary forces hold an initial fluid sample in-between two plates. When the two plates are separated by a distance  $L_0$ , the liquid bridge (or filament) becomes unstable above a critical separation height. It is thus essential that the initial plate separation height,  $L_0$ , is small enough to support a static liquid bridge. Moreover,

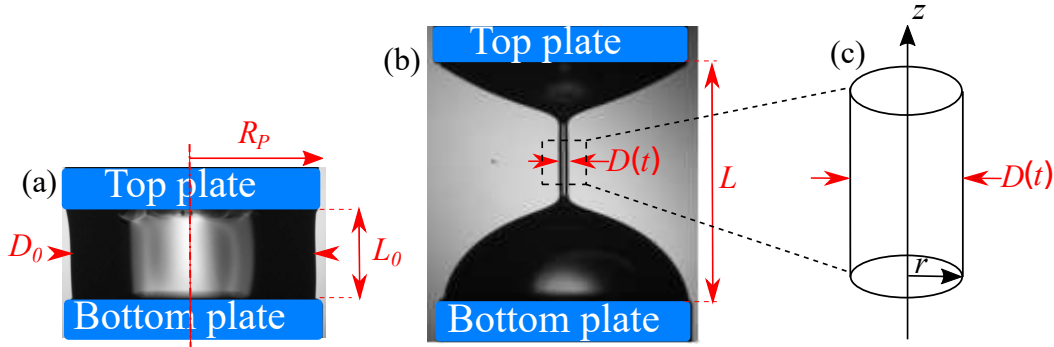


Fig. 1.5 (a) Liquid bridge with initial diameter,  $D_0$ , initial height,  $L_0$  and plate radius,  $R_P$ . (b) Stretched liquid bridge with filament diameter,  $D(t)$ , and final stretching height,  $L$ . (c) Schematic representation of a cylindrical filament.

due to axial gravity, the liquid bridge stability depends on both the fluid volume introduced and the Bond number,  $Bo$ .

**Bond number** Gravitational effects on the liquid bridge are characterised by a dimensionless number, called the Bond number,  $Bo$ . The name commemorates the English physicist Wilfrid Noel Bond [64]. The Bond number represents the balance between gravitational forces and surface tension (capillary) forces:

$$Bo = \frac{\rho g D_P^2}{4\sigma} \quad (1.31)$$

In order to keep the initial configuration close to a cylindrical shape, capillary breakup tests typically employ axial separations equivalent to a condition:  $L_0 \leq l_{cap}$  or  $IAR \leq 1/\sqrt{Bo}$  [14].  $l_{cap}$  is the capillary length of a liquid bridge given as:  $l_{cap} = \sqrt{\sigma/\rho g}$ , where  $\sigma$  is the surface tension of the fluid,  $g$  is the gravitational acceleration and  $\rho$  is the density of the fluid. For  $IAR$  larger than the conditional value, the liquid bridge can ‘sag’ and the stability of the bridge can get affected [12, 14, 65]. In the present thesis,  $Bo$  is varied from 0.66 to 2.88, by using three different plate diameters.

**Stability of a liquid bridge** The filament break-up experiments typically start with a cylindrical-shaped liquid bridge and the total physical volume remains constant as the bridge is elongated axially. The stability of the liquid capillary bridge, formed between two equal-sized plates can be represented by a single closed curve, as shown in Fig. 1.6. The dimensionless volume,  $V_D$  is plotted against the slenderness ratio,  $\Lambda = L_0/D_P = IAR/2$ , to present different initial liquid bridge shapes. Here,  $V_D$  is defined as the ratio of physical

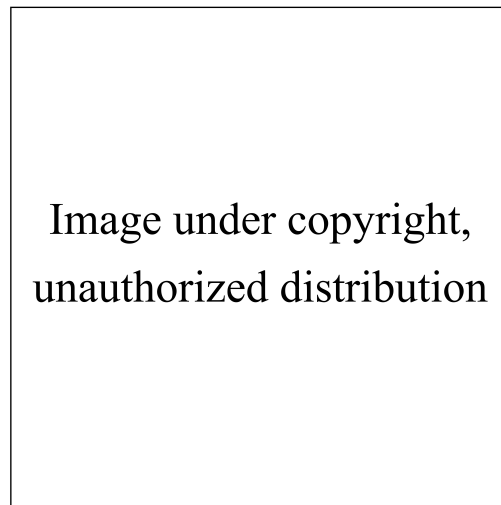


Fig. 1.6 Stability curve for the liquid bridge. Liquid bridge configurations represented by points inside this stability limit curve are stable, while those lying outside are unstable. Curve AB indicates moving contact line, curve BC characterises the minimum liquid volume required and curve AC represents the maximum liquid volume that can be placed in-between two plates. Modified from Bezdenejnykh et al. [66].

volume introduced in the liquid bridge to the cylindrical volume with same  $L_0$  and  $D_p$ . Inside the stability limit enclosed curve, liquid volumes are stable and will not breakup, whereas liquid volumes outside the curve are unstable [66]. This stability curve can be characterised into three different regimes. For the smaller values of dimensionless volumes and the slenderness ratios, the liquid contact line is not pinned to the edges of disks, as represented by the curve AB. The curve BC governs the minimum volume required, characterised by the axisymmetric break-up of the bridge, and called 'minimum volume stability limit'. The breakup of the capillary bridge is observed outside of this curve. The third curve, AC, refers to the maximum volume limit of the bridge, over which the liquid bridge becomes unstable and overflows. In the experiments discussed in the thesis, precautions are taken to make sure the initial liquid bridge will be inside the stability curve.

**Force Balance on a slender filament** When a liquid bridge is stretched, it starts thinning due to capillary forces and a filament along with solution pools is formed, as shown in Fig. 1.5(b). Due to gravitational sagging, the filament diameter is a function of altitude,  $z$ , as  $D(z,t)$ . For slender filaments (i.e. filaments for which  $\partial D/\partial z \ll 1$ ), mathematical analysis are often simplified by neglecting axial curvature caused by sagging. Hence, a simplified force balance equation can be written assuming a filament with a constant diameter,  $D(t)$ , or radius,  $R(t)$ , see Fig. 1.5(c). In this context, the extensional flow has an axial component

$u_z = \dot{\epsilon}z$  and a radial component  $u_r = -\dot{\epsilon}r/2$ , where  $\dot{\epsilon}$  is the extension rate. Since  $u_r$  at  $r = R(t)$  must be equal to  $\dot{R}(t) = dR/dt$ , we have

$$\dot{\epsilon} = -\frac{2\dot{R}(t)}{R(t)} = -\frac{2\dot{D}(t)}{D(t)} \quad (1.32)$$

When the filament thins down to diameter,  $D(t)$ , the total deformation in the element is given by the logarithmic or Hencky strain [67, 68]:

$$\epsilon(t) = \int_0^t \dot{\epsilon}(t^*) dt^* = 2\ln[D_0/D(t)] \quad (1.33)$$

The general form of the force balance for slender viscoelastic filaments was established by McKinley [12] and Tirtaatmadja et al. [69]. Considering inertial, capillary, viscous and elastic forces, the force balance equation can be written as,

$$\frac{1}{2}\rho\dot{R}(t)^2 \approx \frac{F_z(t)}{\pi R(t)^2} - \frac{\sigma}{R(t)} - 3\eta_s\dot{\epsilon} - [\tau(t)_{p,zz} - \tau(t)_{p,rr}] \quad (1.34)$$

Here,  $\sigma/R(t)$  is a capillary pressure,  $3\eta_s\dot{\epsilon}$  is the net viscous extensional stress,  $[\tau(t)_{p,zz} - \tau(t)_{p,rr}]$  is the time-evolving non-Newtonian polymeric stress difference and  $F_z(t)$  is the unknown tensile force in the filament. The solution pools formed at the end plates serve as quasi-static reservoirs which soak up the fluid drained into them from the radially-contracting filament. They also enable the no-slip boundary condition at the plates, which would otherwise induce a radial shear flow at the liquid contact lines on the plates. In CaBER experiments, since there is no external stretching (contrary to fibre-spinning-like experiments for example), the axial force on the filament can be given as  $F_z(t) = 2\pi\sigma R(t)$ . Hence, Eq. 1.34 can be written as,

$$\frac{1}{2}\rho\dot{R}(t)^2 \approx \frac{\sigma}{R(t)} - 3\eta_s\dot{\epsilon} - [\tau(t)_{p,zz} - \tau(t)_{p,rr}] \quad (1.35)$$

However, according to the numerical simulations for viscoelastic solutions by Li and Fontelos [2], the axial force is actually  $F_z(t) \approx 3\sigma R(t)$ . Hence, the theoretical approximated value of  $F_z$  is acceptable, and will only result in moderate errors in the prefactor of the final result.

**Ohnesorge number** Wolfgang von Ohnesorge introduced in 1936 [70] a dimensionless number, later called the Ohnesorge number,  $Oh$ , that relates viscous forces to inertial and

## 18 Basic principles of rheology, beads on a string, liquid transfer, and numerical modelling

surface tension forces [71], as shown in Eq. 1.36. If  $Oh > 1$ , the viscous effects will dominate the filament thinning. The thinning will be controlled by inertia if  $Oh < 1$ . In the present work, we are able to achieve a wide range of  $Oh$  from  $10^{-3}$  to 4.91 by varying polymer solutions and liquid bridge properties.

$$Oh = \frac{\eta_0}{\sqrt{\rho\sigma R_P}} \quad (1.36)$$

**Deborah number** To characterise the material behaviour in time, Reiner [46] introduced a dimensionless number, called Deborah number,  $De$ . A natural or intrinsic Deborah number [12, 14, 72] for free surface viscoelastic flows, represents a ratio of time scales for the elastic stress relaxation,  $\lambda$ , to the ‘Rayleigh time scale’,  $t_R$ , as shown in Eq. 1.37. The Rayleigh time scale is a characteristic time scale for phenomena dominated by the interplay of capillarity and inertia.

$$De = \frac{\lambda}{t_R} = \frac{\lambda}{\sqrt{\frac{\rho D_P^3}{8\sigma}}} \quad (1.37)$$

This definition of Deborah number has been widely used before [3, 9, 12, 56, 72] and is based on material properties and plate diameter. Note that other definitions of  $De$  are possible, where Deborah number is defined as  $\lambda/(\eta_0 D_P/2\sigma)$  [3, 43]. Mainly,  $De$  represents a balancing of the elastic, capillary and inertial forces. For  $De \gg 1$ , the material shows elastic solid-like behaviour, while for  $De \ll 1$ , viscous fluid-like behaviour. If  $De \approx 1$ , the material behaviour can be regarded as a viscoelastic liquid.

**Dynamics of filament thinning** The relevant solution for a particular experimental configuration depends on relative magnitudes of the visco-capillary, inertio-capillary and viscoelastic time scales denoted  $t_v$ ,  $t_R$  and  $\lambda$ , respectively. Here, the viscous time scale,  $t_v$ , is defined as  $t_v = \eta_0 R_P/\sigma$ . Hence,  $Oh$  can be rewritten as a ratio of viscous to Rayleigh time scales,

$$Oh = \frac{t_v}{t_R} \quad (1.38)$$

**Newtonian liquids** For a Newtonian liquid of viscosity  $\eta$ , close to filament breakup, two different behaviours can be observed depending on the relative importance of inertia and viscosity. If inertia overcomes fluid viscosity ( $Oh \ll 1$ ), the force balance equation (Eq. 1.35) reduces to  $\rho \dot{R}(t)^2/2 \approx \sigma/R(t)$ . On the contrary, if fluid viscosity overcomes inertia ( $Oh \gg 1$ ), the force balance equation (Eq. 1.35) becomes  $3\eta_s \dot{\epsilon} \approx \sigma/R(t)$ . Therefore, the respective *inertio-capillary* ( $Oh \ll 1$ ) and *visco-capillary* ( $Oh \gg 1$ ) thinning regimes can be written, as

[12, 14, 61]:

$$R(t)/R_0 = \begin{cases} X \left( \frac{t_b - t}{t_R} \right)^{2/3} & \text{for } Oh \ll 1 \\ X_2 \left( \frac{t_b - t}{t_v} \right) = 0.0709 Oh^{-1} \left( \frac{t_b - t}{t_R} \right) & \text{for } Oh \gg 1 \end{cases} \quad (1.39)$$

Here,  $t_b$  is the filament breakup time. A careful analysis of past measurements in the *inertio-capillary* regime reveals the dimensionless prefactor,  $X$ , exhibits a complex and nonmonotonic behaviour. Early theoretical and experimental studies [14, 63, 69, 73, 74] reported or utilised values of  $X$  in the range of 0.6 to 0.8. However, Deblais et al. [11] and Dinic and Sharma [75] obtained values of the prefactor  $X$  in the range of 0.3 to 0.4. Furthermore, recent numerical simulations by Figueiredo et al. [56] show that the value of prefactor  $X$  depends on  $Oh$ . The authors found that as  $Oh$  decreases, the prefactor increases and  $X = 0.19$  was reported for  $Oh = 0.1$ .

**Viscoelastic liquids** For viscoelastic solutions, thinning dynamics are different in the later stages due to presence of polymers. Initially, a self-similar *inertio-capillary* ( $Oh \ll 1$ ) or *visco-capillary* ( $Oh \gg 1$ ) thinning occurs depending on the value of  $Oh$ . When the stretched liquid bridge suddenly switches to a slender filament shape, the filament diameter decays exponentially at a rate of  $(3\lambda)^{-1}$  with a prefactor, as shown in Eq. 1.40. This thinning is called *elasto-capillary* thinning and during this transition, elastic stresses become dominant due to the rapid stretching of polymer molecules. Physically, in this regime, we obtain a balance of the elastic modulus,  $G = \eta_p/\lambda$ , and ‘squeezing’ effects due to capillary pressure [12].

$$\frac{D(t)}{D_0} = \left( \frac{GD_0}{4\sigma} \right)^{1/3} \exp\left( \frac{-t}{3\lambda} \right) \quad (1.40)$$

As the mass fraction of polymer increases, the elasto-capillary thinning process slows down as a consequence of the increase in the material relaxation time. In the later stages of filament thinning, two effects become evident. Firstly, the thinning diameter systematically deviates from the exponential behaviour due to the finite extensibility of the polymer chains. When the polymer chains reach their full length, the extensional viscosity reaches a plateau value and the liquid behaves like a Newtonian fluid [76]. The filament diameter then decreases linearly with time, see Eq. 1.41. Hence, filament thinning shows quasi-Newtonian behaviour, characterised by a constant observed extensional viscosity,  $\eta_T$ .

$$D(t) = D_0 - (\sigma/\eta_T)t. \quad (1.41)$$

Secondly, the discrete resolution of the laser micrometer can create a ‘stair casing’ like structure in the measured evolution of the filament diameter with time.

**Extensional viscosity** In the elasto-capillary regime, inertia is negligible. Hence, using the force balance equation (Eq. 1.35), the normal stress difference,  $\tau(t)_{zz} - \tau(t)_{rr}$ , in the filament can be estimated.

$$\frac{\sigma}{R(t)} \approx 3\eta_s \dot{\epsilon} + [\tau(t)_{p,zz} - \tau(t)_{p,rr}] \quad (1.42)$$

where  $\tau(t)_{zz} - \tau(t)_{rr} = [\tau(t)_{s,zz} - \tau(t)_{s,rr}] + (\tau(t)_{p,zz} - \tau(t)_{p,rr})$  and the net viscous extensional stress,  $\tau(t)_{s,zz} - \tau(t)_{s,rr} = 3\eta_s \dot{\epsilon}$ . The "apparent extensional viscosity" can be defined as

$$\eta_E = \frac{\tau(t)_{zz} - \tau(t)_{rr}}{\dot{\epsilon}} \quad (1.43)$$

By considering Eq. 1.32 and Eq. 1.42, the apparent extensional viscosity can be directly estimated from the experiments as

$$\eta_E = -\frac{\sigma}{2\dot{R}(t)} = -\frac{\sigma}{\dot{D}(t)} \quad (1.44)$$

Finitely extensible nonlinear elastic (FENE) dumbbell models predict that  $\eta_E$  reaches a plateau value, known as the terminal extensional viscosity,  $\eta_T$ . Yet, according to theory [77], polymer chains are stretched about one-tenth of the extension limit. For the FENE-P model, using Eq. 1.30, the terminal extensional viscosity is given by [12, 78]

$$\eta_E \rightarrow \eta_T = 3\eta_s + 2b\eta_p. \quad (1.45)$$

Here, the value of  $b + 3$  in Eq. 1.30 with FENE-P model is replaced by  $b$  and as we are mainly interested in the order of magnitude of  $b$ , this will not have any consequences in later discussions.

However, there are different methods to measure the extensional viscosity of the solutions. The extensional viscosity can be measured using a micro weight-balance or using the "apparent extensional viscosity" method. Sridhar et al. [79] used a micro-balance to experimentally measure the extensional viscosity. The Trouton ratio, which is the ratio of the extensional viscosity,  $\eta_e$ , to the constant shear viscosity,  $\eta_0$ , is found to be increasing with time from the initial value of 3, to  $10^3$  but it does not attain the steady value. Hence, the authors did not attain the terminal extensional viscosity. Berg et al. [80] measured the extensional viscosity, by stretching liquid bridges, under microgravity. The axial force required to stretch the bridge,

was measured with time. Newtonian, as well as viscoelastic fluids, were tested. Silicone oil was used as a Newtonian fluid. Aqueous solutions of acrylamide polymer, in various concentrations, were used as viscoelastic fluids. Initially, both Newtonian and viscoelastic fluids showed the same behaviour where the extensional viscosity increased to three times the shear viscosity. Then, the extensional viscosity remained constant for the Newtonian fluid. But for viscoelastic fluids, the extensional viscosity keeps on increasing and did not attain the terminal extensional viscosity. Additionally, the extensional viscosity increases linearly with increase in the Hencky strain. Here, the Hencky strain is defined as  $\varepsilon = \ln[L(t)/L_0]$ , where  $L(t)$  and  $L_0$  are the instantaneous and initial lengths of a cylindrical section. Moreover, with the increase in polymer concentration, the extensional viscosity is also found to be increasing.

Furthermore, previously either the midpoint diameter, [1, 78] or the neck diameter [81], of a filament were used to calculate the apparent extensional viscosity. The use of midpoint diameter,  $D_{mid}(t)$ , to calculate the apparent extensional viscosity was proposed by Schümmer and Tebel and was later implemented by Anna and McKinley [1]:

$$\eta_E = -\frac{\sigma}{dD_{mid}/dt}. \quad (1.46)$$

Gaillard et al. [78] measured the apparent extensional viscosity using a custom-made capillary breakup extensional rheometer. Solutions of polyethylene oxide (PEO), with  $M = 8 \times 10^6$  g/mol, in a solvent made of water and polyethylene glycol (PEG) with  $M = 8000$  g/mol was used. The concentration of PEG was fixed with 20 wt% and the concentration of PEO was varied from 0 to 0.4 wt%. Additionally, aqueous solutions of HPAM and NaCl were used. A liquid bridge with  $D_P = 3$  mm, was stretched from initial aspect ratio,  $L_0/R_P \approx 1$  to final aspect ratio,  $L/R_P \approx 2.4$ . The apparent extensional viscosity,  $\eta_E$ , was plotted against the Hencky strain,  $\varepsilon$ , as shown in Fig. 1.7(a). The extensional viscosity increased with the increase in PEO concentration for aqueous solutions of PEO and PEG. Dinic et al. [81] implemented dripping-onto-substrate extensional rheometry and measured optically the apparent extensional viscosity,  $\eta_E$ , for aqueous solutions of PEO with lower molecular weight ( $M = 10^6$  g/mol) than the one used in the present study. The concentration of PEO was varied from 0.01 to 0.3 wt%. The solutions were dispensed through a nozzle with 0.419 mm inner radius onto a glass substrate located at a fixed distance,  $H = 2.514$  mm. The apparent extensional viscosity,  $\eta_E$ , was calculated as,  $\eta_E = -\sigma/(dD_{neck}/dt)$  and plotted, see Fig. 1.7(b), against Hencky strain,  $\varepsilon = 2 \ln[D_0/D_{neck}(t)]$ . Similar to Berg et al. [80] and Gaillard et al. [78], the increase in polymer concentration leads to an increase in the extensional viscosity before pinch-off. In the present study, we will implement a similar

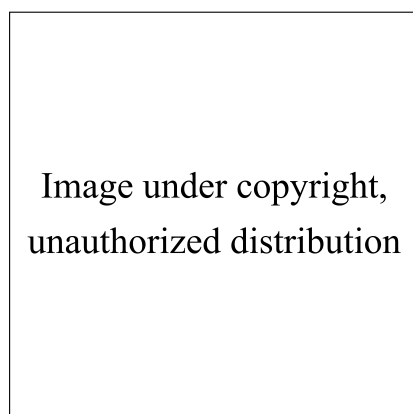


Fig. 1.7 (a) Apparent extensional viscosity as a function of Hencky strain for PEO solutions with 20 wt% PEG solvent and for HPAM solutions using a capillary breakup extensional rheometer. Adapted from Gaillard et al. [78]. (b) Extensional viscosity as a function of Hencky strain for PEO solutions in dripping-onto-substrate extensional rheometry. Reprinted from Dinic et al. [81].

method as Dinic et al. [81] as we use the minimum diameter of the filament to calculate  $\eta_E$ . This approach helps to extract  $\eta_E$  in the neck diameter of the filament.

**Effect of final stretching height** There have been limited studies on the effect of final stretching height on the thinning of a liquid capillary bridge. Rodd et al. [14] investigated the filament thinning using CaBER for aqueous PEO solutions ( $M = 2 \times 10^6$  g/mol) for different final stretching heights ( $FAR \approx 2.9$  to 4). The authors reported that relaxation times remain unchanged with the increase in final aspect ratios. Later, Miller et al. [83] reported a similar behaviour where relaxation times remained unchanged against final aspect ratios ( $FAR = 3$  to 15) for 1 wt.% aqueous polyacrylamide (PAA) solution. Furthermore, when plotted against the Hencky strain, extensional viscosities of the solutions remained unaffected with  $FAR$ . The extensional viscosity evolution of polymer solutions was found to be independent of  $FAR$  once the elasto-capillary balance had been reached. However, in case of wormlike micelle solutions of cationic surfactant cetylpyridinium chloride (CPyCl) and sodium salicylate (NaSal) dissolved in a solution of 100 mM NaCl in distilled water, the Trouton ratio was found to decrease by more than a factor of four as the stretch length was increased from  $FAR = 3$  to  $FAR = 7$ . Furthermore, a decay of relaxation times when increasing from  $FAR = 3$  to  $FAR = 7$  was also reported for CPyCl/NaSal solutions. On the contrary, Kim et al. [84] found an opposite behaviour as relaxation times increase with  $FAR$  was increased from 1.6 to 3.4. According to the authors, this discrepancy could be differences in fundamental properties of wormlike micellar material, but it could be also due to lower values of  $FAR$ . However,

in the present thesis, we investigate filament thinning for aqueous solutions of PEO. Hence, only the findings of Rodd et al. [14] and Miller et al. [83] for the effect of *FAR* on polymer solutions are useful.

## 1.6 Review on beads on a string

In this thesis, the stretching of a liquid bridge is considered and we use aqueous solutions of polyethylene oxide (PEO) and polyethylene glycol (PEG) to create viscoelastic solutions. Hence, in the following text, the relevant literature on filament thinning and formation of BOAS structure, mainly using PEO solutions and stretched liquid capillary bridge are reviewed.

**Formation of BOAS structure** Once extensional viscosity reaches a plateau value, necking occurs at the ends of a filament and the filament then undergoes a Rayleigh-Plateau-like instability. This instability leads to formation of a drop-like pattern on a thin column of viscoelastic liquid, called as the beads on a string [7, 9, 16, 85]. However, BOAS structure is clearly not a simple Rayleigh-Plateau like instability since the beads are very far apart [18, 74, 86]. A "blistering" instability could be a secondary instability leading to smaller beads on a thinner string and sometimes observed at the final stages of thinning. A blistering pattern is superficially similar to a BOAS structure and it is characterised by small droplets that form in between the initially formed BOAS structure. Deblais et al. [18] demonstrated that BOAS and blistering instabilities have self-similar origins. A BOAS structure is controlled by an interplay between capillary and elastic forces and induced by local symmetry breaking in a fluid neck. On the other hand, a blistering instability is due to a dynamical phase separation that takes place in an elongational flow. The phase separation is induced by combined effects of temperature and inhomogeneities of polymer concentration in a polymer filament. Sattler et al. [86] demonstrated that the amplitude of higher generations of drops follows a temporal evolution that starts with an exponential growth and then switches to a power law growth. In this power law growth, a connecting filament pumps solution into drops. As a result, volume of the filament decreases as volume of drops increases. Furthermore, in a blistering pattern, droplets are arranged off-axis relatively to the filament [86], as shown in Fig. 1.8(a). When a BOAS structure was dried, magnified images obtained using a scanning electron microscopy, Fig. 1.8(b)-(d), indicate a thin solid filament. The filament showed the properties of a purely elastic fibre, suggesting phase separation. Even though the filament is in a stretched state, polymers in (liquid) drops are in a relaxed state.

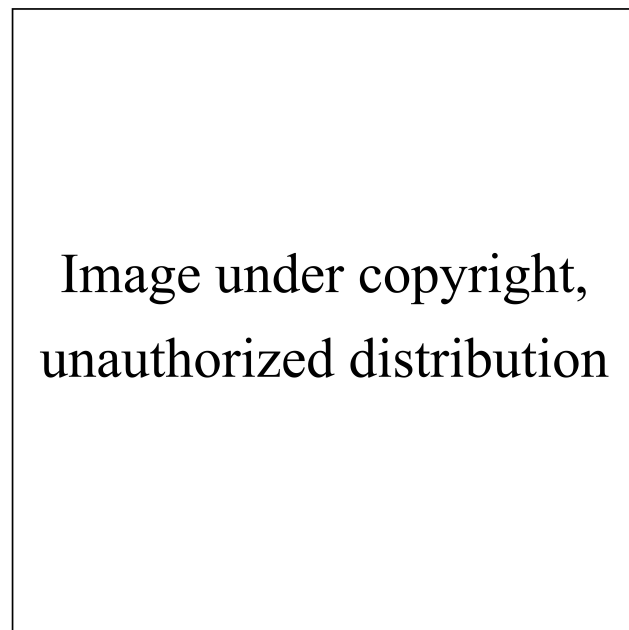


Fig. 1.8 (a) Shadowgraphic image of a beads on a string phenomenon, (b) Scanning electron microscopy image of two drops, connected by a filament (for a BOAS structure dried on a substrate), (c) Another example of the structure, (d) Magnified view of (c). Reprinted from Sattler et al. [86].

In a BOAS structure, the simple one-dimensional force balance equation (Eq. 1.35) becomes invalid. Furthermore, since finite extensibility effects are now important, characteristic *elasto-capillary* thinning equation Eq. 1.40 is not valid anymore. Linear stability analysis by Chang et al. [85] showed that for low viscosity elastic fluids, in the later stages of a BOAS formation, an additional phenomenon introduced as ‘iterated stretching’, should develop in which elasticity, capillarity and inertia are all significant. The authors investigated formation mechanism for a BOAS structure and dynamics at filament necks for viscoelastic liquid jets using 1D Oldroyd-B model. Their numerical calculations indicate that the neck region connecting the primary drop to the elastically dominated cylindrical filament is unstable to small perturbations that further triggered a new instability, called as “elastic recoil” [12] or simply "recoil" [85] of the filament. This elastic recoil leads to formation of a smaller “secondary” spherical drop connected to the primary drop by a new thinner cylindrical filament. This new filament subsequently thins under the action of capillarity. Necks connecting the new filament to the primary drop and the new secondary drop may once again become unstable. This further results in another elastic recoil and formation of a smaller secondary drop connected to the main drop by a finer-scale filament. However, this structure is itself unstable to perturbations and this process of ‘iterated stretching’ repeats

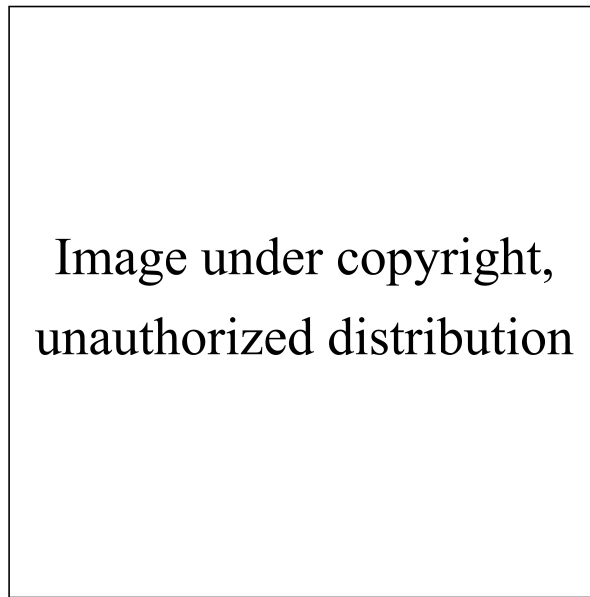


Fig. 1.9 (a) Evolution of filament and droplet sizes during a CaBER experiment. (b) Typical image of a beads on a string ( $138 \mu\text{m} \times 2317 \mu\text{m}$ ) used for image analysis. Droplets corresponding to those represented in (a) are identified as 1, 2 and 3, for the first, second and third generation, respectively. Adapted from Oliveira et al. [9]

indefinitely (for an infinitely extensible fluid model such as the Oldroyd-B model), leading to multiple generations drops in a BOAS structure. The recoiling and formation of multiple generations drops in BOAS structure was later confirmed numerically by Li and Fontelos [2] and experimentally by Oliveira et al. [9]. Moreover, inertial effects are also important for the iteration process. Inertia ensures that growth rates of drops are faster than a thinning rate of a primary elastic filament, otherwise a premature filament breakup without formation of multiple generations of drops may occur. Chang et al. [85] demonstrated that for an iterated stretching, high Deborah numbers ( $De \gg 1$ ), intermediate viscosity ratios ( $0 < S < 1$ ), finite fluid inertia ( $Oh \ll 1$ ) are required so that inertial effects lead to a rapid growth of the capillary instability and recoil. Furthermore, very high finite extensibilities ( $b^2 \gg 1$ ) are needed so that the iterated nature of a BOAS instability and elastic recoil process are not truncated prematurely by the maximum length of the molecules. These criteria for an iterated stretching were later experimentally validated by Oliveira et al. [9] to demonstrate multiple generations of drops in a BOAS structure (see Fig. 1.9).

**Space-time diagrams** To represent a complete spatial and temporal dynamics of filament thinning, digital images can be used to construct a ‘space-time’ diagram. This approach was pioneered by Baumert and Muller [87] to visualise elastic instabilities. Space-time

diagrams for a BOAS structure were reported by Oliveira et al. [9] for a stretched viscoelastic liquid bridge and later by Clasen et al. [15] for a viscoelastic liquid jet. Oliveira et al. [9] represented first stages of droplet formation, along with coalescence through the space-time diagrams. Aqueous solution of polyethylene oxide (PEO) in a mixture of ethylene glycol and water was used as viscoelastic test fluids. Initially, a liquid bridge was formed using CaBER plates, having diameter,  $D_p = 6$  mm, and  $IAR = 1$ . This bridge was stretched to  $FAR = 3.23$  to generate a long slender filament of polymer solution, followed by capillary-driven drainage and breakup. The obtained images of the filament thinning and the BOAS structure are shown in Fig. 1.10(a). A space-time diagram, constructed using a sequence of experimental images, from the appearance of a first-generation drop until filament breakup, is shown in Fig. 1.10(b). Each colour of the pixel in the diagram represents the thickness of a filament in space and time. The dark red colour is for the zero thickness of the filament and the dark blue colour is for the largest drop. The initial homogeneity represents uniform filament and the bright bands in the later stages indicate the appearance of drops. The appearance of the discontinuity, with time, is an indication of the coalescence (indicated by circles in the space-time diagrams). Due to coalescence, drop migration occurs and the filament is pulled towards the direction of coalescence. Yet, this space-time diagram fails to provide any quantitative information about the diameter of filament and drops. The diagram only represents the evolution of the filament when the first drop appears. Besides, the analysis of the space-time diagram is only descriptive, with no further investigation of the drops.

Later, another type of space-time diagram, called '*XLt* diagram', as shown in Fig. 1.11, for liquid jets was developed by Clasen et al. [15], to represent positions of drops in space and time. Thin filaments and drops were produced using downward falling jets, having a nozzle radius of 0.075 mm, of aqueous solutions of polyacrylamide (PAA). Filament thinning results into formation of a big terminal drop followed by small drops. These small drops coalesce with the big terminal drop and this phenomenon is called gobbling. Frame by frame analysis of captured images is enabled by *XLt* diagram. Yet, the *XLt* diagrams offer only the position  $L(t)$  of the centre of the terminal drop, and the following small drops  $X(t)$ , but do not provide sizes of the drops.

**Numerical work on BOAS structure** Formation of a BOAS structure for viscoelastic fluids has a rich history [2, 3, 7, 9, 13–16, 18, 26, 27, 63, 82, 85, 88, 89]. In the last few decades, this phenomenon has received great attention in both experimental and numerical communities. Due to the diversity and complexity associated, recreating a BOAS structure has been chosen by the computational rheology community as a core problem for testing algorithms.

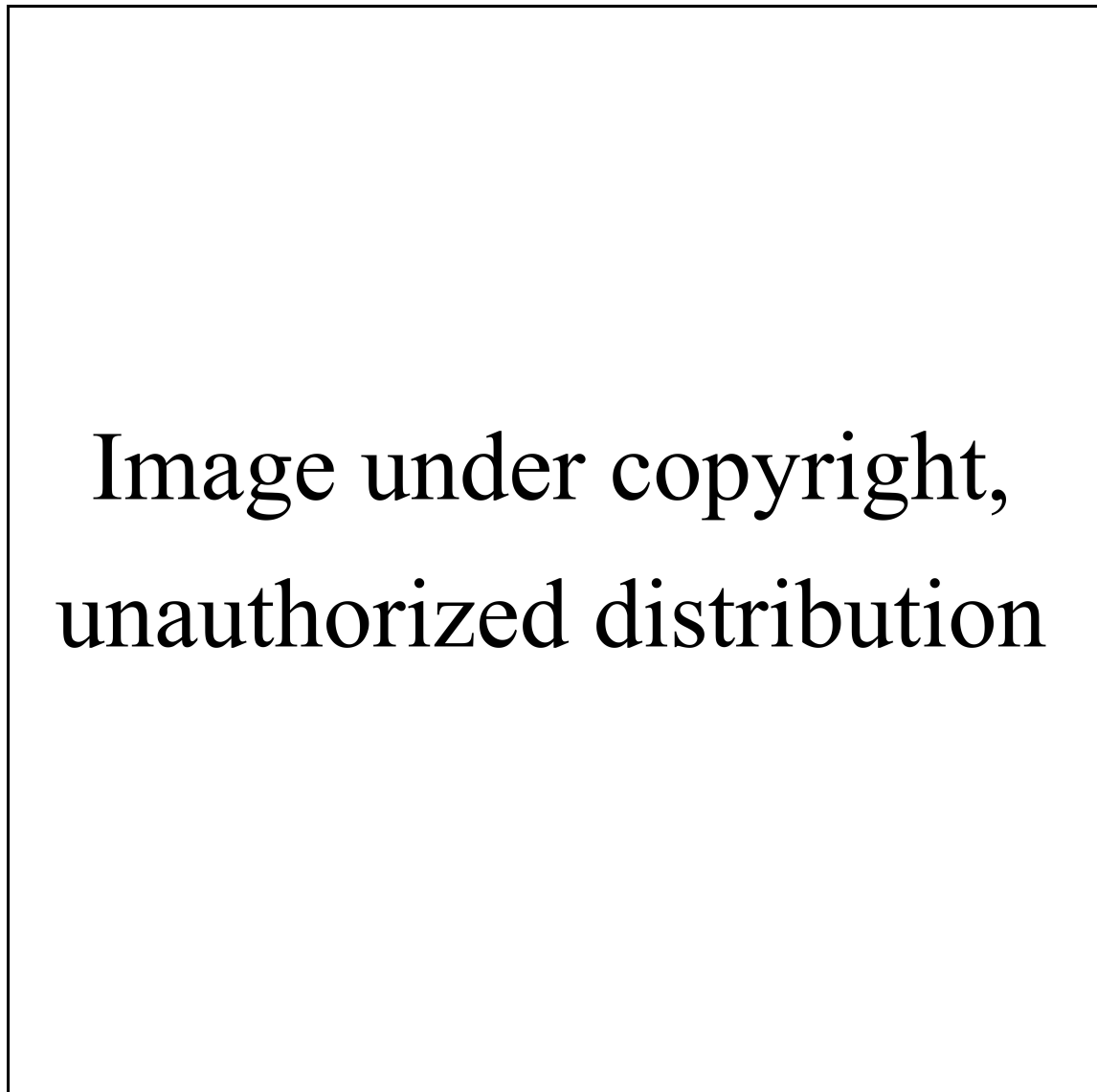


Fig. 1.10 Construction of a space time diagram. (a) Image sequence representing a uniform filament along with a BOAS structure.  $z$  is the position on the filament. (b) A space-time diagram capturing evolution of the filament when BOAS structure starts appearing. Colour of each pixel represents the relative thickness of the filament and drop, in space and time, ranging from zero (dark red) to thickest (dark blue). Initially, the colour intensity is homogeneous in the  $z$ -direction, showing the existence of a uniform filament. Bright bands suggest the appearance of drops. Occurrence of coalescence is indicated by black circles. Drops migrate either upwards or downwards in the direction of the occurrence of coalescence. Adapted from Oliveira et al. [9].

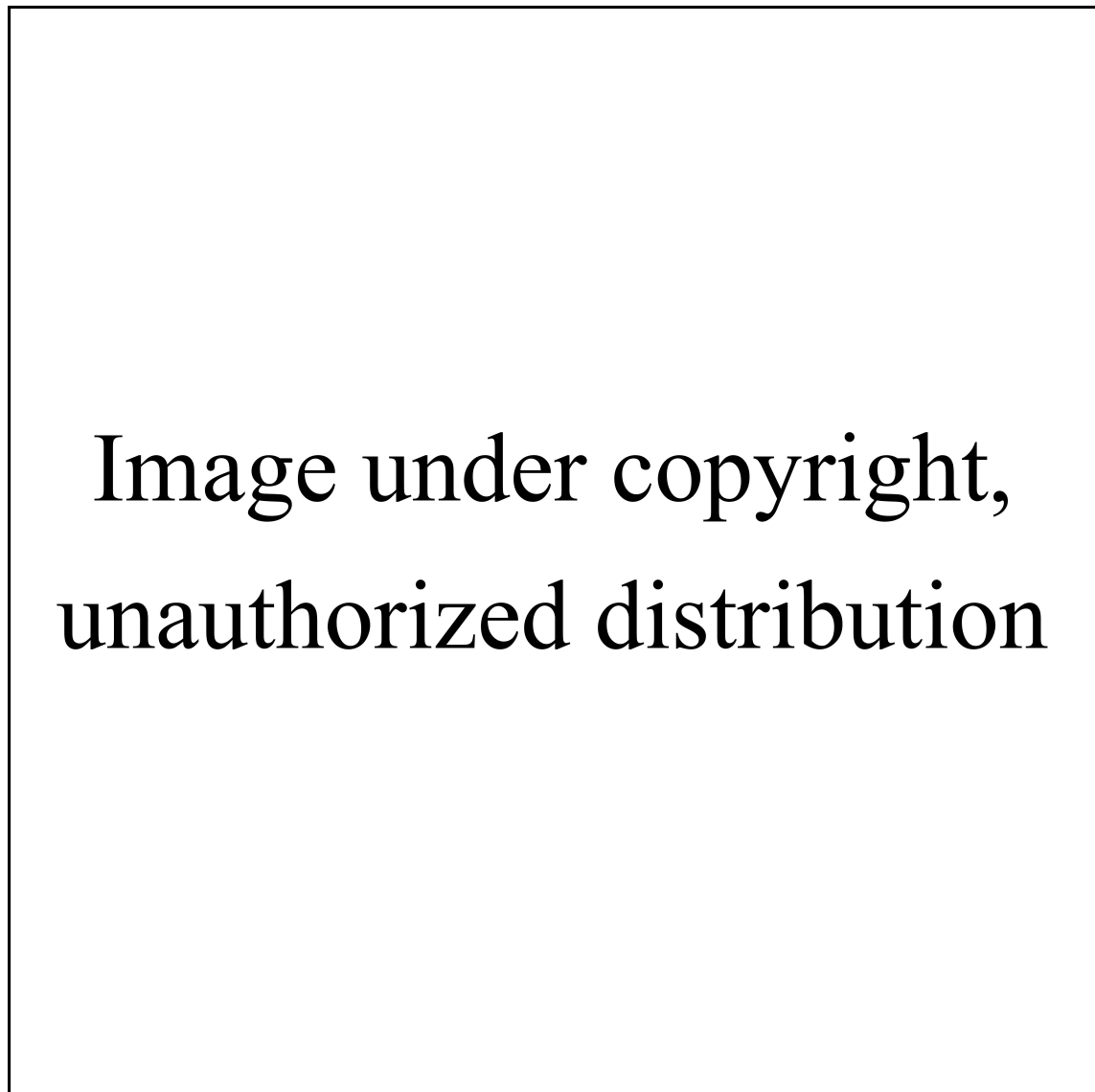


Fig. 1.11 (a)-(b) Construction of a space-time diagram, here called  $XLt$  diagram. The position of the terminal drop  $L(t)$  is represented by a hollow symbol and positions of following drops  $X(t)$  on the falling jet are presented with filled symbols. (c) An example of  $XLt$  diagram, for the falling jet issuing from a nozzle of radius 0.075 mm. The thin solid lines with constant slope indicate that the drops move with constant velocity, resulting in gobbling. Adapted from Clasen et al. [15].

**1D Oldroyd-B model** Preliminary work on formation of a BOAS structure for viscoelastic solutions was done by Bousfield et al. [13]. The authors used 1D thin filament approximations, to understand the breakup mechanism for liquid jets. The same approach was implemented later by other authors [2, 3, 16, 55, 56, 85]. An infinitely-long uniform liquid cylinder was perturbed with a periodic axisymmetric disturbance. Both Newtonian and viscoelastic solution jets were tested, neglecting gravity. For Newtonian solutions, finite element numerical algorithm [90] was implemented. Two cases with  $Oh = 0$  and 32.86 for Newtonian jets were studied and flow domain was subdivided using a finite element mesh. The Oldroyd-B model was used for a 1 mm radius viscoelastic liquid ( $\lambda = 0.17$  s) jet. The authors successfully demonstrated evolution of a filament for Newtonian fluids and predicted a BOAS structure for viscoelastic jets. Initial capillary-driven thinning grows much more rapidly on polymeric filaments than on Newtonian liquid filaments. Extensional stresses stabilise viscoelastic filaments and retard the breakup. Satellite drops in low viscosity liquid jets are formed because of inertia. Due to viscoelasticity, formation of a BOAS structure slows down and thinnest point on the filament is maintained at the midpoint between the drops.

Further investigation of drop dynamics of a BOAS structure was conducted by Li and Fontelos [2] for viscoelastic jets. A small (1%) disturbance was applied to the initial jet profile. The 1D model used here was equivalent to Bousfield et al. [13] and equations for a slender Oldroyd-B filament were integrated forward in time. Finally, the resulting equations were solved numerically by an explicit finite difference scheme [91] on a uniform mesh. Drop migration, oscillation, merging and draining were studied, with Deborah numbers,  $De$  ranging from 94.3 to  $10^5$ . The simulations showed growth of a large ‘primary’ drop and smaller ‘secondary’ drops. Fig. 1.12 shows a typical example of formation of a BOAS structure obtained by a simulation for  $De = 300$ . Necking was observed in Fig. 1.12(a), which leads to recoiling and then formation of small drops at  $t = 50$  (Fig. 1.12(e)). The late BOAS profile with primary and secondary drops, at time,  $t = 2000$ , is shown in Fig. 1.12(f). For all values of  $De$ , the authors found a BOAS structure with a symmetrical drop distribution across the central drop.

Later, in order to investigate formation of a BOAS structure for a weakly elastic ( $De = 0.8$ ) and low viscous ( $Oh \sim 0.04$  and  $S = 0.27$ ) polymeric liquid, Ardekani et al. [16] used the Oldroyd-B constitutive equations for a liquid jet. A BOAS structure with multiple satellite droplets were reported for smaller value of Deborah number ( $De = 0.8$ ) compared to Li and Fontelos [2] ( $De$  ranging from 94.3 to  $10^5$ ). Furthermore, the authors also observed typical drop dynamics such as coalescence and drop migration similar to Li and Fontelos [2]. In a similar attempt to characterise formation of a BOAS structure using  $De$  and  $Oh$ , Bhat

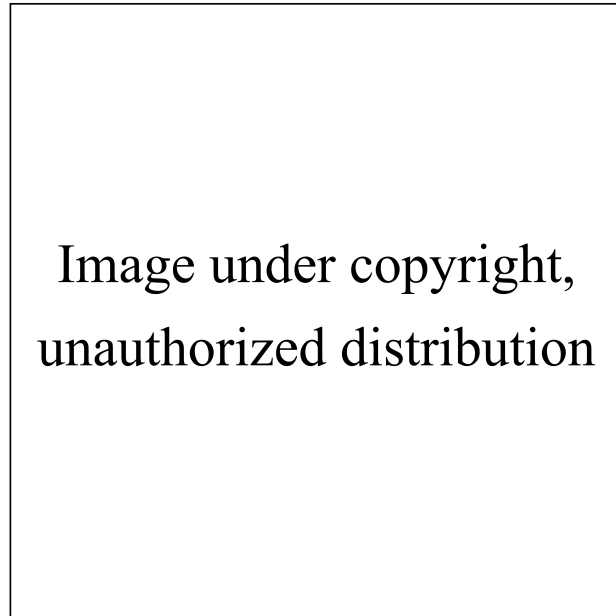


Fig. 1.12 Formation of a BOAS structure for a viscoelastic liquid jet with  $De = 300$ . Evolution of the BOAS structure, with time,  $t =$  (a) 44, (b) 45, (c) 47, (d) 48, (e) 50 and (f) 2000.  $t$  is a dimensionless time. Reprinted from Li and Fontelos [2].

et al. [3] implemented a 1D Oldroyd-B model for a stretched viscoelastic filament. Gravity was neglected. A phase diagram was created for a stretched viscoelastic liquid bridge, as shown in Fig. 1.13, using the Oldroyd-B model, with  $S = 0.6$  and  $FAR = 3$ . This diagram gives different morphologies of a BOAS structure for various values of  $De$  and  $Oh$ . Multiple drops were obtained only for the smaller values of  $De$  and  $Oh$ , i.e.  $De < 0.05$  and  $Oh < 0.5$ . The BOAS structure was symmetrical about the big central drop due to imposed plane of symmetry. The results showed that inertia is needed for the formation of beads. However, no bead was reported for  $De > 0.2$ , although previous numerical and experimental findings [2, 9, 16, 85] report appearance of a BOAS structure for  $De > 1$ . With the same  $S = 0.6$ , as Bhat et al. [3], and  $De > 1$ , Ardekani et al. [16] reported multiple beads for liquid jets.

**2D Oldroyd-B model** Recent advances in numerical methods enable to simulate nonlinear dynamics of viscoelastic liquid bridges and jets, with high resolution and more accuracy. Turkoz et al. [55] used the Oldroyd-B model for 2D flows to investigate the thinning of a viscoelastic liquid bridge. An axisymmetric two-phase incompressible momentum equations system, consisting of air as medium, is numerically solved using the Basilisk solver [92, 93]. The interface between a high-density viscoelastic liquid ( $De = 60$ ,  $Oh = 3.16$  and  $S = 0.25$ ) and low-density ambient air was transported by a volume-of-fluid (VOF) method [94]. An

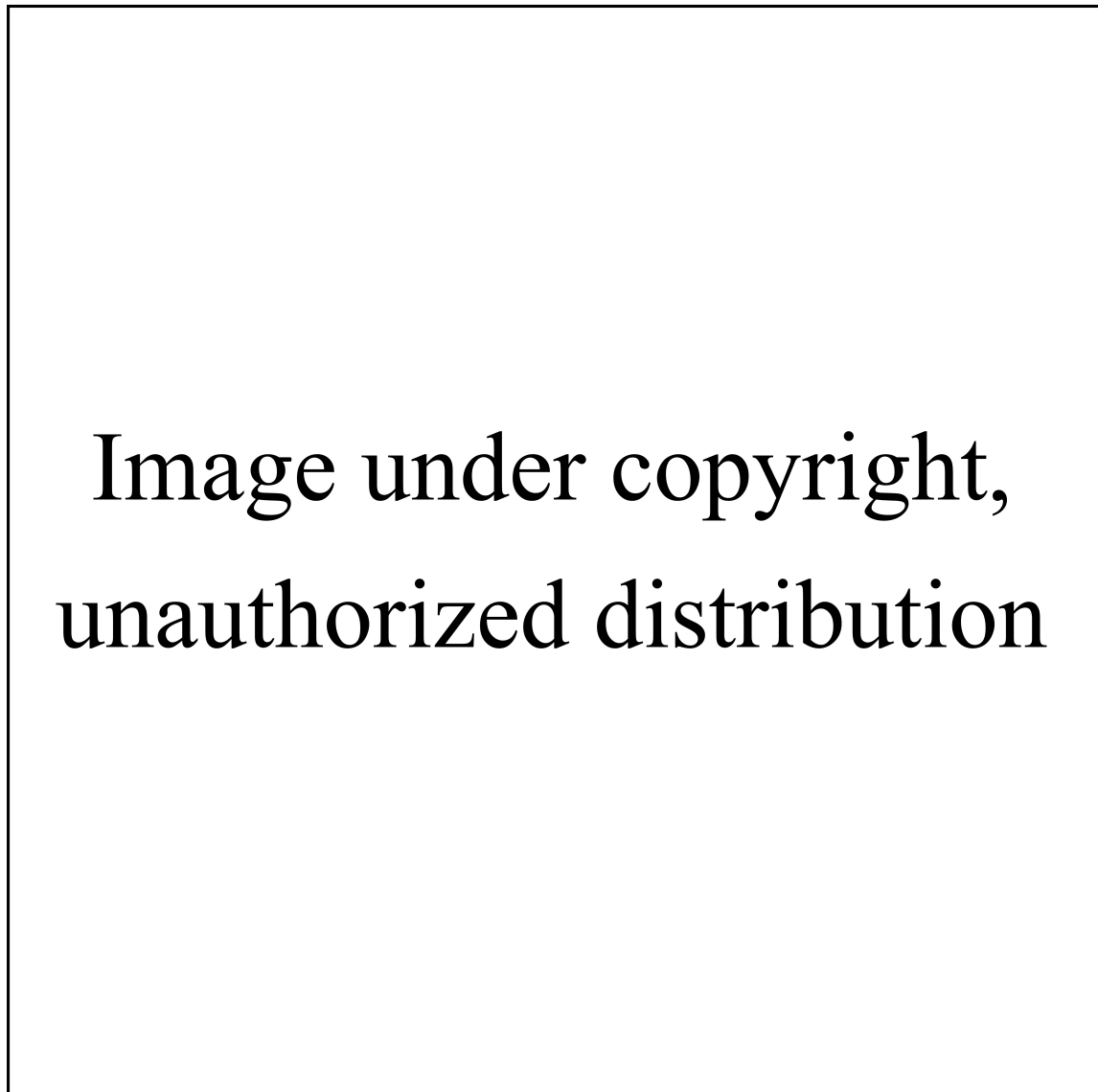


Fig. 1.13 Phase diagram representing different BOAS morphologies as a function of  $De$  and  $Oh$ , for a Oldroyd-B filament with  $S = 0.6$  and  $FAR = 3$ . (A), (B) and (C) show filament shapes, for a viscoelastic liquid bridge, corresponding to a uniform cylindrical filament (no satellite drops), a single satellite drop and multiple drops morphologies, respectively. Adapted from Bhat et al. [3].

adaptive mesh was implemented that refines the domain up to  $2^{12}$  grid points. Again, gravity was not considered. A BOAS structure was observed with a symmetric drop distribution across the central drop. Significant polymeric stress in the off-diagonal direction was found, that can not be captured by 1D simulations.

Further work on a stretched viscoelastic liquid bridge was conducted by Figueiredo et al. [56]. Effect of an outer fluid phase on dynamics of a stretched viscoelastic filament was investigated. The geometry used was similar to the experimental work presented by Sousa et al. [95], where the authors studied a stretched liquid bridge formed in between two small cylindrical rods, confined in an immiscible oil bath. The 2D Oldroyd-B model, neglecting gravity, was considered. A non-uniform mesh, for axisymmetric conditions, was implemented with a higher number of elements closer to the filament. A self-developed two-phase solver was used for the stretched liquid bridge, in various oil baths. Filament thinning was followed by formation of a BOAS structure and single as well as multiple drops were observed. In case of multiple drops, smaller satellite drops were distributed symmetrically across the central drop. Use of different immiscible oils did not affect formation of a BOAS structure.

**Summary and voids in the literature** Evolution of a filament starts from its stretching, followed by necking and formation of a drops on a filament pattern, and then finally ends with its breakup. Previous studies have consistently evidenced *visco-capillary* or *inertio-capillary* thinning, an exponential polymeric *elasto-capillary* thinning and existence of a BOAS structure with multiple generations of drops attached to a thin filament [1, 9, 14, 15, 18, 26, 27, 63, 74, 81, 89, 96, 97], depending on viscoelastic liquid properties. Formation of drops on a filament for viscoelastic solutions has been reported experimentally and numerically for continuous capillary jets [2, 7, 13, 15, 16, 26, 55, 82, 85, 89], dripping-from-nozzle [27, 81, 98] and stretching of capillary bridges [1, 3, 9, 12, 14, 56, 63, 76, 80, 88, 99]. In most of the previous numerical work, BOAS structure was reproduced using 1D [2, 3, 13, 16, 85, 100] and 2D [55, 56] Oldroyd-B models. Most of the previous study of a BOAS structure was focused on viscoelastic jets [2, 13, 16, 55, 85], but little work was done on viscoelastic liquid bridges [3, 56]. In BOAS instability, multiple generations of drops are formed due to 'iterated stretching' [9]. Drop migration, oscillation, merging and draining for viscoelastic liquid filament were observed experimentally [9, 15] and numerically for various  $De$  and  $Oh$  [2, 16]. However, previous numerical studies neglected gravity and hence, observed a symmetric drop distribution along the filament length. Hence, these results show an identical and equal number of drops on either side of a central drop. Furthermore, even though there

is a significant experimental and numerical work on drops on a filament phenomenon, yet there is not much analysis on the position, trajectories of the drops and number of drops.

Spatial and temporal dynamics of filament thinning and formation of a BOAS structure can be represented by using space-time diagrams and yet, these diagrams have received little attention. A space-time diagram for stretched liquid capillary bridge has been reported by Oliveira et al. [9] and for continuous jets, Clasen et al. [15] reported a space-time diagram called '*XLt* diagram'. The authors reported multiple generations of drops along with drop migration and coalescence. However, space-time diagram by Oliveira et al. [9] only represent relative thickness of drops and space-time diagram by Clasen et al. [15] provide only positions of drops. Both diagrams fail to provide actual drop sizes along with thinning and breakup dynamics of filament. Hence, there is a need to create space-time diagrams that can depict filament thinning and monitor spatial-temporal dynamics of drops along with their sizes and numbers.

Increase in filament thinning and breakup times due to increasing polymer concentration is already well established and has been reported previously [78, 101]. However, there is no information available on effect of polymer concentration on drop dynamics of a BOAS instability. Therefore, this influence of polymer concentration on drop dynamics needs to be studied and effects can be depicted for each concentration by space-time diagrams. Effect of capillary bridge stretching heights on filament thinning dynamics was documented [14, 83, 84]. In addition, a BOAS instability has been previously demonstrated only for a single geometrical (plate diameter and initial liquid bridge height) or stretching (final stretching height and stretching speed) parameter [9, 14]. However, there is no study on effect of various geometrical and stretching parameters on formation of a BOAS pattern and drop dynamics. Hence, influence of these geometric and stretching properties on a BOAS instability needs to be investigated. These results can be further represented through space-time diagrams to depict variations in filament thinning and drop dynamics for each parameter.

After a stretched filament breaks up, solution pools are formed on end plates of a liquid bridge. This formation of solution pools depends on various factors [20, 30]. Moreover, size of solution pools reflects liquid transfer, which will be further reviewed in the next section.

## 1.7 Review on liquid transfer

Up to now, we have been focused on stretching of a viscoelastic liquid bridge, filament thinning, beads on a string structure and filament breakup. However, from printing field

point of view, formation of filaments and a BOAS structure for viscoelastic solutions can affect volume of liquid transferred from one surface (carrier or donor) to another surface (substrate or acceptor). Hence, dynamics of a stretched liquid bridge and volume of liquid transferred play an important role in printing processes. In practice, a successful transfer printing requires a sufficiently large volume of liquid transferred from one surface to another [20], whereas, in 3D lithographic printing, desired liquid shapes (BOAS structured wires) need to be preserved [23]. Yet this liquid transfer is a complex problem in fundamental fluid dynamics. First, liquid-air interfaces play an important role in liquid bridge dynamics. Shape of a liquid bridge needs to be determined along with velocity and pressure fields. This leads to highly nonlinear time-dependent free-boundary problems. Second, liquid-solid-air contact lines are present on carrier-substrate surfaces and many basic issues regarding their behaviour are still being actively studied [100, 102–107]. Third, rheology provides another source of non-linearity as most of printing inks are typically multi-component mixtures that may contain colloidal particles (pigments or conductors), polymers and surfactants (to control interfacial tension and wetting) [20]. These inks may exhibit shear thinning, viscoelasticity and thixotropy [42, 107]. Solvent evaporation also occurs during printing that causes ink rheology to change with time and temperature. Furthermore, liquid transfer may involve a combination of extensional, shear, and rotational motion that further complicates understanding of the problem.

More detailed study of different types of printing and their origins can be found in the review article by Kumar [20]. However, in the present study, printing methods having liquid bridges formed in-between two flat plates are considered. The fundamental problem of liquid transfer between two flat surfaces is relevant to direct printing methods and offset printing methods. In direct printing methods, liquid transfer occurs directly from a carrier to a substrate. Examples of direct printing methods are gravure, flexography (Fig. 1.14), additive manufacturing (Fig. 1.15), screen printing and letterpress printing processes. In the offset printing methods (e.g. offset gravure), see Fig. 1.16, liquid transfer occurs between an offset roll and a substrate. In these printing methods, both carrier and substrate surfaces are locally flat. In a typical micro-gravure-offset printing system, diameters of offset cylinders are of an order of  $10^5 \mu\text{m}$ , and pattern on a plate or printed width is of an order of 10 to  $10^2 \mu\text{m}$  [108]. The large difference between these sizes means that dynamic effects caused by the rotational motion of cylinders during an ink transfer process can be neglected. Hence, it is convenient to consider liquid transfer between two chemically homogeneous flat surfaces as a starting point for a basic understanding of the problem.

In the following text, we will discuss the current state of the art for liquid transfer. In the present study, we study a uniaxial stretching of both viscoelastic and Newtonian liquid

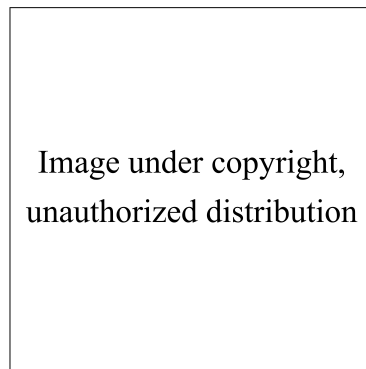


Fig. 1.14 Schematic of a flexographic printing platform. A metering roll withdraws inks from an ink reservoir and transfers the ink to a printing cylinder. The printing cylinder has a flexible printing plate with patterns to be printed. The ink is further transferred from the printing cylinder to a substrate surface, through a formation of a liquid bridge. Adapted from Lorenz et al. [109].

bridges. A detailed study on dynamics of liquid bridges can be found in the review article by Montanero and Ponce-Torres [30].

### 1.7.1 Contact lines and angles

Chadov and Yakhnin [102, 103] were the first to identify and systematically investigate liquid transfer phenomenon. By using Newtonian solutions of water-glycerol and ethanol-glycerol mixtures, experiments were conducted for liquid bridges undergoing uniaxial extensional stretching. Effects of surface tension, viscosity of solutions and stretching speeds of surfaces are reported. Bottom surfaces were made of different materials (such as Teflon, polyethylene, Mylar and zinc) and the top surface was made of zinc. Both surfaces were large compared to the capillary lengths of the liquids. In their experiments, a droplet of volume  $5 \mu\text{l}$  was placed on the fixed bottom surface and then, the zinc surface, from the top, was brought in contact with the droplet to create a liquid bridge (with a plate gap of  $\sim 0.1 \text{ mm}$ ). Contact lines between the surface and liquid were not pinned and hence, were free to move as there is no edge to prevent the slip due to large size of surfaces. However, in the present thesis, liquid volumes are such that contact lines on CaBER plates are pinned to the edges of small plates. Then, the top surface was moved upwards at a desired height at a constant speed ( $\sim 0.001 \text{ cm/s}$ ). As a result, solution pools were formed on each surface. Solution pools formed were weighed, to measure the amount of liquid transferred. These authors observed that receding liquid contact angles on the polymer surfaces were larger than that on the zinc surface and majority of the liquid (60–97%) is transferred to the zinc surface. Hence, more liquid was

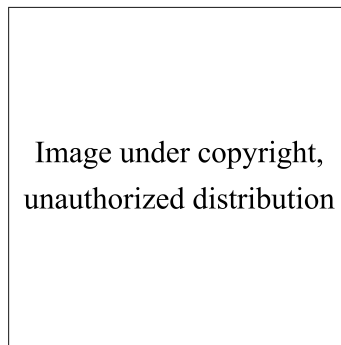


Fig. 1.15 Schematic of additive printing method. Ink is first deposited on a carrier surface which has engraved printing patterns. Then, the ink is transferred from the carrier surface and added on to a receiver surface to manufacture the patterns. Adapted from Carlson et al. [110].

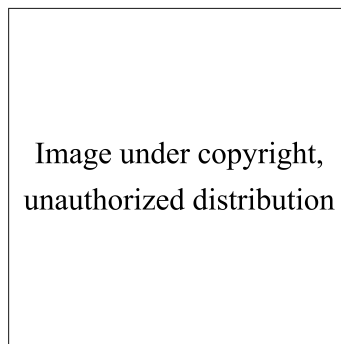


Fig. 1.16 Schematic of an offset-gravure printing method. Ink is transferred from a gravure plate to an offset pad. Then, the ink is deposited from the offset pad on to a substrate. Adapted from Huang et al. [111].

transferred to the more wettable surface and in this case, zinc was more wettable than other surfaces. Furthermore, amount of liquid transferred increased with a larger difference in contact angles between the two surfaces. However, when two zinc surfaces were used, an equal amount of liquid was left on each surface.

Differences in liquid transfer observed by Chadov and Yakhnin [102, 103] for different surfaces suggest that contact-line dynamics play a key role in liquid transfer. Kang et al. [112] experimentally studied liquid transfer and performed measurements of contact-line motion. Their experimental method, see Fig. 1.17(a), was the same as Yakhnin and Chadov [103]. A water drop of volume  $4 \mu\text{l}$  was placed on a bottom plate and a top plate was brought in contact to the drop (with a plate gap of  $\sim 0.25 \text{ mm}$ ). Then, the top plate is moved up with a stretching speed of  $2.8 \text{ mm/s}$  to a desired height. Initial liquid bridge and formation of solution pools were recorded with a camera. However, instead of measuring actual weight or

volume of solution pools, each solution pool image was analysed in units of pixels. Width and height of the cross-section of each droplet were estimated by counting pixels in respective directions. Volumes of solution pools on plates were calculated using 'spherical cap' method, by assuming the solution pool to be a truncated axisymmetric sphere. In the present thesis, we have used the same method to calculate volumes of solution pools on both plates and details of this method are discussed in the next chapter. The 'spherical cap' method is a non-contact liquid volume measurement method and during the measurement, no fluid is lost (as no liquid is transferred from plates to weighing instrument). In their study, two methods were used by Kang et al. [112] to vary contact angles: first by altering the liquid properties and second, by altering the surface properties. Effect of contact angles, at a bottom plate,  $\beta$ , and top plate,  $\alpha$ , as represented schematically in Fig. 1.17(a), on a transfer ratio was studied. The transfer ratio is defined as a ratio of volume of liquid transferred to an acceptor plate to the total volume of liquid in-between the plates. It is important to notice that the initial shape of their liquid bridge is concave, while, contact lines between the plates and liquid are unpinned (free to move). These liquid bridge dynamics are similar to [40, 106, 112, 113], where the initial concave-shaped bridge has moving contact lines. Results obtained are presented in Fig. 1.17(b), and for the same value of  $\beta$ , it is found that the transfer ratio decreases with an increase in  $\alpha$ . But when contact angles of both plates are equal,  $\alpha = \beta$ , the transfer ratio is close to 50%. This is similar to Chadov and Yakhnin [102, 103] where the transfer ratio obtained by the authors is close to 50% due to same plate material (and hence same contact angle). Role of contact angles in liquid transfer between two flat plates with unpinned contact lines was further studied by Huang et al. [106]. Their numerical findings show that liquid transfer can be enhanced, not only by the use of a hydrophobic donor surface but can also be improved by using a pair of surfaces with a large difference in contact angles. (Details of their findings will be discussed later in this chapter.) In addition, Kang et al. [112] reported that if two plates have the same contact angle, two pinch-off events can happen simultaneously, one near each plate. This can result in formation of a detached drop. These detached drops have been observed experimentally in stretching of liquid bridges with moving contact lines. In our experiments, we also have observed a detached drop for Newtonian fluids with pinned contact lines. This is generally undesirable in printing because these drops can ruin the image quality if they land on a substrate or printing plate. Also, these drops are wasteful and can be a potential health hazard if inhaled [20].

However, moving contact lines is a complex problem and out of the scope of this work. Further details on dynamics of moving contact lines can be found in review articles by Snoeijer and Andreotti [114] and Kumar [20]. The above discussion on intricacy due to

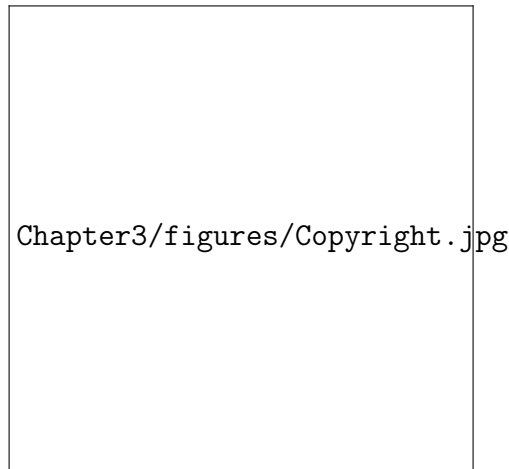


Fig. 1.17 (a) Schematic diagram of a liquid bridge, of volume  $4 \mu\text{l}$ , representing contact angle at the bottom plate,  $\beta$ , and contact angle at top plate,  $\alpha$ . Contact lengths on the bottom plate and top plates are  $W_L$  and  $W_U$  respectively. Here, the stretching speed,  $U$ , and the initial bridge length,  $d$ , are  $2.8 \text{ mm/s}$  and  $0.25 \text{ mm}$ , respectively.  $W_M$  is the width of the filament at the midplane. (b) Transfer ratio in percentage (%) for different values of  $\alpha$  and  $\beta$ . Transfer ratio in percentage (%) can be defined as a ratio percentage volume of liquid transferred to the top plate to the total volume (100 %) of liquid in-between the plates. Adapted from Kang et al. [112].

different surfaces and moving contact lines highlights a need to focus on a simpler version of liquid transfer problem. To investigate liquid contact line motions in a liquid transfer, Qian and Breuer [115] formed a bridge with a glass plate (similar to Chadov and Yakhnin [102] and Kang et al. [112]) and a cylindrical rod (similar to CaBER plates). In their study, the authors observed that contact line on the (glass) plate slips, but on the cylindrical rod, the contact line is effectively pinned. In the present study, cylindrical plates of the same material are used. Our contact lines can therefore be regarded as fixed contact lines and the effect of plate material on liquid transfer is avoided. This simpler version of liquid transfer has been previously studied by Zhang et al. [100].

## 1.7.2 Effect of parameters

**Plate radius** Zhang et al. [100] investigated, experimentally and numerically, the stability and breakup of a liquid bridge with pinned contact lines. In their numerical study, a one-dimensional model, based on a slender jet approximation, was used to simulate the dynamic response of a liquid bridge, under a continuous uniaxial stretching. For experiments, two coaxial, circular, solid disks with radii,  $R_P$ , ranging between  $0.08$  and  $0.32 \text{ cm}$  were used. The bottom plate was fixed and the top plate was moved upwards. A liquid bridge with

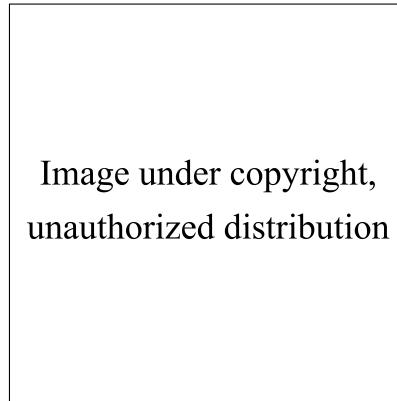


Fig. 1.18 Liquid bridge dynamics and liquid transfer for  $IAR = 2$  and  $U = 0.006$  m/s. (a) Dimensionless ratio of the limiting length of bridge,  $L_d$  to the plate radius,  $R_p$ , as a function of  $R_p$ , for experimental and numerical studies.  $L_d$  is the maximum stretching length attained by a liquid bridge at the time of breakup. The liquid bridges are stretched until the breakup of the filament occurs (i.e. until  $L_d$ ). With the increase in  $R_p$ , the conical shape of the solution pool at the top plate, at the time of breakup, changes from convex to concave. (b) A non-dimensional ratio,  $V_l/V$  (%) as a function of  $R_p$ , for experimental and numerical studies. Here,  $V_l$  is the volume of the solution pool on the bottom plate and  $V$  is the total volume of the bridge. Adapted from (Zhang et al. [100]).

$IAR = 2$ , having pinned contact lines is stretched at  $U = 0.006$  m/s. Water and glycerol are used as testing fluids either separately or as mixtures with different concentrations. In their study, liquid transfer is expressed by as a ratio of liquid volume on the bottom plate,  $V_l$ , to the total volume of the bridge,  $V$ . However, in the present and previous studies [103, 106, 112], liquid transfer is defined as a ratio of solution volume on the top plate to the total volume of the bridge. Their numerical and experimental results are in good agreement as shown in Fig. 1.18. In their study, the Bond number is varied by using different plate radii and results obtained for liquid bridge dynamics are presented in Fig. 1.18(a). With increase in plate radius, liquid volume and limiting length,  $L_d$ , of the bridge before breakup increases.  $L_d$  is the maximum stretching length attained by a liquid bridge at the time of breakup. However, the dimensionless ratio  $L_d/R_p$  shows an opposite trend and decreases linearly with increasing  $R_p$ . For  $R_p \geq 0.32$  cm, most of the liquid accumulates on the bottom plate (bottom solution pool) while liquid in the top solution pool decreases considerably. Hence, with increase in  $R_p$ , at the time of breakup, the conical shape of the top solution pool changes from convex to concave in the vertical plane. As  $IAR = 2$  was used by these authors, the increase in  $R_p$  resulted in increased liquid volume. Increase in thickness of a filament and the concave shape of the top solution pool considerably delay the filament breakup. Hence, liquid transfer to the top plate decreases with an increase in plate radius. Furthermore, for larger plate radius

with  $Bo > 1$ , influence of gravitational force increases. Therefore, more liquid is accumulated on the bottom portion of a liquid bridge before the breakup. However, Zhang et al. [100] investigated only Newtonian fluids (aqueous solutions of glycerol). The authors state that with the increase in  $R_p$ , filament breakup is delayed. Yet, no detailed study was conducted to investigate effect of formation of a viscoelastic filament and resulting delayed filament thinning on liquid transfer.

**Stretching velocity** Influence of stretching speed on liquid transfer was investigated for unpinned contact lines [102, 103, 113] and for pinned contact lines [100]. The authors reported the same trend for both pinned and unpinned contact lines as liquid transfer to a top plate increased with increasing stretching speed. Furthermore, results obtained by Chadov and Yakhnin [102, 103] and Chen et al. [113] indicate three distinct regimes for liquid transfer depending on stretching speeds. A first regime corresponds to low stretching speeds and a quasi-equilibrium transfer, where liquid transfer is determined by wetting properties of a surface and capillary effects of a liquid. A second regime is a transition zone. A third regime occurs at high speeds ( $U > 0.01$  m/s) and an equal amount of liquid is left on each surface. Liquid transfer in this third zone remains unchanged with increasing speed, and independent of surface and liquid properties. In addition, Chen et al. [113] observed that, in the dynamic regime, liquid contact angles do not affect liquid transfer and the same volume of liquid is deposited on both the surfaces. Later, in their numerical simulations, Huang et al. [106] studied the transfer ratio as a function of the Capillary numbers,  $Ca = \eta_0 U / \sigma$ . Their results are represented in Fig. 1.19 for different values of  $\Delta\theta_r$ . Here,  $\Delta\theta_r$  is the difference between contact angle at the bottom plate,  $\beta$ , and contact angle at the top plate,  $\alpha$ . When  $\Delta\theta_r = 0$ , the same volume of liquid is observed on both plates for all values of  $Ca$  (since the liquid does not preferentially wet either plate). As  $Ca$  increases, the transfer ratio approaches value of 50% for all values of  $\Delta\theta_r$ . With the increase in  $Ca$ , viscous forces become stronger and influence of wettability differences reduces.

**Initial aspect ratio** Further investigation was done by Huang et al. [106] to explore influence of initial liquid bridge height,  $L_0$ , on liquid transfer. This effect of  $L_0$  was studied by varying  $IAR$  from 1 to 4, where  $IAR = L_0 / R_p$ . Different values of  $IAR$  are obtained by varying  $L_0$  and by keeping  $R_p$  constant. Rayleigh-Plateau limit for a cylindrical column corresponds to  $IAR = 2\pi$  and suggests that longer bridges will breakup earlier [106, 116, 117]. Due to this early breakup, less time is available for liquid transfer to the top surface. As a result, with the increase in  $IAR$ , liquid transferred to the top plate decreases. However, these numerical results are for moving contact lines and values of  $IAR$  studied are limited.

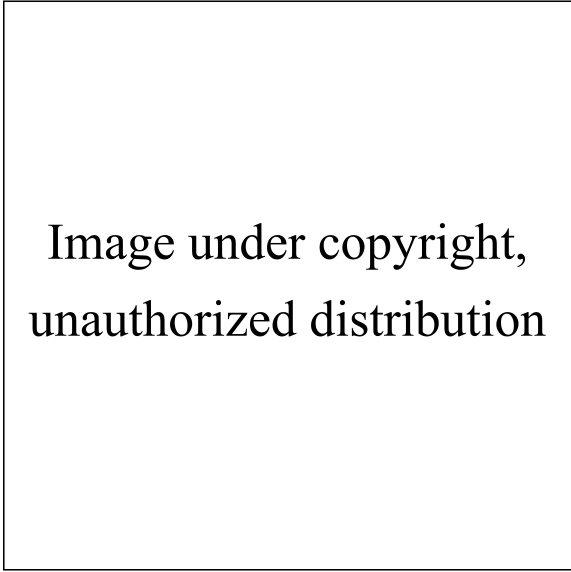


Image under copyright,  
unauthorized distribution

Fig. 1.19 Effect of  $Ca$  on transfer ratio (in percent) for different values of  $\Delta\theta_r$ . Here,  $\Delta\theta_r$  is a difference between contact angle at the bottom plate,  $\beta$ , and contact angle at the top plate,  $\alpha$ . Value of  $\alpha$  is fixed at 60 and  $\beta$  is varied. Transfer ratio in percentage (%) can be defined as a ratio percentage volume of liquid transferred to the top plate to the total volume (100 %) of liquid in-between the plates. Reprinted from Huang et al. [106].

**Viscosity and surface tension** Effect of solution properties, such as liquid viscosity,  $\eta_0$ , and surface tension,  $\sigma$ , on liquid transfer was investigated by Chadov and Yakhnin [102, 103]. As previously discussed, liquid transfer only gets affected in the first characteristic regime, where liquid properties determine the final volume of liquid transferred to a top plate.  $\eta_0$  is increased by adding glycerol to water. As value of  $\eta_0$  increases, volume of liquid transferred to the top plate decreases. On the contrary, liquid transferred to the top plate decreases when surface tension of a solution is reduced by adding ethanol. As expected, in both cases, at high stretching speeds, equal volume of solution pools were formed on the top and bottom plates in the characteristic third regime.

### 1.7.3 Viscoelastic inks

Even though most of the printing inks have viscoelastic or shear thinning behaviour, there have been very limited studies on liquid transfer for viscoelastic solutions. The first systematic investigation of liquid transfer for viscoelastic solutions was reported by Sankaran and Rothstein [42]. Their experimental study was carried out for a liquid transfer in-between different gravure cells and flat plate. These authors used polyethylene glycol (PEG) with molecular weight,  $M$ , of 20 000 g/mol to obtain Newtonian solutions. For viscoelastic

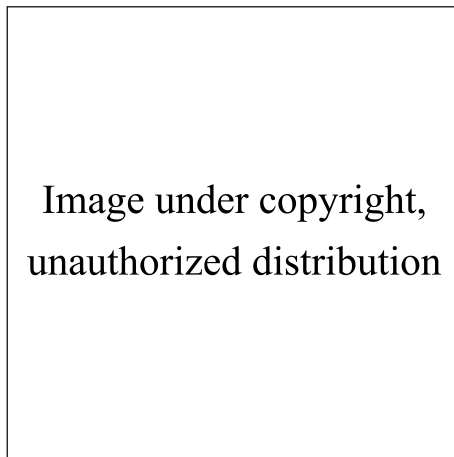


Fig. 1.20 Single curve for transfer ratio vs.  $Ca$ . The data include: (■) for 20% of 20k PEG, (●) for 15% of 20k PEG, (▲) for 10% of 20k PEG. Adapted from Sankaran and Rothstein [42]

solutions, polyethylene oxide (PEO) of two different molecular weights,  $M = 2 \times 10^6$  and  $8 \times 10^6$  g/mol, in combination with 20% PEG were investigated. The polymers tested by the authors are similar to the polymers used in the present thesis. For the Newtonian fluids, when a liquid bridge was stretched, one detached drop and two static solution pools on the plate and inside the cell were formed. For a viscoelastic solution, a typical long-lived self-thinning filament was observed along with a capillary breakup. To calculate the fraction of liquid transferred to the top plate, a high precision weight balance was used. The transfer ratio increased with increasing  $Ca$  and a single curve (see Fig. 1.20) was obtained for all polymer solutions. For  $Ca > 0.05$ , the transfer ratio reached a plateau, similar to Huang et al. [106], but lower values of transfer ratio (less than 0.5) were obtained. These lower values of  $TR$  were probably due to different surface geometries of the flat plate and gravure cells.

Further investigation on the effect of viscoelasticity in liquid transfer was carried out numerically by Lee et al. [43]. The simulations were performed under the same conditions as the experiments of Sankaran and Rothstein [42] with a corresponding gravure system geometry and similar liquid properties. A liquid bridge, formed in between a fixed gravure cell cavity at the bottom and a moving flat disk at the top, is considered as an initial condition. Their numerical results for fraction of liquid transferred against  $Ca$  are shown in Fig. 1.21. Two effects of viscoelasticity are evident: first, for all values of  $Ca$ , due to increase in elasticity, liquid transferred to the flat plate reduces with increase in  $De$ , and second, to obtain a maximum liquid transfer, there is an optimal capillary number  $Ca$ . The authors reported that computations could not be reliably carried out for  $De > 5$  due to numerical difficulties associated with high elasticity flow. However, these results are useful in our liquid transfer

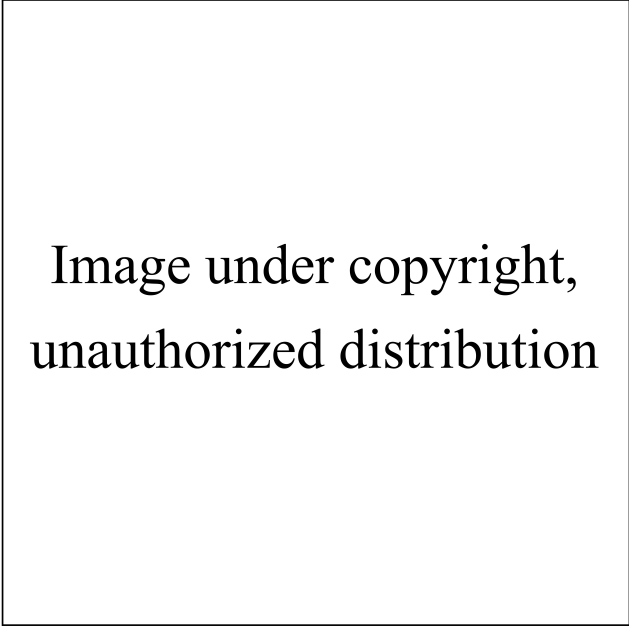


Image under copyright,  
unauthorized distribution

Fig. 1.21 Effect of Deborah number,  $De$ , on a fraction of liquid transferred for  $S \approx 0.8$ . Here,  $Bo = 1.2$  and  $Oh \sim 0.57$ . Adapted from Lee et al. [43].

experiments as we have obtained a wide range of  $De$  for the same polymers used by Sankaran and Rothstein [42]. Furthermore, in their study, draining of viscoelastic solutions occurred in two stages. In the first stage, liquid transfer is decided by strong initial elastic forces, which pull the solution back into the cavity. This stage is independent of gravity and dominated by shearing forces. In the second stage, thinning is dominated by extensional forces and delayed filament breakup allows prolonged drainage in the direction of gravity. Similar behaviour was observed by Wu et al. [107] for a moving liquid contact line liquid transfer. For PEO solution, in the first stage, the contact-line motion was influenced by shear viscosity because of strong shear deformation at slipping contact lines on plates. However, in the second stage, after stretching of a liquid bridge, formation of a thin filament was controlled by extensional viscosity. The authors found that filament formation had little effect on liquid transfer, contrary to the findings of Lee et al. [43] who reported prolonged gravitational drainage due to filament formation. Therefore, the effect of filament formation on liquid transfer remains an open question.

**Summary and voids in the literature** Most of the previous investigations on liquid transfer were done by using Newtonian fluids [40, 100, 102, 103, 106, 112, 113], and limited work was done on viscoelastic fluids [42, 43, 107]. Effect of viscoelastic PEO solutions on liquid transfer was studied experimentally by Sankaran and Rothstein [42] as well as Wu et al.

[107] and numerically by Lee et al. [43]. Limited results [42, 43, 107] suggest an effect of viscoelasticity on liquid transfer. In case of moving liquid contact lines, shear forces influence contact line motion and extensional viscosity only controls filament thinning time [107]. Formation of a filament delayed liquid bridge breakup and allowed prolonged gravitational drainage in the direction of gravity. However, these findings are only limited to gravure cells and moving contact surfaces. Numerical results from Lee et al. [43] suggest that with increase in  $De$ , liquid transfer to the top plate decreases. Hence, it would be interesting to study the effect of  $De$  on liquid transfer by varying polymer mass fraction and plate diameter.

Furthermore, liquid transfer for viscoelastic solutions must be explored by varying polymer mass fractions using pinned contact lines. Effects of stretching dynamics of a liquid bridge on liquid transfer have been explored before [42, 43, 100, 102, 103, 106, 107, 113, 118]. Increase in liquid transfer to a moving top plate with increasing stretching speed and the capillary number is well established for Newtonian fluids using moving contact lines [102, 103, 106, 113] and fixed contact lines [100]. However, effect of stretching velocity on viscoelastic liquid transfer with pinned contact lines remains to be investigated. Size and shape of an initial bridge liquid are other factors that should be considered to understand the dynamics of liquid transfer. Effect of plate diameters on liquid transfer for Newtonian fluids was studied before [100]. In their numerical study, Huang et al. [106] reported a decrease in transfer ratio with increasing initial aspect ratio for moving contact lines. However, there is no study that addresses the influence of final stretching heights on liquid transfer. Hence, influences of plate diameter, initial and final stretching heights on liquid transfer of viscoelastic solutions for pinned contact lines need to be investigated. In addition, most of the previous works focused on liquid transfer for non-cylindrical shaped (initial) liquid bridges with moving contact lines [40, 42, 102, 103, 106, 107, 112, 113, 118]. Therefore, liquid transfer for cylindrical and non-cylindrical shaped liquid bridges remains to be investigated.

Previous limited numerical studies investigated Newtonian fluids using cylindrical disks [100] and viscoelastic fluids using combinations of gravure cells-flat plate [43]. Additionally, liquid transfer was studied numerically mostly with moving contact lines [106], and there is no significant work done with fixed contact lines on flat plates [100]. Therefore, liquid transfer for circular flat plates having fixed contact lines needs to be studied numerically.

Hence, the present study focuses on liquid transfer for a cylindrical-shaped liquid bridge of viscoelastic fluids, as well as Newtonian fluids. Solutions will be prepared by varying mass fraction and molecular weight of polymers to investigate effect of viscoelasticity on liquid transfer. Previous studies showed liquid contact angles vary for different surface materials [102, 103, 107]. Hence, to minimise influence of surface properties, the same types of plates will be used [107]. Contact lines will be pinned, like Zhang et al. [100], to overcome the

shearing effect of moving contact lines. Different plate diameters, initial aspect ratio and final aspect ratio will be explored for both Newtonian and viscoelastic liquid bridges. By varying stretching profile curvatures, liquid transfers for different shapes and sizes of initial liquid bridges will be investigated.

## 1.8 Numerical modelling

Current state of the art on beads on a string and liquid transfer, along with their limitations, has been discussed in the previous sections. Numerical modelling of capillary thinning of a viscoelastic filament can be done using various models, especially Oldroyd-B [2, 3, 13, 16, 55, 56, 85, 100] and FENE models [74, 119–121]. However, the Oldroyd-B model has attracted considerable earlier attention because it exhibits formation of a BOAS structure along with its typical drop dynamics such as coalescence and drops migration [2]. In most of the previous numerical works, a BOAS structure was reproduced using 1D [2, 3, 13, 16, 85, 100] and 2D [55, 56] Oldroyd-B models. To fully capture a filament and a BOAS structure, distribution of stress components in the neck region connecting a filament with a drop should be resolved in detail. This can not be achieved by 1D slender formulation because the structure of drops attached to the thin filament is not slender [55]. For this purpose, the 2D Oldroyd-B equations should be simulated in an axially symmetric domain to examine the velocity and stress field in the filament. The Oldroyd-B model allows infinite stress to be built up so that the filament should not break up as long as the numerical grid is small enough. As the filament does not breakup with the Oldroyd-B model, a BOAS structure can develop due to necking and localised pinching.

Although there are several options, both commercial and open-source, to handle Newtonian and also non-Newtonian fluids, the range of options for viscoelastic fluid flow simulations is more limited. Previously, different solvers have been used to solve 2D Oldroyd-B equations. Turkoz et al. [55] implemented Basilisk solver [92, 93] and Figueiredo et al. [56] developed an in-house two-phase viscoelastic fluid flow solver. Open-source packages are especially appealing because they are cost-free for the user and usually allow the customisation of the available source code. In the present study, we will use a specialised open-source solver for viscoelastic flows, implemented in OpenFOAM, called *rheoTool*. The OpenFOAM is a versatile finite-volume solver for CFD simulations in general which can handle general unstructured meshes and perform parallel computations [122]. Favero et al. [123] created a library containing a wide range of constitutive equations to model viscoelastic fluids, along with a solver named *viscoelasticFluidFoam* that makes use of this library. *rheoTool* was

introduced recently in 2016 by Pimenta and Alves [124, 125]. Then, the authors modified the solver with enhanced stability and developed a solver called `rheoInterFoam` that can be used for viscoelastic models in two-phase flows [126–128]. Results obtained using this solver agree with numerical studies of impacting drop [53] and extruded swell of viscoelastic fluids [54]. Details of the solver are given in the article by Pimenta and Alves [124].

Few previous numerical studies investigated viscoelastic filament thinning and BOAS structure for a stretched liquid bridge [3, 56]. As *rheoTool* allows us to implement the 2D Oldroyd-B model, dynamics of filament thinning along with a BOAS structure and liquid transfer could be investigated in details for our stretched liquid bridge. In addition, the use of *rheoTool* for viscoelastic filament thinning remains to be tested. Therefore, we would like to validate the use of *rheoTool* solver using our Newtonian and viscoelastic solutions. The present study focuses on numerically reproducing BOAS and transfer ratio phenomena, using properties of test fluids and respective stretched liquid bridge profiles.

**Mathematical modelling of viscoelastic solutions and liquid-air interface** In *rheoTool*, for viscoelastic fluid flow simulation, the total extra-stress tensor is divided into the solvent contribution,  $\underline{\underline{\tau}}_S$  and the polymeric contribution  $\underline{\underline{\tau}}_p$ , as shown in Eq. 1.47. For details refer to section 1.4.2. The present work only considers the Oldroyd-B model, with constant polymer viscosity,  $\eta_p$ .

$$\underline{\underline{\tau}} = \underline{\underline{\tau}}_p + \underline{\underline{\tau}}_S \quad (1.47)$$

However, usually simulations for highly viscoelastic fluids experience stability issues [129]. To tackle this problem, the log-conformation tensor approach [130] and the both-sides-diffusion (BSD) technique are implemented in the *rheoTool* solver, which enables stable simulations [124, 125]. The polymeric extra-stress tensor is related to the conformation tensor  $A$ . For the Oldroyd-B model, for example, this relation is expressed as

$$\underline{\underline{\tau}}_p = \frac{\eta_p}{\lambda} (\underline{\underline{A}} - \underline{\underline{I}}). \quad (1.48)$$

Since  $A$  is positive definite, it can be diagonalised in the form

$$\underline{\underline{A}} = \underline{\underline{R}} \underline{\underline{\Lambda}} \underline{\underline{R}}^T. \quad (1.49)$$

$\underline{\underline{R}}$  is a matrix whose columns are the eigen vectors of  $\underline{\underline{A}}$  and  $\underline{\underline{\Lambda}}$  is a matrix whose diagonal elements are the respective eigenvalues resulting from the decomposition of  $\underline{\underline{A}}$ . In the log-conformation tensor methodology, a new tensor  $\underline{\underline{\Theta}}$  is defined as the natural logarithm of the

conformation tensor:

$$\underline{\underline{\Theta}} = \ln(\underline{\underline{A}}) = \underline{\underline{R}} \ln(\underline{\underline{\Lambda}}) \underline{\underline{R}}^T \quad (1.50)$$

Evolving  $\underline{\underline{\Theta}}$  in time and then transforming back to the conformation and stress tensors leads to generally enhanced stability [124]. In addition, both-side-diffusion (BSD) is a technique already incorporated in the *rheoTool* solver to stabilise viscoelastic flows [124]. It consists of adding a diffusive term on both sides of the momentum equation (Eq. 1.4). On the left-hand side,  $\underline{\underline{\nabla}} \cdot (\eta_s + \eta_p) \underline{\underline{\nabla}} u$ , is added implicitly, while on the right-hand side,  $\underline{\underline{\nabla}} \cdot (\eta_p \underline{\underline{\nabla}} u)$ , is added explicitly in Eq. 1.4. Once steady-state is reached, both terms cancel each other exactly. Such method increases stabilising effect, mostly when there is no solvent contribution to the extra-stress tensor. More details on the BSD technique can be found in *rheoTool* document by Pimenta and Alves [125].

For two-phase flows, the Volume of Fluid (VOF) method [94] is used to model a free surface boundary (fluid-fluid interface) in OpenFOAM. In this method, the volume of fluid in a cell is computed as  $F_{vol} = \alpha_1 \cdot V_{cell}$  where  $V_{cell}$  is the computational cell volume and  $\alpha_1$  is the liquid fraction in this cell. The value of  $\alpha_1$  in a cell varies between 0 and 1. A cell filled with one fluid can be represented as  $\alpha_1 = 1$  and a filled cell with another different fluid can be represented as  $\alpha_1 = 0$ . At the interface, the value of  $\alpha_1$  is in-between 0 and 1, and follows the equation:

$$\frac{\partial \alpha_1}{\partial t} + \underline{\underline{\nabla}} \cdot (\alpha_1 \underline{\underline{u}}) + \underline{\underline{\nabla}} \cdot [\alpha_1 (1 - \alpha_1) \underline{\underline{u}}_{\perp}] = 0 \quad (1.51)$$

where  $\underline{\underline{u}}_{\perp}$  is the velocity field in the directions subjected to the interface compression [123]. The last term is only activated in the region of interface due to a product of liquid fractions  $\alpha_1 (1 - \alpha_1)$ . To use the VOF method for the two-phase flows, the physical properties in any control volume domain are given by the corresponding values of  $\alpha_1$ , in that volume. It is mathematically obtained, considering any property,  $H$ , as

$$H = \alpha_1 H_1 + (1 - \alpha_1) H_2 \quad (1.52)$$

Many viscoelastic models, such as Oldroyd-B, FENE and Giesekus, can be solved using *rheoTool* in standard extra-stress or conformation tensor variables. *rheoTool* allows us to define various liquid properties such as  $\eta_s$ ,  $\eta_p$  and  $\lambda$  to implement these viscoelastic models. For Newtonian fluids, we only need to define liquid parameter  $\eta_0$  to solve Newtonian constitutive equations. In *rheoTool*, the solver `rheoInterFoam` is a library used for two-phase flows. The `rheoInterFoam` solves the constitutive equation for each phase and the extra-stress tensor,  $\underline{\underline{\tau}}$ , which contributes to the momentum equation, is calculated by the average of the extra-stress tensor for each phase.

## 1.9 Summary of objectives of the present work

The present work is motivated by the need to understand fundamental dynamics regarding drops on a filament and liquid transfer phenomena, experimentally. While there is significant experimental and numerical work on drops on a filament phenomenon, yet there is not much investigation on position, trajectories and number of drops. Considering the literature [9, 15], there is a need to create space-time diagrams that can depict filament thinning and monitor spatial-temporal dynamics of drops along with their sizes and numbers. Moreover, there is no information available on effect of polymer concentration on drop dynamics of a BOAS instability and liquid transfer. Hence, in the present study, large range of mass fractions of polyethylene oxide (PEO) and polyethylene glycol (PEG), either separately or in combination, will be considered to understand their effect on BOAS structure and liquid transfer.

Taking into account the voids in the literature review, in our experimental study, we aim to understand the influence of geometrical parameters such as plate diameter, initial stretching height, final stretching height, and stretching speed of a liquid capillary bridge, on drop dynamics and liquid transfer. These results can be further represented through space-time diagrams to depict variations in filament thinning and drop dynamics for each parameter. Moreover, we plan to investigate liquid transfer for cylindrical and non-cylindrical shaped initial liquid bridges using fixed contact lines.

Few numerical studies are available for liquid transfer in a stretched capillary bridge. Thus, for such a case, further numerical study would be helpful. The OpenFOAM toolbox *rheoTool* will be tested to reproduce liquid transfer and the BOAS structure.

# Chapter 2

## Test fluids, their properties, and numerical setup

### Contents

---

<b>2.1</b>	<b>Test fluids and their properties</b>	<b>50</b>
2.1.1	Polymers and solution preparation	50
2.1.2	Solution properties	52
2.1.2.1	Density measurements	52
2.1.2.2	Surface tension measurements	53
2.1.2.3	Shear rheometry	54
<b>2.2</b>	<b>Extensional rheology of polymer solutions</b>	<b>56</b>
2.2.1	Experimental setup and instrumentation	57
2.2.2	Experimental method and image analysis	58
2.2.2.1	Filament thinning and BOAS	59
2.2.2.2	Relaxation time	62
2.2.2.3	Apparent extensional viscosity	65
2.2.3	Experimental details for liquid transfer	68
<b>2.3</b>	<b>Solution property table</b>	<b>70</b>
<b>2.4</b>	<b>Numerical setup</b>	<b>70</b>
2.4.1	Newtonian solution: PEG20	72
2.4.2	Viscoelastic solution: PEG20PEO1000	76

---

This chapter is devoted to test fluids and their characteristic properties, descriptions of test facilities, instruments employed and details of image analysis techniques. We first present protocols for the preparation of the solutions. The solutions are characterised using a density meter, a rotational rheometer and a drop shape analyser. Next, we turn our attention to rheological characterisations of the test fluids, both in shear and extensional flows. Experimental method and image analysis for drops-on-a-filament and liquid transfer are described. The experimental results associated with this set-up for drops-on-a-filament and liquid transfer will be discussed in chapters 3 and 4, respectively. In addition, numerical simulations for a stretched liquid bridge using the Oldroyd-B model are discussed. The present chapter is primarily organised as per the following sections: (i) test fluids and their properties, (ii) extensional rheology of polymer solutions and (iii) numerical setup using *rheoTool*.

## 2.1 Test fluids and their properties

The experiments are performed with two high molecular weight polymers with different rheological behaviours. In this study, aqueous solutions of polyethylene oxide (PEO), and polyethylene glycol (PEG) polymers are used either separately or in combination. The relatively high mass fraction of PEG, in PEG+PEO solution, makes the solution particularly dependent on PEG for the shear viscosity and on PEO for the elasticity. Broadly, our strategy is to control the shear viscosity of the solutions with PEG and extensional viscosity with the mass fraction of PEO, noted  $w_{PEO}$ .

### 2.1.1 Polymers and solution preparation

Both PEO and PEG polymers have the same molecular structure:  $H - (O - CH_2 - CH_2)_n - OH$ , where  $n$  is the number of repeatable units. But both polymers have different chain lengths. PEO is a long-chain polymer, with an average molecular weight,  $M \sim 8 \times 10^6$  g/mol. Whereas PEG is a relatively short-chain polymer, with an average molecular weight,  $M \sim 20\,000$  g/mol. The polymers and their molecular weights are provided by Sigma Aldrich. Commercial PEO is known to be polydisperse. The same supplier was used by Latrache et al. [131] and the authors found a low polydispersity index of 1.25 for PEO. Both polymers are soluble in water and their aqueous solutions are transparent, non-ionic and non-toxic.

Three different types of solutions: PEG, PEO and PEG+PEO solutions are prepared in degassed deionised water. In the first type of solution, PEG is added into water; specifically,

20 wt% in water. This solution is highly viscous and labelled as "PEG20". The mass of PEG represents 20% of the total mass of the solution. PEG20 is a Newtonian solution and the corresponding shear viscosity is 0.034 Pa·s (details are given later in this chapter). "PEG20" solution is prepared without isopropyl alcohol (IPA). In the second type, to have highly elastic solutions, PEO is mixed with water in various mass fractions and designated as "PEO solutions". The PEO mass fraction ranges from 100 to 2000 wppm. In the third type of solutions, hereafter "PEG+PEO solutions", both PEO and PEG are added separately to the water and then mixed to create viscoelastic solutions. In the "PEG+PEO solutions", the mass fraction of PEG is kept constant at 20 wt%. Hence, the corresponding solvent viscosity,  $\eta_s$ , is 0.034 Pa·s (as PEG20 acts as solvent). The mass fraction of PEO varies from 100 to 2000 wppm. The preparation and storage of all types of solutions are carried out at room temperature, 20°C.

For all solutions containing PEO, 0.5 wt% of IPA is included. IPA is mixed with water before PEO being added to the mixture. As previously demonstrated by Layec and Layec-Raphalen [132], the addition of IPA helps in easy molecular dispersion of PEO polymers. The presence of IPA also helps to prevent bacterial degradation of the solutions. Hence, the solutions can be used over a longer period, typically two to three weeks.

Moreover, if the solutions are stirred, degradation of polymer chains may occur. Mechanical stirrers produce high shear rates. Hence, the polymer chains can break and result in lower average molecular weights. Gaillard [61] observed that, if a mechanical stirrer is used, relaxation times of PEO solutions with the same PEO mass fraction can vary by a factor of 4. However, in our study, no mechanical stirring is done while preparing the solutions. This technique takes longer preparation times than stirring, but mechanical degradation due to stirring is avoided.

The "PEG+PEO solutions" are prepared in two stages. In the first stage, two vessels are used to prepare aqueous mixtures of PEG and PEO separately. In the first vessel, PEG flakes are dropped slowly into the water. In another vessel, initially, iso-propyl alcohol (IPA) is added in the water. The mass fraction of IPA in the final blend is 0.5 wt%. Then, PEO powder, depending upon the required mass fraction, is weighed and poured into this mixture. Both vessels are covered with plastic films and aluminium foils. Depending upon the polymer mass fraction, the vessels are kept for 3 to 7 days to ensure complete mixing of the polymers. In the second stage, when the mixtures are well dissolved, the PEG solution from the first vessel is poured into the PEO solution in the second vessel, resulting in the final blend. All mass fractions of PEO, PEG and IPA refer to this final blend, which is obtained in the second vessel and is kept for 3 to 7 additional days without stirring, to produce a homogeneous mixture. The solutions are considered homogeneous when the white-coloured

layer of polymers disappears from the eyes of the experimenters, and no polymer blobs are observed.

**Mark-Houwink equation** The Mark-Houwink equation is a common way to estimate the critical overlap mass fraction,  $w^*$  [47]. For a polymer solution,  $w^*$  is defined as a mass fraction at which different polymer coils touch each other. A dilute regime corresponds to  $w < w^*$  and a semidilute regime, in which polymers are entangled, corresponds to  $w > w^*$ . The equation takes the form  $[\eta] = K_M \times M^{\alpha_M}$ , where  $[\eta]$  is the intrinsic viscosity [47] and  $M$  is the molecular weight of the polymer.  $K_M$  and  $\alpha_M$  depend on the chemical nature of both polymer and solvent. Investigations by Tirtaatmadja et al. [69] with PEO in various solvents (water, glycerol-water) suggest that solvent play a minor role. Hence, in the present study, the following Mark-Houwink formula [69] is used:

$$[\eta] = 0.072 \times M^{0.65}. \quad (2.1)$$

The formula agrees well for PEO in water over the range of molecular weight,  $M = 8 \times 10^3$  to  $5 \times 10^6$  g/mol as reported by Tirtaatmadja et al. [69]. For PEO solution at 20°C, we find  $[\eta] \approx 2210$  ml/g and  $w^* = 0.77/[\eta] \approx 348$  wppm. For PEG solution at 20°C, we obtain  $[\eta] \approx 45$  ml/g and  $w^* \approx 1.71$  wt%. Hence, we can assume, for PEG+PEO solutions with 20 wt% PEG, interactions between PEG molecules are significant. To cover a wide range of mass fractions, our solutions are thus prepared above as well as below 348 wppm of PEO.

## 2.1.2 Solution properties

Different relevant properties, such as density, surface tension, shear viscosity, relaxation time and extensional viscosity of test fluids are measured. These properties are used to calculate characteristic non-dimensional numbers. All the measured properties and the characteristic non-dimensional numbers are summarised at the end of the chapter.

### 2.1.2.1 Density measurements

A portable density meter DMA 35 (Anton Paar) is used to measure density,  $\rho$ , of all the solutions. The instrument measures the density of solutions using the oscillating U-tube method. In the oscillating U-tube method, a sample in the U-shaped glass tube is excited to its characteristic frequency and this frequency is used to calculate the density of the sample. The samples are filled in the measuring tube using built-in pipette type syringe. A temperature

sensor measures temperatures of the solutions. For the solutions having a density less than 2 g/cm<sup>3</sup>, the accuracy of the density meter is 0.001 g/cm<sup>3</sup> and resolution is 0.0001 g/cm<sup>3</sup>. The density measurements for each solution are the average over three tests. A fresh liquid sample is used for each test. Details of the values obtained for densities,  $\rho$ , for all the solutions are reported in Tab. 2.1. The PEG, as well as PEG+PEO solutions, have higher densities than the PEO solutions, as expected.

### 2.1.2.2 Surface tension measurements

Another important property to characterise the free surface flow of the solutions is surface tension,  $\sigma$ . A pendant drop method [133] is used with the help of computer-aided image processing [134] to calculate the surface tension. In the pendant drop method, an axisymmetric drop of test fluid is formed at the end of a needle with known diameter. The pendant drop shape at equilibrium is influenced only by surface tension and gravity. The pendant drop at equilibrium is described by the Young-Laplace equation:  $\Delta p = \sigma[(1/R_1) + (1/R_2)]$ , where  $\Delta p$  is the pressure difference (Laplace pressure) across the interface,  $R_1$  and  $R_2$  are the principal radii of curvature of the drop surface and  $\sigma$  is the surface tension of the solution. Due to gravitational effects, the drop deforms as its weight generates a hydrostatic pressure,  $\Delta p_{hyd}$ , within the drop and this hydrostatic pressure is defined as  $\Delta p_{hyd} = gl\Delta\rho$ . Here,  $\Delta\rho$  is the difference in densities between heavier (pendant) drop and lighter (air) phase,  $g$  is the gravitational acceleration and  $l$  is a vertical distance between the measuring point and the needle opening. This hydrostatic pressure contributes to the inner pressure and therefore, influences the primary radii of curvature  $R_1$  and  $R_2$ . During the measurement, a magnification of a video image is first determined to be able to assess actual drop dimensions ( $R_1$ ,  $R_2$  and  $l$ ). Then, an inbuilt (Kruss) software uses a numerical method to generate a drop shape that coincides with the actual drop shape. When both the shapes coincide, a surface tension value is extracted [134] by equating the Young-Laplace equation and the hydrostatic pressure equations.

The surface tension measurements are done using a (Kruss) Drop Shape Analyser (series 100), with a resolution of 0.01 mN/m. A suspended drop of the solution is created at the tip of a syringe. The syringe has a needle diameter of 1.825 mm. A box, made of transparent glass, is partially filled with the solution. Then, the box is covered with a paraffin film having a small hole. The size of the hole is limited so that the syringe needle can just pass through it. This method helps to create a saturated environment to prevent evaporation of the pendant drop. Furthermore, any other outside contamination and airflow are restricted. At least three

drops are analysed for each test fluid. The values obtained of surface tension,  $\sigma$ , for all the solutions are reported in Tab. 2.1. The values of  $\sigma$  are fairly constant for all the solutions.

### 2.1.2.3 Shear rheometry

We measure the shear viscosity,  $\eta(\dot{\gamma}) = \tau/\dot{\gamma}$ , and the measurements are done with a rotational rheometer (Discovery HR-3 from TA Instrument). A double-wall concentric cylinder geometry, as schematically shown in the inset of Fig. 2.1, is used. The large contact area between the solution and geometry surfaces enables accurate measurements of the low-viscosity solutions with torque resolution of 0.05 nN.m. After machine self-calibration, the test fluid is loaded into the cavity between the two fixed cylinders of the double-wall concentric geometry. The detailed geometry of the double-wall concentric cylinder is as follows: inside cup diameter is 30.2 mm, outside cup diameter is 37 mm, inside bob diameter is 32 mm, outside bob diameter is 35 mm, and inner cylinder height is 55 mm. The rotating bob drives the flow. Then, the geometry is covered with the protective plates to avoid solution evaporation and outside contamination. Range of shear rate,  $\dot{\gamma}$ , is maintained in-between 0.001 to 1000 s<sup>-1</sup>, with at least 5 points per decade. To ensure the repeatability of the measured points, shear rate is increased from 0.001 to 1000 s<sup>-1</sup>, and then decreased from 1000 to 0.001 s<sup>-1</sup>. Only overlapped data points are validated and unstable data are removed. The low shear rates were limited by the instrumental constraints and the high shear rates were limited by elastic instabilities [135]. For shear rates larger than 100 s<sup>-1</sup>, apparent shear thickening is indeed observed, probably due to elastic instabilities. Over-night tests are performed to ensure the steady-state condition is reached. Each point takes at least 1200 seconds so that at least one complete rotation of the bob is obtained for the low shear rates and many more for the highest shear rate. For each experiment, the same protocol and a new test fluid is used. The shear viscosity experiments are carried out in a temperature-controlled room at 20°C and a thermal bath (ThermoFisher scientific) is also used to ensure that the rheometer remains at a constant temperature (20°C).

Experimental measurements of  $\eta$  versus  $\dot{\gamma}$  for all the solutions are presented in Fig. 2.1. At small shear rates, the viscosity attains a constant value, called first Newtonian plateau viscosity or zero-shear viscosity,  $\eta_0$ . At high shear rates, a second plateau called the second Newtonian plateau viscosity or infinite-shear viscosity,  $\eta_\infty$ , is expected. For the results obtained, the Carreau model [47] is used to calculate the zero shear viscosity,  $\eta_0$ . The Carreau model represents the approximation of the relationship between zero-shear rate, infinite-shear rate, and shear viscosity:

$$\frac{\eta - \eta_{\infty}}{\eta_0 - \eta_{\infty}} = [1 + (K_1 \dot{\gamma})^a]^{(n-1)/a} \quad (2.2)$$

where  $K_1$  is a time constant at which shear thinning starts,  $n$  is the power law exponent, and  $a$  is a dimensionless parameter describing the transition between the zero-shear rate region and the power law region. When  $a = 2$ , Eq. 2.2 is referred to as the Carreau equation [136]. The variable parameter  $a$  was added later by Yasuda et al. [137]. In our calculations, we use  $a = 2$ . Furthermore, since the second Newtonian plateau is not accessible by our measurements (it is beyond elastic instabilities), a solvent viscosity,  $\eta_s$ , is considered as the infinite-shear viscosity. The minimum torque for Discovery HR-3 is 5 nN·m, according to the manufacturer. However, the bob is used for both rotation control and torque measurement. Hence, in practice, as shown in Fig. 2.1, it is difficult to reach the minimum torque.

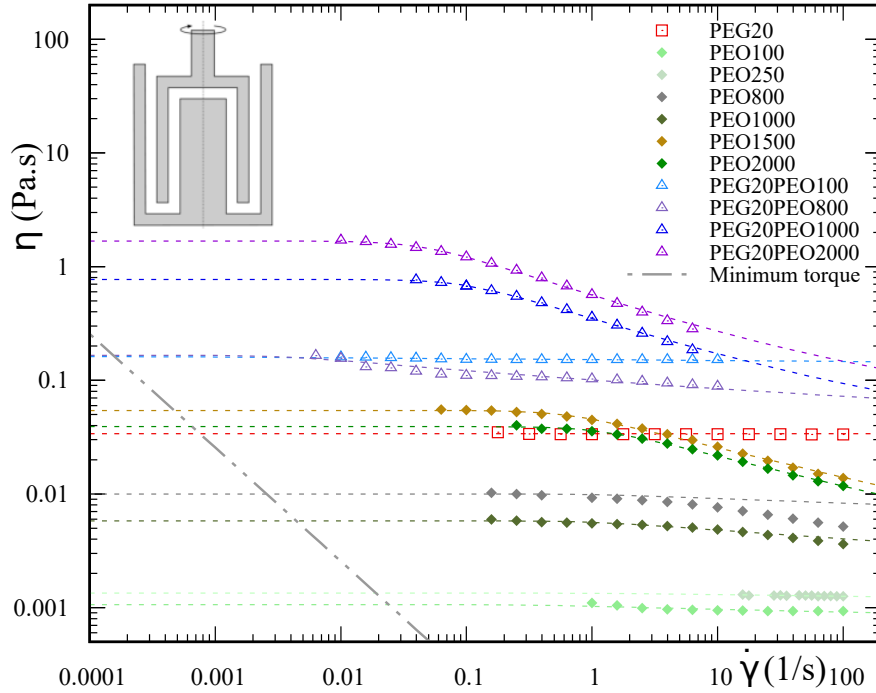


Fig. 2.1 Shear viscosity,  $\eta(\dot{\gamma})$ , for all tested solutions at 20°C. The inset schematic diagram is the double-wall concentric cylinder geometry, used for the shear viscosity measurements. For PEO and PEG+PEO solutions, the data are fitted with the Carreau law (Eq. 2.2). For PEG20 solution, the red dashed line shows the average value of  $\eta$ . The minimum torque limit is indicated by the dashed-dotted line.

The corresponding values of the zero shear viscosity,  $\eta_0$ , the power law exponent,  $n$ , and the time constant,  $K_1$ , are reported in Tab. 2.1. It can be observed that PEG+PEO solutions have higher  $\eta_0$  than PEO solutions, as expected. Hence, the addition of PEG in PEO solutions enhance the shear viscosity of the solutions. When  $n$  is less than one, fluids

Table 2.1 Density, surface tension and shear rheological parameters for PEG20, PEO and PEG+PEO solutions at 20°C. For all solutions containing PEO, 0.5 wt% of isopropyl alcohol is added. For PEO and PEG+PEO solutions, shear viscosity data are fitted with the Carreau law (Eq. 2.2).  $n$  is the power law exponent and  $K_1$  is a time constant. Values of  $n$  and  $K_1$  are obtained from the Carreau fits. The solvent viscosity,  $\eta_s$ , is considered as  $\eta_\infty$ . For PEG20, average value of shear viscosity is considered as  $\eta_0$ . \* indicate inconsistent values of  $\eta_0$  caused probably by shear viscosity measurements performed later than three weeks after solution preparation.

Abbreviation	$w_{PEG}$ wt (%)	$w_{PEO}$ (wppm)	$\rho$ ( $kg/m^3$ )	$\sigma$ (mN/m)	$\eta_0$ (Pa·s)	$\eta_\infty$ (Pa·s)	$n$	$K_1$ (s)
PEG20	20	0	1032.5	58	0.034	-	-	-
PEO100	0	100	997	59	0.0011	0.001	0.940	3.319
PEO250	0	250	997.1	59	0.0013	0.001	0.973	0.774
PEO800	0	800	997.3	59	0.0100*	0.001	0.957	0.999
PEO1000	0	1000	997.3	59	0.006	0.001	0.900	0.998
PEO1500	0	1500	997.5	59	0.054*	0.001	0.724	1.651
PEO2000	0	2000	997.6	59	0.039	0.001	0.717	0.887
PEG20PEO100	20	100	1032.8	57	0.160	0.034	0.99	348.8
PEG20PEO250	20	250	1033.4	57	0.165	0.034	0.99	319.1
PEG20PEO800	20	800	1033.6	57	0.170	0.034	0.880	300.1
PEG20PEO1000	20	1000	1033.6	57	0.771	0.034	0.634	10.28
PEG20PEO2000	20	2000	1033.4	57	1.682	0.034	0.641	23.65

experience shear thinning behaviour. In the present study, for both PEO and PEG+PEO solutions, the shear-thinning behaviour is observed and this behaviour is predominant beyond  $w^* = 350$  wppm. Values of the time constant,  $K_1$ , are higher for PEG+PEO solutions than PEO solutions. Higher values of  $K_1$  for PEG+PEO solutions indicate that the shear-thinning behaviour occurs earlier (at lower shear rates) than PEO solutions.

## 2.2 Extensional rheology of polymer solutions

In this section, initially, details of the experimental setup and instrumentation used are given. Then, experimental methods along with image analysis for filament thinning and BOAS structure are discussed. Furthermore, relaxation time and apparent extensional viscosity values for test fluids are presented. Finally, the experimental details and image analysis for the liquid transfer are discussed.

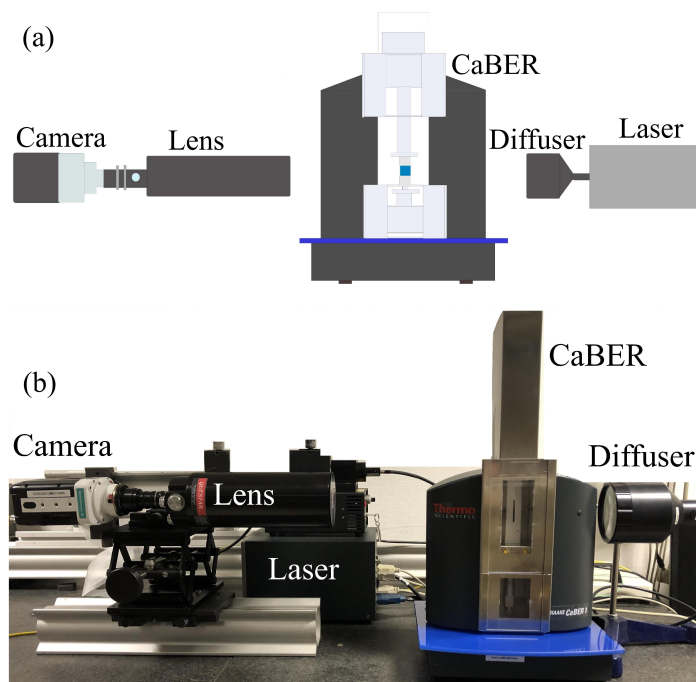


Fig. 2.2 (a) Schematic and (b) photograph of the experimental setup. In the schematic, the small blue rectangle represents a polymer solution sample.

### 2.2.1 Experimental setup and instrumentation

The experimental setup to study extensional rheology consists of a CaBER, a high-speed camera (Phantom), a 2 W power-adjustable continuous green laser (RayPower), and a diffuser. The camera is fitted with a catadioptric lens (Questar). The diffuser is an anti-speckle optic that allows shadowgraph images. A schematic and photograph of the experimental setup is shown in Fig. 2.2 Details of the instrumentation used in the experimental setup are given below:

**Capillary Breakup Extensional Rheometer (CaBER)** CaBER is a commercial extensional rheometer by Thermo Haake and it can be used to obtain a precise stretching of a capillary liquid bridge. A solution sample is placed in-between two horizontal stainless steel cylindrical plates to form the liquid bridge. The liquid volume introduced is controlled with the help of a pipette (Eppendorf research plus, range of 10 to 100  $\mu\text{L}$ ). The bottom plate of the CaBER is fixed. The top plate can be moved at the desired speed (minimum speed of approximately 0.001 m/s and a maximum speed of approximately 0.134 m/s). The liquid bridge is stretched upwards to a requisite height with the help of a linear motor having a resolution of 0.02 mm. Hence, a highly precise, repeatable, and controllable stretching can

be achieved. Three sets of plates with diameters 4, 6 and 8 mm are used, as shown in Fig. 2.3.



Fig. 2.3 CaBER (top) plates with diameters,  $D_P =$  (a) 4, (b) 6, and (c) 8 mm.

**Camera and lens** The high-speed camera (Miro series from Phantom) records the evolution of the capillary liquid bridge. Images can be acquired at a maximum rate of 3260 images per seconds. Each image having a resolution of  $800 \times 1280$  pixels. A long-distance catadioptric lens from Questar (with working range 560 to 1520 mm and resolution up to  $3 \mu\text{m}$  at 560 mm) is attached to the camera.

**Laser** A continuous laser from Dantec dynamics (RayPower 2000) with 2 W power is used as a light source. The laser power can be adjusted to capture good-contrasting images. A diffuser (shadowStrobe from Dantec), which is an optical device used for shadowgraphy, is connected to the laser. The diffuser helps to avoid speckles and to make a uniform light distribution.

**Temperature** For all experiments, the experimental setup is kept in a temperature-controlled room, maintained at  $20^\circ\text{C}$ . A thermal bath (ThermoFisher scientific) is also used to ensure that the CaBER remains at a constant temperature ( $20^\circ\text{C}$ ). Furthermore, storage and characterisation of the solutions are done at the same temperature ( $20^\circ\text{C}$ ).

## 2.2.2 Experimental method and image analysis

In the present study, liquid bridge is stretched in the upward direction. Stretching of a viscoelastic liquid bridge leads to the formation of a filament. To measure the time-evolution of the filament diameter, a CaBER micrometer, as well as a high-speed image processing have been used. The images are acquired at a rate from 100 to 1000 fps. Capillary thinning of the filament leads to necking at its both ends and the solution is pulled towards the centre of the filament. Then, due to localised pinching, a big central drop along with several smaller drops is formed. The camera records stretching, filament thinning, necking, localised pinching, as

well as the formation of drops on the filament. Calibration of images is required to optimise reproducibility and accuracy of geometric measurements. The pixel size has to be determined to produce scaled measurements. We acquire only the filament to extract filament diameters and to study the drops-on-a-filament structure. We record the complete stretched liquid bridge to visualise the evolution of the liquid bridge and to investigate the liquid transfer. Therefore, the camera is fixed at a position to capture the complete stretched liquid bridge or only the filament, depending upon the objective of measurement. Then, a reticle (from Max Levy Autograph) is placed in-between the plates and an image is acquired. The reticle has standard graduated markings (range: 0 to 15 mm) and the smallest measurement on the scale is 0.1 mm. The numbers of pixels for 0.1 mm are measured and this obtained scaling is used to convert the number of pixels into  $\mu\text{m}$ . The resolution for typical experiments (with  $D_P = 6$  mm and  $FAR = 2$ ) in the BOAS study is 1 pixel  $\approx 2.3 \mu\text{m}$ , and in the liquid transfer study: 1 pixel  $\approx 1.9 \mu\text{m}$ .

### 2.2.2.1 Filament thinning and BOAS

In this section, a typical example of a stretched viscoelastic liquid bridge is described. Time evolution of the stretched liquid bridge until the formation of BOAS, for PEO2000, is depicted in Fig. 2.4(a-g). Initially, at  $t = 0$  s, the liquid bridge is formed in-between two CaBER plates with diameter,  $D_P = 6$  mm, as shown in Fig. 2.4(a). The bridge is initially separated by the initial height,  $L_0 = 2$  mm. Then, the top plate is moved upwards (with a simple linear motion) and reaches the final stretching height,  $L = 6$  mm, at  $t = 0.05$  s, as shown in Fig. 2.4(b). Thinning of the stretched liquid bridge continues and a filament forms, as shown in Fig. 2.4(c). Moreover, solution pools can be seen at both ends of the filament. Necking appears first at the top end of the filament, see Fig. 2.4(d), and then at the bottom end. After necking of the filament occurs at both ends, the solution sample is pulled towards the centre of the filament. This is termed as recoil [2, 85]. A big central drop is formed as shown in Fig. 2.4(e). Furthermore, due to localised pinching, smaller satellite drops are formed across the length, on either side of the big drop, as shown in Fig. 2.4(f). The number of drops grows with time. Hence, a structure appears with all drops connected by thin and small random lengths of the filaments. This structure is called the drops-on-a-filament or BOAS structure. A zoomed view of the BOAS structure is shown in Fig. 2.4(g). The size of the big central drop is around  $300 \mu\text{m}$ . The drops move across the length of the filament and coalescence of the drops occurs. However, the filament continues to thin at both ends and breaks at either its top or bottom end. As a result, the drops either merge into the bottom or top solution pool. However, in the present study, we mostly observed drops falling into

the bottom solution pools. More details about the coalescence of the drops and the breakup of the filament are discussed in the next chapter. The formation of solution pools is further discussed at the end of this chapter.

**Filament diameters** Now to further investigate the filament thinning, the camera is focused on the region around the filament and images are captured. A self-developed code in MATLAB is used to extract the data from the calibrated images. Neck or minimum diameters,  $D_{min}(t)$ , and mid-plane diameters,  $D_{mid}(t)$ , of the filaments are obtained for each image. As the name suggests, the mid-plane diameter,  $D_{mid}$ , is captured at the mid-plane of the filament. The position of  $D_{mid}$  on the liquid bridge is indicated in Fig. 2.4(h) by blue-dashed lines. The measured filament diameters,  $D(t)$ , are plotted against time,  $t$  and presented in Fig. 2.4(h). The shaded regions (b-f) represent different filament thinning stages corresponding to photographs (b-f). For the same experiment, after  $t \simeq 1.8$  s, the minimum diameter curve deviates from the mid-plane diameter curve. Furthermore, both diameters are compared with the filament diameter,  $D_{CaBER}(t)$ , obtained from CaBER measurements. In CaBER, the diameter of the filament is monitored by an inbuilt laser micrometer. The position of the CaBER micrometer is fixed at the mid-height of the liquid bridge. The fixed mid-height position of the CaBER micrometer is represented as a red dotted line in Fig. 2.4(a-f). The CaBER experiments and high-speed image analysis experiments can not be conducted together because of experimental limitations (as the CaBER micrometer obstructs the laser path). Hence, the CaBER experiments are conducted separately to measure the filament diameter. In Fig. 2.4(h), the vertical shift between the red and blue curves, for  $D$ , can be explained by the position of the extracted diameters on the *filament*. Moreover, the horizontal shift between the red and blue curves, for  $t$ , can be due to different experiments. When all three diameters are considered, the filament does not have the same diameter over time.

In the later stages of the filament thinning, due to the recoiling and the coalescence, the drops move axially along the thread. Hence, for  $D_{mid}$  measurements, in the later stages of Fig. 2.4(h), crests and troughs are observed. The appearance of crests and troughs are highlighted in this  $D$  versus  $t$  plot by the shaded regions (e) and (f). The crests and troughs are not observed for  $D_{min}$ , as it only measures the minimum diameter across the filament. Position of  $D_{min}$  on the filament is also tracked in time and space. The details of the position of  $D_{min}$  are discussed in the next chapter. In the present thesis, we use  $D_{mid}$  to calculate relaxation times and  $D_{min}$  to measure extensional viscosity.

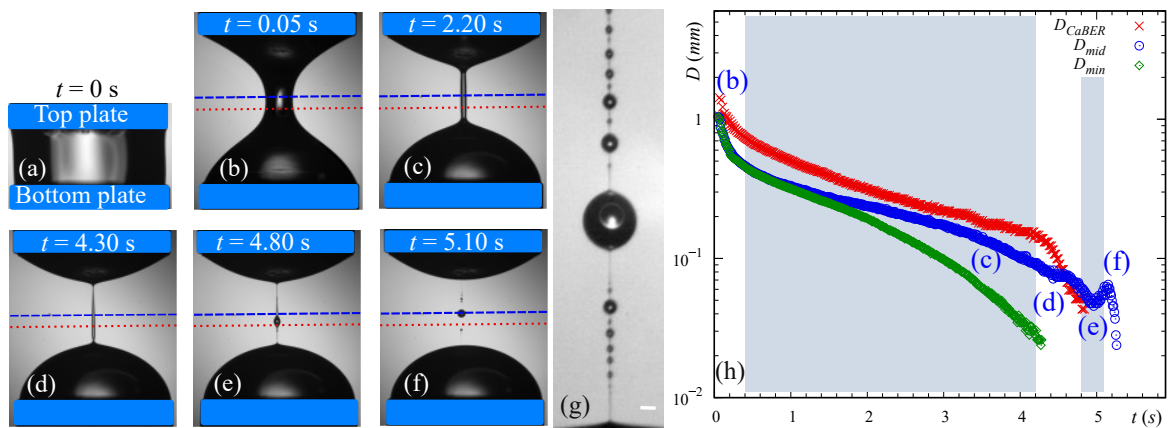


Fig. 2.4 A typical example of stretching of a liquid bridge, filament thinning and formation of a beads-on-a-string (BOAS) structure. Here, a liquid bridge, formed in-between the two plates having  $D_p = 6$  mm and volume  $56 \mu\text{l}$ , is stretched from  $IAR = 0.66$  to  $FAR = 2$  at  $U = 0.08$  m/s. (a-f) Photographs of the time evolution of stretching of a capillary bridge until the formation of drops for PEO2000. The fixed mid-height position of CaBER micrometer is represented as a red dotted line. The mid-plane position of the filament is represented by a blue dashed line. (g) Zoomed view of BOAS pattern, where the size of the big central drop is  $300 \mu\text{m}$ . Scale bar:  $100 \mu\text{m}$ . (h)  $D$  versus  $t$  for PEO2000, measured by the micrometer (red crosses) and by image processing at mid-plane of the filament,  $D_{mid}$  (blue circles), and at the minimum diameter along the filament,  $D_{min}$  (green diamonds). The shaded regions (b-f) represent the different thinning stages corresponding to photographs (b-f).

### 2.2.2.2 Relaxation time

Relaxation time is the time required for a material to adjust itself to the applied deformation. The relaxation times of the solutions are calculated using the CaBER. When the solution sample, loaded in-between the two plates, is stretched, filament forms. Here, the liquid bridge formed with the plate diameter,  $D_P = 6$  mm,  $IAR = 0.66$ , is stretched at the speed,  $U = 0.08$  m/s, to  $FAR = 2$ . Thinning of the filament occurs due to the capillary forces. The time evolution of  $D_{CaBER}$  for the PEG20, PEO and PEG+PEO solutions are presented in Fig. 2.5. For all the solutions, the filament diameter,  $D_{CaBER}$ , decreases with time, as expected, and finally the filament breaks. For both the PEO and PEG+PEO solutions, the filament breakup time increases with increasing PEO mass fraction,  $w_{PEO}$ . Furthermore, for the same  $w_{PEO}$ , the filament breakup time is higher for PEG+PEO solutions than PEO solutions.

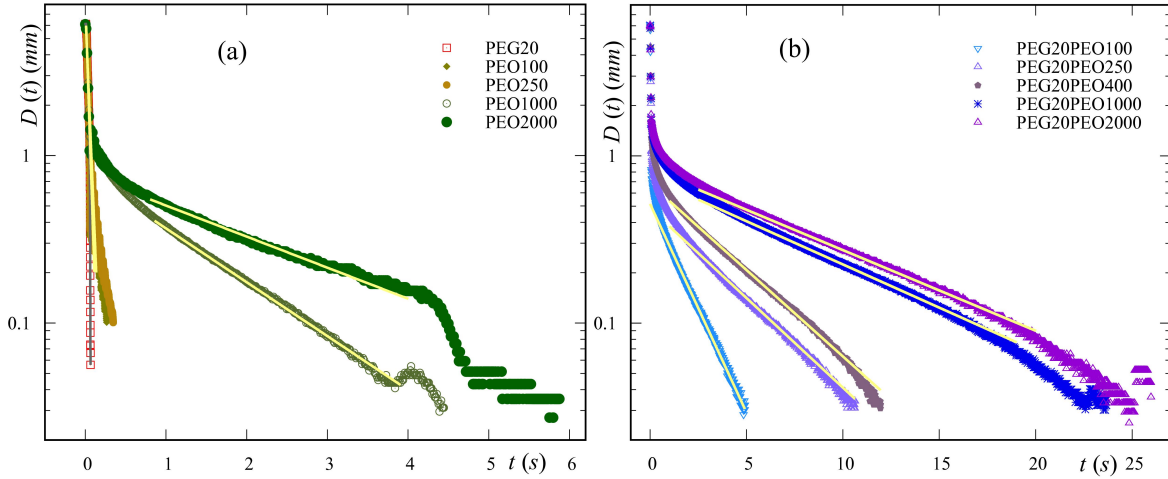


Fig. 2.5 Evolution of the average CaBER diameter,  $D_{CaBER}$ , versus time for all measured solutions, for (a) PEG20 and PEO solutions, and (b) PEG+PEO solutions.  $D_{CaBER}$  is an average over at least 5 experiments. Here, the liquid bridge, formed in-between the two plates having  $D_P = 6$  mm and volume  $56 \mu\text{l}$ , is stretched from  $IAR = 0.66$  to  $FAR = 2$  at  $U = 0.08$  m/s. Solid lines represent *elasto-capillary* fits (Eq. 2.3) for PEO as well as PEG+PEO solution, and *inertio-capillary* fit (Eq. 2.4) for PEG20. The relaxation times,  $\lambda$ , are calculated using Eq. 2.3. Only overlapped data points of  $D_{CaBER}$  and the *elasto-capillary* fits are considered to calculate  $\lambda$ . In the final stages of the present graphs, crests and troughs are observed due to the BOAS structure.

When the filament thinning enters into the *elasto-capillary* regime, exponential decrease of the filament diameter is observed. In this regime, the relaxation time,  $\lambda$ , is calculated as shown:

$$\frac{D_{CaBER}}{D_0} = \left( \frac{GD_0}{4\sigma} \right)^{1/3} \exp\left( \frac{-t}{3\lambda} \right) \quad (2.3)$$

where  $G$  and  $\sigma$  are the modulus and surface tension of test fluids [12]. Values of the relaxation time,  $\lambda$ , are calculated considering the average over at least five experiments. For each experiment, a new solution sample is used. Fits are obtained in the elasto-capillary regime for  $D > 0.1$  mm,  $t > 0.05$  s and the fit error less than 2%. Furthermore, only the overlapped data points of  $D_{CaBER}$  and the fits are used to calculate  $\lambda$ .

The values of  $\lambda$  for the PEO and PEG+PEO solutions are presented in Fig. 2.6. Detailed values of  $\lambda$  for all the solutions are reported at the end of the chapter. As expected, for both the PEO and PEG+PEO solutions,  $\lambda$  increases with increasing PEO concentration,  $w_{PEO}$ . This behaviour has also been reported previously for PEO solutions [88] and for PEG+PEO solutions [78, 101]. Stelter et al. [88], Martínez-Arias and Peixinho [101] and Gaillard et al. [78] used the same molecular weight ( $M = 8 \times 10^6$  g/mol) of PEO as in the present study. Hence, values of  $\lambda$  from the present study are compared with the values obtained by these authors. For PEO solutions, we have obtained higher values of  $\lambda$  compared to Stelter et al. [88]. The difference in  $\lambda$  measured in the present study and Stelter et al. [88] can be due to differences in the average molecular weights of PEO provided by the manufacturers and the different protocols in the solution preparations. It is important to recall that we have not used any mechanical stirrer to prepare the solutions and use of a mechanical stirrer reduces relaxation times as reported by Gaillard [61]. Furthermore, when  $\lambda$  for both PEO and PEG+PEO solutions are compared, at the same  $w_{PEO}$ , larger  $\lambda$  is observed for PEG+PEO solution. For example,  $\lambda$  for PEG20PEO1000 solution is higher compared to  $\lambda$  for PEG7PEO1000 and PEO1000 solutions. Hence, it can be concluded that the addition of PEG in the aqueous solutions of PEO enhances the relaxation time of the solution. Finally, power law fits are used to capture the trend of increase in  $\lambda$  with  $w_{PEO}$ . The exponents of the fits suggest the increase in  $\lambda$  with  $w_{PEO}$  is fairly similar for all mass fractions of PEG. The exponent found in the present experiments for all mass fractions of PEG varies between 0.64 to 0.84. These exponents are in agreement with the previous values by Stelter et al. [88] (0.63), by Martínez-Arias and Peixinho [101] (0.59) and by Gaillard et al. [78] (0.84).

**Relaxation time using  $D_{min}$**  We want to verify if  $D_{min}$ , obtained from the image processing, can be used to calculate the relaxation time,  $\lambda$ . Hence, additional experiments are performed for all PEO and PEG+PEO solutions. Relaxation time from  $D_{min}$  is calculated using an exponential fit :  $D_{min} \propto D_0 \exp(-t/3\lambda)$ . These results are compared with  $\lambda$  obtained from CaBER measurements and are presented in Fig. 2.6. For the PEO solutions,  $\lambda$  calculated from  $D_{min}$  increases with increase in  $w_{PEO}$ . For the PEG+PEO solutions,  $\lambda$  from both methods, are in the same range. However, for each concentration, the difference in the values of  $\lambda$  from both methods is around 30%. Hence, due to large differences in the values of  $\lambda$ ,

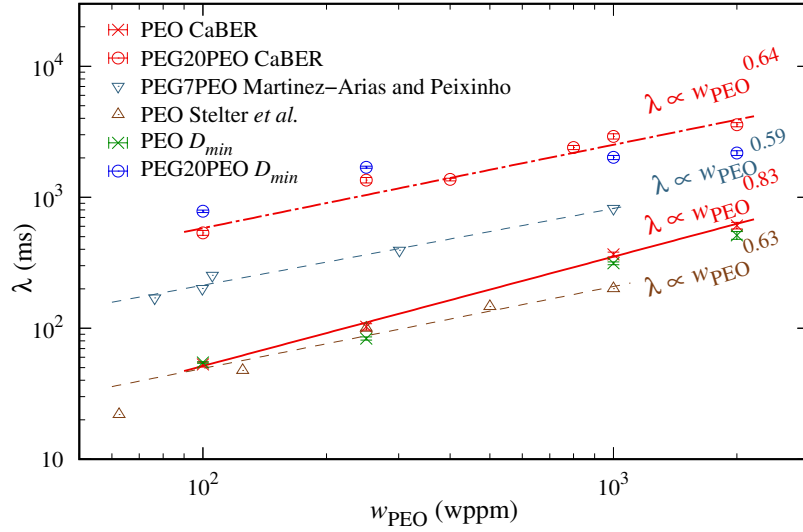


Fig. 2.6 Relaxation time,  $\lambda$ , as a function of the mass fraction of PEO,  $w_{PEO}$ , for PEO and PEG+PEO solutions. The initial liquid bridge is formed in-between two plates having  $D_P = 6$  mm and volume  $56 \mu\text{l}$ . The graph also represents the comparison of  $\lambda$  calculated by  $D_{min}$ , obtained from the image processing, and from CaBER. Martínez-Arias and Peixinho [101] used aqueous PEO solutions with 7 wt% PEG, whereas Stelter et al. [88] used aqueous PEO solutions only. The lines indicate power law fits with coefficient of determination of 0.96 and 1 for PEG20PEO (CaBER) and PEO (CaBER) solutions.

we only consider relaxation times obtained from  $D_{CaBER}$  to calculate the non-dimensional numbers.

**Filament thinning for PEG20** For PEG20 solution, we found  $Oh = 0.08$  with  $D_P = 6$  mm, and hence, the filament undergoes *inertio-capillary* thinning. Data points in Fig. 2.5 are fitted using Eq. 2.4. The filament necking time (or breakup time for Newtonian PEG20 solution),  $t_b = 0.063$  s, is obtained from the CaBER measurements and the Rayleigh time scale is calculated from the solution properties,  $t_R = 0.022$  s. In the present study, we obtained prefactor value of  $X = 0.33$  that agrees well with the previous studies [11, 14, 56, 63, 69, 73–75] where the authors reported values of  $X$  in the range of 0.19 to 0.8.

$$\frac{D_{CaBER}}{D_P} = X \left( \frac{t_b - t}{t_R} \right)^{2/3} \quad (2.4)$$

### 2.2.2.3 Apparent extensional viscosity

In the present study, the apparent extensional viscosity,  $\eta_E$ , is calculated, using the concept proposed by Anna and McKinley [1]. In their work, the authors considered mid-plane diameter,  $D_{mid}$ , of the filament to determine  $\eta_E$ . Later, other authors [9, 78, 138] followed the same approach. However, Dinic et al. [27] used the neck diameter,  $D_{min}$ , of the filament to evaluate  $\eta_E$ . In the present work, we use the same approach, proposed by Dinic et al. [81]. As previously observed, the filament diameter,  $D$ , varies across its length. Hence, this approach helps to accurately measure  $\eta_E$  at the neck or minimum diameter,  $D_{min}$ . Calculating extensional viscosity at  $D_{min}$  allows measuring the maximum extensional viscosity in the filament. The apparent extensional viscosity,  $\eta_E$ , is calculated using  $D_{min}$ :

$$\eta_E = \frac{-\sigma}{dD_{min}(t)/dt}. \quad (2.5)$$

Furthermore, a similar approach was used previously [1, 9, 78, 138] to calculate the Hencky strain by using  $D_{mid}$ . However, again, we use the same minimum diameter extracted from the images to determine the Hencky strain,

$$\epsilon_{min} = 2 \ln \left[ \frac{D_0}{D_{min}(t)} \right]. \quad (2.6)$$

Experiments are performed by stretching a liquid bridge formed in-between two plates with  $D_P = 6$  mm. The liquid bridge is stretched upwards with  $U = 0.08$  m/s from  $IAR = 0.66$  to  $FAR = 2$ . Since the minimum measurable diameter with this experimental setup is  $2.16$   $\mu\text{m}$  and the plate diameter,  $D_0 = 6$  mm, the maximum Hencky strain that can be calculated is 15.86.

The results obtained for the apparent extensional viscosity, using PEG, PEO and PEG+PEO solutions, are plotted against time in Fig. 2.7(a) and against the Hencky strain in Fig. 2.7(b). For both PEO and PEG+PEO solutions,  $\eta_E$  increases with time and the Hencky strain. Furthermore, all PEG+PEO solutions have comparatively higher  $\eta_E$  than PEO solutions. The trend of increase in  $\eta_E$  with  $\epsilon_{min}$  is similar to the previous studies by Yu et al. [138] and Gaillard et al. [78]. Both authors used 20% of PEG with various concentrations of PEO. However, both authors calculated  $\eta_E$  and  $\epsilon_{min}$  using midplane diameter,  $D_{mid}$ . Moreover, Yu et al. [138] used lower molecular weights of PEG ( $M = 10000$  g/mol) and PEO ( $M = 6.72 \times 10^5$  to  $1.03 \times 10^6$  g/mol) in their study of viscoelastic liquid jets. Gaillard et al. [78] used the same molecular weight of PEO as in the present study ( $M = 8 \times 10^6$  g/mol). But

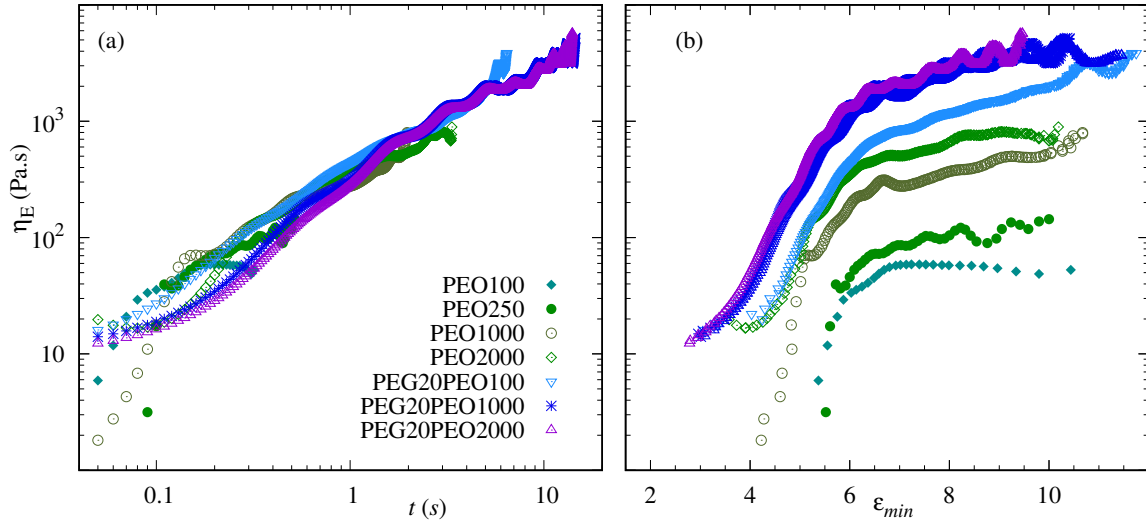


Fig. 2.7 Apparent extensional viscosity,  $\eta_E$ , as a function of  $t$  and the Hencky strain,  $\epsilon_{min}$ , for PEO and PEG+PEO solutions.  $\eta_E = -\sigma/[dD_{min}(t)/dt]$  and  $\epsilon_{min}(z,t) = 2\ln[D_0/D_{min}(z,t)]$ .  $D_{min}$  is extracted from the images. The liquid bridge, formed in-between the two plates with  $D_P = 6$  mm, is stretched from  $IAR = 0.66$  to  $FAR = 2$  at  $U = 0.08$  m/s.

the molecular weight of PEG ( $M = 8000$  g/mol) is lower compared to us. Even though, the authors used smaller plate diameter ( $D_P = 3$  mm), stretching parameter  $FAR = 2.33$  is fairly similar to us. As a result, both authors found similar trends for  $\eta_E$  vs.  $\epsilon_{min}$  but lower values compared to the present work.

More detailed observation of Fig. 2.7(b) indicates that the increase in  $\eta_E$  with  $\epsilon_{min}$  can be characterised in two distinct regimes. The first regime ( $\epsilon_{min} < 6$ ), the polymer chains are stretched and a small increase in  $\epsilon_{min}$  results in a large increase of  $\eta_E$ . This regime corresponds to the development of the cylindrical shaped filament in the axial, as well as radial direction. Then,  $\eta_E$  transits to the second regime. For  $\epsilon_{min} > 6$ ,  $\eta_E$  does not increase considerably. This behaviour is called strain hardening and corresponds to polymers being closer to a fully stretched state. In this regime, the filament thins in the radial direction only.

**Finite extensibility parameter** Furthermore, terminal extensional viscosity,  $\eta_T$ , at large strains is estimated considering the maximum values of  $\eta_E$ . Hence, knowing values of  $\eta_0$  and  $\eta_s$ , we can use Eq.1.45 to estimate the finite extensibility parameter,  $b$ :

$$b \equiv \frac{\eta_T - 3\eta_s}{2(\eta_0 - \eta_s)}. \quad (2.7)$$

For PEO solutions, water is considered as the solvent. Hence, to calculate the finite extensibility parameter of PEO solutions, viscosity of water (0.001 Pa·s at 20 °C) is considered as solvent viscosity. For PEG+PEO solutions, PEG20 is considered as the solvent. Hence, to calculate the finite extensibility parameter for PEG+PEO solutions, viscosity of PEG20 ( $\eta_0$  from table 2.1) is considered as solvent viscosity. Values of  $\eta_T$  and  $b$  are reported in table 2.2. At the same  $w_{PEO}$ ,  $b$  values are higher for PEO solutions than PEG+PEO solutions. The values of  $\eta_T$  obtained in the present study are higher for the same  $w_{PEO}$  compared to Gaillard et al. [78]. The difference can be due to the lower molecular weight of PEG and different solution preparation protocols (with a mechanical stirrer) used by the authors.

Table 2.2 Rheological parameters for PEO and PEG+PEO solutions at 20°C. For PEG+PEO solutions, PEG20 is considered as solvent with  $\eta_s = 0.034$  Pa·s and for PEO solution, water is considered as solvent with  $\eta_s = 0.001$  Pa·s. In the present study, a liquid bridge with  $D_P = 6$  mm is stretched from  $IAR = 0.66$  to  $FAR = 2$  at  $U = 0.08$  m/s. The results are compared with Gaillard et al. [78], note the authors only used PEG+PEO solutions. The authors used same molecular weight of PEO as in the present study ( $M = 8 \times 10^6$  g/mol) but lower molecular weight of PEG ( $M = 8000$  g/mol).

Abbreviation	$w_{PEG}$ wt (%)	$w_{PEO}$ (wppm)	$\eta_0$ (Pa·s)	$\eta_s$ (Pa·s)	$\eta_T$ (Pa·s)	$b$ $\times 10^3$	$\eta_T$ [78] (Pa·s)	$b$ [78] $\times 10^3$
PEO100	0	100	0.0011	0.001	53	264.98	-	-
PEO250	0	250	0.0013	0.001	144	239.99	-	-
PEO1000	0	1000	0.006	0.001	798	79.8	-	-
PEO2000	0	2000	0.039	0.001	893	11.75	-	-
PEG20PEO100	20	100	0.160	0.034	3856	15.30	400	100
PEG20PEO1000	20	1000	0.771	0.034	5192	3.52	2000	40
PEG20PEO2000	20	2000	1.682	0.034	5676	1.72	5000	20

Moreover, in Fig. 2.8, the terminal extensional viscosity,  $\eta_T$ , is plotted against the relaxation time,  $\lambda$ , of the solutions.  $\eta_T$  increases with an increase in  $\lambda$ . This trend has been reported previously by Stelter et al. [88], Gaillard et al. [78] (see Tab. 2.2) and Tirel et al. [139]. According to Stelter et al. [88],  $\eta_T$  is proportional to  $\lambda$  by a prefactor which is larger for flexible polymers than rigid polymers. In the present study, only flexible polymers are used and  $\eta_T$  varies with  $\lambda$  by a prefactor of  $1.7 \times 10^3$  Pa. Gaillard [61] obtained a different prefactor value such that  $\eta_T \approx 8 \times 10^3 \lambda$ . The shift in the prefactors can be justified by the

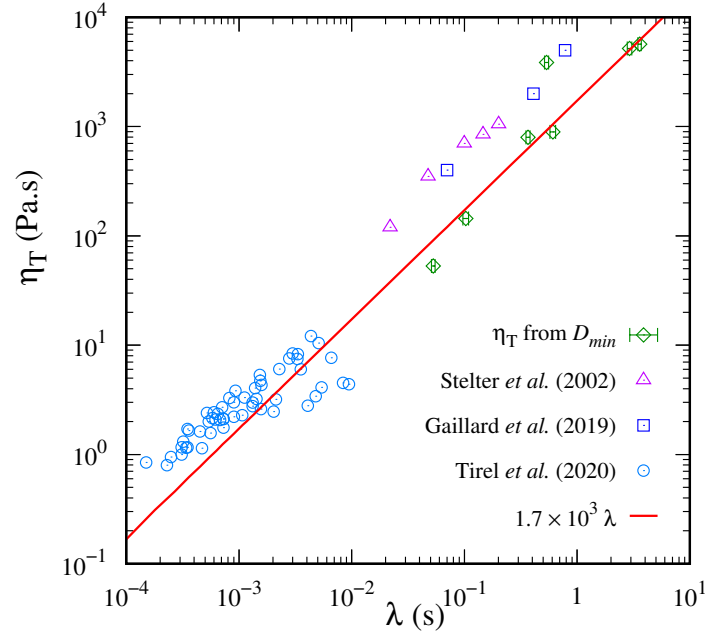


Fig. 2.8 The terminal extensional viscosity,  $\eta_T$ , from Tab. 2.2, as a function of the relaxation time,  $\lambda$ . The results are compared with Stelter et al. [88], the data in Tab. 2.2 by Gaillard et al. [78] and Tirel et al. [139]. The red line represents a fit  $\eta_T = 1.7 \times 10^3 \lambda$  for the present data.

higher values of  $\lambda$  obtained in the present study, as we do not use any mechanical stirrer. Furthermore, for PEO solutions ( $M = 8 \times 10^6$  g/mol) used by Tirel et al. [139],  $\eta_T$  values lie between the prefactors  $1.7 \times 10^3$  Pa and  $8 \times 10^3$  Pa. This difference in the prefactor values may be due to the use of different IPA mass fractions, as Tirel et al. [139] used 5 wt% of IPA whereas we used 0.5 wt% of IPA for PEO solutions.

### 2.2.3 Experimental details for liquid transfer

When a liquid bridge is stretched, solution pools are formed along with a filament. The formation of the solution pools lasts until the breakup of the filament. In the present study, the formation of solution pools is studied experimentally with the CaBER and the camera, as shown schematically in Fig. 2.9. Initially, a liquid capillary bridge, as shown in Fig. 2.9(a), is created by placing a solution sample in-between the two parallel circular flat CaBER plates. The volume of the solution introduced in the liquid bridge depends upon the size of the plate diameter and the initial liquid bridge height,  $L_0$ , and can be calculated as  $V = (\pi/4)D_P^2 L_0$ . Special care is taken to ensure that no air bubbles have been trapped inside the liquid bridge to eliminate any uncertainty in the bridge volume and shape. After stretching of the liquid

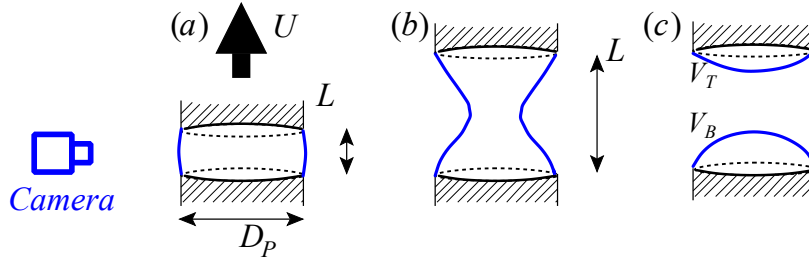


Fig. 2.9 Schematic of the experimental setup. The small blue region represents the polymer solution sample. (a) Liquid bridge, before stretching, with plate diameter,  $D_P$ , initial stretching height,  $L_0$  and stretching speed,  $U$ . (b) Liquid bridge stretched to the final stretching height,  $L$ , and (c) Volumes of the solution pools on the top plate,  $V_T$ , and on the bottom plate,  $V_B$ . The contact lines are pinned throughout the experiments.

bridge, solution pools are formed on the top and bottom plates, as shown in Fig. 2.9(c). Throughout the experiment (from stretching of the liquid bridge until the formation of the solution pools), liquid contact lines are pinned at the corners of the plates. Before and after stretching of the liquid bridge, we measured lengths of liquid contact lines on the top and bottom plates. We found that the lengths before and after stretching are the same. Previously, similar pinned contact lines for plate devices have been observed by Qian and Breuer [115] and Zhang et al. [100]. The experiments are performed 20°C.

The camera captures stretching, filament thinning, and breakup, as well as the solutions pools on the top and bottom plates of the CaBER. Considering the axisymmetric capillary bridge, images of the vertical cross-section of the solution pools are captured. As the images are obtained from the shadowgraphy technique, it is straightforward to achieve binary images using the ImageJ software. These images are further analysed to calculate the number of pixels for both solution pools. The numbers of pixels are converted into the corresponding length unit. Then, the contact line diameter,  $a_0$ , and the height,  $h_0$ , of the cross-section of each solution pool are estimated by counting the pixels in the appropriate directions. Finally, considering a spherical shape of the solution pool, the "spherical cap" method [112, 140] is implemented to calculate the volume,  $V$ , of any solution pool, as shown in Fig. 2.10. In the present study, the liquid contact lines are pinned, and hence, the contact line diameter,  $a_0$  is equal to the plate diameter,  $D_P$ . Therefore, the volume of the solution pool formed on the plate can be given as:

$$V = \frac{1}{6} \pi h_0 \left( \frac{3}{4} D_P^2 + h_0^2 \right) \quad (2.8)$$

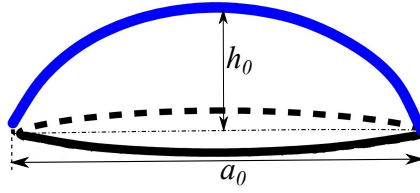


Fig. 2.10 Schematic of a solution pool, having volume,  $V$ , on any flat surface, considering asymmetric liquid distribution. The blue line represents a spherical cap or dome containing liquid, with height  $h_0$  and contact line diameter,  $a_0$ , on the surface.

### 2.3 Solution property table

All measured rheological properties and the non-dimensional numbers calculated using CaBER plates (with diameters 4, 6 and 8 mm) are summarised for the polymer solutions in Tab. 2.3.  $\lambda$  is considered as the characteristic time of a solution and hence, assumed to be constant for all plate diameters. Hence,  $\lambda$  is measured with  $D_P = 6$  mm.  $\eta_0$  data for PEG20PEO400 is acquired by fitting a trend obtained with  $\eta_0$  data for other PEG+PEO solutions.

The non-dimensional numbers are recalled: Bond number,  $Bo = \rho g D_P^2 / (4\sigma)$ , Ohnesorge number,  $Oh = \eta_0 / \sqrt{\rho \sigma D_P / 2}$  and Deborah number,  $De = \lambda / \sqrt{\rho D_P^3 / 8\sigma}$ . By changing  $D_P$  from 4 to 8 mm,  $Bo$  is varied from 0.66 to 2.87. For  $D_P = 8$  mm,  $Bo$  is greater than two, which suggests the higher influence of gravity on the liquid bridge dynamics. Furthermore, a wide range of  $De$  is obtained by varying  $w_{PEO}$  and  $w_{PEG}$ . The experiments on the BOAS structure are mostly carried out using  $D_P = 6$  mm and for these experiments,  $De$  is varied from 3.5 to 296.4. These values of  $De$  greater than one indicate the influence of elastic forces and hence, the presence of the elasto-capillary thinning. Finally,  $Oh$  values are varied by changing the zero shear viscosity of the solutions. For example, when  $D_P = 6$  mm,  $Oh$  for PEO solutions is varied from 0.001 to 0.13, but for PEG+PEO solutions,  $Oh$  is varied from 0.38 to 4.01.

### 2.4 Numerical setup

In this section, details of numerical simulations for a stretched liquid bridge using OpenFOAM toolbox *rheoTool* [125] are discussed. The objective of this work is to test the use of OpenFOAM toolbox *rheoTool* to simulate capillary thinning of a stretched liquid bridge. To recreate an initial state of a bridge as similar to that of Fig. 2.4(b), we will extract stretched liquid bridge profiles from experiments. Previously, to initiate capillary thinning of the

Table 2.3 Rheological parameters for all the solutions at 20°C. For PEG+PEO solutions, PEG20 is considered as solvent with  $\eta_s = 0.034$  Pa·s and for PEO solution, water is considered as solvent with  $\eta_s = 0.001$  Pa·s. In the present study, a liquid bridge with  $D_P = 6$  mm is stretched from  $IAr = 0.66$  to  $FAR = 2$  at  $U = 0.08$  m/s. Values of  $\lambda$  are measured with  $D_P = 6$  mm.  $Bo = \rho g D_P^2 / (4\sigma)$ ,  $Oh = \eta_0 / \sqrt{\rho \sigma D_P / 2}$  and  $De = \lambda / \sqrt{\rho D_P^3 / 8\sigma}$ .

Abbreviation	$w_{PEG}$ wt (%)	$w_{PEO}$ (wppm)	$\rho$ ( $kg/m^3$ )	$\sigma$ (mN/m)	$\eta_0$ (mPa·s)	$\lambda$ (s)	$D_P = 4$ mm			$D_P = 6$ mm			$D_P = 8$ mm		
							$Bo$	$De$	$Oh$	$Bo$	$De$	$Oh$	$Bo$	$De$	$Oh$
PEG20	20	0	1032.5	57	34	-	0.70	-	0.10	1.59	-	0.08	2.82	-	0.07
PEO100	0	100	997	59	1.1	0.041	0.66	3.5	$\approx 10^{-3}$	1.48	1.9	$\approx 10^{-3}$	2.63	1.2	$\approx 10^{-3}$
PEO250	0	250	997.1	59	1.3	0.106	0.66	9.1	$\approx 10^{-3}$	1.48	4.9	$\approx 10^{-3}$	2.63	3.2	$\approx 10^{-3}$
PEO800	0	800	997.3	59	10	0.135	0.66	11.7	0.03	1.48	6.3	0.02	2.63	4.1	0.02
PEO1000	0	1000	997.3	59	6	0.344	0.66	29.7	0.02	1.48	16.1	0.01	2.63	10.5	0.01
PEO1500	0	1500	997.5	59	54	0.382	0.66	33.0	0.16	1.48	17.9	0.13	2.63	11.7	0.11
PEO2000	0	2000	997.6	59	39	0.696	0.66	60.0	0.11	1.49	32.7	0.09	2.64	21.2	0.08
PEG20PEO100	20	100	1032.8	56	160	0.535	0.72	44.2	0.47	1.62	24.0	0.38	2.88	15.6	0.33
PEG20PEO250	20	250	1033.4	56	165	1.350	0.72	111.7	0.48	1.61	60.8	0.39	2.87	39.5	0.34
PEG20PEO400	20	400	1033.4	56	166	1.367	0.71	113.4	0.48	1.60	61.7	0.40	2.85	40.1	0.34
PEG20PEO800	20	800	1033.6	56	170	2.396	0.72	198.4	0.50	1.61	108.0	0.41	2.86	70.1	0.35
PEG20PEO1000	20	1000	1033.6	56	771	2.952	0.72	224.0	2.26	1.61	132.8	1.84	2.87	86.3	1.60
PEG20PEO2000	20	2000	1033.4	56	1682	3.580	0.72	296.4	4.91	1.61	161.3	4.01	2.86	104.8	3.48

filament, other authors introduced an initial perturbation [2, 16, 55] or used interface profile generated by an equation [56] or planar symmetry [3] neglecting gravity. However, our method is closer to actual experimental profile of filament compared to these authors and also accounts gravitational, viscous as well as inertial effects on a stretched capillary bridge. With the aid of OpenFOAM software, we will design a mesh and use the specific solver `rheoInterFoam` for fluids under study. In addition, we will extract data for drops-on-a-filament and liquid transfer, and then compare it with the experimental results in chapters 3 and 4.

Using *rheoTool*, various viscoelastic models such as Oldroyd-B, Giesekus or FENE-P can be solved. As discussed in the previous chapter, the Oldroyd-B model is most commonly used for viscoelastic capillary thinning and BOAS structure [2, 3, 13, 16, 55, 56, 85, 100]. Furthermore, log-conformation tensor approach is known for stabilised viscoelastic fluid flows [124, 130]. Hence, in the present work, we use the log-conformation tensor approach of the Oldroyd-B model for simulations of viscoelastic fluids. To implement the Oldroyd-B model in *rheoTool*, we need to define liquid properties such as  $\eta_s, \eta_p, \rho, \sigma$  and  $\lambda$ . These values are obtained experimentally as discussed in the previous sections of this chapter and are used in the numerical simulations. Simulations for a Newtonian case are carried out with liquid properties of PEG20 solution, and for a viscoelastic case, simulations are performed with liquid properties of PEG20PEO1000 solution. This preliminary work aims to explore the potential use of *rheoTool* for stretching of a liquid capillary bridge of Newtonian and viscoelastic fluids and to give a direction for future numerical works on beads-on-a-string structure and transfer ratio. In the next sections, geometrical, mesh and boundary condition details are presented along with results for capillary thinning of Newtonian as well as viscoelastic liquid bridge.

### 2.4.1 Newtonian solution: PEG20

In this section, a Newtonian fluid case is simulated considering liquid properties of the PEG20 solution. As polymeric extra-stress field does not come into play, the Newtonian fluid case will serve as a reference for the next viscoelastic fluid simulation.

**Geometry and mesh** To make our numerical study closer to experimental conditions, a stretched liquid bridge profile is used to obtain the liquid-air interface, as shown in Fig. 2.11(a) and (b). As in the experiments, the plate radius is 3 mm. By considering an axisymmetric stretched profile along Y-axis, only the right side of the axis of symmetry is used. This profile is used as an initial numerical interface and volume fraction. Outline of the stretched liquid bridge is obtained from an experimental image at  $t = 0.05$  s (when the top

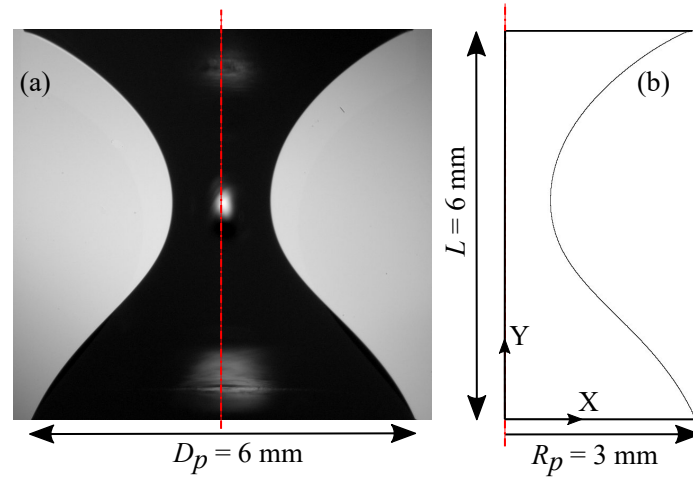


Fig. 2.11 (a) Experimental axisymmetric stretched liquid bridge profile for PEG20. The profile is acquired when the top plate reaches the final stretching height,  $L = 6$  mm, at  $t = 0.05$  s. Experimental conditions for the stretched profile are:  $D_p = 6$  mm,  $IAR = 0.66$ ,  $FAR = 2$  and  $U = 0.08$  m/s. (b) Liquid-air interface and volume fraction of the stretched liquid bridge profile used as an initial condition for numerical simulations.

plate reaches the final stretching height,  $L = 6$  mm) using the ImageJ software. Then, points on the outline, along with their coordinates, are extracted by using image analysis. After that, the stretched profile is recreated and converted into a plane using another software SALOME, and finally, to create a .stl file. This .stl file is imported in `setFieldsDict` file.

A 2D uniform axisymmetric mesh is created using the OpenFOAM meshing tool as shown in Fig. 2.12. Liquid contact lines are pinned on both plates. To have a well-defined interface, at least three to four elements in X-direction on the interface are required. Five meshes with the number of elements up to 1 625 000 have been tested. All meshes have uniform cell size and square mesh elements. Details of all meshes for PEG20 are provided in Table 2.4. Element size ( $\Delta x_{min}$ ) decreases from M1 to M5. Fig. 2.13 presents numerical results for dimensionless mid-height filament radius  $[R(t)/R_p]$  as a function of dimensionless time  $[(t - t_b)/t_R]$  considering different meshes with values of  $De = 0$  and  $Oh = 0.08$  (same definitions as in section 1.5). For all meshes,  $R(t)/R_p$  decreases with increasing  $(t - t_b)/t_R$ . Furthermore, with decreasing element size, for meshes M4 and M5, thinning radius curves superimpose over each other. Hence, the numerical results obtained using meshes M4 and M5 show a good agreement as decreasing element size does not affect the filament thinning. Larger breakup times for liquid bridge are observed as element size decreases from M1 to M5. Additionally, these results are compared with the experimental values for PEG20 (obtained from Fig. 2.5). The experimental and numerical results are in a good agreement

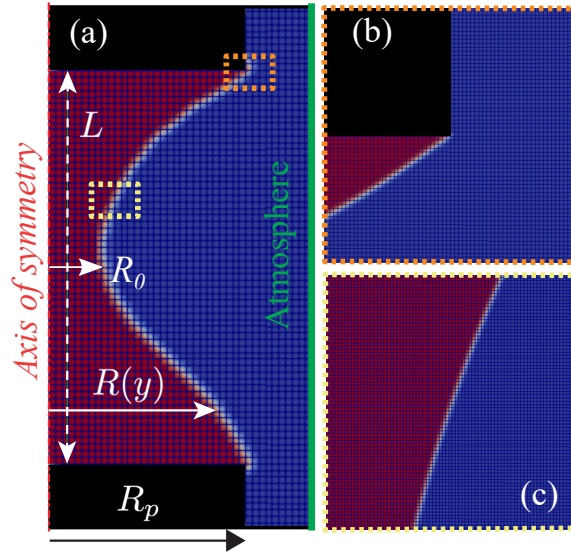


Fig. 2.12 Computational domain used with a uniform mesh for PEG20. Experimental conditions are:  $R_p = 3$  mm,  $R_0 = 0.816$  mm,  $IAR = 0.66$ ,  $FAR = 2$  and  $U = 0.08$  m/s. Liquid phase (PEG20) is represented by the red region and the air is represented by the blue region. (a) Description of uniform mesh used for numerical simulations. (b) Zoomed view of the mesh around pinned contact line at the corner of the top plate. (c) Zoomed view of the mesh around the liquid-air interface.

below  $R(t)/R_p = 0.1$ . Note that in Fig. 2.13, time is scaled using  $t_b$ , which is a breakup time considering the Newtonian case.

**Initial conditions** The extracted outline of the liquid-air interface gives liquid contact angles that will be considered as initial conditions. On both plates, `dynamicAlphaContactAngle` conditions are imposed for liquid-air contact angles. The liquid bridge has zero initial velocity. Internal pressure,  $p$ , of the liquid bridge is uniform and  $p = 0$  condition is imposed.

**Boundary conditions** At the plate, no-slip boundary conditions are imposed with a zero velocity and zero normal gradient for the pressure. A `fixedFluxExtrapolatedPressure` condition is assigned to the pressure, for multi-phase flows. Regions representing open boundaries (atmosphere) are assumed not to interfere with thinning dynamics and the atmospheric pressure is fixed at  $p = 0$ .

**Numerical details** The `rheoInterFoam` solver is used, with the algebraic VOF method of OpenFOAM, thus enabling the simulation of two-phase flows. Newtonian model is used

Table 2.4 Various uniform meshes tested and their parameters for PEG20. Experimental conditions used are:  $R_p = 3$  mm,  $IAR = 0.66$ ,  $FAR = 2$  and  $U = 0.08$  m/s. All meshes are uniform and hence aspect ratio is 1.

Mesh	Number of elements	$\Delta x_{min}/R_p$ or $\Delta y_{min}/R_p$
M1	2 600	$33.3 \times 10^{-3}$
M2	10 400	$16.7 \times 10^{-3}$
M3	260 000	$3.33 \times 10^{-3}$
M4	1 040 000	$1.67 \times 10^{-3}$
M5	1 625 000	$1.33 \times 10^{-3}$

to solve the constitutive equations. The SIMPLEC algorithm is used for the pressure-velocity coupling. To control time steps, Courant number,  $Co$ , defined as  $Co = a(\delta t/\delta x)$  is considered as 0.1. Here  $a$  is a velocity magnitude,  $\delta t$  is a time step and  $\delta x$  is a spacing between mesh elements. Solvers that use VOF, such as `rheoInterFoam`, can also limit the time-step using an interface Courant number, `AlphaCo` [141], which is set to 0.1 in the present study. Relevant scripts used for PEG20 are provided in Appendix 3.

**Numerical results** Thinning of a stretched liquid bridge for PEG20 using mesh M4 is shown in Fig. 2.14. `alpha.water = 1` indicates presence of liquid (PEG20) and `alpha.water = 0` indicates presence of air. No filament is observed. As we are running the case for Newtonian fluid, the liquid bridge breaks early, i.e. at  $t = 0.15$  s and solution pools are formed. In these simulations, we used  $Oh = 0.08$  and thus, we expect *inertio-capillary* thinning of the stretched liquid bridge. Hence, when thinning dynamics of mesh M4 are compared with characteristic *inertio-capillary* thinning equation,  $R(t)/R_p = X[(t - t_b)/t_R]^{(2/3)}$ , we obtain  $X = 0.1$  with a coefficient of determination of 0.86. A good agreement between both numerical solutions and fit can be observed. Furthermore, the prefactor value of  $X = 0.1$  agrees well with the previous studies [11, 14, 56, 63, 69, 73–75] where the authors reported values of  $X$  in the range of 0.19 to 0.8. Recently, Figueiredo et al. [56] found that as  $Oh$  decreases the prefactor  $X$  increases and  $X = 0.19$  was reported for  $Oh = 0.1$ . In our numerical simulation of PEG20 solution, we have  $Oh = 0.08$ . Hence our value of  $X = 0.1$  can be justified because of lower value of  $Oh$  compared to Figueiredo et al. [56]. In addition, liquid contact lines at both plate surfaces are tracked by measuring contact line velocities with time. Contact

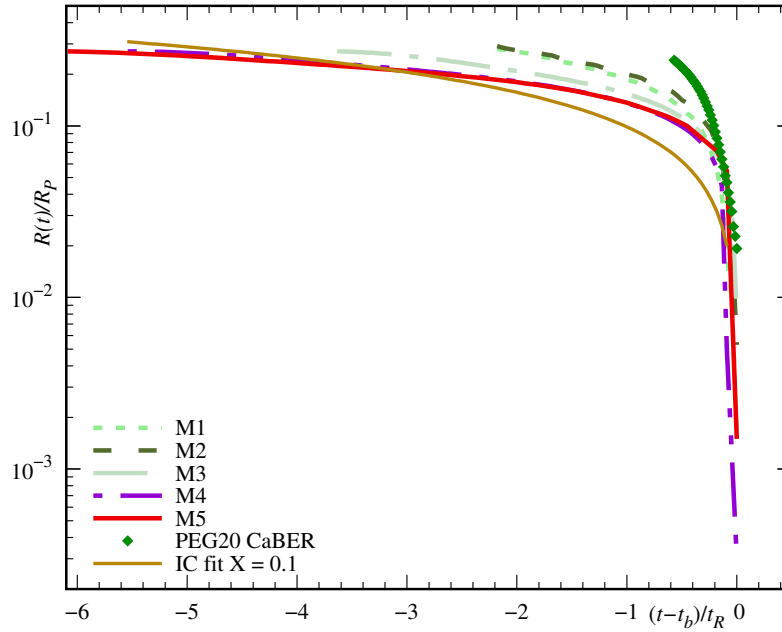


Fig. 2.13 Transient computation of the filament radius for PEG20.  $R_p = 3$  mm,  $FAR = 2$  and  $Oh = 0.08$ . Also, we compared the numerical results with experimental results obtained using CaBER. Furthermore, filament thinning for M4 is compared with *inertio-capillary* (IC) thinning equation to calculate  $X$ :  $R(t)/R_p = X[(t - t_b)/t_R]^{(2/3)}$ .

lines velocities remained at zero and thus, the liquid contact lines are pinned similar to the CaBER experiments.

## 2.4.2 Viscoelastic solution: PEG20PEO1000

In this section, we present preliminary numerical results for thinning of a stretched liquid bridge of PEG20PEO1000. These preliminary results are obtained using simple geometry and mesh will serve as a reference than can be refined by using a higher number of elements.

**Geometry and mesh** An experimental stretched liquid bridge interface profile is used as shown in Fig. 2.15, from image analysis, to obtain the liquid-air interface. Considering an axisymmetric stretched profile along Y-axis, only the right side of the axis of symmetry is used. This profile will be used as an initial numerical interface and volume fraction of PEG20PEO1000 solution. Outline of the stretched liquid bridge is obtained from an experimental image at  $t = 0.05$  s (when the top plate reaches the final stretching height,  $L = 6$  mm) using the ImageJ software. A.stl file is generated and then imported into `setFieldsDict` file as mentioned above for the PEG20 solution.

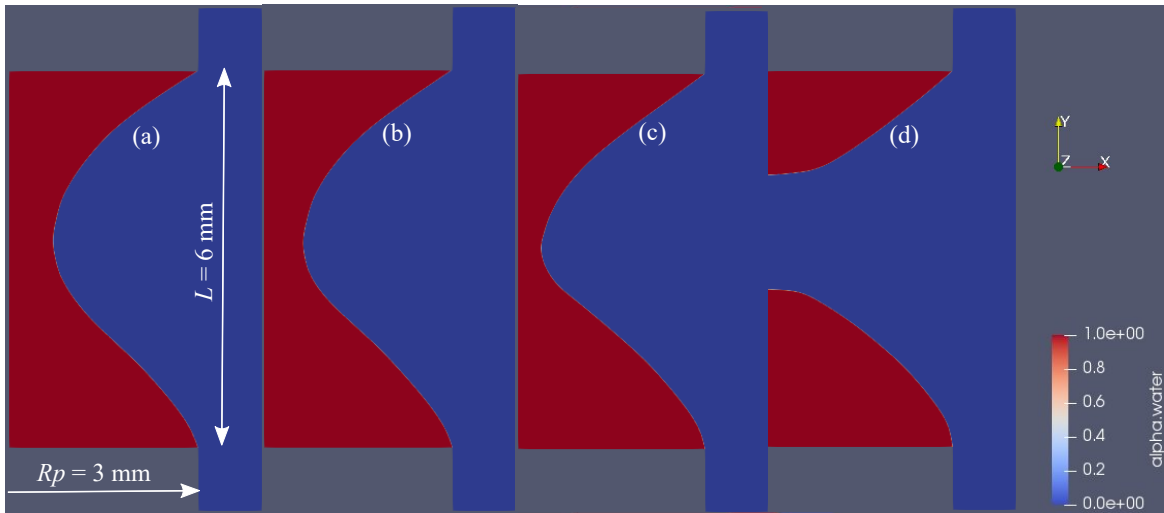


Fig. 2.14 Visualisation of the axisymmetric numerical solution of the filament thinning for PEG20 using Mesh M4.  $\alpha.\text{water} = 1$  indicates presence of liquid (PEG20) and  $\alpha.\text{water} = 0$  indicates air. In these simulations we used:  $R_p = 3$  mm,  $FAR = 2$  and  $Oh = 0.08$ . The snapshots are at (a)  $t = 0.03$ , (b)  $t = 0.05$ , (c)  $t = 0.1$  and (d)  $t = 0.15$  s. No filament is observed, as expected.

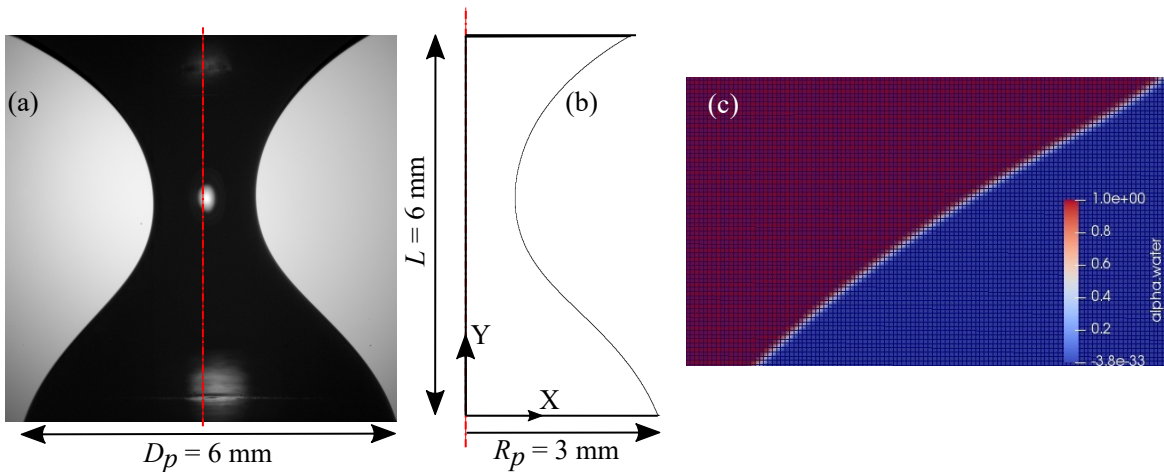


Fig. 2.15 (a) Experimental axisymmetric stretched liquid bridge profile for PEG20/PEO1000. The profile is acquired when the top plate reaches fully stretched position,  $L = 6$  mm, at  $t = 0.05$  s. Experimental conditions for the stretched profile are:  $D_p = 6$  mm,  $IAR = 0.66$ ,  $FAR = 2$  and  $U = 0.08$  m/s. (b) Outline of the stretched liquid bridge interface profile, used as an initial condition of the simulations. (c) Description of a typical uniform mesh used in the numerical simulations.

A 2D uniform axisymmetric mesh is created using the OpenFOAM meshing tool as shown in Fig. 2.15(c). Liquid contact lines are pinned on both plates. Several mesh sizes with the number of elements up to 173 160 have been tested. All meshes have uniform cell size and square mesh elements. Details of all meshes for PEG20PEO1000 are given in Tab. 2.5. Element size ( $\Delta x_{min}/R_P$ ) decreases from N1 to N3. The numerical filament time increases with a decrease in element size from N1 to N3. However, the experimental thinning time is around 22 s, which is larger than the numerical thinning time of 0.028 s for N3 mesh. The filament thinning and breakup time increase with the decrease in element size as also previously demonstrated for PEG20 solution. Hence, it is expected that with smaller element sizes, i.e. refined meshes, the thinning time can be increased. Fig. 2.16 presents numerical results for filament thinning considering different meshes tested with  $De = 132.8$  and  $Oh = 1.84$ . Note that time is scaled using  $t_b$ , which is a filament necking time considering the viscoelastic case.

**Initial conditions** Similar to PEG20, the extracted outline of the liquid-air interface will be considered as an initial condition. For liquid-air contact angles, `dynamicAlphaContactAngle` conditions are imposed on both plates. The liquid bridge has zero initial velocity. Internal pressure,  $p$ , of the liquid bridge is uniform and  $p = 0$  condition is implemented.

Table 2.5 Various uniform mesh tested and their parameters for PEG20PEO1000. Experimental conditions used are:  $D_P = 6$  mm,  $IAR = 0.66$ ,  $FAR = 2$  and  $U = 0.08$  m/s. All meshes are uniform and thus aspect ratio is 1. Experimental thinning time before appearance of a BOAS structure for PEO20PEO1000 solution is around 22 s. Note that meshes N1 to N3 have nearly the same element size as M1 to M3 for PEG20 (see Tab. 2.4).

Mesh	Number of elements	$\Delta x_{min}/R_P$ or $\Delta y_{min}/R_P$	$t_b$ (s)
N1	4 330	$20 \times 10^{-3}$	0.023
N2	86 580	$10 \times 10^{-3}$	0.024
N3	173 160	$5 \times 10^{-3}$	0.028

**Boundary conditions** At plate surface, no-slip boundary conditions are imposed with zero velocity, linearly extrapolated polymeric extra-stress components and a zero normal gradient for pressure, as in the PEG20 case. A `fixedFluxExtrapolatedPressure` is assigned

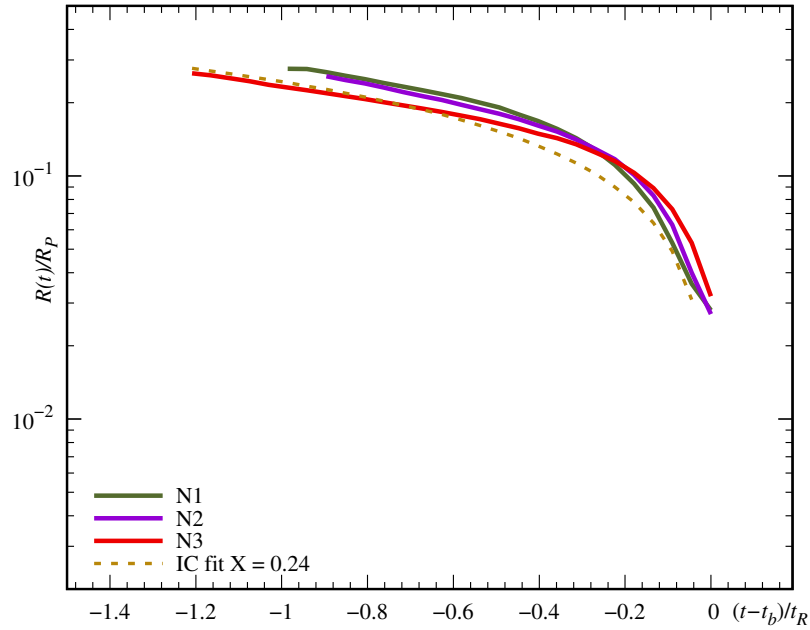


Fig. 2.16 Transient computation of the filament radius for PEG20PEO1000. In these simulations, we used:  $R_p = 3$  mm,  $FAR = 2$ ,  $De = 132.8$  and  $Oh = 1.84$ . Furthermore, filament thinning for N3 is compared with *inertio-capillary* (IC) thinning equation to calculate  $X$ :  $R(t)/R_p = X[(t - t_b)/t_R]^{(2/3)}$ . We obtain  $X = 0.24$  with a coefficient of determination of 0.93.

to pressure, for multi-phase flows. Regions representing open boundaries (atmosphere) are assumed not to interfere with thinning dynamics and atmospheric pressure is fixed at  $p = 0$ .

**Numerical details** The `rheoInterFoam` solver is used, along with the algebraic VOF method in OpenFOAM, for the simulation of two-phase flows. To solve viscoelastic constitutive equations, the Oldroyd-B model (with log-conformation tensor approach) is used. The pressure-velocity coupling is defined by the SIMPLEC algorithm. The Multidimensional Universal Limiter with Explicit Solution (MULES) method is used to avoid either oscillation or diffusion in the interface. Courant number,  $Co = 0.05$  is considered, to assure the right balance between convergence and numerical time required. Relevant scripts used for PEG20PEO1000 are provided in Appendix 3.

**Numerical results** Thinning of a stretched liquid bridge for PEG20PEO1000 solution using mesh N3 is shown in Fig. 2.17. `alpha.water = 1` indicates presence of liquid (PEG20PEO1000) and `alpha.water = 0` indicates presence of air. Thinning of the liquid bridge is observed until  $t = 0.020$  s and a filament is formed as shown in Fig. 2.17(c). In these simulations, we used  $Oh = 1.84$  and hence, we expect *inertio-capillary* thinning of the

stretched liquid bridge. Therefore, when thinning dynamics of mesh N3 are compared with characteristic *inertio-capillary* thinning equation,  $R(t)/R_p = X[(t - t_b)/t_R]^{(2/3)}$ , we obtain  $X = 0.24$  with a coefficient of determination of 0.93. The prefactor value of  $X = 0.24$  agrees well with the previous studies [11, 14, 56, 63, 69, 73–75] where the authors reported values of  $X$  in the range of 0.19 to 0.8. However, as a low resolution mesh with  $\Delta x_{min}/R_p = 5 \times 10^{-3}$  has been used, we only achieve *inertio-capillary* thinning but we do not attain *elasto-capillary* thinning. Figueiredo et al. [56] used a mesh with  $\Delta x_{min}/R_p = 1.25 \times 10^{-4}$  to observe both *inertio-capillary* and *elasto-capillary* thinning. Due to necking, formation of a drop and solution pools occur at  $t = 0.021$  s, see Fig. 2.17(d). We only acquire a single drop, which is the first generation of drops. Even after using a mesh with resolution  $\Delta x_{min}/R_p = 1.25 \times 10^{-4}$ , Figueiredo et al. [56] achieved only a single first generation drop for  $De = 4.272$  and  $Oh = 0.129$ . Furthermore, Turkoz et al. [55] previously demonstrated that a higher mesh refinement is needed at later times when the filament thins significantly because thinning reaches a width close to the mesh size. Instead of a complete stretched liquid bridge, the authors considered only a filament interface domain and obtained a satellite drop for  $De = 0.8$  and  $Oh = 0.04$ . In their numerical study, at least 40 grid points were used in the radial direction of a thin filament, while for the N3 mesh, there are only 5 elements in the radial direction of the filament. Hence, we need a high-resolution mesh to achieve localised pinching that will further lead to the formation of smaller and higher generations of drops.

Pressure ( $p$ ) map, excluding hydrostatic pressure, for the liquid bridge is shown in Fig. 2.18. Initially, as expected, there is no significant capillary pressure across the liquid bridge, as indicated in Fig. 2.18(a) and (b). Then, once the filament appears, pressure starts developing in the filament, Fig. 2.18 (c). Similar observation of larger pressure in the filament has been reported by Entov and Hinch [119] and Li and Fontelos [2]. When the filament appears, at  $t = 0.027$  s, the capillary pressure inside the quasi-cylindrical filament can be estimated using Laplace equation:  $p = \sigma/R(t)$ . Using this formula, value of  $p$  in the filament is around 444 Pa, whereas the average value of  $p$  from the numerical simulations [see Fig. 2.18(c)] is around 432 Pa. Pressure inside the drop is observed to be higher than in the solution pools, as expected.

Then, filament breakup and formation of the drop occur, Fig. 2.18(d). Also, velocity distribution across the liquid bridge is shown in Fig. 2.19. Higher magnitude of velocity,  $U$ , is observed only when the filament appears, Fig. 2.19(c). Thinning velocity keeps increasing in the necking area and then suddenly becomes smaller, once formation of the drop occurs, Fig. 2.19(d). In addition, liquid contact lines at both plate surfaces are tracked by measuring contact line velocities,  $U_x$ , with time. Contact lines velocities remained at zero and thus,

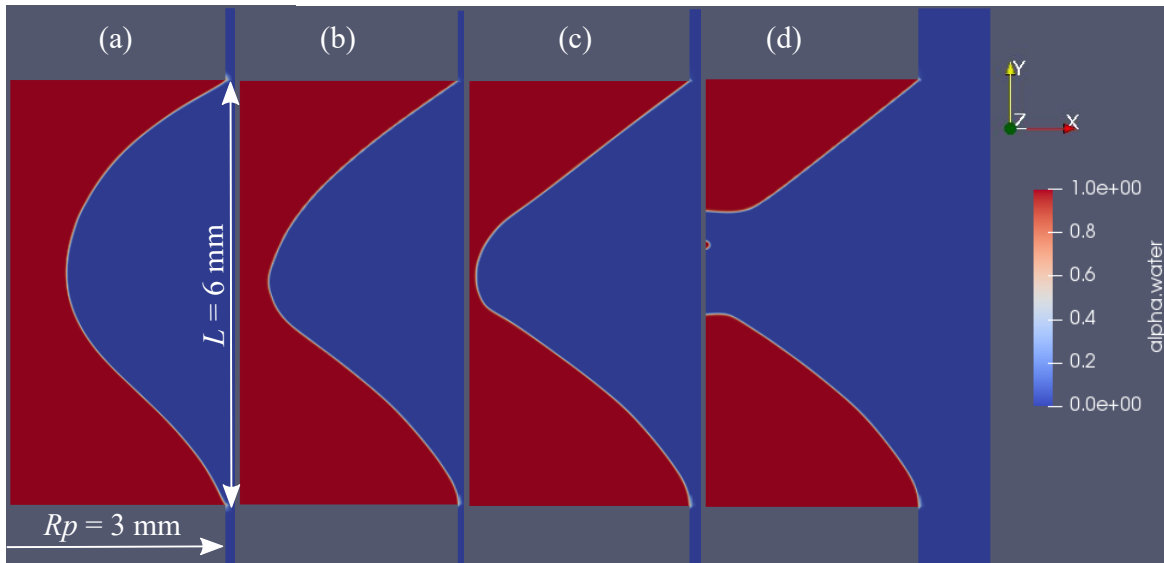


Fig. 2.17 Visualisation of the axisymmetric numerical solution of stretched liquid bridge for PEG20PEO1000 solution using Mesh N3. `alpha.water = 1` indicates presence of liquid (PEG20PEO1000) and `alpha.water = 0` indicates air. In these simulations, we used:  $R_p = 3$  mm,  $FAR = 2$ ,  $De = 132.8$  and  $Oh = 1.84$ . (a) Initial stretched liquid bridge at  $t = 0$  s. (b) Stretched liquid profile at  $t = 0.020$  s. (c) Filament is formed at  $t = 0.027$  s. (d) Formation of a first generation drop at  $t = 0.029$  s.

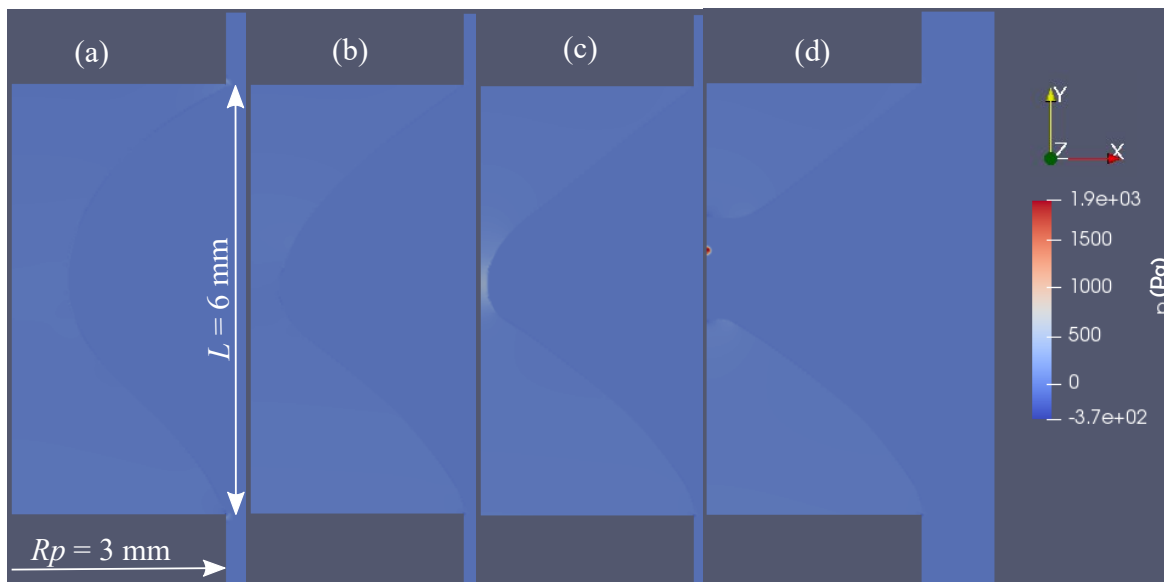


Fig. 2.18 Visualisation of pressure,  $p$  (Pa), inside stretched liquid bridge for PEG20PEO1000 solution using Mesh N3. In these simulations, we used:  $R_p = 3$  mm,  $FAR = 2$ ,  $De = 132.8$  and  $Oh = 1.84$ . Pressure,  $p$  (Pa), at (a)  $t = 0$ , (b)  $t = 0.020$ , (c)  $t = 0.027$ , and (d)  $t = 0.029$  s.

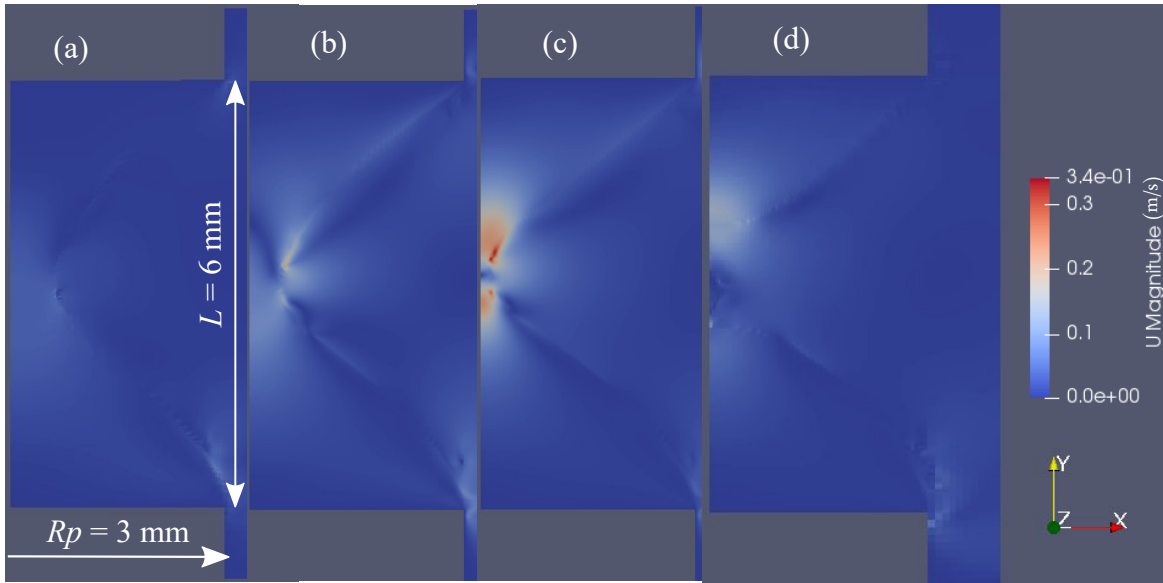


Fig. 2.19 Visualisation of velocity inside stretched liquid bridge for PEG20PEO1000 solution using Mesh N3. In these simulations we used:  $R_p = 3$  mm,  $FAR = 2$ ,  $De = 132.8$  and  $Oh = 1.84$ . Velocity,  $U$  (m/s), distribution at (a)  $t = 0$ , (b)  $t = 0.020$ , (c)  $t = 0.027$ , and (d)  $t = 0.029$  s.

in our numerical simulations, the liquid contact lines are pinned similar to the CaBER experiments.

Distribution of polymeric stress,  $\tau_{auMF}$ , across the stretched liquid bridge is shown in Fig. 2.20. Average value of  $\tau_{auMF}$  across midplane of the filament is measured and plotted against time, as shown in Fig. 2.20 (a). The polymeric stress increases with time and this trend is captured using an exponential fit. It is important to note that this exponential increase of polymeric stress is in the *inertio-capillary* regime. Previously, Turkoz et al. [55] reported exponential increase of polymeric stress in the *elasto-capillary* regime. The numerical simulation slows down in *elasto-capillary* thinning as an extra equation of polymeric stress becomes significant. When the filament forms, the polymeric stress continues to grow and reaches the maximum value in necking area, as previously reported [2, 16, 55, 119, 142]. This increasing polymer stress causes recoiling and formation of a drop.

When solution pools are formed on both plates, solution pool heights ( $h_0$ ) on both plates are measured and the transfer ratio is calculated by using the "spherical drop" method. Corresponding results of transfer ratio for PEG20 and PEG20PEO1000 solutions are reported in chapter 4.

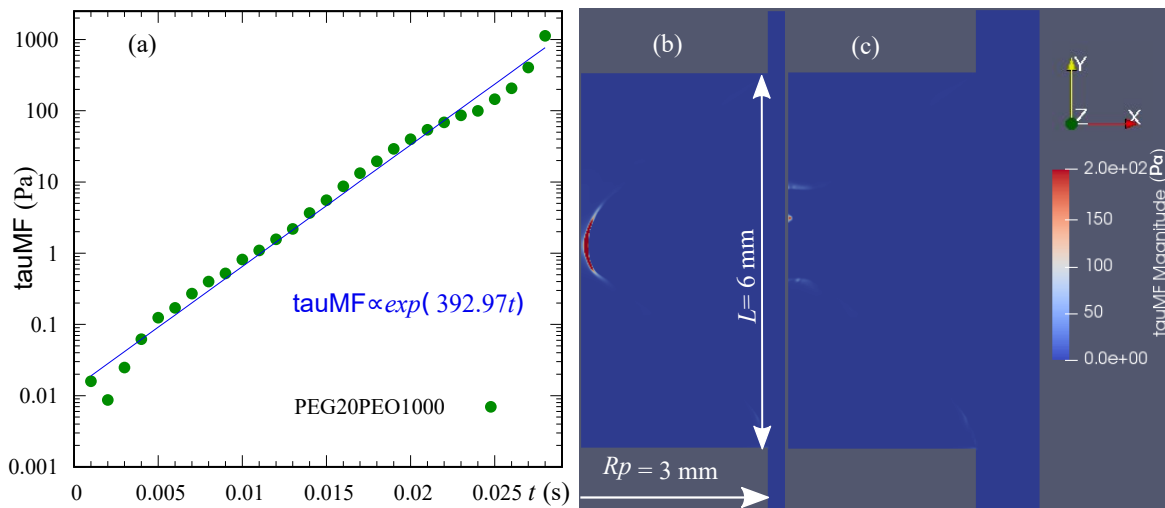


Fig. 2.20 Numerical results for polymeric stress,  $\tau_{MF}$  distribution for PEG20PEO1000 solution using mesh N3. In these simulations, we used:  $R_p = 3$  mm,  $FAR = 2$ ,  $De = 132.8$  and  $Oh = 1.84$ . (a) Average value of  $\tau_{MF}$  across midplane of the filament as a function of time. The line is an exponential fit with a coefficient of determination of 0.99. Distribution of  $\tau_{MF}$  inside stretched liquid bridge at (b)  $t = 0.027$ , and (c)  $t = 0.029$  s.



# Chapter 3

## Beads on a string

### Contents

---

<b>3.1</b>	<b>Diameter-space-time (DST) and Hencky strain-space-time (HSST) diagrams</b>	<b>86</b>
3.1.1	Analysis of space-time diagrams	88
3.1.2	Drop dynamics	96
<b>3.2</b>	<b>Effect of different parameters on the beads on a string</b>	<b>98</b>
3.2.1	Plate diameter	98
3.2.2	Initial aspect ratio	101
3.2.3	Final aspect ratio	103
3.2.4	Stretching speed	109
<b>3.3</b>	<b>Partial conclusion</b>	<b>111</b>

---

In this chapter, experimental results for beads on a string dynamics will be presented. It has been known for 50 years [6, 7] that capillary jets of viscoelastic polymer solutions may exhibit a BOAS structure. The BOAS structure has also been observed in the stretching of capillary bridges using extensional rheometer such as CaBER [3, 14, 63, 76, 88, 143, 144]. For viscoelastic filaments, studies have consistently evidenced the linear *viscous-capillary* thinning ( $Oh \gg 1$ ), the exponential *inertio-capillary* thinning ( $Oh \ll 1$ ), the exponential *elasto-capillary* thinning and in the later stages, the existence of drops attached to a thin filament (BOAS or blistering pattern) [1, 12, 14, 16, 18, 27, 74, 81, 88, 97]. Space-time diagrams have been previously reported to represent spatial and temporal dynamics of a drop formation along with their coalescence and migration [9, 15].

In the present chapter, homologous polymer mixtures or bi-disperse polymers at different mass fractions are tested covering a large range of dimensionless numbers. In the first part of the chapter, new types of space-time diagrams called diameter-space time diagrams and Hencky strain-space time diagrams will be presented. These novel diagrams will help to illustrate filament thinning, multiple generations of drops along with their diameters, positions, coalescence, migration and Hencky strain. Moreover, the space-time diagrams will be further investigated to study drop dynamics (diameters and number of drops). Previously, the influence of the initial aspect ratio and the final aspect ratio on filament thinning were reported [14, 83]. However, their influence on the formation of a BOAS structure has not been discussed yet. Hence, in the second part of the chapter, space-time diagrams will be developed and analysis of the diagrams will allow us to uncover effects of (i) plate diameter, (ii) initial aspect ratio, (iii) final aspect ratio and (iv) stretching speed upon the dynamics of the BOAS structure. Additionally, we present preliminary numerical results obtained using *rheoTool* for PEG20PEO1000 solution.

### 3.1 Diameter-space-time (DST) and Hencky strain-space-time (HSST) diagrams

Initially, we would like to recall and briefly discuss the limitations of previous space-time diagrams for a stretched viscoelastic liquid bridge. Oliveira et al. [9] and Ardekani et al. [16] reported space-time diagrams in their experimental and numerical study, respectively. The space-time diagrams by Oliveira et al. [9] only represent a BOAS structure but not the entire filament thinning process along with its breakup. Also, drops are presented only through colour intensity but the space-time diagram does not provide any data about actual drop

diameters. Furthermore, only one space-time diagram is presented by Oliveira et al. [9] for a solution of 2000 ppm PEO ( $M = 3.8 \times 10^6$  g/mol) in water and PEG mixture. As a result, differences in space-time diagrams for various polymer mass fractions were not explored. Conversely, space-time diagrams obtained from numerical simulations have been produced by Ardekani et al. [16] for a range of  $De$  from 0.8 to 300. These diagrams show a small number (up to 6) of regularly spaced drops and no coalescence in their BOAS structure. We aim to produce experimental space-time diagrams taking into account a complete filament and drop dynamics of a BOAS structure. A wide range of mass fractions is tested for both PEO and PEG+PEO solutions.

**Construction of DST and HSST diagrams** To obtain a complete filament along with a BOAS structure, a trial experiment is initially performed to create a liquid filament, as shown in Fig. 3.1(a). Depending upon PEO and PEG concentrations in a solution, sizes of the top and bottom solution pools vary and hence, the position of the filament in a liquid bridge changes along the  $z$ -direction. (Details of the variation of the sizes of the solution pools with PEO and PEG concentration are discussed in the next chapter). Therefore, the camera needs to be adjusted to locate the position of the filament along the  $z$ -direction. Finally, in an additional separate experiment, the camera is re-positioned, as shown in Fig. 3.1(b), to capture the entire filament and to have a better resolution in space. As we aim to capture only a BOAS structure, our DST and HSST diagrams will only represent a filament, but not an entire stretched liquid bridge.

Experiments are performed for PEG20, PEO and PEG+PEO solutions. Liquid bridges, formed in-between the two plates of  $D_p = 6$  mm, are stretched from  $IAR = 0.66$  to  $FAR = 2$  at  $U = 0.08$  m/s. For all PEO and PEG+PEO solutions, a filament and a BOAS structure are observed. By using a self-developed MATLAB code, the calibrated images are converted into DST diagrams. Diameters,  $D(z, t)$ , of the filament and drops, are converted into a colour code, to obtain any local diameter in space and time. White colour represents the thinnest part of the filament below the resolution of the camera. The black part at the top end of the filament indicates a region around the bottom part of the top solution pool. The black part at the bottom end of the filament indicates a region around the top part of the bottom solution pool. Intermediate values for smaller to larger diameters are presented by a spectrum of red and blue colours, respectively. For a liquid bridge with  $D_p = 6$  mm and  $IAR = 0.66$ , stretched to  $FAR = 2$  at  $U = 0.08$  m/s, the top plate reaches the final stretching height at  $t = 0.05$  s. Hence, to construct DST diagrams, images are captured from  $t = 0.05$  s until a majority of drops merge into the solution pools. A constructed DST diagram for PEO1000 solution is presented in figure 3.1(c). The DST for PEO1000 solution is a sequence of more than

700 images. Additionally, the value and position of the minimum diameter,  $D_{min}$ , along the filament are tracked in space and time. This position of  $D_{min}$  is presented by a green line in the DST diagram.

Furthermore, HSST diagrams are constructed to depict the Hencky strain,  $\epsilon$ , in space and time. As already observed, a filament diameter varies axially (see Fig. 2.4); it would be interesting to monitor deformation along the filament with time. Hence, using HSST diagrams, total deformation of a fluid element will be tracked by plotting Hencky strain along the filament with time. As previously introduced, the Hencky strain is defined as,  $\epsilon(z,t) = 2\ln[D_0/D(z,t)]$ , where  $D$  is the diameter of the filament. The axial coordinate,  $z$ , is relative to the camera position needed to capture the entire filament as already described. Hence, to construct HSST diagrams, the instantaneous diameters,  $D$ , of the filament extracted from the images are used to calculate  $\epsilon$ . Then, the values of  $\epsilon$ , are converted into a colour code. White colour represents the smallest values of  $\epsilon$  and the black colour represents the largest values of  $\epsilon$ . The intermediate values of  $\epsilon$ , from smaller to larger  $\epsilon$ , are presented by a spectrum of red and blue colours, respectively. A constructed HSST diagram for PEO1000 is presented in Fig. 3.1(d). To construct the HSST diagrams, the images captured from  $t = 0.05$  s until merging of drops into solution pools are considered, with the same time resolution as DST diagrams. The HSST for PEO1000 solution is a sequence of more than 700 images. HSST diagrams also enhance visibility of drops in a BOAS structure.

### 3.1.1 Analysis of space-time diagrams

Another example of HSST diagram, for PEG20PEO1000 solution, is presented in Fig. 3.2. The longer time scale indicates the longer filament thinning time for PEG20PEO1000 compared to PEO1000 solution. In this example, the liquid bridge, formed in-between the two plates of  $D_P = 6$  mm, is stretched from  $IAR = 0.66$  to  $FAR = 2$  at  $U = 0.08$  m/s.  $t = 0$  is when the separation of the CaBER plates starts. The top plate reaches the final stretching height,  $L = 6$  mm, at  $t = 0.05$  s. HSST is constructed from  $t = 0.05$  s until merging of drops into solution pools. For each second, 100 images are analysed and hence, the HSST presented here is a sequence of more than 2500 images. The green coloured line indicates the position of the minimum diameter,  $D_{min}$ , of the filament. From this  $D_{min}$ , the values of  $\epsilon_{min}$  and  $\eta_E$  are calculated. These local  $\epsilon_{min}$  and  $\eta_E$  can be recovered using Fig. 2.7(b). For example, the Hencky strain corresponding to the green line in Fig. 3.2 is  $\epsilon_{min}$  for PEG20PEO1000 solution in 2.7(b). Note that after initial oscillation between both ends of the filament,  $D_{min}$  is always located, probably due to gravity, at the top end of the filament where  $\epsilon_{min}$  is maximum.

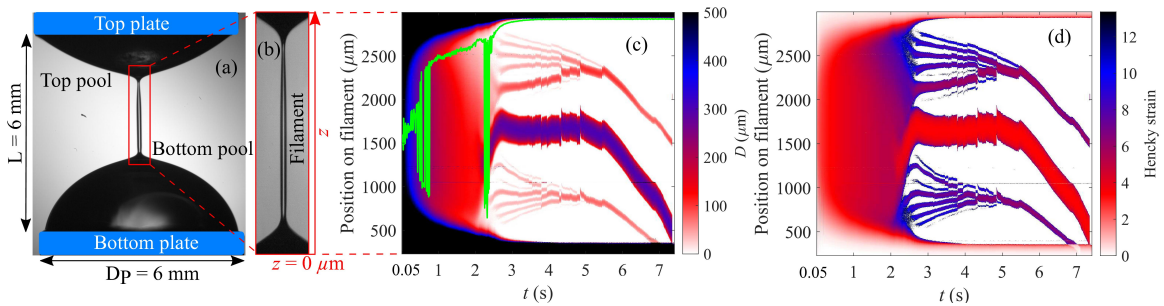


Fig. 3.1 Construction of the space-time diagrams for filament thinning and BOAS structure, using PEO1000 solution. The liquid bridge, formed in-between the two plates of  $D_p = 6$  mm, is stretched from  $IAR = 0.66$  to  $FAR = 2$  at  $U = 0.08$  m/s.  $t = 0$  is when a separation of the CaBER plates starts. The top plate reaches the final stretching height,  $L = 6$  mm, at  $t = 0.05$  s. Images are captured from  $t = 0.05$  s until merging of drops into solution pools. (a) A filament formed for PEO1000 solution, along with top and bottom solution pools. (b) The region, around the filament, considered to construct the space-time diagrams. Hence, our space-time diagrams only represent this region, but not the entire stretched liquid bridge.  $z$  is the direction along the filament and  $z = 0 \mu\text{m}$  at the baseline of the region. (c) The DST diagram for PEO1000 solution constructed from the obtained images. For each second, 100 images are captured and hence, the DST presented here is a sequence of more than 700 images. The green line represents the position of the minimum diameter of the filament. The position of the drop on the filament can be represented along the  $z$  direction. The colour code represents diameters of a filament or a drop. Multiple generations of drops can be identified by their diameters and colour code. (d) HSST diagram for PEO1000 solution. The Hencky strain is defined as,  $\varepsilon(z, t) = 2 \ln [D_0 / D(z, t)]$ , where  $D$  is a diameter of a filament. The position of any drop on the filament is represented along the  $z$  direction. The HSST presented here is a sequence of more than 700 images.

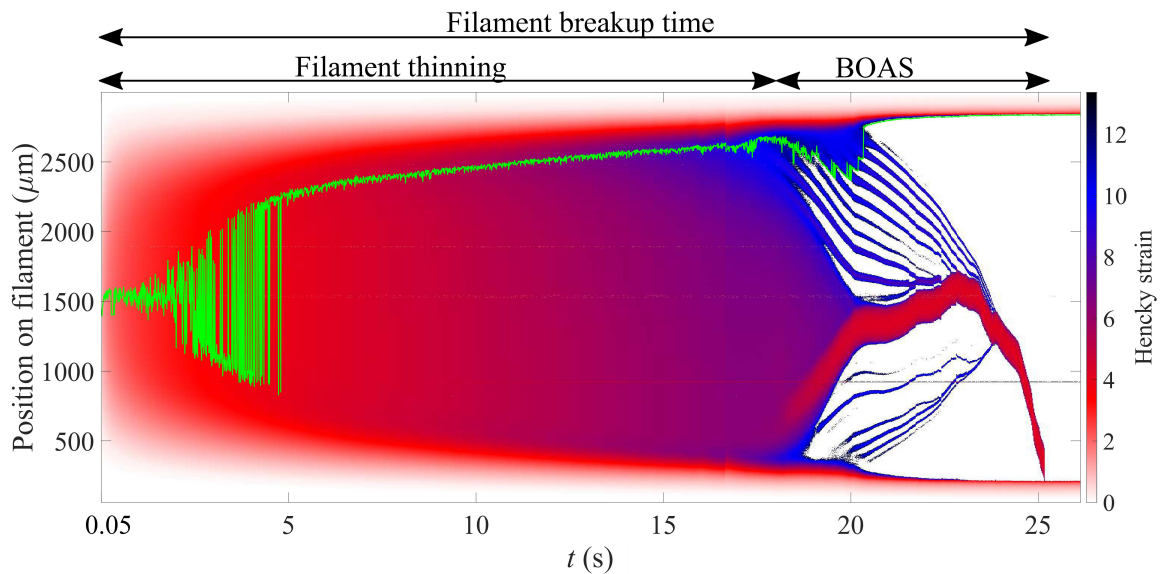


Fig. 3.2 HSST diagram for PEG20PEO1000 solution. Filament thinning and appearance of the BOAS structure are represented by arrows above the diagram. The total time for filament thinning and appearance of BOAS is considered as the filament breakup time. The longer filament thinning time for PEG20PEO1000 solution can be observed compared to PEO1000 solution. The liquid bridge, formed in-between the two plates of  $D_p = 6$  mm, is stretched from  $IAR = 0.66$  to  $FAR = 2$  at  $U = 0.08$  m/s.  $t = 0$  is when the separation of the CaBER plates starts. The top plate reaches the final stretching height,  $L = 6$  mm, at  $t = 0.05$  s. The HSST diagram is calculated from  $t = 0.05$  s until merging of drops into solution pools. For each second, 100 images are captured and hence, the HSST diagram presented here is a sequence of more than 2500 images. The green line represents the position of the minimum diameter of the filament. The position of any drop on the filament is represented along the  $z$  direction.

In this section, the DST and HSST diagrams from Fig. 3.1 and Fig. 3.2 are analysed. For both PEO1000 and PEG20PEO1000 solutions, the stretching of the liquid bridges leads to filament thinning. Initially, the colour intensity is homogeneous in the  $z$ -direction, showing the existence of a uniform filament. Filament thinning time for PEG20PEO1000 solution is longer than PEO1000 solution. The filament continues to thin until the necking has occurred at both ends and then  $D_{min}$  systematically remains at the top end of the filament. For both solutions, this thinning process can be characterised as an initial *inertio-capillary* thinning followed by an *elasto-capillary* thinning. After  $t = 2.5$  s for PEO1000 and  $t = 18$  s for PEG20PEO1000, a BOAS instability appears through the formation of a first generation of drop. Following the initial capillary instability (*inertio-capillary* and *elasto-capillary* filament thinning) and formation of a primary generation of drop, new interconnecting liquid filaments in-between the first generation of drop and solution pools are developed. These filaments again become unstable and then, second and third generation of drops are created. The largest diameter is observed for the first generation of the drops and then drop diameters further decrease for higher generations of drops. In DST diagrams, the multiple generations of drops can be recognised by their size and the colour code: blue/dark red for the first generation of drops and lighter shades of red for the higher generations of drops. The repeated or ‘iterated’ nature of the drop formation process is clear. The relatively large drop (first generation of the drop) is formed around the mid-height with diameter varying from 220 (for PEG20PEO1000) to 320 (for PEO1000)  $\mu\text{m}$ . Typically, in our BOAS structure, a central big drop is accompanied by smaller drops on both sides. Interestingly, the second-largest drop is often a satellite drop above the big central drop. Other than the first two generations of drops, the third and higher generation of drops have diameters less than 50  $\mu\text{m}$ . For Oliveira et al. [9], for PEG20PEO1000 solution, drop diameters for the first three generations are approximately 110, 75 and 31  $\mu\text{m}$ , respectively. The authors used an aqueous solution of PEO ( $M = 3.8 \times 10^6$  g/mol) in a mixture of ethylene glycol and water as a viscoelastic test fluid. Geometrical details of the liquid bridge used by the authors are  $D_p = 6$  mm,  $IAR = 1$  and  $FAR = 3.23$ . In the present study, for PEG20PEO1000, the diameter of the second generation drop (second largest drop) is approximately 50  $\mu\text{m}$ . The differences in the diameters of the first generation of drops can be explained by differences in  $M$  of PEO used and  $FAR$ . The authors used  $FAR = 3.23$  which is larger than the present  $FAR = 2$ . The influence of larger  $FAR$  on the diameter of the first generation of drop is explained later in this chapter. Moreover, for all PEO and PEG+PEO solutions, more satellite drops can be seen above the big central drop compared to below it, presumably due to gravity. Because of gravity, the big central drop is closer to the bottom end of the filament. As a result, a larger filament length is available for localised pinching above the big central drop. This larger filament length leads

to the formation of higher generations of drops, resulting in more number of drops above the big central drop.

In HSST diagrams, for both solutions,  $\varepsilon$  increases along the filament with time until necking occurs on both ends. Once the necking occurs,  $\varepsilon$  increases further with time at both ends of the filament, before the appearance of multiple-generations of drops in a BOAS structure. Furthermore, the position of the minimum diameter,  $D_{min}$ , represented by a green line, is initially located at the mid-height of the liquid bridge. Once the filament forms, the thinning continues and then  $D_{min}$  oscillates in between both ends of the filament. After necking,  $D_{min}$  is systematically located at the top of the filament. From Fig. 3.1(c), it can be seen that, after necking,  $\varepsilon$  corresponding to green line varies significantly over time.

However, once all drops are fully formed, they migrate axially along the filament, usually in the direction of gravity, and coalescence occurs. As a result, coalescence between the drops leads to a coarsening of the pattern in the space-time diagrams, in the form of sudden axial displacements. Similar coarsening of a space-time diagram due to coalescence was previously observed by Oliveira et al. [9]. The authors also suggested that the tension in the filament is relieved after every coalescence, that further implies the elastic behaviour of the filament. Migration of the drops occurs in the direction of the coalescence. The filament along with drops is pulled towards the location of coalescence. Hence, drops above the location of the coalescence migrate downwards and the drops below the location of coalescence migrate upwards. These axial displacements are noticeably visible in Fig. 3.1(c) for PEO1000 solution at  $t = 4.3$  and  $4.8$  s. At least three scenarios predicted numerically by Li and Fontelos [2] can be observed in our space-time diagrams: the appearance of drops due to the stretching of a viscoelastic liquid bridge, drops migration and coalescence. Eventually, for both solutions, in the later stages, the BOAS structure is reorganised (due to coalescence) into a few large drops. For PEO1000, two relatively medium-size satellite drops, with diameters varying from  $50$ - $150$   $\mu\text{m}$ , are observed on either side of the big drop. Finally, the breakup occurs at the top of the filament, for both solutions, presumably because of the gravitational effect.

Additional DST and HSST diagrams are depicted in Fig. 3.3 and 3.4. Here, liquid bridges, formed in-between the two plates of  $D_p = 6$  mm, are stretched from  $IAR = 0.66$  to  $FAR = 2$  at  $U = 0.08$  m/s. In Fig. 3.3, the DST and HSST diagrams for PEO100, PEO2000 and PEG20 are presented. For PEG20 (Fig. 3.3(e) and (f)), the filament breaks rapidly (less than  $0.01$  s) and a drop forms then rebound before falling into the bottom solution pool. The DST and HSST diagrams for PEG20PEO100, PEG20PEO1000 and PEG20PEO2000, are shown in Fig. 3.4. For all PEO and PEG+PEO solutions, the formation of a filament and a BOAS structure can be observed. For both PEO and PEG+PEO solutions, filament thinning time

and filament breakup time increase with the increase in  $w_{PEO}$ . Furthermore, for the same value of  $w_{PEO}$ , filament thinning time and filament breakup time are larger for PEG+PEO solutions than PEO solutions, as previously seen in Fig. 2.5.

Another feature of the DST diagrams is the systematic fall of the big drop towards the bottom solution pool. The diagrams can be used to measure falling dynamics of the big drop. From the solution properties of PEG20PEO1000 and diameter of the big central drop ( $d_{PEG20PEO1000} = 224 \mu\text{m}$ ), assuming a spherical drop shape, the calculated weight of the drop is 59.4 nN. At the equilibrium condition, the tension in the filament is equal to the weight of the drop. Then, the drop starts to fall. From Fig. 3.2, the equilibrium condition occurs at  $t \simeq 24$  s and at  $z_0 = 1312 \mu\text{m}$ . Here,  $z_0$  is the vertical position of the drop on the filament. The falling speed of the drop can then be measured; for PEG20PEO1000,  $V_{PEG20PEO1000} = z_0/\Delta t \simeq 1$  mm/s.  $\Delta t$  is the time taken by the drop to fall into the bottom solution pool. In comparison, the velocity of the drop in a free fall,  $V_{Free\ fall} = \sqrt{2gz_0} = 160$  mm/s, is higher than  $V_{PEG20PEO1000}$ . The time taken for the drop in the free fall is 0.02 s. While the actual time taken by the drop is longer than 1 s, which suggests that there is a non-negligible pulling force on the drop. From our calculations, for a drop of diameter 224  $\mu\text{m}$  with a falling speed of 1 mm/s, the aerodynamic drag force is  $10^{-3}$  times the weight and hence, the aerodynamic drag can be neglected.

Even though several publications deal with the formation of the beads on a string phenomenon, there is limited data on the position, trajectories, diameters and number of drops. The present space-time diagrams give the accurate measurements of the drops diameter and Hencky strain, whereas previous works by Oliveira et al. [9] and Clasen et al. [15] are based on the grey-scale intensity to indicate a relative thickness of the drops or positions of the drops, respectively. Additionally, both authors presented space-time diagrams for a single polymer concentration: 2000 ppm of PEO ( $M = 3.8 \times 10^6$  g/mol) in a mixture of PEG and water [143] and 100 ppm of PAAM ( $M = 7.5 \times 10^6$  g/mol) in water [15]. In the present study, a large range of space-time diagrams is constructed for a systematic variation of polymer mass fractions. Overall, our space-time diagrams represent quantitative descriptions of the drop dynamics studied numerically by Li and Fontelos [2], Ardekani et al. [16] and Turkoz et al. [55] where filament thinning, drop migration and coalescence were predicted. Furthermore, our experiments indicate a hierarchy and asymmetric distribution of satellite drops for all PEO and PEG+PEO solutions. This asymmetric distribution of satellite drops is in contrast with the previous numerical prediction [2, 16, 55]. These numerical simulations indicated that higher generations of drops are distributed equally on either side of the first generation of drops. However, our space-time diagrams show that more satellite drops are above the big central drop than below, presumably due to the gravity effects.

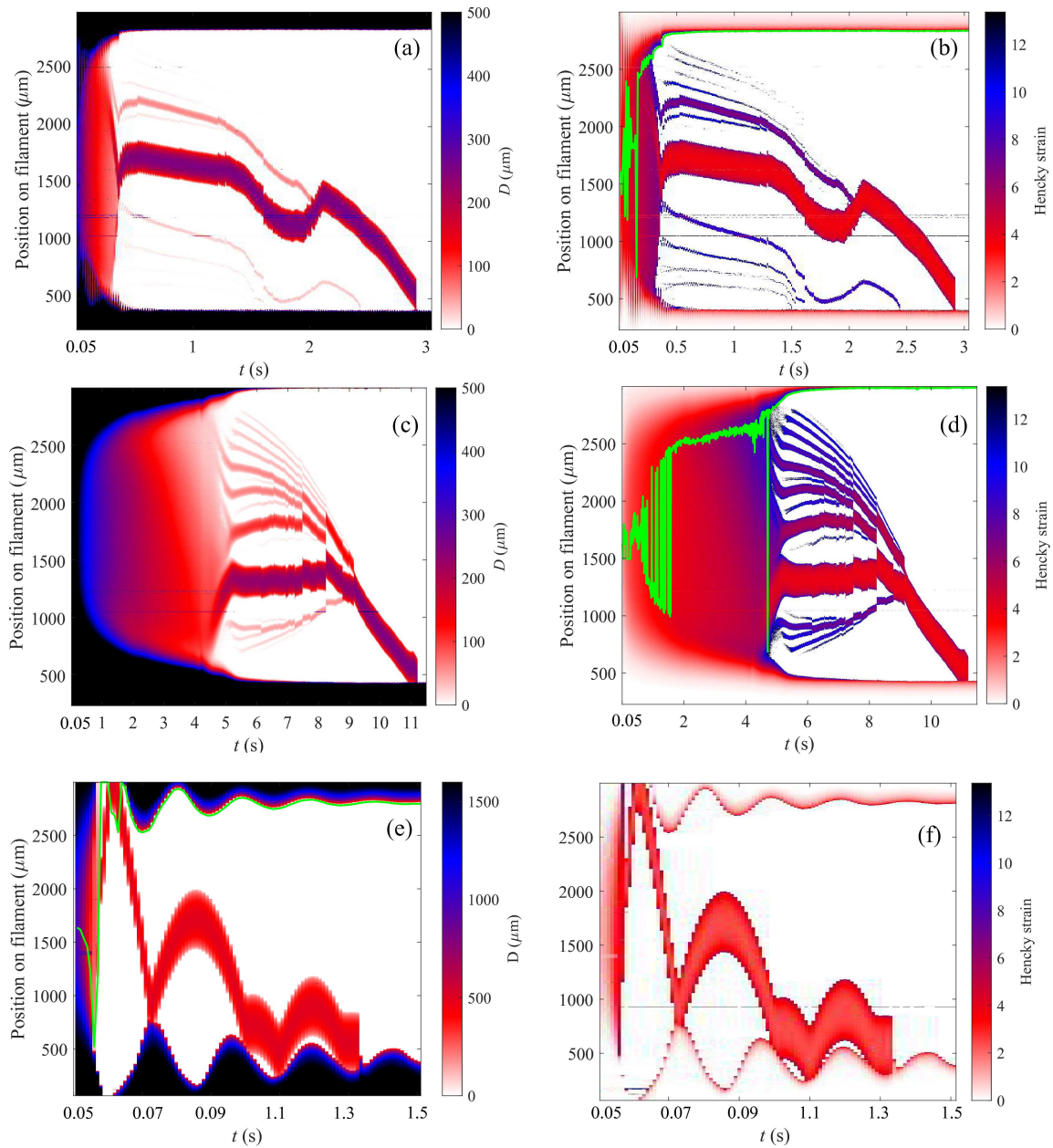


Fig. 3.3 Space-time diagrams for filament thinning and BOAS structure, for PEO solutions and PEG20. Filament thinning time and appearance of multiple generations of drops vary with  $w_{PEO}$ . The liquid bridge, formed in-between the two plates of  $D_p = 6$  mm, is stretched from  $IAR = 0.66$  to  $FAR = 2$  at  $U = 0.08$  m/s.  $t = 0$  is when a separation of the CaBER plates starts. The top plate reaches the final stretching height,  $L = 6$  mm, at  $t = 0.05$  s. HSST is captured from  $t = 0.05$  s until merging of drops into solution pools. The green line represents the position of the minimum diameter of the filament. The position of any drop on the filament is represented along the  $z$  direction. For PEO100 and PEO2000 solutions, for each second, 100 images are captured. For PEG20, the images are acquired at a rate of 1000 frames per seconds. As PEG20 is a Newtonian fluid, no BOAS structure is observed. (a) DST for PEO100 and (b) HSST for PEO100, (c) DST for PEO2000 and (d) HSST for PEO2000, (e) DST for PEG20 and (f) HSST for PEG20.

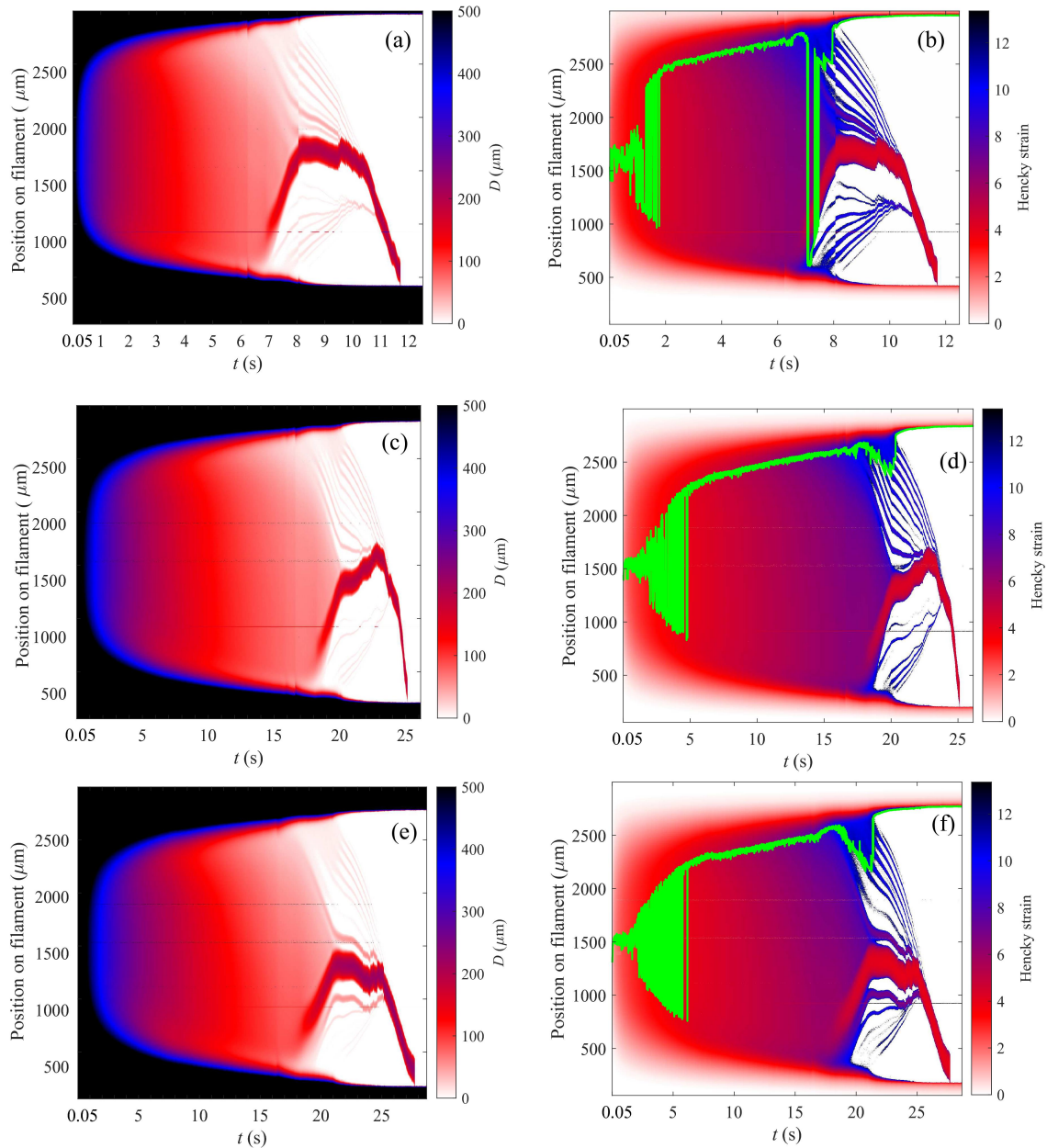


Fig. 3.4 Space-time diagrams representing filament thinning and BOAS structure for PEG+PEO solutions. Filament thinning time and appearance of multiple generations of drops vary with  $w_{PEO}$ . The liquid bridge, formed in-between the two plates of  $D_P = 6$  mm, is stretched from  $IAR = 0.66$  to  $FAR = 2$  at  $U = 0.08$  m/s.  $t = 0$  is when a separation of the CaBER plates starts. The top plate reaches the final stretching height,  $L = 6$  mm, at  $t = 0.05$  s. HSST is captured from  $t = 0.05$  s until merging of drops into solution pools. For each second, 100 images are captured. The green line represents the position of the minimum diameter of the filament. The position of any drop on the filament is represented along the  $z$  direction. For these solutions, the images are acquired at a rate of 100 frames per second. (a) DST for PEG20PEO100 and (b) HSST for PEG20PEO100, (c) DST PEG20PEO1000 and (d) HSST for PEG20PEO1000, (e) DST for PEG20PEO2000 and (f) HSST for PEG20PEO2000.

### 3.1.2 Drop dynamics

Further insights into drop dynamics obtained from the space-time diagrams are presented in this section. The maximum number of drops,  $N$ , on the filament after pinching are counted. Only drops (up to the third generation) with diameter larger than  $25 \mu\text{m}$  are considered. The results for the number of drops are plotted in Fig. 3.5(a) against the Deborah number,  $De$ . Detailed values of the Deborah number for  $D_P = 6 \text{ mm}$  are given in Tab. 2.3. The maximum number of drops in a BOAS structure grows with an increase in the Deborah number. Moreover, the number of drops are higher for PEG+PEO solutions than PEO solutions. For PEG+PEO solutions, the filament lasts longer after necking and hence, more time is available for the localised pinching. This localised pinching further leads to the formation of higher generations of drops. Furthermore, a power law fit is used to represent the trend of growing  $N$  with  $De$ . The fit has an exponent of 0.17 and the coefficient of determination is 0.93. However, no theoretical model has been found to compare this scaling law. Additionally, we compare our results with the maximum number of drops (up to the third generation),  $N$ , obtained by Oliveira et al. [9] (see Fig. 1.9). From their solution properties,  $De$  is calculated and plotted in Fig. 3.5(a). The differences in the number of drops could be explained by differences in  $M$  of PEO used and larger  $FAR$  by the authors than the present  $FAR$  of 2. Hence, in their study, the authors obtained a larger number of drops. The influence of larger  $FAR$  on the number of drops is explained in details later in this chapter.

Also, diameters,  $d$ , of the first generation (largest) drops are measured for the PEO, PEG+PEO and PEG20 solutions. For PEO and PEG+PEO solutions,  $d$  is determined once multi-generation of drops in the BOAS structure are formed. The results obtained are shown in Fig. 3.5(b), where  $d$  is plotted against  $w_{PEO}$ . The error bars represent the dispersion over at least three repetitions of the experiment. A detached drop instead of a BOAS structure is observed for PEG20. For PEG20, the drop diameter is  $480\text{-}500 \mu\text{m}$ . For the solutions containing PEO, the diameters of first generation of drops range in-between  $220\text{-}320 \mu\text{m}$ . The average diameters of the first generation of drops for the PEO solutions are comparatively larger than the PEG+PEO solutions. In the case of PEG+PEO solutions, more number of drops are created than PEO solutions. Hence, for PEG+PEO solutions, the available liquid volume in the filament is distributed in more number of drops. Therefore, the liquid volume available for each drop is less, resulting in a smaller diameter of the big central drop. However, for both PEO and PEG+PEO solutions, the diameter of the first generation of drops remains constant with the increase in PEO mass fraction.

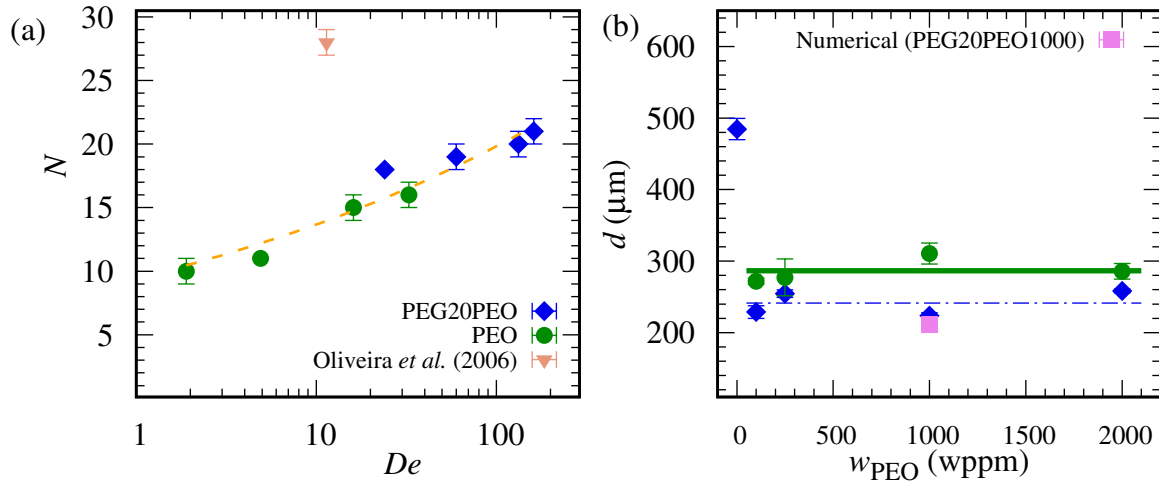


Fig. 3.5 Summary of maximum number of drops,  $N$ , and drop diameter,  $d$ , of the first generation (largest) drop in a BOAS structure obtained from the DST diagrams for PEO and PEG+PEO solutions. Here, PEG20PEO indicates 20 wt% of PEG in PEG+PEO solutions. The liquid bridge, formed in-between the two plates with  $D_P = 6$  mm, is stretched from  $IAR = 0.66$  to  $FAR = 2$  at  $U = 0.08$  m/s. The error bars indicate the dispersion over three measurements. (a) The maximum number of drops,  $N$ , in a BOAS structure as a function of  $De$ . Only the drops (up to the third generation) with diameter,  $D > 25 \mu\text{m}$ , are considered. Values of  $De$  for PEO and PEG+PEO solutions using  $D_P = 6$  mm are given in Tab. 2.3. The dashed line is a power law fit with  $N \propto De^{0.17}$  and a coefficient of determination of 0.94. Additionally,  $N$  (up to the third generation) and  $De$  by Oliveira et al. [9] are obtained (see Fig. 1.9). The authors used an aqueous solution of PEO ( $M = 3.8 \times 10^6$  g/mol) in a mixture of ethylene glycol and water as the viscoelastic test fluid. Geometrical details of the liquid bridge used by the authors:  $D_P = 6$  mm,  $IAR = 1$  and  $FAR = 3.23$ . (b) Diameter,  $d$ , of the first generation (largest) drop on the filament versus PEO mass fraction,  $w_{PEO}$ . For PEO and PEG+PEO solutions,  $d$  is determined once multi-generation of drops in the BOAS structure are formed. A detached drop instead of a BOAS structure is observed for PEG20. The thick and dash-dotted lines indicate the average drop diameter,  $d$ , for PEO and PEG+PEO solutions, respectively. Also, the pink square symbol represents an average diameter of the single first generation drop for PEG20PEO1000 solution from our numerical simulations (see Tab. 3.1).

**Numerical results for diameter of first generation of drops** As discussed in the previous chapter, we obtained a single first generation drop for PEG20PEO1000 solution in our numerical simulations. Experimental conditions for the stretched profile used in our numerical simulations were  $D_P = 6$  mm,  $IAR = 0.66$ ,  $FAR = 2$  and  $U = 0.08$  m/s. These conditions are similar to the experimental results in Fig. 3.5. For the numerical simulations, we consider all three meshes (N1 to N3) to calculate an average  $d$ , see Tab. 3.1. Furthermore, we compare the average diameter,  $d$ , of the first generation drop with the experimental results for PEG20PEO1000 solution, as shown in Fig. 3.5(b). Hence, the numerical and experimental results for the diameter of the first generation drop are in a good agreement.

Table 3.1 Diameter,  $d$ , of first generation of drops for numerical and experimental study. In the numerical simulations, we used:  $R_P = 3$  mm,  $FAR = 2$ ,  $De = 132.8$  and  $Oh = 0.46$ . For the numerical simulations, we consider all three meshes (N1 to N3) to calculate an average  $d$  plus standard deviation. Experimental conditions are:  $D_P = 6$  mm,  $IAR = 0.66$ ,  $FAR = 2$  and  $U = 0.08$  m/s.

Solution	Numerical $d$ ( $\mu\text{m}$ )	Experimental $d$ ( $\mu\text{m}$ )
PEG20PEO1000	$211 \pm 6$	$224 \pm 4$

## 3.2 Effect of different parameters on the beads on a string

There is no remarkable study of the influence of different parameters, such as the plate diameter,  $D_P$ , the initial stretching height,  $L_0$ , the final stretching height,  $L$ , and the stretching speed,  $U$ , on the formation of the beads on a string and the drop dynamics. Hence, in this section, the influence of these parameters is studied by constructing and analysing DST and HSST diagrams.

### 3.2.1 Plate diameter

Three different plate diameters,  $D_P = 4, 6$  and  $8$  mm are tested. The liquid bridge, formed in-between the two plates is stretched from  $IAR = 0.66$  to  $FAR = 2$  at  $U = 0.08$  m/s. However, even-though  $IAR = 0.66$ , the liquid volume introduced in the initial liquid bridge varies from  $16$  to  $133 \mu\text{l}$  with the increase in  $D_P$  from  $4$  to  $8$  mm, respectively. Therefore, larger plate diameters are stretched to larger final stretching heights but  $FAR$  is kept constant so that same extensibility can be applied for all three diameters. DST and HSST diagrams for all three

plate diameters using PEO1000 solution are presented in Fig. 3.6. For all plate diameters, filament thinning is followed by the formation of a BOAS structure with multi-generation of drops. Moreover, the typical BOAS structure with a big central drop at the centre and smaller satellite drops is evident for all three plate diameters. More satellite drops are observed above the big central drop. Additionally, recoiling, drop migration and coalescence are also observed.

In the initial stages of thinning, the position of minimum diameter,  $D_{min}$ , of the filament shifts in-between both ends of the filaments and then systematically moves to the top end of the BOAS structure. To get insights into effect of plate diameters on filament thinning, for all three diameters, the minimum diameter,  $D_{min}$ , is plotted in Fig. 3.7. For each plate diameter,  $D_{min}$  presented in Fig. 3.7 is the average over three experiments. Large  $D_P$  leads to larger filament diameter. For larger plate diameters, pinching of the filament gets delayed and the filament lasts longer. For the tests shown in Fig. 3.6, pinching occurs earlier for  $D_P = 8$  mm than  $D_P = 6$  mm. However, the average values of  $D_{min}$  from Fig. 3.7 indicate that with the increase in  $D_P$ , the pinching gets delayed. This delayed pinching enhances gravitational drainage through the filament. The effects of this gravitational drainage will be discussed later in the next chapter.

The DST diagrams are further analysed to investigate the drop dynamics of the BOAS structure. The maximum number of drops,  $N$ , on the filament in BOAS structure are counted and plotted against the Deborah number in Fig. 3.8(a). Only the drops (up to the third generation) with diameter,  $D > 25 \mu\text{m}$ , are considered. Detailed values of the Deborah number for all three plate diameters are given in Tab. 2.3. As previously observed, for all three plate diameters, the number of drops,  $N$ , increases with  $De$ . Additionally, for  $De > 4$ , the number of drops for  $D_P = 8$  mm, is higher than the number of drops for  $D_P = 4$  and 6 mm. The growth of number of drops with  $De$  is captured using a power-law fit. Out of three plate diameters, a higher exponent of the fit (0.42) is obtained for  $D_P = 8$  mm. This further suggests that, for larger plate diameters, the Deborah number has a higher influence on the number of drops. Even though  $IAR$  and  $FAR$  are the same for all three diameters, the final stretching height,  $L$ , is larger for  $D_P = 6$  and 8 mm. Hence, available length for the localised pinching, for  $D_P = 6$  and 8 mm, is larger than  $D_P = 4$  mm. This larger available length for  $D_P = 6$  and 8 mm than  $D_P = 4$  mm leads to the formation of higher generations of drops and hence, more number of drops.

Furthermore, diameter,  $d$ , of the first generation (largest) drop on the filament versus PEO mass fraction,  $w_{PEO}$ , for all plate diameters is reported Fig. 3.8(b). Each symbol represents the average over three experiments. As previously reported, for all three plate diameters, in the range of  $w_{PEO}$  tested, the drop diameter remains constant against  $w_{PEO}$ . The average

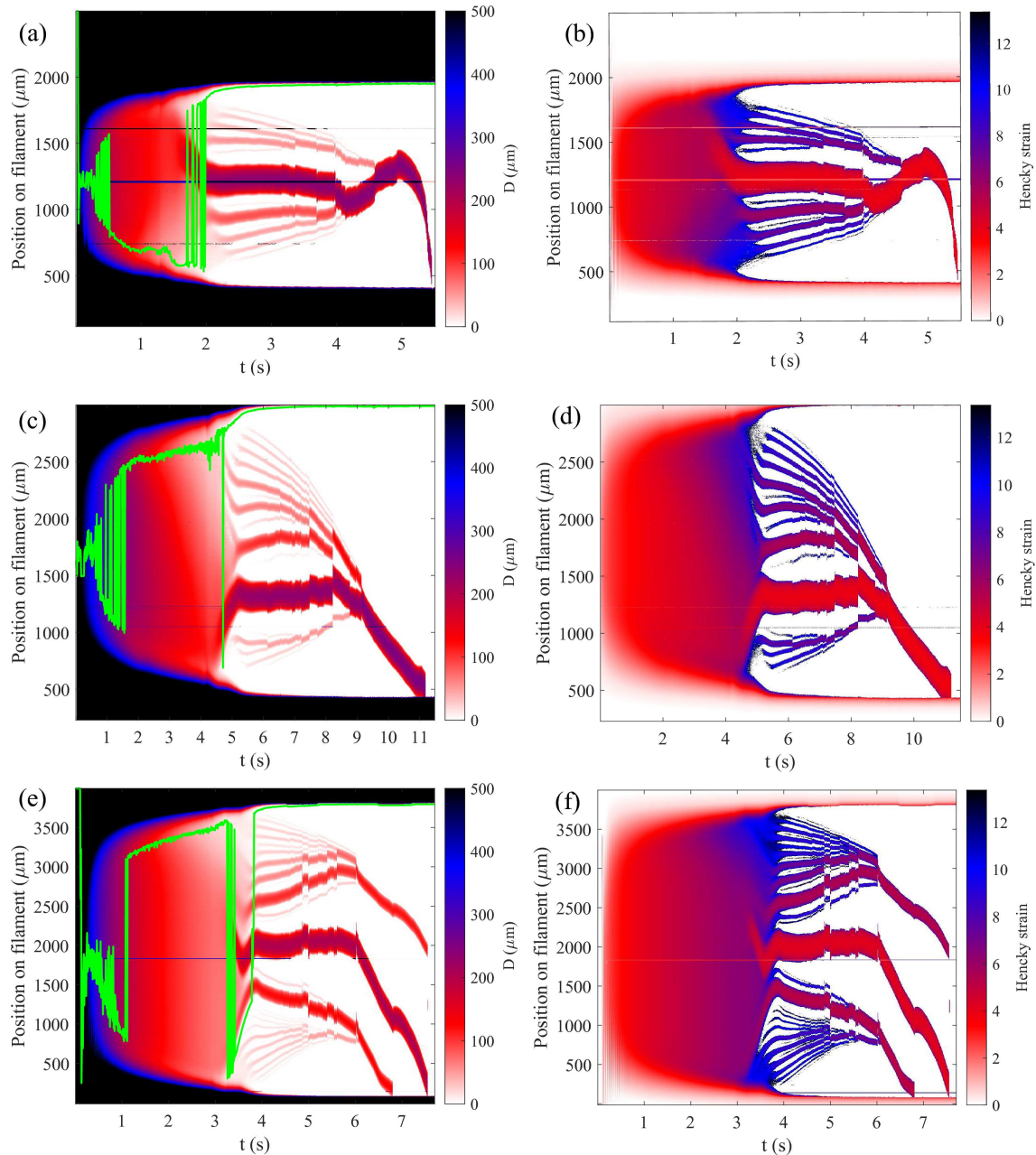


Fig. 3.6 Space-time diagrams of filament thinning and BOAS structure, for PEO1000 solution, with  $D_p = 4, 6$  and  $8$  mm. The liquid bridge, formed in-between the two plates is stretched from  $IAR = 0.66$  to  $FAR = 2$  at  $U = 0.08$  m/s.  $t = 0$  is when a separation of the CaBER plates starts. The top plate reaches the final stretching height,  $L = D_p$ . The DST and HSST diagrams are captured when the top plate reaches the final stretching height until merging of drops into solution pools. The liquid volume introduced in the initial liquid bridge varies from  $16$  to  $133 \mu\text{l}$  with the change in  $D_p$  from  $4$  to  $8$  mm, respectively. For each second,  $100$  images are captured. The green line represents the position of the minimum diameter of the filament. The position of any drop on the filament is represented along the  $z$  direction. Multiple generations of drops can be identified by their diameters and colour code. (a) DST for  $D_p = 4$  mm and (b) HSST for  $D_p = 4$  mm, (c) DST for  $D_p = 6$  mm and (d) HSST for  $D_p = 6$  mm, (e) DST for  $D_p = 8$  mm and (f) HSST for  $D_p = 8$  mm.

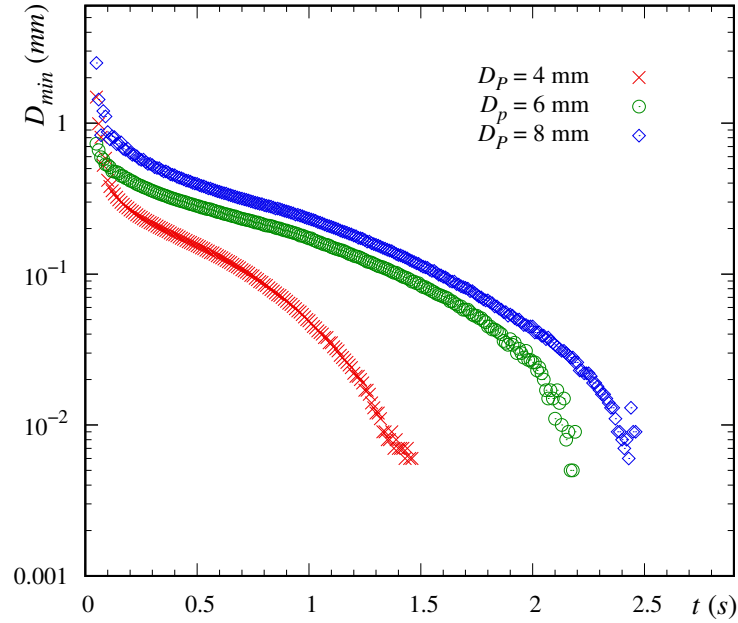


Fig. 3.7 Average minimum diameter,  $D_{min}$ , extracted from captured images for PEO1000 solution and using  $D_p = 4, 6$  and  $8$  mm. The liquid bridge formed in-between the two plates is stretched from  $IAR = 0.66$  to  $FAR = 2$  at  $U = 0.08$  m/s. Here,  $t = 0$  is when the separation of the CaBER plates starts.

drop diameter,  $d = 256, 286$  and  $356 \mu\text{m}$ , for  $D_p = 4, 6$  and  $8$  mm, respectively, suggesting for larger plate diameters,  $d$  becomes larger. The length of the filament for  $D_p = 4$  mm is around  $1600 \mu\text{m}$ , whereas the length of the filament for  $D_p = 8$  mm is around  $3500 \mu\text{m}$ . Furthermore, with increasing plate diameter, the volume of liquid introduced in the initial liquid bridge increases, resulting in the larger volume of the solution available in the filament. Consequently, when a BOAS structure appears, larger values of  $d$  are observed for  $D_p = 6$  and  $8$  mm than for  $D_p = 4$  mm.

### 3.2.2 Initial aspect ratio

The influence of the initial stretching height on a BOAS structure is studied by varying  $IAR$  from  $0.3$  to  $0.97$ , for PEO1000 solution. The liquid bridge, formed in-between the two plates of  $D_p = 6$  mm, is stretched to  $FAR = 2$  at  $U = 0.08$  m/s. For all  $IAR$  tested, filament thinning is followed by the appearance of a BOAS structure with multiple generations of drops. The evolution of the filament and BOAS structure are presented with DST and HSST diagrams in Fig. 3.9. For all the cases of  $IAR$  tested, the typical configuration of a big central drop, accompanied by smaller satellite drops on its either side, is again observed. Moreover, more

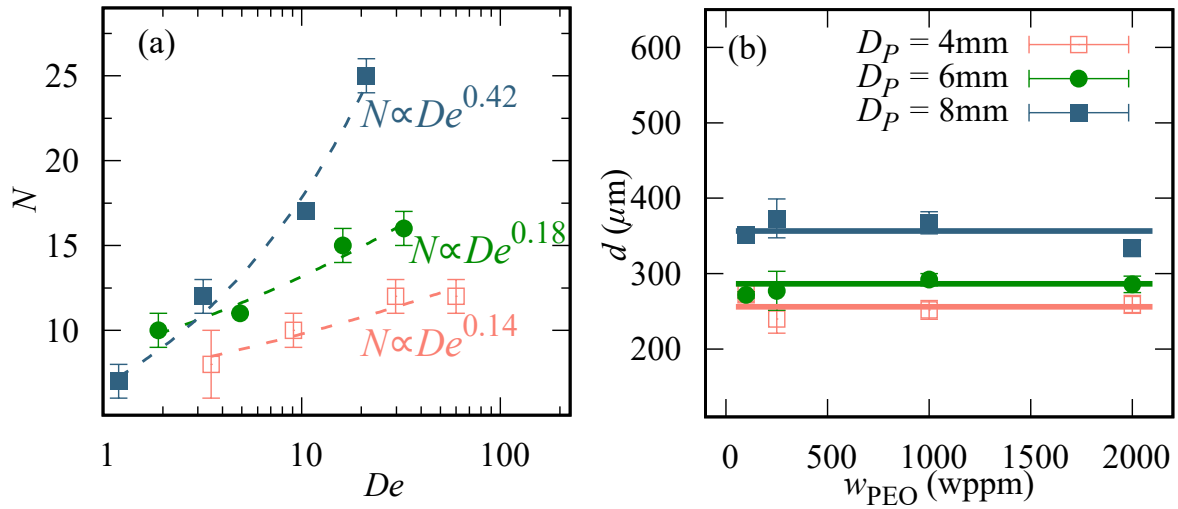


Fig. 3.8 Effect of plate diameters on maximum number of drops,  $N$ , and drop diameter,  $d$ , of the first generation (largest) drop in a BOAS structure for PEO solutions. The liquid bridge, formed in-between the two plates is stretched from  $IAR = 0.66$  to  $FAR = 2$  at  $U = 0.08$  m/s. The error bars indicate the dispersion over 3 to 5 measurements. (a) Maximum number of drops,  $N$ , in a BOAS structure as a function of  $De$ . Only the drops (up to the third generation) with diameter,  $D > 25 \mu\text{m}$ , are considered. Here,  $De = \lambda / \sqrt{\rho D_P^3 / 8\sigma}$  and detailed values of  $De$  for all three plate diameters are given in Tab. 2.3. The dashed pink, green and blue lines represent the power law fit for  $D_P = 4, 6$  and  $8$  mm, respectively. (b) Diameter,  $d$ , of the first generation (largest) drop on the filament versus PEO mass fraction,  $w_{PEO}$ . The pink, green and blue lines represent the average drop diameter,  $d$ , for  $D_P = 4, 6$  and  $8$  mm, respectively.

satellite drops can be seen above the big central drop than below. Typical characteristics of BOAS dynamics such as recoil, coalescence and migration of drops can be noted. In the initial stages of thinning, the position of minimum diameter,  $D_{min}$ , of the filament shifts in-between both ends of the filament and then systematically moves to the top end of the BOAS structure. The length of the filament for the studied case of  $IAR = 0.3$  is around 4000  $\mu\text{m}$ , but the length of the filament for  $IAR = 0.97$  is only around 2000  $\mu\text{m}$ . With the increase in  $IAR$ , the volume of liquid introduced in the initial liquid bridge increases.

The further analysis of the DST and HSST diagrams is shown in Fig. 3.10. Each symbol indicates the average over five experiments. The maximum number of drops,  $N$ , in BOAS structure is measured and plotted against the respective  $IAR$ , in Fig. 3.10(a). Only the drops (up to the third generation) with diameters larger than 25  $\mu\text{m}$  are considered. As shown by the trend line, the number of drops decreases when  $IAR$  increases. For larger  $IAR$ , larger solution pools are formed and the available length of the filament to form higher generations of drops (iterated instability) decreases. Hence, for  $IAR = 0.97$ , smaller number of drops are observed than  $IAR = 0.3$ . Diameter,  $d$ , of the first generation (largest) drop on the filament is plotted against  $IAR$ , in Fig. 3.10(b). With an increase of  $IAR$ , the diameter of the central drop,  $d$ , decreases gradually. The available length of the filament is smaller for larger  $IAR$ , and therefore, a lower liquid volume is trapped in the filament. Consequently, with the increase in  $IAR$ , the diameter of the first generation (largest) drop on the filament decreases.

### 3.2.3 Final aspect ratio

Effect of the final stretching height on the formation of BOAS is investigated using four different  $FAR$ , ranging from 2 to 3.5. The liquid bridge, formed by PEO1000 solution, in-between the two plates of  $D_P = 6$  mm, is stretched from  $IAR = 0.66$  at the stretching speed of 0.08 m/s. For all the cases of  $FAR$  tested, filament thinning is followed by a BOAS structure with multiple generations of drops. The evolution of filament and BOAS structure are presented with DST diagrams and HSST diagrams in Fig. 3.11. The minimum diameter,  $D_{min}$ , is tracked in space and time. When the liquid bridge is stretched, for all  $FAR$  tested, the position of the minimum diameter shifts in-between both ends of the filaments until  $t \lesssim 1$  s. The minimum diameter is then systematically located at the top end of the BOAS structure.

This minimum filament diameter is used to calculate the apparent extensional viscosity,  $\eta_E$ , and the Hencky strain,  $\epsilon_{min}$ , for various  $FAR$  values, as discussed in section 2.2.2.3. The results for obtained  $\eta_E$  are plotted against time,  $t$ , in Fig. 3.13(a), and against Hencky strain,  $\epsilon_{min}$ , in Fig. 3.13(b). For all  $FAR$  tested, the apparent extensional viscosity,  $\eta_E$ , increases with increasing  $t$ , and the Hencky strain,  $\epsilon_{min}$ . Yet, there is no significant difference in  $\eta_E$

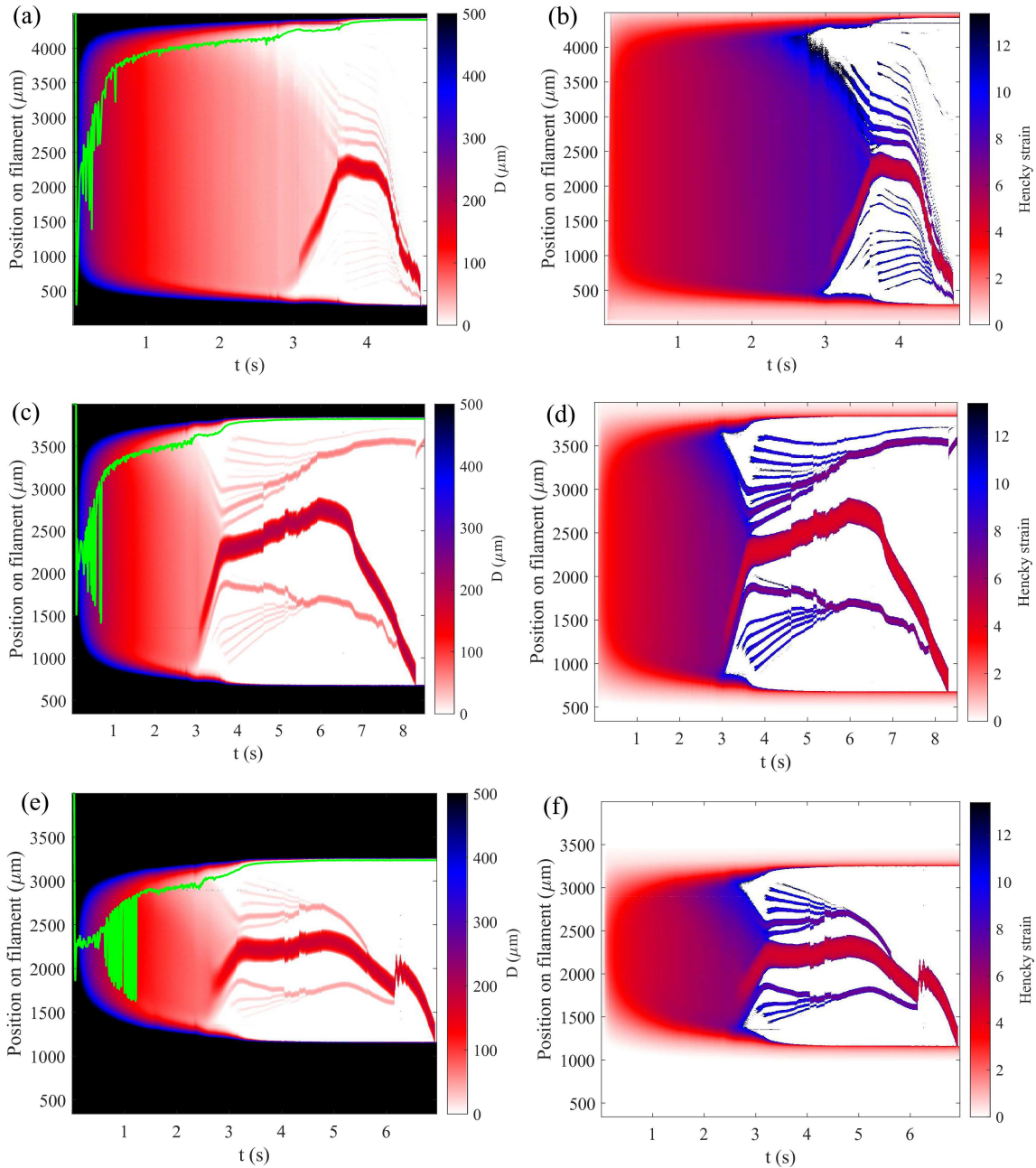


Fig. 3.9 Space-time diagrams for filament thinning and BOAS structure for PEO1000 solution with  $IAR = 0.3, 0.5$  and  $0.97$  mm.  $t = 0$  is when the separation of the CaBER plates starts. The DST and HSST diagrams start when the top plate reaches the final stretching height until merging of drops into solution pools. The green line represents the position of the minimum diameter of the filament. Multiple generations of drops can be identified by their diameters and colour code. The liquid bridge, formed in-between the two plates of  $D_P = 6$  mm, is stretched to  $FAR = 2$  at  $U = 0.08$  m/s. (a) DST for  $IAR = 0.3$  and (b) HSST for  $IAR = 0.3$ , (c) DST for  $IAR = 0.5$  and (d) HSST for  $IAR = 0.5$ , (e) DST  $IAR = 0.97$  and (f) HSST for  $IAR = 0.97$ . For (c) and (d), in the later stages, movement of coalesced drops towards the top solution pools may be due to pulling force on the drops by the top end of the filament. This movements of drops, especially in the upper part of the filament, towards the top solution pool, is not systematic. We observed that for higher  $IAR$ , i.e.  $IAR = 0.97$ , drops mostly fall downwards.

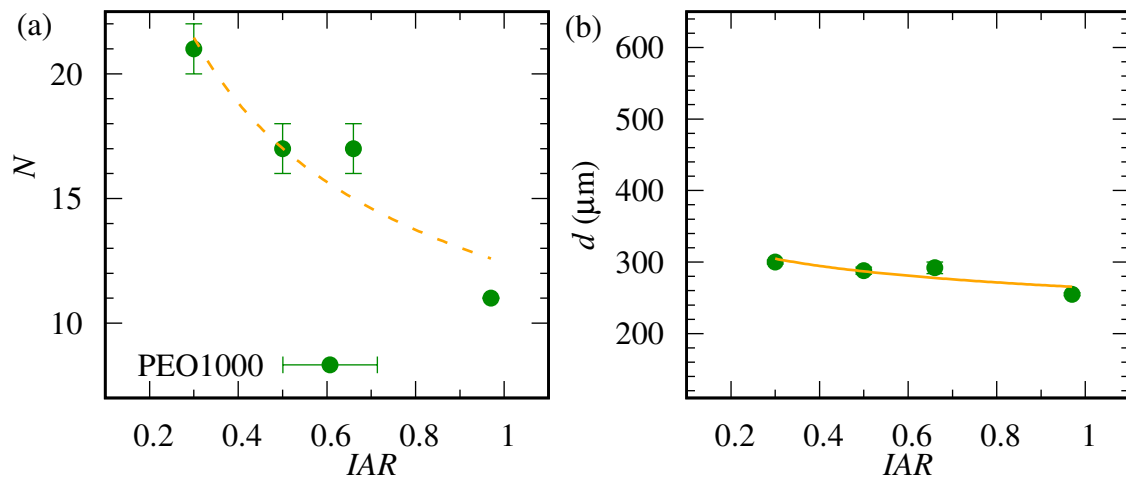


Fig. 3.10 Effect of initial aspect ratio,  $IAR$ , on maximum number of drops,  $N$ , and drop diameter,  $d$ , of the first generation (largest) drop in a BOAS structure. The liquid bridge, formed in-between the two plates of  $D_p = 6$  mm, is stretched to  $FAR = 2$  at  $U = 0.08$  m/s. PEO1000 solution is used as a test fluid. For  $IAR = 0.66$ , DST and HSST diagrams from Fig. 3.1 are considered. The error bars indicate the dispersion over five experiments. (a) The maximum number of drops,  $N$ , in a BOAS structure as a function of  $IAR$ . Only the drops (up to the third generation) with diameter,  $D > 25 \mu\text{m}$ , are considered. The dashed line is a trend line to serve as a guide to the eyes of a reader. (b) Diameter,  $d$ , of the first generation (largest) drop on the filament versus  $IAR$ . The solid line is a trend line as a guide to the eyes.

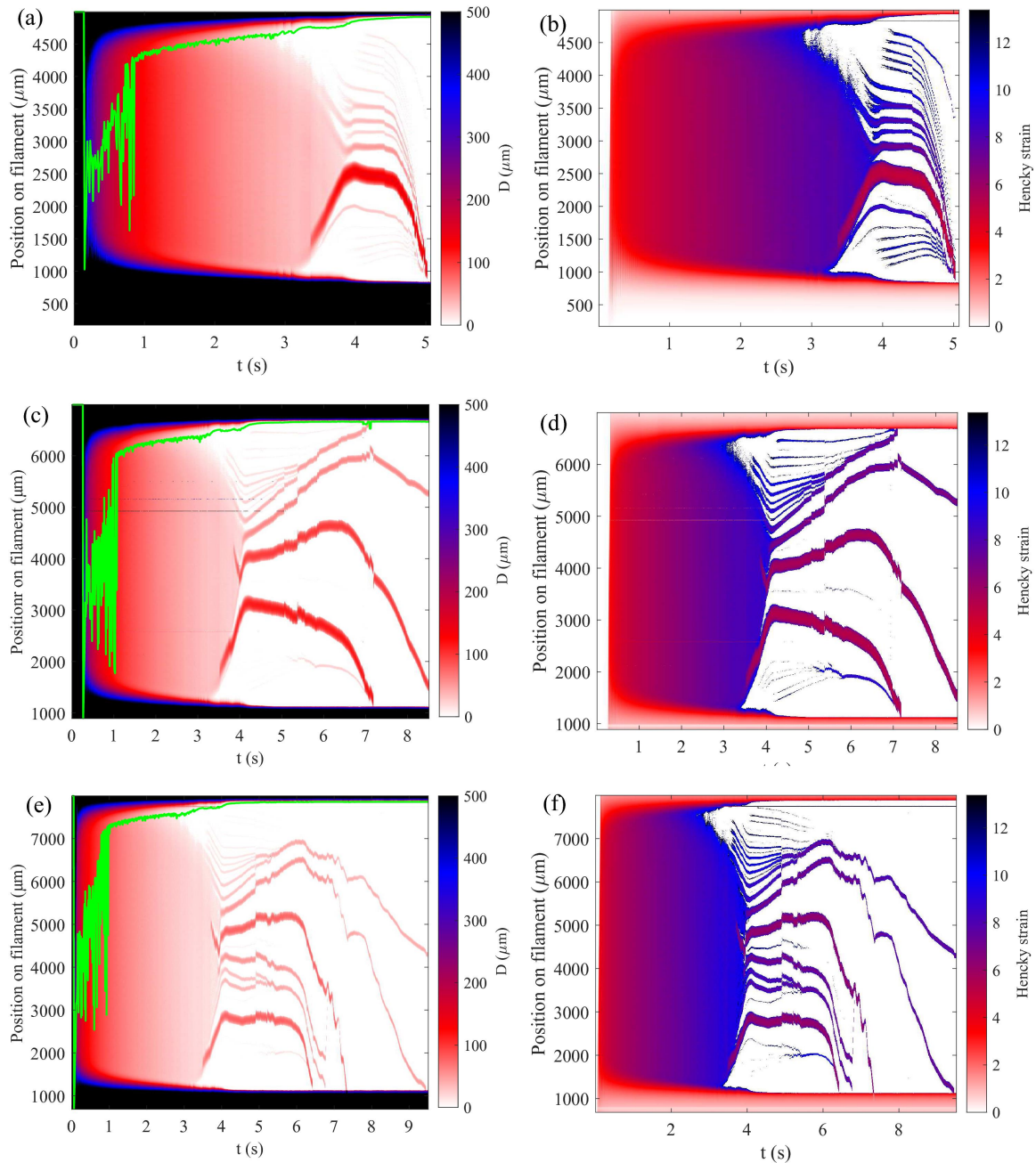


Fig. 3.11 Space-time diagrams for filament thinning and BOAS structure, at  $FAR = 2.5, 3$  and  $3.5$ , for PEO1000 solution.  $t = 0$  is when the separation of the CaBER plates starts. The DST and HSST diagrams are captured when the top plate reaches the final stretching height until merging of drops into solution pools. The green line represents the position of the minimum diameter of the filament. The liquid bridge, formed in-between the two plates of  $D_p = 6$  mm is stretched from  $IAR = 0.66$  at  $U = 0.08$  m/s. Multiple generations of drops can be identified by their diameters and colour code. (a) DST for  $FAR = 2.5$  and (b) HSST for  $FAR = 2.5$ , (c) DST for  $FAR = 3$  and (d) HSST for  $FAR = 3$ , (e) DST  $FAR = 3.5$  and (f) HSST for  $FAR = 3.5$ . For (c) and (d), in the later stages, movement of coalesced drops towards the top solution pools could be due to pulling force on the drops by the top end of the filament. This movements of drops, especially in the upper part of the filament, towards the top solution pool, is not systematic. We observed that for smaller  $FAR$ , i.e.  $FAR \leq 2.5$ , drops mostly fall downwards.

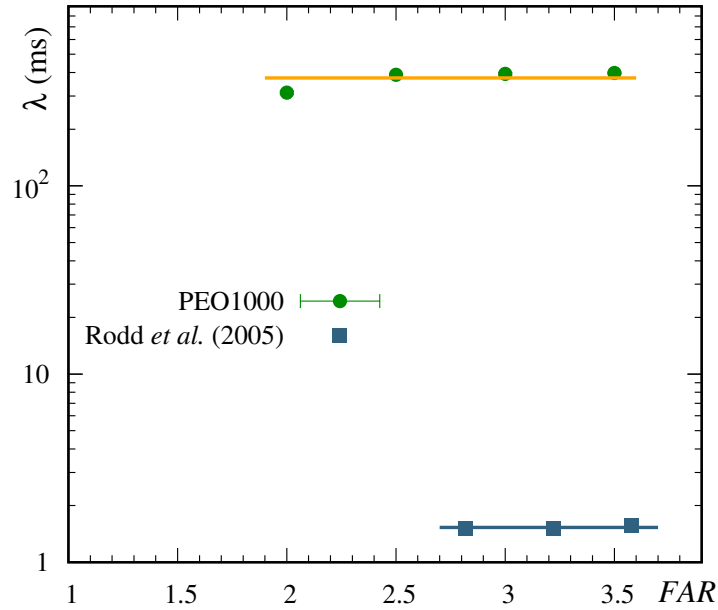


Fig. 3.12 Relaxation time as a function of final aspect ratio. The liquid bridge, formed in-between the two plates of  $D_P = 6$  mm is stretched with  $U = 0.08$  m/s from  $IAR = 0.66$  to different  $FAR$ . Results are compared with Rodd et al. [14] for aqueous PEO ( $M = 2 \times 10^6$  g/mol) solution with PEO mass fraction of 1000 *wppm*. The authors used an initial liquid bridge of  $D_P = 6$  mm and  $IAR = 1$ . Lines represent average relaxation times.

with time, for the increase in  $FAR$ . However, in the case of  $\eta_E$  versus  $\epsilon_{min}$ , larger apparent extensional viscosity,  $\eta_E$ , is observed for higher  $FAR$ . Later stages of the Hencky strain, i.e.  $\epsilon_{min} > 6$ , suggest higher strain hardening as  $FAR$  increases. For all  $FAR$ , two distinct regimes are observed for  $\eta_E$  against  $\epsilon_{min}$  at  $\epsilon_{min} = 6$ , as previously discussed. The apparent extensional viscosity continues to increase for all the cases of  $FAR$  studied, which indicates that the polymers are not in the fully stretched state. Larger final stretching height is required to achieve fully stretched polymer condition. Additionally, for all  $FAR$  tested, we calculated the relaxation time,  $\lambda$ , using the minimum diameter,  $D_{min}$ , as previously discussed in section 2.2. But, there is no significant change observed in  $\lambda$  for the increase in  $FAR$ , as shown in Fig. 3.12. Similar observations have been reported previously by Rodd et al. [14] (see Fig. 3.12) and Miller et al. [83] where in their experimental study, relaxation times remain unchanged with increasing  $FAR$ . Rodd et al. [14] used same plate diameter ( $D_P = 6$  mm) and PEO concentration (1000 *wppm*) as the present study. The authors obtained lower relaxation times due to lower molecular weight of PEO ( $M = 2 \times 10^6$  g/mol) used compared to the present study ( $M = 8 \times 10^6$  g/mol).

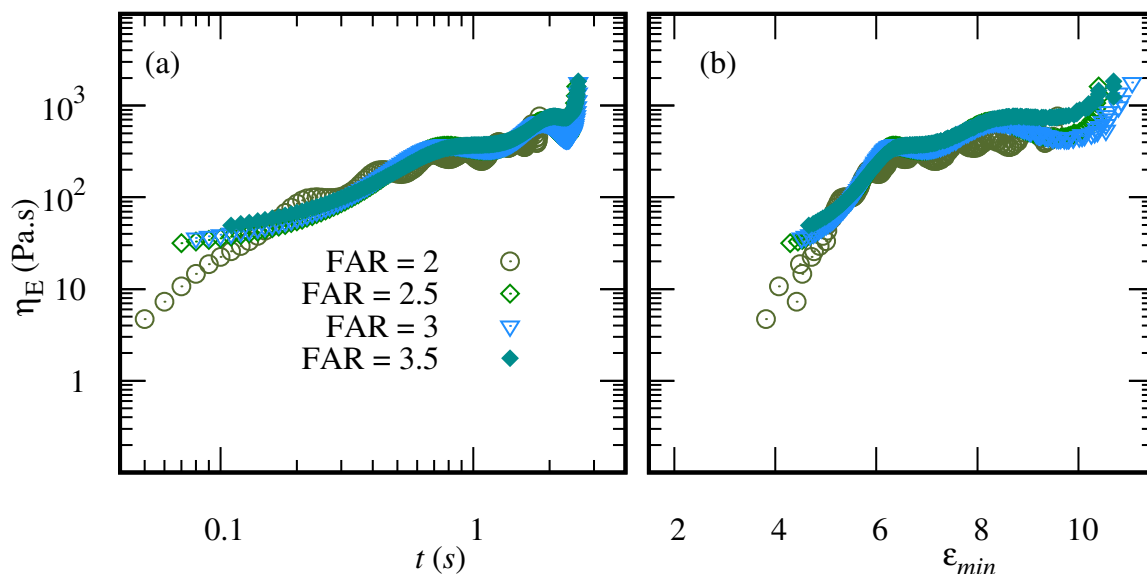


Fig. 3.13 Apparent extensional viscosity,  $\eta_E$ , for PEO1000, extracted using the minimum diameters obtained for different final aspect ratios,  $FAR$ . The liquid bridge, formed in-between the two plates of  $D_p = 6$  mm, is stretched from  $IAR = 0.66$  at  $U = 0.08$  m/s. The top plate is stretched from  $IAR = 0.66$  to various  $FAR$ , ranging from 2 to 3.5.  $t = 0$  is when the separation of the CaBER plates starts. (a) The apparent extensional viscosity,  $\eta_E$ , for different  $FAR$  as a function of time,  $t$ . (b)  $\eta_E$  versus Hencky strain,  $\epsilon_{min}$ .

In Fig. 3.11, the typical structure of a big central drop, accompanied by the smaller drops on either side, is only observed until  $FAR = 2.5$ . For  $FAR > 2.5$ , pinching occurs at different locations along the filament and multiple large (first generation) drops with a diameter greater than  $200 \mu\text{m}$  appear. Also, until  $FAR = 2.5$ , more number of drops can be seen above the big central drop than below. Typical features of any BOAS structure such as recoil, coalescence and drop migration can also be seen for all  $FAR$ . The maximum number of drops,  $N$ , in a BOAS structure are plotted in Fig. 3.14(a), against  $FAR$ . Each green circle symbol represents an average over five experiments. Only the drops (up to the third generation) with diameter,  $D > 25 \mu\text{m}$ , are considered. The maximum number of drops in the BOAS structure increases with increasing  $FAR$ , as shown by the trend line. Thus, it can be concluded that the  $IAR$  and  $FAR$  cases studied have the opposite effect as the maximum number of drops in a BOAS structure decreases with increasing  $IAR$ . In the further analysis of DST and HSST, diameter,  $d$ , of the first generation drop on the filament (largest in case of multiple big drops), is measured and plotted against  $FAR$ , in Fig. 3.14(b). As  $FAR$  increases, as shown by the trend line, the average diameter,  $d$ , decreases gradually. After the necking, the amount of solution available in the filament increases with an increase of  $FAR$ . The larger average diameter,  $d$ , for  $FAR = 2$  can be attributed to the observation that there is only one large drop. In the

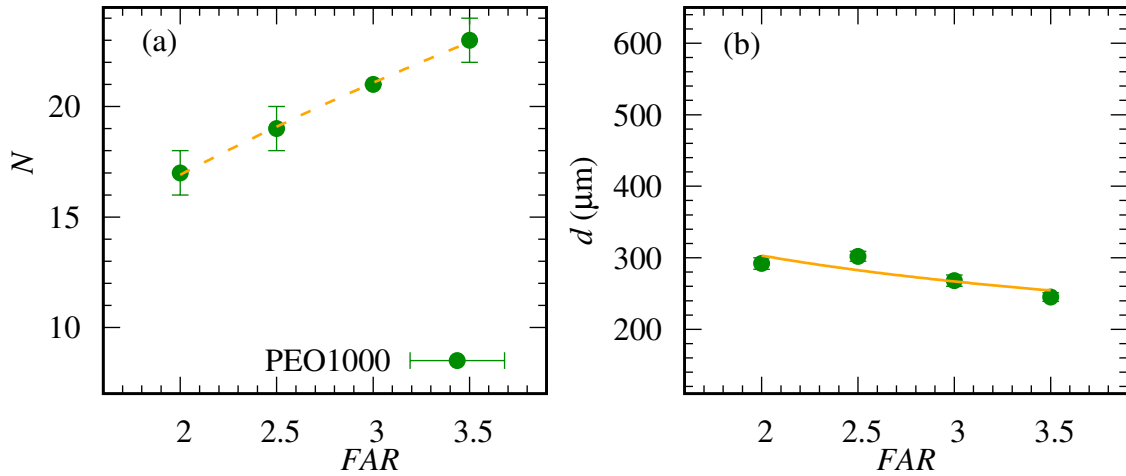


Fig. 3.14 Effect of final aspect ratio,  $FAR$ , on maximum number of drops,  $N$ , and drop diameter,  $d$ , of the first generation (largest) drops in a BOAS structure. PEO1000 solution is used as a test fluid. The liquid bridge, formed in-between the two plates of  $D_P = 6$  mm, is stretched from  $IAR = 0.66$  at  $U = 0.08$  m/s. The top plate is stretched from  $IAR = 0.66$  to various  $FAR$ , ranging from 2 to 3.5. The error bars indicate the dispersion over five experiments. (a) The maximum number,  $N$ , of drops in a BOAS structure as a function of  $FAR$ . Only the drops (up to the third generation) with diameter,  $D > 25$   $\mu\text{m}$ , are considered. The dashed line is a trend line to serve as a guide to the eyes of a reader. (b) Diameter,  $d$ , of the first generation (largest) drop on the filament versus  $FAR$ . The solid line is a trend line as a guide to the eyes.

case of multiple drops ( $FAR \geq 3$ ), the solution available after necking is distributed into three or more large drops. Therefore, for  $FAR \geq 3$ , the drops are observed with a smaller average diameter,  $d$ .

### 3.2.4 Stretching speed

To understand effect of the stretching speed,  $U$ , on the BOAS structure,  $U$  is varied from 0.008 to 0.2 m/s. The liquid bridge, formed by PEO1000 solution, in-between the two plates of  $D_P = 6$  mm, is stretched from  $IAR = 0.66$  to  $FAR = 2$ , with different speeds. For all the stretching speeds tested, we observed filament thinning and multiple generations of drops in a BOAS structure. DST and HSST diagrams are constructed but these diagrams are not reported here as there is no significant difference from the previous diagrams at  $U = 0.08$  m/s (see Fig. 3.1). These DST diagrams and the HSST diagrams are analysed. The maximum number of drops,  $N$ , in the BOAS structure is measured and plotted, against Weissenberg

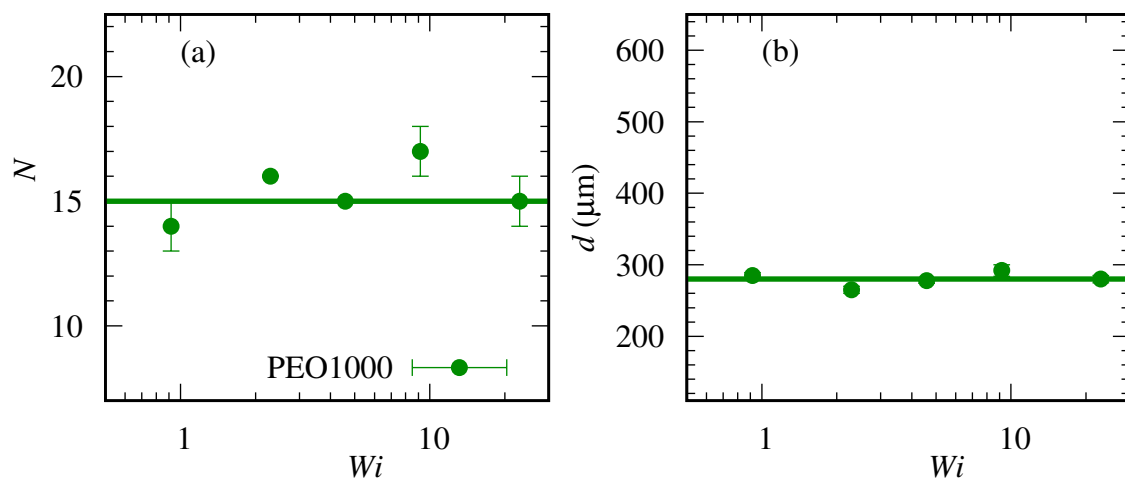


Fig. 3.15 Effect of Weissenberg number on maximum number of drops,  $N$ , and drop diameter,  $d$ , of the first generation (largest) drop in a BOAS structure. PEO1000 solution is used as a test fluid. The liquid bridge, formed in-between the two plates of  $D_p = 6$  mm, is stretched from  $IAR = 0.66$  to  $FAR = 2$ . The error bars indicate the dispersion over five measurements. (a) The maximum number,  $N$ , of drops in a BOAS structure as a function of  $Wi$ . Only the drops (up to the third generation) with diameter,  $D > 25 \mu\text{m}$ , are considered. The thick green line represents the average number of drops,  $N$ , for different  $Wi$ . (b) Diameter,  $d$ , of the first generation (largest) drop on the filament versus  $Wi$ . The thick green line represents the average diameter,  $d$ , for different  $Wi$ .

number,  $Wi$ , in Fig. 3.15(a) and (b). The Weissenberg number [12] can be defined as:

$$Wi = \frac{\lambda U}{R_p}. \quad (3.1)$$

For  $U$  ranging from 0.008 to 0.2 m/s,  $Wi$  varies from 0.92 to 22.93, respectively, for PEO1000. Only the drops (up to the third generation) with diameter,  $D > 25 \mu\text{m}$  are considered. No conclusive trend can be established for the maximum number of drops with a variation of  $Wi$  and an average of  $N$  is found to be 15. Also, the results obtained for the diameter,  $d$ , of the first generation drop on the filament are plotted, against  $Wi$  in Fig. 3.15(b). Each symbol represents the average over five experiments. There is no significant change in  $d$  with a variation of  $Wi$  and the average value of  $d$  is found to be  $280 \pm 5 \mu\text{m}$ . Hence, it can be concluded that in the tested range of the stretching speed, there is no significant influence of the Weissenberg numbers on the drop diameters and the maximum number of drops measured in the BOAS structure.

### 3.3 Partial conclusion

In conclusion, our DST and HSST diagrams quantify numbers and diameters of drops of a viscoelastic filament in space and time. From the diagrams, it is possible to extract the filament height and diameter at any time during the thinning as well as BOAS dynamics. By testing the polymer solutions of various mass fractions, it is found that there is a robust configuration of the drops on the filament with a large central drop accompanied by smaller drops on both sides. The diagrams also quantify filament thinning, drop migration, coalescence and draining, together with the position of the minimum diameter. As the filament (along with drops) is pulled towards the location of coalescence, the space-time diagrams allow us to show the systematic movement of drops in the direction of coalescence. In printing, these space-time diagrams can be used to track the diameter, number and fall of the drops on either donor or acceptor surface. In the present study, we observed that drops often fall into the bottom solution pool (donor surface). Hence, there is no risk of contamination of the top plate (substrate surface) and thus, no degradation of printing quality. Interestingly, the size of the first generation (largest) drop remains constant even after changing the PEO mass fraction. During a BOAS instability with multi-generation of drops, the maximum number of drops,  $N$ , in the BOAS structure grows with  $De$ , and this increasing trend for  $N$  can be predicted by using a power law scaling.

The drop dynamics in a BOAS instability are studied by varying different stretching parameters, to understand their effect on the diameter of the first generation drop and the number of drops in the BOAS structure. When the plate diameter is increased, the diameter of the first generation of drop and the number of drops increase. However, the average diameter of the first generation of drop remains constant with increasing  $w_{PEO}$ , for all three diameters investigated. The increase in the number of drops with the plate diameter can be attributed to the larger filament length available for the iterated instability. Furthermore, the initial and final aspect ratios have the opposite effect on the number of drops in a BOAS structure. The number of drops,  $N$ , decreases with increasing  $IAR$ , while  $N$  increases with an increasing  $FAR$ . With the same geometric parameters, the stretching speed seems to have no effect on the drop dynamics, within the range of the speeds studied.

In 3D lithography, 3D microstructures (polymer wires, needles, pillars, cones, or microspheres) are manufactured and a BOAS structure is desirable to produce a polymer wire with beads. Hence, high polymer mass fraction, larger surface diameter as well as larger final stretching height along with a smaller initial stretching height of the liquid bridge should be preferred to maximise the number of drops in a BOAS structure. However, in printing, the formation of beads on a string is an undesirable effect. Due to drops, the quality of the print

can get affected. Hence, smaller sizes and fewer drops are expected. Therefore, low polymer mass fraction solutions should be used to minimise the number of drops. Furthermore, smaller surface diameter, larger initial stretching height and smaller final stretching height for the liquid bridge should be selected to reduce the number of drops.

# Chapter 4

## Liquid transfer

### Contents

---

<b>4.1</b>	<b>Experimental results and discussion</b>	<b>115</b>
4.1.1	Polymer mass fraction	115
4.1.2	Geometrical parameters	118
4.1.2.1	Plate diameter	118
4.1.2.2	Initial aspect ratio	120
4.1.2.3	Final aspect ratio	123
4.1.3	Stretching speed	125
4.1.4	Initial bridge shape	127
<b>4.2</b>	<b>Partial conclusion</b>	<b>130</b>

---

In this chapter, experimental results obtained for the liquid transfer of Newtonian and viscoelastic solutions are presented. We quantify liquid transfer for an upward stretching of a liquid bridge having pinned contact lines, as shown in Fig. 2.9. However, this liquid transfer from one surface (donor) to another surface (accepter) is a complex phenomenon. Gravity, solution properties (capillarity, viscosity and elasticity), geometrical and stretching properties, along with contact surface properties (material, roughness) affect the amount of liquid transferred to the accepter surface. In the present study, to avoid complexities introduced by the surface properties, a similar type of plate material (stainless steel) for both plates is used. Additionally, in our experiments, we tracked the liquid contact lines on the CaBER plates. We observed that the contact lines are pinned from the beginning of the stretching of the liquid bridge until the end of the liquid transfer. This observation has been previously demonstrated by Qian and Breuer [115], where the authors reported pinned contact lines for a cylindrical rod (similar to CaBER plate). Moreover, the geometry of the capillary bridge is considered axisymmetric, that further simplifies the analysis of our experimental system.

A relevant parameter, called transfer ratio,  $TR$ , is defined (similar to [40, 103, 106, 112]) as a ratio of the volume of the liquid transferred to the moving plate (accepter), to the total volume,  $V$ , of the liquid between both plates, see Eq. 4.1. As shown in Fig. 2.9(c), the total volume,  $V$ , is the sum of the volume of liquid transferred to the top plate,  $V_T$ , and the volume of liquid left on the bottom plate,  $V_B$ .

$$TR = \frac{V_T}{V} = \frac{V_T}{V_T + V_B} \quad (4.1)$$

In printing, inks can contain polymers and exhibit Newtonian or viscoelastic liquid properties. As previously discussed in chapter 1, for a stretched viscoelastic liquid bridge, effect of polymer mass fraction on the liquid transfer had not been reported in the past. Hence, in this chapter, the liquid transfer will be investigated by varying the mass fraction of PEO in the aqueous PEO and PEG+PEO solutions. For Newtonian liquids, a smaller  $TR$  for larger plate diameters with pinned contact lines was reported by Zhang et al. [100]. Numerical simulations performed by Huang et al. [106] showed a decrease in  $TR$  with increasing  $IAR$  for moving contact lines. With increasing the stretching speed, larger volume of Newtonian liquid was transferred to a top plate with moving contact lines [102, 103, 106] and pinned contact lines [100]. Also, similar behaviour had been documented for viscoelastic solutions in gravure plates [42, 43]. Here, we explore effects of  $D_p$ ,  $FAR$  and  $U$  on liquid transfer with pinned liquid contact lines. Finally, the influence of initial liquid bridge shape will be explored and reported by varying the volume of the solution introduced in between the plates.

## 4.1 Experimental results and discussion

In this section, results obtained for effects of the polymer mass fraction, geometrical properties (plate diameter, initial aspect ratio, final aspect ratio), stretching speed and initial bridge shape on the liquid transfer are discussed.

### 4.1.1 Polymer mass fraction

Experiments are performed using water, PEG20, PEO and PEG+PEO solutions. As discussed in chapter 2, PEO mass fraction is varied from 100 to 2000 wppm. A liquid bridge, having volume  $56 \mu\text{l}$ , is formed in-between the two plates ( $D_p = 6 \text{ mm}$ ) with  $IAR = 0.66$ . Then, the liquid bridge is stretched at  $U = 0.08 \text{ m/s}$  until  $FAR = 2$ . The results obtained are presented in Fig. 4.1. For both the PEO and PEG+PEO solutions, the liquid transferred to the top plate decreases with an increase in  $w_{PEO}$ . The same can be confirmed from the inset photographs. A large difference in sizes of the top and bottom solution pools for PEO2000 solution compared to water can be observed.

Typically, for a viscoelastic liquid bridge, the liquid transfer occurs in two stages. In the first stage, when the liquid bridge is stretched, based on the geometrical parameters, an initial liquid transfer occurs from the bottom plate to the top plate. For  $D_p = 6 \text{ mm}$ , the gravitational forces play a significant role in the liquid transfer as  $Bo > 1$ , see Tab. 2.3. In this case, the initial asymmetry (sagging) decides the primary liquid distribution along the stretched liquid bridge. Hence, when the liquid bridge is stretched, initially a larger bottom solution pool is formed compared to the top solution pool. However, these solution pools are formed along with a filament that plays a significant role in liquid transfer. The second stage of liquid transfer takes place from the top to the bottom solution pool due to gravitational drainage through the filament. As previously observed in Fig. 2.5, with increasing  $w_{PEO}$ , the filament lasts longer and the breakup of the liquid bridge gets delayed. Hence, there is more time for the gravity-driven drainage and more liquid is transferred from the top to bottom solution pool. In the dilute regime, i.e.  $w_{PEO} \approx 100 \text{ wppm}$ , for both PEO and PEG+PEO solutions, the filament breakups early. Hence, there is less time available for the liquid transfer from the top to bottom solution pool. Therefore, in the dilute regime, the viscoelastic fluids nearly reproduce the response of PEG20. Finally, above dilute regime ( $w_{PEO} > w^*$ ), with increasing  $w_{PEO}$ , a combined effect of both stages results in a smaller volume of liquid transferred to the top plate. For Newtonian solutions, no filaments are observed. Hence, the liquid

transfer occurs in the first stage depending on the gravitational parameters. Effect of these gravitational parameters is discussed in the following sections.

Additionally, as shown in Fig. 2.5, above the dilute regime, with increasing  $w_{PEO}$ , the filament lasts longer for the PEG+PEO solutions than for the PEO solutions. Hence, more liquid is transferred from the top to bottom solution pool through the filament. Therefore, for the PEG+PEO solutions, lower values of  $TR$  are observed, because of the higher gravity-driven drainage. The change in  $TR$  with  $w_{PEO}$  is tracked using power law fits for both the PEO and PEG+PEO solutions. The larger exponent of the fit for the PEG+PEO solutions than the PEO solutions suggests that effect of change in  $w_{PEO}$  is higher for the PEG+PEO solutions. As already discussed, with increase in  $w_{PEO}$ , filament lasts longer for the PEG+PEO solutions than for the PEO solutions. This allows more time for the liquid transfer from top to bottom solution pool that leads to smaller values of  $TR$  for the PEG+PEO solutions.

Furthermore, for PEO and PEG+PEO solutions,  $TR$  is plotted as a function of Deborah number, as shown in Fig. 4.1(d). For both solutions,  $TR$  decreases with increasing  $De$ . Similar behaviour was observed numerically by Lee et al. [43], see Fig. 1.21, where the authors found that liquid transferred to the top plate decreases with increase in  $De$ . However, these results were obtained for a combination of gravure cell-flat plate. In our study, we have covered a wide range of  $De$  and a power law is used to capture the variation of  $TR$  with  $De$ . This relationship between  $TR$  and  $De$  through the power law regression has been established for the first time. Again, higher exponent for the fit is observed for PEG+PEO solution than PEO solution.

Hence, in printing, increase in polymer mass fraction of viscoelastic inks leads to a lower liquid transfer to the acceptor surface (top plate). Also, for the viscoelastic solutions studied, it is important to recall that the filament thinning leads to formation of a BOAS structure. This process is tracked by using the space-time diagrams as demonstrated in the previous chapter. It is observed that when the filament breakup occurs, the drops systematically fall downwards towards the donor surface (bottom plate). Hence, the BOAS structure does not affect the quality of the printing.

**Numerical results for liquid transfer** Once the solution pools are formed in our numerical simulations (section 2.4), solution pool heights ( $h_0$ ) on both plates are measured to calculate solution pool volumes by using the "spherical drop" method:  $V = \frac{1}{6}\pi h_0(3R_p^2 + h_0^2)$ . Then, transfer ratio is calculated using Eq. 4.1. For the numerical simulations, we consider all meshes for PEG20 and PEG20PEO1000 to calculate average  $TR$ , see Tab. 4.1. Experimental and numerical  $TR$  are in good agreement with each other for Newtonian PEG20 solution, as shown in Fig. 4.1. However, for viscoelastic PEG20PEO1000 solution, we were only

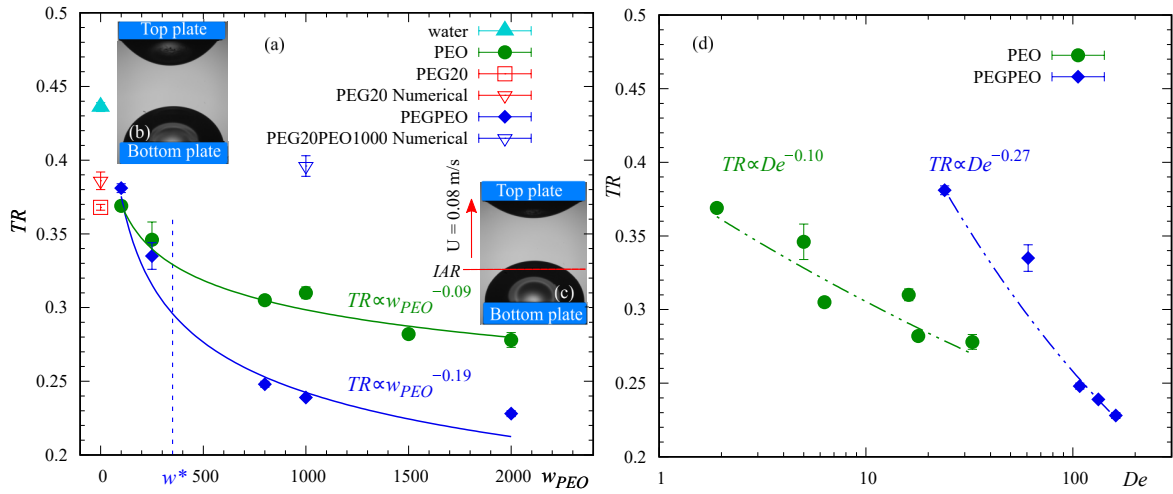


Fig. 4.1 Effect of  $w_{PEO}$  and  $De$  on liquid transfer. The liquid bridge, formed in-between the two plates having  $D_P = 6$  mm and volume  $56 \mu\text{l}$ , is stretched from  $IAR = 0.66$  to  $FAR = 2$  at  $U = 0.08$  m/s. The error bars indicate the dispersion over five tests. (a)  $TR$  as a function of  $w_{PEO}$  (wppm). The inserts are photographs for (b) water and (c) PEO2000 depicting the solution pools on the bottom and top plates after the filament breakup.  $IAR = 0.66$  is shown by a horizontal red line and the direction of the stretching is presented with a red arrow. Additionally, average  $TR$  for PEG20 and PEG20PEO1000 solutions (see Tab. 4.1) from the numerical simulations using *rheoTool* are compared. The green and blue lines are trend lines for the PEO and the PEG+PEO solutions, respectively. The vertical blue dashed line shows the critical mass fraction,  $w^*$ , of PEO, from a dilute to semi-concentrated regime. (d)  $TR$  as a function of Deborah number:  $De = \lambda / \sqrt{\rho D_P^3 / 8\sigma}$ . The lines represent power law fits with coefficient of determination of 0.85 and 0.94 for PEO and PEG+PEO solutions.

able to achieve the first stage of liquid transfer where geometrical parameters determine the volume of the solution pools formed. Therefore, in the numerical simulation, liquid transfer for PEG20PEO1000 solution occurs in a similar way to the Newtonian PEG20 solution because of the short-lived filament. In our simulations, we do not attain the *elasto-capillary* thinning and hence, we do not achieve the second stage of liquid transfer where gravitational drainage takes place from a top solution pool to a bottom solution pool through the filament. Hence, use of *rheoTool* is promising for liquid transfer of Newtonian fluids (as there is no gravitational draining through a filament) but for viscoelastic solutions, as discussed in the previous chapter, we need a higher resolution mesh to produce a persistent filament to enhance gravitational draining, as already explained in section 2.4.2.

Table 4.1 Comparison of numerical and experimental transfer ratios for PEG20 and PEG20PEO1000 solutions. In numerical simulations we used:  $D_p = 6$  mm,  $FAR = 2$  and  $Oh = 0.08$ . Experimental conditions are:  $D_p = 6$  mm,  $IAR = 0.66$ ,  $FAR = 2$  and  $U = 0.08$  m/s.

Solution	Numerical $TR$	Experimental $TR$
PEG20	$0.386 \pm 0.006$	$0.368 \pm 0.006$
PEG20PEO1000	$0.396 \pm 0.007$	$0.239 \pm 0.001$

## 4.1.2 Geometrical parameters

### 4.1.2.1 Plate diameter

Size of the plate diameter,  $D_p$ , is one of the important parameters for the liquid transfer. Depending upon  $D_p$ , Bond number,  $Bo = \rho g D_p^2 / 4\sigma$ , varies (from 0.66 to 2.63) and hence, liquid transfer can be influenced by gravity. Effect of  $D_p$  on the liquid transfer for Newtonian fluids has already been established by Zhang et al. [100]. However, we would like to explore effect of  $D_p$  and  $Bo$  for viscoelastic solutions. To understand influence of the plate diameter on  $TR$ , three plates diameters with  $D_p = 4, 6$  and  $8$  mm, are tested. All other geometrical parameters are kept constant. A liquid bridge, formed in-between the two plates is stretched from  $IAR = 0.66$  to  $FAR = 2$  at  $U = 0.08$  m/s. Liquid volume introduced varies from 16 to 133  $\mu$ l with the change in  $D_p$  from 4 to 8, respectively.

Initially, the experiments are performed using water, PEG20 and PEO1000. The results obtained for the liquid transfer with different plate diameters are plotted in Fig. 4.2(a). Each symbol represents the average over five experiments. For all three solutions tested,

$TR$  decreases with increasing  $D_p$ . A similar trend for water by Zhang et al. [100] is also represented. However, the difference in the results for water between the present study and by the authors is because of different geometrical and stretching parameters. The authors stretched liquid bridges having  $IAR = 2$  with a stretching speed of 0.006 m/s. Their stretching speed is lower than the stretching speed in the present study ( $U = 0.08$  m/s) and their  $IAR$  is higher than the present study ( $IAR = 0.66$ ). The combined effect of both parameters leads to lower values of  $TR$  for Zhang et al. [100] than the present study. The details of influence of both parameters on the liquid transfer are discussed later in this chapter.

Photographs of the stretched liquid bridge profiles (when the top plate reaches the final stretching height) for PEO1000 are presented in Fig. 4.2(b-d). With increasing plate radius, at fixed  $FAR$ , the final stretching height is increasing and as a result, the hydrostatic pressure difference between the top and bottom solution pool also increases. When the plate radius increases from 4 to 8 mm, the shape of the top solution pool gradually changes from convex to concave. The shape of the bottom solutions pool remains convex for all three plate diameters. When the shape of the top solution pool is concave, capillary pressure inside the top solution pool is lower compared to the bottom solution pool, but this phenomenon is dominated by hydrostatic pressure difference. As a result, in the early stages, the solution is pushed from the top solution pool towards the bottom solution pool. Hence, with increasing  $D_p$ , more solution is pushed towards the bottom solution pool from the top solution pool. Furthermore, with increasing  $D_p$ , the filament diameter and the filament thinning time increase, as shown in Fig. 3.7. Hence, the gravitational draining through the filament is enhanced by the larger plate diameter. As a result of this, more liquid is pushed from the top to bottom solution pool and lower values of  $TR$  are obtained.

Moreover, additional experiments are performed using PEO solutions for different plate diameters. Therefore,  $Bo$  varies from 0.66 to 2.63 for  $D_p$  ranging from 4 to 8 mm, respectively, and  $De$  varies from 1.2 to 60 (see Tab. 2.3). Results for  $TR$  are plotted against the Deborah number, as shown in 4.2(e). As previously discussed, for all three plate diameters and hence the Bond numbers,  $TR$  decreases with an increase in  $De$ . Furthermore, for smaller values of  $Bo$ , higher  $TR$  are obtained. For  $Bo > 1$ , gravitational forces overcome the capillary forces. Hence, for  $Bo > 1$ , the combined effect of gravity and delayed filament thinning (caused by increasing  $De$ ) leads to a decrease in liquid transfer to the top plate.  $TR > 0.5$  can be achieved with smaller values of  $Bo$  and  $D_p$ . However, the smallest plate diameter available in the present study is 4 mm. Hence, throughout our experimental study, we have not observed  $TR > 0.5$ . For each  $Bo$ , power law fits are used to capture the change in  $TR$  with  $De$ . With increasing  $Bo$ , larger values of the power law exponents are observed. These larger values of the exponents suggest that for higher  $Bo$ , effect of  $De$  on the liquid transfer increases.

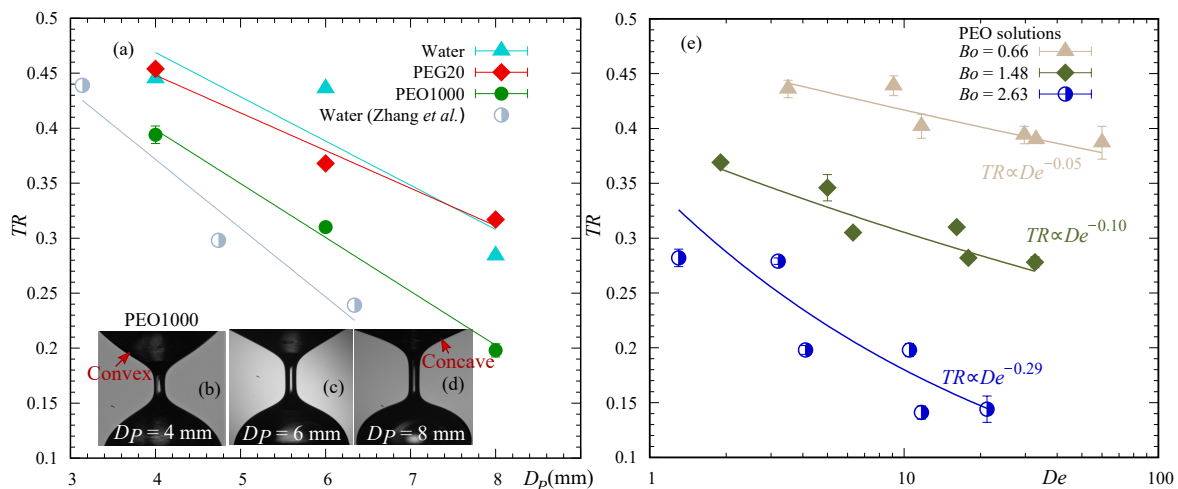


Fig. 4.2 Effect of plate diameter,  $D_p$ , on liquid transfer. The liquid bridge, formed in-between the two plates having  $IAR = 0.66$  is stretched to  $FAR = 2$  at  $U = 0.08$  m/s. The error bars indicate the dispersion over three to five tests. (a)  $TR$ , as a function of  $D_p$ . The results are compared with Zhang et al. [100] (see Fig. 1.18) where the authors varied plate diameters and stretched liquid bridges, formed with water, from  $IAR = 2$  at  $U = 0.006$  m/s. The solid lines represent trends for  $TR$  against  $D_p$ . Photographs (b-d) present liquid capillary bridges at  $t = 0.05$  s for PEO1000 for  $D_p = 4$ , 6 and 8 mm, respectively. The transition of the top solution pool from convex to concave shape is indicated by red arrows. (e)  $TR$  as a function of  $De$  for different  $Bo = \rho g D_p^2 / 4\sigma$  for PEO solutions (see Tab. 2.3).  $Bo$  is varied from 0.66 to 2.63 by increasing  $D_p$  from 4 to 8 mm.

In printing, to increase the amount of liquid transferred to the acceptor surface, smaller plate diameter and hence smaller initial liquid volume should be preferred. Influence of  $Bo$  on the viscoelastic liquid transfer is reported for the first time and its effect will be further discussed at the end of the chapter.

#### 4.1.2.2 Initial aspect ratio

Influence of the initial liquid bridge height,  $L_0$ , on the liquid transfer is investigated. Experiments are performed using PEG20 solution as a test fluid. The initial aspect ratio,  $IAR = L_0/R_p$ , is varied from 0.2 to 2, above which the instability of the initial capillary bridge is observed for PEG20 solution [65, 66]. Below  $IAR = 0.2$ , the liquid bridge can not be formed because of experimental limitations (pipette tip can not be inserted to form a liquid bridge). A liquid bridge, formed in-between the two plates having  $D_p = 4$  mm is stretched at  $U = 0.134$  m/s from different  $IAR$  to  $FAR = 4$ . To avoid effect of change in  $D_p$  on the liquid transfer, the different values of  $IAR$  are obtained by only varying  $L_0$ . The liquid volume is varied from 5 to 50  $\mu\text{l}$  with the change in  $IAR$  from 0.2 to 2, respectively.

The results obtained for  $TR$  are plotted against  $IAR$ , as shown in Fig. 4.3(a). Each symbol represents an average over five experiments. With increasing  $IAR$ ,  $TR$  decreases and this trend has been previously observed numerically for a Newtonian liquid by Huang et al. [106]. In their study, the contact line on the top plate was pinned and the contact line on the bottom plate was free to slip. However, in the present study, the contact lines on both plates are fixed and more number of data points are reported. According to Rodd et al. [14], for a static liquid bridge, in order to keep the initial configuration close to a cylindrical shape (without sagging),  $IAR \leq 1/\sqrt{Bo}$ . For the liquid bridge of PEG20 solution with  $D_p = 4$  mm and  $Bo = 0.70$ , this critical  $IAR$  is 1.19. Hence, in the present study, for  $IAR > 1.2$ , instabilities are caused by the imbalance between gravity and capillarity. With increasing  $IAR$ , gravitational forces overcome the capillary forces and axial sagging in the direction of gravity is observed. Therefore, the liquid bridge becomes non-cylindrical and bulged shaped closer to the bottom plate. Transition of the initial capillary bridge from the cylindrical shape to the non-cylindrical (bulged) shape due to increase in  $IAR$  can be seen in photographs presented in Fig. 4.3(a). Due to this change in the initial bridge shape, dynamics of the stretched liquid bridge are modified. For  $IAR \leq 0.5$ , when the top plate is stretched upwards, the liquid bridge breakup first occurs closer to the bottom solution pool, as shown by a green arrow in Fig. 4.3(b). Then, the breakup also occurs closer to the top solution pool and a detached drop is formed. This drop falls into the bottom solution pool. However, when the top plate is stretched upwards, for  $IAR > 0.5$ , the breakup point moves towards the top solution pool. Additionally, for  $IAR > 1.2$ , when the liquid bridge is stretched, the bulge shaped liquid (on the bottom plate) turns into the bottom solution pool. Hence, larger liquid volume is enclosed below this breakup point. Furthermore, with increase in  $IAR$ , the top solution pool curvature changes from convex to a concave shape. This change in the curvature (from convex to a concave shape) suggests that the liquid is pushed away from the top solution pool towards the bottom solution pool. Therefore, with increasing  $IAR$ , smaller solution pool is formed on the top plate and the amount of liquid transferred to the top plate decreases. From the printing point of view, if the initial distance between the donor and acceptor surface is larger, then less liquid will be transferred to the acceptor surface. Hence, to maximise the liquid transfer to the donor surface,  $IAR$  should be smaller than the critical  $IAR$ . Also, care should be taken for small  $IAR$ , as the detached drop formed can be hazardous if inhaled.

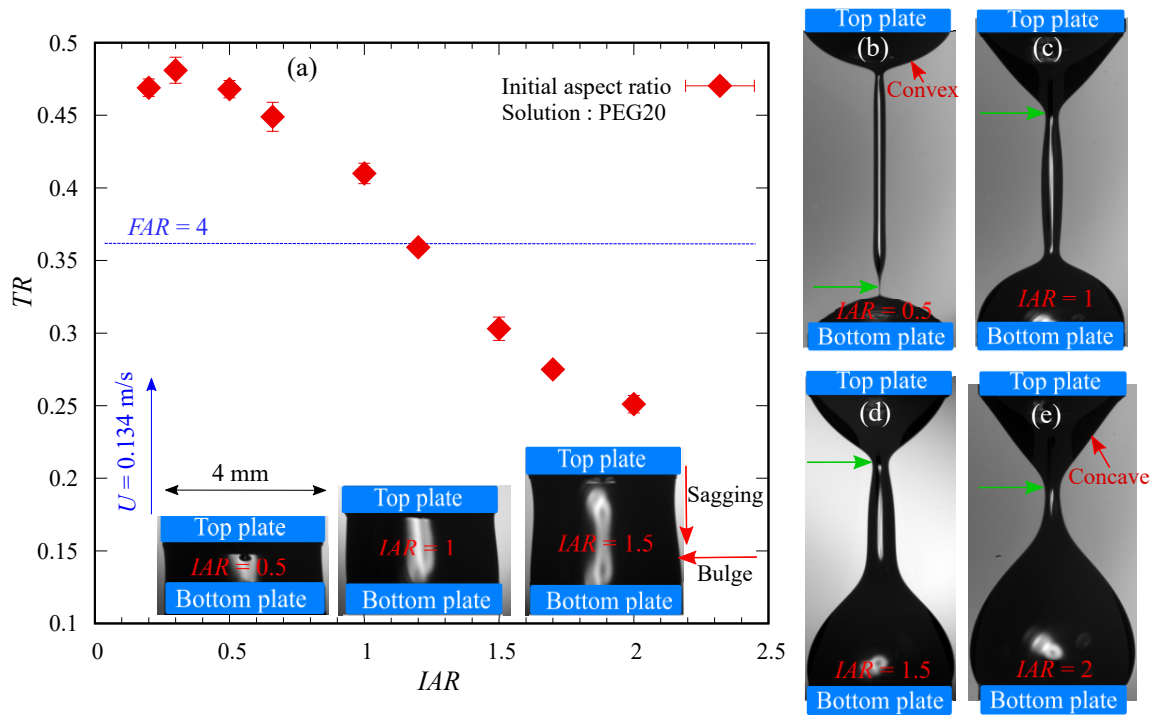


Fig. 4.3 Effect of initial liquid bridge height on the liquid transfer. The liquid bridge, formed in-between the two plates having  $D_p = 4 \text{ mm}$  is stretched at  $U = 0.134 \text{ m/s}$  with different  $IAR$  to  $FAR = 4$ . The experiments are conducted using PEG20 solution. Liquid volume is varied from 5 to 50  $\mu\text{l}$  with the change in  $IAR$  from 0.2 to 2, respectively. The error bars indicate the dispersion over five tests. (a)  $TR$ , as a function of  $IAR$ , for PEG20. Inset photographs depict the initial capillary bridge for  $IAR = 0.5$ , 1 and 1.5. For  $IAR = 1.5$ , sagging of the initial liquid bridge along with a bulged shape is shown. The stretching direction of the bridge is represented by the vertical blue arrow and  $FAR = 4$  is represented by a horizontal blue line. Photographs (b-e) present the stretched liquid bridge before the breakup for  $IAR$  from 0.5 to 2, respectively. The green arrows indicate the breakup point on the stretched liquid bridge. Transition of the top solution pool from a convex to a concave shape is marked with the red arrows.

### 4.1.2.3 Final aspect ratio

Effect of the final stretching height on the liquid transfer is explored by varying the final aspect ratio,  $FAR$ , from 2 to 6. The minimum value of  $FAR$  is limited due to the least value of the stretching height required for breaking of the capillary bridge. The maximum value of  $FAR$  is limited by the experimental constraints (lack of space in the experimental setup to move the camera to capture the breakup of liquid bridge formed with higher  $FAR$ ). Two different experimental studies are carried out for the PEG20 and PEO solutions. A liquid bridge, formed in-between the two plates having  $D_p = 4$  mm and volume  $16 \mu\text{l}$  is stretched from  $IAR = 0.66$  to various  $FAR$  ranging from 2 to 6. For the PEG20 solution,  $U = 0.134$  m/s and for the PEO solutions,  $U = 0.08$  m/s.

**PEG20 solution** Change in  $TR$  with  $FAR$ , for PEG20 solution, is plotted in Fig. 4.4(a). Each point represents the average over five experiments.  $TR$  decreases with increasing  $FAR$ . Fig. 4.4(b), (c) and (d) illustrate the different shapes of the capillary bridges formed, just before their breakup, when the top plate is at  $FAR = 2, 4,$  and  $6,$  respectively. For  $FAR = 6,$  the breakup occurs at the top of the bridge, close to the top solution pool, compared to the breakup at the middle of the bridge, for  $FAR = 2.$  This further suggests that, after breakup, the liquid transferred to both plates will be nearly the same for  $FAR = 2.$  But, with increasing  $FAR,$  as the breakup point moves closer to the top solution pool, more liquid volume will be enclosed below this breakup point and a larger solution pool is formed on the bottom plate. Hence, with increasing final stretching height, less liquid will be transferred to the top plate.

**PEO solutions** Moreover, additional experiments are performed using PEO solutions for  $FAR$  2, 4 and 6. Results for  $TR,$  using different values of  $FAR,$  are plotted against  $w_{PEO},$  as shown in Fig. 4.5. Each data point represents the average over five experiments. As previously observed in section 4.1.1, for all  $FAR,$  with increasing  $w_{PEO},$   $TR$  decreases. Additionally, for the same value of  $w_{PEO},$  it can be noted that smaller values of  $TR$  are obtained for larger  $FAR.$  This behaviour is more significant for higher values of  $w_{PEO},$  than in the dilute regime. As discussed in the previous section, the location of the necking point, on the liquid bridge, varies with the final stretching height. Length of the filament increases with increasing  $FAR$  and hence, larger liquid volume is enclosed below this breakup point. Also, with increasing  $w_{PEO},$  the filament lasts longer. Therefore, more liquid is drained from the top solution pool to the bottom solution pool. At higher  $FAR$  and  $w_{PEO},$  this combined effect of the larger liquid volume enclosed and the enhanced drainage leads to larger values of the solution pools formed on the bottom plate. Therefore, smaller values of  $TR$  are observed for  $FAR = 6.$  Power law fits are used, for each  $FAR,$  to capture the variation of  $TR$  with  $w_{PEO}.$

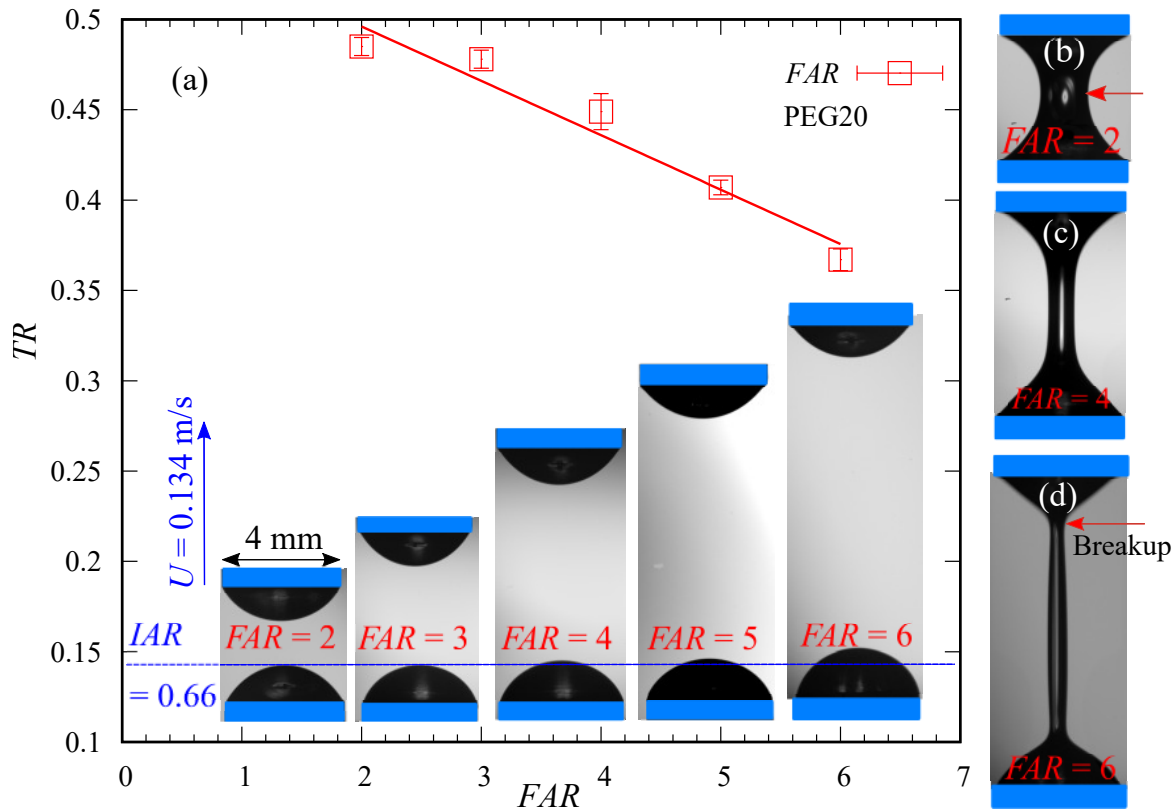


Fig. 4.4 (a)  $TR$ , as a function of  $FAR$ , for PEG20 solution. The insets are photographs illustrating the solution pools formed on the plates, for different  $FAR$ . The liquid bridge, formed in-between the two plates having  $D_p = 4 \text{ mm}$  and volume  $16 \mu\text{l}$  is stretched from  $IAR = 0.66$  to  $FAR = 2$  to  $6$ , at  $U = 0.134 \text{ m/s}$ . The horizontal blue line shows the initial stretching height. The blue arrow indicates the stretching direction of the initial capillary bridge. The error bars represent the dispersion over five experiments and the red line is a guide to the eye. Photographs (b), (c) and (d) display stretched liquid capillary bridges, just before their breakup, at  $FAR = 2, 4$  and  $6$ , respectively.

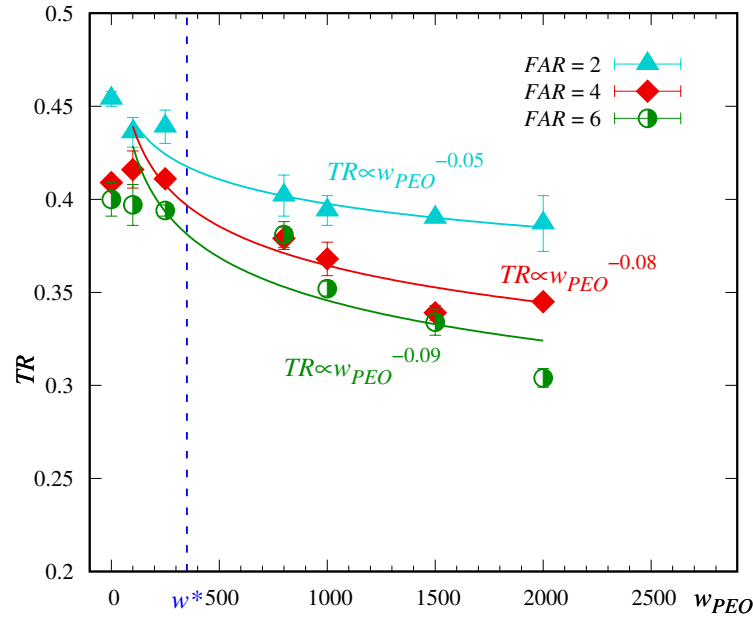


Fig. 4.5  $TR$  as a function of  $w_{PEO}$  for different  $FAR$ . The liquid bridge, formed in-between the two plates having  $D_P = 4$  mm and volume  $16 \mu\text{l}$  is stretched from  $IAR = 0.66$  to different  $FAR$  (2, 4 and 6) at  $U = 0.08$  m/s. The error bars indicate the dispersion over five tests. The blue, red and green lines represent power law fits, for the PEO solutions, with  $FAR = 2, 4$  and 6, respectively. The vertical dashed line shows the critical mass fraction,  $w^*$ , of PEO.

With increasing  $FAR$ , the value of the power law exponent increases. From printing point of view, if the final stretching height between the donor and acceptor surface is larger, less liquid will be transferred to the donor surface. Hence, to maximise the liquid transfer to the donor surface, a smaller final stretching height is required.

### 4.1.3 Stretching speed

Typical extensional stretching (printing) speeds,  $U$ , associated with roll separation are estimated to be around 0.01 to 0.1 m/s [20, 104]. In this section, influence of the stretching speed on the liquid transfer is investigated, by varying  $U$  from 0.001 to 0.134 m/s. These are the minimum and maximum values of  $U$  that can be achieved with the current experimental setup. A liquid bridge, formed in-between the two plates having  $D_P = 4$  mm and volume  $16 \mu\text{l}$  is stretched from  $IAR = 0.66$  to  $FAR = 2$ . PEO1000 and PEG20 solutions are used as test fluids. The results obtained are presented in Fig. 4.6(a). For both PEG20 and PEO1000 solutions, with increasing  $U$ ,  $TR$  increases. The increase in liquid transfer to the top plate with increasing stretching speed is already well established for Newtonian

fluids [100, 102, 103, 106, 113]. However, in our study, we found the similar trend for the viscoelastic fluid. The results obtained are compared with Zhang et al. [100]. It is important to recall that the authors have pinned contact lines similar to the present study. We have recalculated  $TR$  using their results and the similar trend of increase in  $TR$  with increasing  $U$  is found. For the authors, a liquid bridge with  $D_p = 3.2$  mm,  $IAR = 2$  and initial volume introduced,  $V = 40 \mu\text{l}$ , is stretched at different speeds.  $IAR$  in their experiments is higher than the present study ( $IAR = 0.66$ ). As discussed in the previous section, higher values of  $IAR$  leads to smaller values of  $TR$ . However, irrespective of geometrical properties (pinned or moving contact lines), for both Newtonian and viscoelastic solutions, the liquid transferred to the top plate increases with increasing  $U$ .

For further analysis, values of  $U$  are used to calculate capillary numbers,  $Ca = \eta_0 U / \sigma$ . Higher stretching (printing) speeds would tend to enhance the importance of viscous forces relative to interfacial-tension (higher  $Ca$ ). The transfer ratios are plotted against  $Ca$ , as shown in Fig. 4.6(b). For both solutions,  $TR$  increases with increasing  $Ca$ . For all the values of  $Ca$ , linear regression is used to capture this trend. However, this trend is already well established for Newtonian fluids [40, 102, 103, 106]. Furthermore, the results are compared with experimental results by Chen et al. [40] and numerical simulation by Huang et al. [106]. Chen et al. [40] stretched a liquid bridge of glycerol, formed in between two similar (poly ethyl methacrylate) surfaces, with increasing  $U$ . We have calculated values of  $Ca$  from their data and as expected,  $TR$  increases with increasing  $Ca$ . In their numerical work, Huang et al. [106] observed the similar trend (see Fig. 1.19).

The change in  $TR$  with  $Ca$  can be distinguished in three regimes. These regimes have been previously described for stretching speed [40, 102, 103] and capillary numbers [106]. For low values of  $Ca$  i.e.  $Ca < 0.01$ , liquid transfer is determined by wetting properties of the surface and capillary forces. This regime is called a quasi-static regime and in this regime,  $TR$  values remain constant. In our study, the curve also has a plateau when  $Ca < 0.01$ . Similar plateau for  $Ca < 0.01$  was observed by Chen et al. [40] and Huang et al. [106]. A transition regime is observed for  $0.01 < Ca < 1$ , where for a small increase in  $Ca$ ,  $TR$  values increase significantly. This behaviour indicates strong influence of viscous forces and stretching speeds over capillary forces, yet the detailed mechanism still remains unrevealed. In the present study, only  $TR$  values of PEG20 are observed in this regime. For PEO1000 solution,  $TR$  values are in the quasi-static regime only due to smaller values of  $\eta_0$  and experimental limitation of the stretching speed. A third regime called dynamic regime is expected for  $Ca > 1$ . However, in the present study, we could not achieve this regime as with our experimental setup, the maximum stretching speed of 0.134 m/s ( $Ca = 0.317$  for PEG20) could be achieved. In this regime, equal volume of solution pools are formed on the both

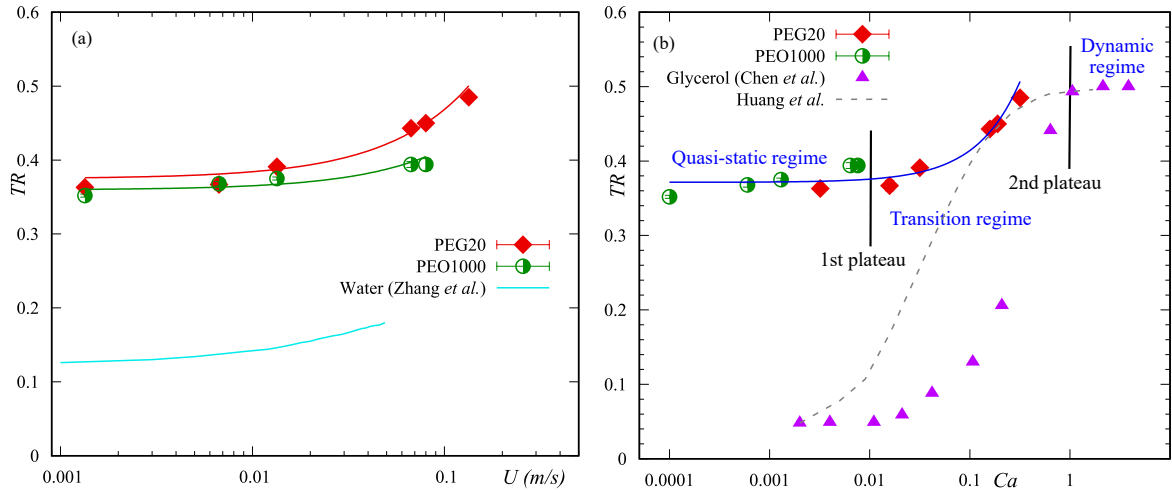


Fig. 4.6 Effect of stretching velocity and capillary number on the liquid transfer for PEG20 and PEO1000 solutions. The liquid bridge, formed in-between the two plates having  $D_P = 4$  mm and volume  $16 \mu\text{l}$  is stretched from  $IAR = 0.66$  to  $FAR = 2$ . The error bars exhibit the dispersion over five experiments. (a)  $TR$  as a function of  $U$ . The results are compared with Zhang et al. [100], with  $V = 40 \mu\text{l}$ ,  $IAR = 2$  and  $D_P = 3.2$  mm. (b)  $TR$  as a function of  $Ca$ . For both solutions, different values of  $Ca = \eta_0 U / \sigma$  are obtained by varying only  $U$  and by keeping solution properties constant. The blue line represents a linear trend line given as  $TR = 0.384Ca + 0.373$  and a coefficient of determination of 0.91. Results are compared with Huang et al. [106] and Chen et al. [40] who have moving contact lines and different values of the contact angles.

plates irrespective of the surface and liquid properties. Huang et al. [106] and Chen et al. [40] have found  $TR = 0.5$  in this regime. It is worth noting that both authors have moving contact lines. These three regimes have been previously defined only for moving contact lines and Newtonian fluids. However, in the present study, we have successfully demonstrated effect of  $U$  and  $Ca$  for both Newtonian and viscoelastic fluids for pinned contact lines. In printing, larger liquid transfer to the donor surface can be achieved with higher stretching speeds and  $Ca > 1$ .

#### 4.1.4 Initial bridge shape

By varying the volume of the liquid introduced in the initial capillary bridge, the shape of the bridge is controlled, and hence, the initial contact angles are modified. When 100% volume is introduced, a cylindrical shaped liquid bridge is created and this volume can be calculated as  $V = (\pi/4)D_P^2 L_0$ . Then, solution volumes introduced are varied from 50 to 125% of  $V$  to obtain different contact angles. For the cylindrical-shaped liquid bridge, an initial contact angle of  $90^\circ$  is observed, as shown in Fig. 4.7(b). The contact angles less than  $90^\circ$ , Fig.

4.7(a), and the contact angles greater than  $90^\circ$ , Fig. 4.7(d), are obtained for the volumes less than or greater than 100% of the cylindrical shaped volume, respectively. For the volumes, less than 50%, the minimum volume limit of the bridge is observed and for the volumes larger than 125%, the bridge is found to be unstable.

Four types of fluids, such as water, PEG20, PEO1000 and PEG20PEO1000, are tested to characterise effect of the initial bridge shape on  $TR$ . The liquid bridge, formed in-between the two plates having  $D_P = 4$  mm is stretched from  $IAR = 0.66$  to  $FAR = 2$ , at  $U = 0.134$  m/s. The liquid volume is varied from 8 to 20  $\mu\text{l}$  for 50% to 125% of  $V$ , respectively. The initial bridge shape with the contact angles less than  $90^\circ$  is similar to previous works [40, 107, 112, 118], where slipping contact lines are observed. Yet, in our case, for all initial bridge shapes, the liquid contact lines are pinned at the corners of the plates, possibly because of the pre-wetting of the plate surface (that causes a decrease in contact angles) [145]. The obtained  $TR$  results are plotted against  $\%V$ , in Fig. 4.7. For each symbol, the error bar represents the average over five experiments. For Newtonian fluids (water and PEG20),  $TR$  increases with increase in  $\%V$ . But, for the viscoelastic solutions (PEO1000 and PEG20PEO1000), increasing the volume introduced has exactly the opposite effect and  $TR$  decreases with  $\%V$ . Yet, for all solutions, with 50%  $V$ ,  $TR$  are found to be nearly the same. But for larger values of  $\%V$ , the liquid volume introduced has a stronger and opposite effect on Newtonian and viscoelastic fluids.

Additional experiments are performed to investigate effect of the initial bridge shape on the liquid transfer. The liquid bridge formed in-between two plates having  $D_P = 6$  mm is stretched from  $IAR = 0.66$  to  $FAR = 2$ , at  $U = 0.08$  m/s. The liquid volume introduced is varied from 28 to 70  $\mu\text{l}$  for 50% to 125% of  $V$ , respectively. The results obtained for effect of initial bridge shape on the liquid transfer, for  $D_P = 6$  mm, are shown in Fig. 4.8. The results for the viscoelastic solutions and the Newtonian solutions are presented in 4.8(a) and (b), respectively. These results are compared with  $TR$  obtained with the respective solutions for  $D_P = 4$ . Similar trends are observed for PEG20 and PEO1000 solutions, with both  $D_P = 4$  and 6 mm. For viscoelastic solutions,  $TR$  decreases with increasing  $\%V$ . Whereas, for Newtonian solutions,  $TR$  increases with increasing  $\%V$ .

Effect of the initial bridge shape is further analysed, for PEO1000, for all  $\%V$  studied. The midplane diameters of the initial liquid bridge, for  $D_P = 4$  and 6 mm are obtained from the images. Then, the Bond number,  $Bo_m$ , is calculated using the initial midplane diameter. Additionally, the data from Fig. 4.2 for PEO1000, for effect of plate diameter on  $TR$  is also considered for comparison. For these data points, the cylindrical-shaped liquid bridge is observed and hence, the midplane diameters are equal to the corresponding plate diameters. The results obtained for  $TR$  are plotted against  $Bo_m$ , as shown in Fig. 4.9. With increasing

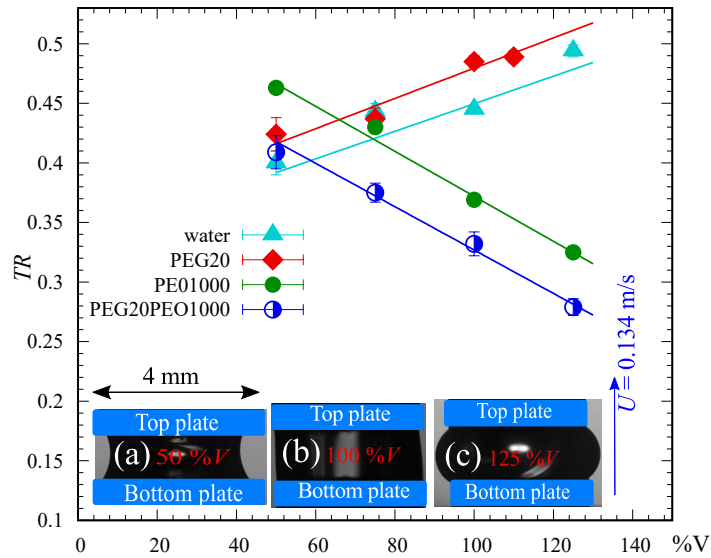


Fig. 4.7 Effect of the initial bridge on liquid transfer.  $TR$  is plotted as a function of % of the liquid volume introduced ( $V$ ) in the bridge. Insets (a), (b) and (c) are photographs the initial bridge for water, depicting 50, 100 and 125% of the liquid volume introduced. The liquid bridge, formed in-between the two plates having  $D_P = 4$  mm is stretched from  $IAR = 0.66$  to  $FAR = 2$ , at  $U = 0.134$  m/s. The liquid volume is varied from 8 to 20  $\mu\text{l}$  for 50% to 125% of  $V$ , respectively. The blue arrow denotes the stretching direction, with the stretching speed,  $U = 0.134$  m/s. The error bars represent the dispersion over five experiments. The red, sky-blue, dark blue and green lines are trend-lines for water, PEG20, PEO1000 and PEG20PEO1000 solutions.

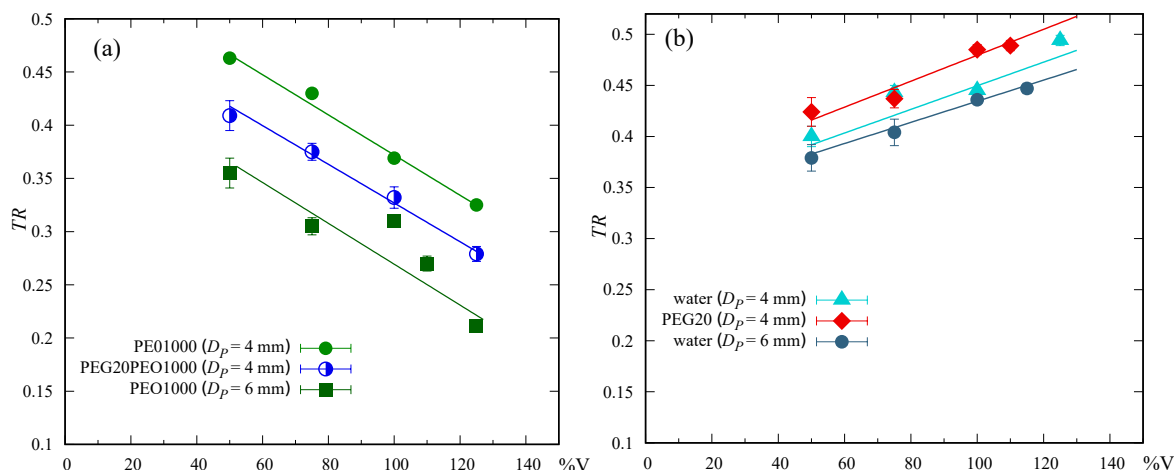


Fig. 4.8 Effect of the initial bridge on liquid transfer.  $TR$  is plotted as a function of  $\%$  of the liquid volume introduced ( $V$ ) in the bridge. Here, the liquid bridge is stretched from  $IAR = 0.66$  to  $FAR = 2$ . For experiments with  $D_P = 4$  mm,  $U = 0.134$  m/s, whereas for  $D_P = 6$  mm,  $U = 0.08$  m/s. The error bars represent the dispersion over three to five experiments. (a) The green, blue and dark green lines are trend lines for PEO1000 and PEG20PEO1000 solutions with  $D_P = 4$  mm, and PEO1000 solution with  $D_P = 6$  mm, respectively. (b) The red, sky-blue, blue lines are trend lines for water and PEG20 solution, with  $D_P = 4$  mm, and water with  $D_P = 6$  mm, respectively.

$Bo_m$ ,  $TR$  decreases, as already discussed in section 4.1.2.1. Therefore, for viscoelastic solutions, the decrease in  $TR$  with increasing  $\%V$ , can be interpreted as effect of increasing midplane diameter and hence, increasing  $Bo_m$ . To capture the trend, a power law fit is used, with the coefficient of determination of 0.94. This fit can be used to predict  $TR$  for any plate diameter and the initial bridge shape, for PEO1000 solution.

## 4.2 Partial conclusion

In this chapter, we presented the experimental investigation of the liquid transfer for Newtonian and viscoelastic polymer solutions. The cylindrical-shaped liquid capillary bridge, with pinned contact lines, was stretched at the desired speed and height. Then, the role of viscoelasticity in liquid transfer is established through the relationship between the polymer mass fraction and  $TR$ , experimentally for the first time. We show that  $TR$  decreases with increasing  $w_{PEO}$  and may be explained by the gravitational draining enhanced by the delayed filament thinning. Furthermore, the Deborah number is calculated for each mass fraction and its relationship with  $TR$  is demonstrated with a power law regression. In printing, a large volume of liquid needs to be transferred from donor to acceptor surfaces. Therefore to

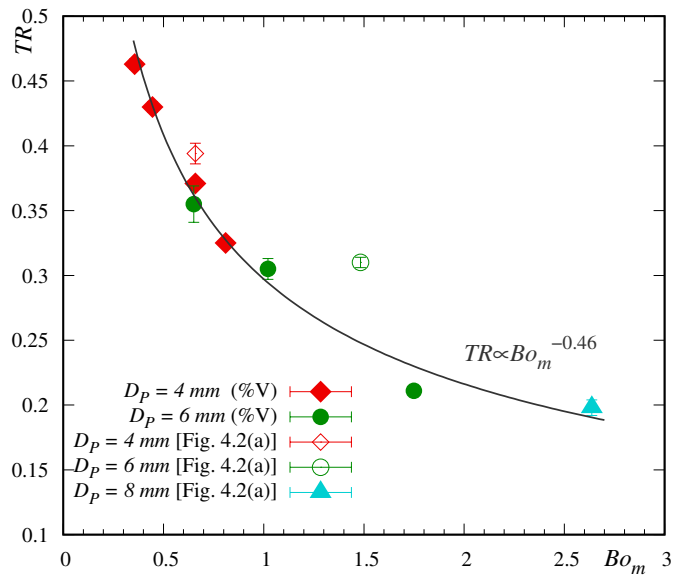


Fig. 4.9  $TR$  as a function of  $Bo_m$ . Here,  $Bo_m$  is calculated from the midplane diameters obtained from the initial bridge shapes, for PEO1000 solution. Here, the liquid bridge is stretched from  $IAR = 0.66$  to  $FAR = 2$ . For the experiments with  $D_p = 4$  mm,  $U = 0.134$  m/s, whereas for  $D_p = 6$  mm,  $U = 0.08$  m/s. The data is compared with the initial diameters obtained from effect of plate diameters on  $TR$ , see Fig. 4.2(a). For the points from Fig. 4.2(a), the initial midplane diameters are equal to the corresponding plate diameters, as the cylindrical-shaped liquid bridge are observed. The trend line is a power law fit with a coefficient of determination of 0.92. Error bars represents the dispersion over three to three to five experiments.

maximise liquid transfer, smaller PEO polymer mass fraction solutions should be preferred. Furthermore, it is recalled that sometimes our space-time diagrams showed migration of drops towards the top solution pool. These drops can affect the printing quality but their upward migration is largely prevented by coalescence.

Gravitational influence is studied by using different plate diameters and we found the similar trend as Zhang et al. [100] where smaller values of  $TR$  are obtained for larger plate diameters. Then, we establish a relationship between liquid transfer and  $Bo$ . We observed that the liquid transfer to the top plate decreases with increasing  $Bo$ . Then, we present influence of initial liquid bridge height and the final stretching height on the liquid transfer by using two dimensionless parameters,  $IAR$  and  $FAR$ , respectively. The liquid transfer to the top plate decreases with increasing  $IAR$  and  $FAR$ , for both Newtonian and viscoelastic solutions. From the printing point of view, smaller values of surface diameter, as well as initial stretching height (and hence initial liquid volume) along with final stretching height, should be favoured.

We also show that with increasing stretching speed, liquid transfer to the top plate increases. This trend was previously established for Newtonian fluids, but in the present study, we demonstrate that this trend is valid for viscoelastic fluids as well. When  $TR$  was plotted against  $Ca$ , we obtained points in the quasi-static ( $Ca < 0.01$ ) and the transition regime ( $0.01 < Ca < 1$ ). Hence, in printing, liquid transfer can be enhanced by using higher values of the capillary number ( $Ca > 0.01$ ). Finally, when the initial liquid bridge shape was varied by varying the (liquid) volume introduced, liquid transfer behaviour is strikingly different for Newtonian and viscoelastic solutions. For viscoelastic solutions, the liquid transfer to the top plate decreases with increasing the liquid volume introduced. This behaviour can be replotted as a function of the Bond number ( $Bo_m$ ), calculated using the initial midplane diameter. It is observed that  $TR$  follows a power law regression with this  $Bo_m$  (Fig. 4.9).

# Chapter 5

## Conclusions and future work

### Contents

---

5.1	Conclusions . . . . .	134
5.2	Future work . . . . .	137

---

## 5.1 Conclusions

In the present thesis, we have experimentally investigated the role of viscoelasticity in the drops-on-a-filament, also known as beads-on-a-string (BOAS) and liquid transfer phenomena. The drops-on-a-filament and the transfer ratio phenomena were investigated by using viscoelastic polymer solutions. The experimental study was carried out with aqueous solutions of polyethylene oxide (PEO) and polyethylene glycol (PEG), separately and in combination, at varying polymer mass fractions. The solutions were characterised by measuring density, surface tension, zero shear viscosity and relaxation times. The experimental high-speed image microscopy setup was maintained under thermally controlled conditions. The setup consisted of a Capillary Breakup Extensional Rheometer (CaBER), a high-speed camera, a catadioptric lens and a laser. The CaBER enabled precise and repetitive stretching of the liquid capillary bridge with the desired speed.

New types of space-time diagrams called Diameter-space-time (DST) and Hencky strain-space-time (HSST) diagrams were introduced to capture stretching of an initial liquid bridge, filament thinning, until falling of drops into solution pools. The diagrams were constructed from images, where filament and drop diameter was converted into a colour code, to obtain local diameter and the Hencky strain, in space and time. For both PEO and PEG+PEO solutions, a BOAS structure with multi-generations of drops was observed. Additionally, in our space-time diagrams, at least three scenarios predicted numerically by Li and Fontelos [2] can be observed: presence of drops due to stretching of a viscoelastic liquid bridge, drop migration and coalescence. Sudden vertical jumps in the diagrams were observed because of the coalescence of small drops, and the filament was pulled in the direction of the coalescence. For both PEO and PEG+PEO solutions, a hierarchy, as well as asymmetry of satellite drops around a big central drop were demonstrated. The present space-time diagrams provide actual measurements of drop diameter and the Hencky strain, whereas previous works by Oliveira et al. [9] and Clasen et al. [15] were based on the grey-scale intensity to indicate the relative thickness of drops or positions of drops. Further analysis of DST diagrams suggests that even after changing the PEO mass fraction, the diameter of the first generation (largest) drop remains constant. These findings indicate that the diameter of the first generation of drop remains unaffected by polymer mass fractions within our experimental range. Also, the diameter of the big central drop was smaller for PEG+PEO solutions than PEG20 and PEO solutions. During a BOAS instability with multi-generation drops, we measure the maximum number of drops in the BOAS structure and interestingly, the number of drops is higher for the PEG+PEO solutions than that for the PEO solutions. The maximum number of drops

in the BOAS structure increase with the Deborah number, and we show that this increasing trend can be captured by a power law fit.

Furthermore, the DST and HSST diagrams enabled to locate the minimum diameter of a filament in space and time. By using the minimum diameter, the apparent extensional viscosity,  $\eta_E$ , and the Hencky strain,  $\epsilon_{min}$  were calculated. For both PEO and PEG+PEO solutions,  $\eta_E$  increases with time and the Hencky strain. Moreover, the apparent extensional viscosity increases with the mass fraction of PEO. The increase in  $\eta_E$  can be distinguished in two regimes, at  $\epsilon_{min} \approx 6$ . The first regime corresponds to development of a cylindrical shaped filament in axial (due to formation of solution pools) as well as radial direction, while the second regime corresponds to the filament thinning in radial direction only. Also, a similar increase in  $\eta_E$  with time and the Hencky strain was also noticed for various  $FAR$ .  $\eta_E$  increases with the increase in  $FAR$  and two distinct regions are again observed at  $\epsilon_{min} \approx 6$ . In addition, for both PEO and PEG+PEO solutions, relaxation time increases as a power law of the mass fraction of PEO and with the addition of PEG, in accordance with previous studies [88, 101].

Various geometric aspects were investigated in order to study their effect on diameter of the first generation drop and the maximum number of drops in a BOAS structure. For larger plate diameters, we observe a larger diameter of the first generation drop and a higher number of drops in a BOAS structure. We also show that initial aspect ratio and final aspect ratio have the opposite effect on the number of drops in a BOAS instability. Higher number of drops in the BOAS structure is observed for smaller initial aspect ratio and larger final aspect ratio. For all three geometrical aspects studied, the maximum number of drops in a BOAS structure depends on the filament length available to form higher generations of drops (iterated instability). Surprisingly, stretching speed did not affect the diameter of the first generation drop and the maximum number of drops in the tested range. This further suggests that only initial and final bridge geometries may have influence on the studied drop dynamics of a BOAS instability.

Liquid transfer was experimentally investigated, for both Newtonian and the viscoelastic solutions, by varying PEO mass fraction, geometrical properties, stretching properties and initial liquid bridge shape. We used a cylindrical-shaped initial liquid capillary bridge, formed in-between two circular flat plates with pinned contact lines, in contrast to most of the previous studies for moving contact lines [40, 42, 102, 103, 106, 107, 112, 113, 118]. The relationship between the transfer ratio and polymer mass fraction is established experimentally for the first time. With the increase in the PEO mass fraction,  $TR$  decreases and with the addition of PEG to the PEO solutions,  $TR$  decreases further. In addition, we demonstrate the role of viscoelasticity in a liquid transfer by using a power law regression for a decrease in  $TR$

with Deborah number. This regressive trend can be explained by gravitational drainage, enhanced by a delayed filament thinning due to increased PEO mass fraction and viscosity of the solution. Gravitational influence on the  $TR$  was also verified by using different plate diameters. Liquid transfer to the top plate reduces significantly for the larger plate diameters, similar to [100] for both Newtonian and viscoelastic solutions. This reduced liquid transfer can be explained by higher Bond numbers and, therefore, by an increase in the gravitational effect. We show that liquid transfer to a top plate decreases with increase in initial and final stretching heights of a liquid capillary bridge, for both Newtonian and viscoelastic solutions. With increasing  $IAR$ , gravitational forces overcome capillary forces and axial sagging occurs in the direction of gravity, which leads to lower liquid transfer when a liquid bridge is stretched.  $FAR$  governs liquid transfer of Newtonian and viscoelastic fluids in a similar way as increasing stretching height leads to the more liquid volume enclosed below a liquid bridge breakup point and then, resulting in a larger bottom solution pool. We also show that with increase in stretching speed and the capillary number, liquid transfer to the top plate increases. This trend was previously established for Newtonian fluids [100, 102, 103, 106, 113], but in the present study, we demonstrate that this trend is valid for viscoelastic fluids as well. Finally, liquid transfer behaviour is strikingly different for Newtonian and viscoelastic solutions, when the initial liquid bridge shape or liquid volume,  $V$ , introduced is varied. For Newtonian solutions,  $TR$  increases with an increase in the liquid volume, while for viscoelastic solutions,  $TR$  decreases with an increase in the liquid volume. For viscoelastic solutions, a decrease in  $TR$  is observed with increasing  $\%V$ . Furthermore, for PEO1000, a relationship between  $TR$  and  $Bo_m$  is found and follows a decreasing power law function.

In practice, a successful printing involves a sufficiently large volume of liquid transferred from one surface to another, defect-free liquid transfer and desired liquid shapes (a BOAS structured wire) to be preserved. In 3D lithography, a BOAS structure is required and, thus, we demonstrate that a high polymer mass fraction, a larger surface diameter as well as a larger final stretching height along with a smaller initial stretching height of the liquid bridge should be favoured to maximise the number of drops in a BOAS structure. On the contrary, formation of drops is a defect in printing and hence, a smaller surface diameter, a larger initial stretching height and a smaller final stretching height for a liquid bridge should be preferred to minimise the number of drops in a BOAS structure. Moreover, we show that to maximise the liquid transfer, smaller polymer mass fraction solutions should be used. In addition, smaller surface diameter and liquid volume, a smaller initial stretching height, a smaller final stretching height configuration, but a higher stretching speed should be preferred to increase liquid transfer. Our DST and HSST diagrams also allow tracking drop trajectories, which can be helpful in the printing industry to track falling of drops on either carrier or

substrate surface. In the present study, we observed that drops often fall into the bottom solution pool (donor surface). Therefore, there is no risk of contamination of the top plate (substrate surface) that can result into deterioration of printing quality.

We tested and validated the OpenFOAM toolbox *rheoTool* to simulate capillary thinning of a stretched liquid bridge. Liquid properties of the sample solutions and experimentally obtained stretched liquid bridge profiles are used to reproduce capillary thinning of a stretched liquid bridge. For Newtonian PEG20 solution, transfer ratios obtained experimentally and numerically are in good agreement. For viscoelastic PEG20PEO1000 solution, after necking, a short-lived filament thinning is observed, along with a single first generation drop. Diameter of the first generation drop obtained numerically and experimentally for the PEG20PEO1000 solution is similar. However, for PEG20PEO1000, numerical  $TR$  is higher than experimental  $TR$  as a consequence of inadequate gravitational draining caused by a short-lived filament. Presumably, this short lived filament may be due to the coarse meshes used. Hence, liquid transfer for Newtonian fluids using *rheoTool* produces satisfactory results. For viscoelastic solutions, we need a higher resolution mesh to produce a persistent filament to enhance gravitational draining in liquid transfer and localised pinching to achieve higher generations of drops in a BOAS structure. Therefore, preliminary results using *rheoTool* are promising and our numerical scripts can be further used to investigate other Newtonian and viscoelastic fluids.

## 5.2 Future work

Scope of this thesis was to understand the influence of viscoelasticity on drop dynamics of a BOAS structure and liquid transfer. In the future, by using various mass fractions of PEG in PEG+PEO solutions, validity of the power law equation for number of drops in a BOAS instability against the Deborah number could be tested. A similar equation can be acquired, for the transfer ratio to capture the effect of PEG mass fraction on liquid transfer. Low molecular weights of PEO can be used to study the influence of molecular weights on drop dynamics of a BOAS structure and liquid transfer. The current experimental results suggest that smaller plate diameters and higher stretching speeds can be used to achieve 50% transfer ratios. Drop dynamics and liquid transfer can be further investigated by using different diameters at top and bottom plates. More experimental work is also needed to thoroughly describe the effect of stretching direction on liquid transfer. By using a Polarised Light Microscopy, polymer distribution in a filament, as well as in a drop can be further estimated. A BOAS structure could be dried [86], and studied under a microscope to observe polymer distribution.

Concerning numerical simulations, liquid transfer for other Newtonian fluids should be further investigated using *rheoTool*. A higher resolution mesh could be implemented to produce a persistent filament to enhance gravitational draining in liquid transfer and localised pinching to achieve higher generations of drops in a BOAS structure. The power law equations for the influence of viscoelasticity on the number of drops and liquid transfer can be further investigated numerically. Additionally, to make a numerical study even closer to stretching of liquid capillary bridge experiments, a moving top plate with a required stretching speed, along with a dynamic mesh can be implemented. Using a dynamic mesh, we hope that the experimental results obtained for BOAS structure and liquid transfer could be reproduced for varying polymer concentrations along with the geometrical and stretching properties.

# References

- [1] S. L. Anna and G. H. McKinley. Elasto-capillary thinning and breakup of model elastic liquids. *Journal of Rheology*, 45(1):115–138, 2001.
- [2] J. Li and M. A. Fontelos. Drop dynamics on the beads-on-string structure for viscoelastic jets: A numerical study. *Physics of Fluids*, 15(4):922–937, 2003.
- [3] P. P. Bhat, S. Appathurai, M. T. Harris, M. Pasquali, G. H. McKinley, and O. A. Basaran. Formation of beads-on-a-string structures during break-up of viscoelastic filaments. *Nature Physics*, 6(8):625–631, 2010.
- [4] H. Pingulkar, J. Peixinho, and O. Crumeyrolle. Drop dynamics of viscoelastic filaments. *Physical Review Fluids*, 5:011301, Jan 2020.
- [5] B. D. Opell, D. Jain, A. Dhinojwala, and T. A. Blackledge. Tuning orb spider glycoprotein glue performance to habitat humidity. *Journal of Experimental Biology*, 221(6), 2018.
- [6] S. Middleman. Stability of a viscoelastic jet. *Chemical Engineering Science*, 20(12): 1037–1040, 1965.
- [7] M. Goldin, J. Yerushalmi, R. Pfeffer, and R. Shinnar. Breakup of a laminar capillary jet of a viscoelastic fluid. *Journal of Fluid Mechanics*, 38(4):689–711, 1969.
- [8] G. Brenn, Z. Liu, and F. Durst. Linear analysis of the temporal instability of axisymmetrical non-newtonian liquid jets. *International journal of multiphase flow*, 26(10): 1621–1644, 2000.
- [9] M. S. N. Oliveira, R. Yeh, and G. H. McKinley. Iterated stretching, extensional rheology and formation of beads-on-a-string structures in polymer solutions. *Journal of Non-Newtonian Fluid Mechanics*, 137(1–3):137–148, 2006.
- [10] J. Eggers. Nonlinear dynamics and breakup of free-surface flows. *Reviews of Modern Physics*, 69:865–930, Jul 1997.
- [11] A. Deblais, M. A. Herrada, I. Hauner, K. P. Velikov, T. Van Roon, H. Kellay, J. Eggers, and D. Bonn. Viscous effects on inertial drop formation. *Physical Review Letters*, 121(25):254501, 2018.
- [12] G. H. McKinley. *Visco-elasto-capillary thinning and breakup of complex fluid*, pages 1–48. Annual Rheology Reviews, edited by M. D. Binding and K. Walters, British Society of Rheology, Wales, UK, 2005.

- [13] D. W. Bousfield, R. Keunings, G. Marrucci, and M. M. Denn. Nonlinear analysis of the surface tension driven breakup of viscoelastic filaments. *Journal of Non-Newtonian Fluid Mechanics*, 21(1):79–97, 1986.
- [14] L. E. Rodd, T. P. Scott, J. J. Cooper-White, and G. H. McKinley. Capillary break-up rheometry of low-viscosity elastic fluids. *Applied Rheology*, 15(1):12–27, 2005.
- [15] C. Clasen, J. Bico, V. M. Entov, and G. H. McKinley. ‘Gobbling drops’: the jetting–dripping transition in flows of polymer solutions. *Journal of Fluid Mechanics.*, 636: 5–40, 2009.
- [16] A. M. Ardekani, V. Sharma, and G. H. McKinley. Dynamics of bead formation, filament thinning and breakup in weakly viscoelastic jets. *Journal of Fluid Mechanics*, 665:46–56, 2010.
- [17] R. Sattler, C. Wagner, and J. Eggers. Blistering pattern and formation of nanofibers in capillary thinning of polymer solutions. *Physical Review Letters*, 100:164502, 2008.
- [18] A. Deblais, K. P. Velikov, and D. Bonn. Pearling instabilities of a viscoelastic thread. *Physical Review Letters*, 120(19):1–5, 2018.
- [19] F. W. Kroesser and S. Middleman. Viscoelastic jet stability. *AIChE Journal*, 15(3): 383–386, 1969.
- [20] S. Kumar. Liquid transfer in printing processes: liquid bridges with moving contact lines. *Annual Review of Fluid Mechanics*, 47:67–94, 2015.
- [21] J.-U. Park, M. Hardy, S. J. Kang, K. Barton, K. Adair, D. K. Mukhopadhyay, C. Y. Lee, M. S. Strano, A. G. Alleyne, J. G. Georgiadis, P. M. Ferreira, and Rogers J. A. High-resolution electrohydrodynamic jet printing. *Nature Materials*, 6(10):782–789, 2007.
- [22] G. M. Whitesides. The origins and the future of microfluidics. *Nature*, 442(7101): 368–373, 2006.
- [23] S. Grilli, S. Coppola, V. Vespini, F. Merola, A. Finizio, and P. Ferraro. 3D lithography by rapid curing of the liquid instabilities at nanoscale. *Proceedings of the National Academy of Sciences*, 108(37):15106–15111, 2011.
- [24] B. K. Brettmann, S. Tsang, K. M. Forward, G. C. Rutledge, A. S. Myerson, and B. L. Trout. Free surface electrospinning of fibers containing microparticles. *Langmuir*, 28 (25):9714–9721, 2012.
- [25] A. Jaworek and A. T. Sobczyk. Electrospinning route to nanotechnology: An overview. *Journal of Electrostatics*, 66(3–4):197–219, 2008.
- [26] C. Tirel, M.-C. Renoult, C. Dumouchel, D. Lisiecki, O. Crumeyrolle, and I. Mutabazi. Multi-scale analysis of a viscoelastic liquid jet. *Journal of Non-Newtonian Fluid Mechanics*, 245:1–10, 2017.
- [27] J. Dinic, L. N. Jimenez, and V. Sharma. Pinch-off dynamics and dripping-onto-substrate (DoS) rheometry of complex fluids. *Lab on a Chip*, 17(3):460–473, 2017.

- [28] A. M. Alencar, A. Majumdar, Z. Hantos, S. V Buldyrev, H. E. Stanley, and B. Suki. Crackles and instabilities during lung inflation. *Physica A: Statistical Mechanics and its Applications*, 357(1):18–26, 2005.
- [29] J. Kim, B. Guenthart, J. D. O’Neill, N. V. Dorrello, M. Bacchetta, and G. Vunjak-Novakovic. Controlled delivery and minimally invasive imaging of stem cells in the lung. *Scientific reports*, 7(1):1–13, 2017.
- [30] J. Montanero and A. Ponce-Torres. Review on the dynamics of isothermal liquid bridges. *Applied Mechanics Reviews*, 72(1), 2020.
- [31] G. M. Harrison, R. Mun, G. Cooper, and D. V. Boger. A note on the effect of polymer rigidity and concentration on spray atomisation. *Journal of Non-Newtonian Fluid Mechanics*, 85(1):93–104, 1999.
- [32] E. Miller, B. Gibson, E. McWilliams, and J. P. Rothstein. Collision of viscoelastic jets and the formation of fluid webs. *Applied Physics Letters*, 87(1):014101, 2005.
- [33] J. C. Thompson and J. P. Rothstein. The atomization of viscoelastic fluids in flat-fan and hollow-cone spray nozzles. *Journal of Non-Newtonian Fluid Mechanics*, 147(1–2):11–22, 2007.
- [34] R. P. Mun, B. W. Young, and D. V. Boger. Atomisation of dilute polymer solutions in agricultural spray nozzles. *Journal of Non-Newtonian Fluid Mechanics*, 83(1–2):163–178, 1999.
- [35] L. Xing, J. E. Glass, and R. H. Fernando. Parameters influencing the spray behavior of waterborne coatings. *Journal of Coatings Technology*, 71(890):37, 1999.
- [36] G. Brenn, Z. Liu, and F. Durst. Three-dimensional temporal instability of non-newtonian liquid sheets. *Atomization and Sprays*, 11(1), 2001.
- [37] F. C. Krebs. Fabrication and processing of polymer solar cells: A review of printing and coating techniques. *Solar Energy Materials and Solar Cells*, 93(4):394–412, 2009.
- [38] B. J. De Gans, P. C. Duineveld, and U. S. Schubert. Inkjet printing of polymers: state of the art and future developments. *Advanced materials*, 16(3):203–213, 2004.
- [39] X. Wang, M. Jiang, Z. Zhou, J. Gou, and D. Hui. 3d printing of polymer matrix composites: A review and prospective. *Composites Part B: Engineering*, 110:442–458, 2017.
- [40] H. Chen, T. Tang, and A. Amirfazli. Liquid transfer mechanism between two surfaces and the role of contact angles. *Soft Matter*, 10(15):2503–2507, 2014.
- [41] Q. Huang, L. Hengeller, N. J. Alvarez, and O. Hassager. Bridging the gap between polymer melts and solutions in extensional rheology. *Macromolecules*, 48(12):4158–4163, 2015.
- [42] A. K. Sankaran and J. P. Rothstein. Effect of viscoelasticity on liquid transfer during gravure printing. *Journal of Non-Newtonian Fluid Mechanics*, 175:64–75, 2012.

- [43] J. A. Lee, J. P. Rothstein, and M. Pasquali. Computational study of viscoelastic effects on liquid transfer during gravure printing. *Journal of Non-Newtonian Fluid Mechanics*, 199:1–11, 2013.
- [44] J. Cen, R. Kitsomboonloha, and V. Subramanian. Cell filling in gravure printing for printed electronics. *Langmuir*, 30(45):13716–13726, 2014.
- [45] J. W. Goodwin and R. W. Hughes. *Rheology for chemists: An introduction*. Royal Society of Chemistry, 2008.
- [46] M. Reiner. The Deborah number. *Physics Today*, 17(1):62, 1964.
- [47] R. B. Bird, R. C. Armstrong, and O. Hassager. *Dynamics of polymeric liquids. Vol. 1: Fluid mechanics*. Wiley-Interscience, 1987.
- [48] G. Plohl. *Polymeric time scales for viscoelastic flow modelling*. PhD thesis, Graz University of Technology, 2019.
- [49] C. Tropea and A. L. Yarin. *Springer handbook of experimental fluid mechanics*. Springer Science & Business Media, 2007.
- [50] P. J. G. Schreurs. Material models, 2013. URL <http://www.mate.tue.nl/~piet/edu/mmm/pdf/mmmsyl1213.pdf>.
- [51] J. G. Oldroyd. On the formulation of rheological equations of state. *Proceedings of the Royal Society of London. Series A. Mathematical and Physical Sciences*, 200 (1063):523–541, 1950.
- [52] M. G. N. Perera and K. Walters. Long-range memory effects in flows involving abrupt changes in geometry: Part I: Flows associated with I-shaped and T-shaped geometries. *Journal of Non-Newtonian Fluid Mechanics*, 2(1):49–81, 1977.
- [53] R. A. Figueiredo, C. M. Oishi, A. M. Afonso, I. V. M. Tasso, and J. A. Cuminato. A two-phase solver for complex fluids: Studies of the Weissenberg effect. *International Journal of Multiphase Flow*, 84:98–115, 2016.
- [54] R. Comminal, F. Pimenta, J. H. Hattel, M. A. Alves, and J. Spangenberg. Numerical simulation of the planar extrudate swell of pseudoplastic and viscoelastic fluids with the streamfunction and the VOF methods. *Journal of Non-Newtonian Fluid Mechanics*, 252:1–18, 2018.
- [55] E. Turkoz, J. M. Lopez-Herrera, J. Eggers, C. B. Arnold, and L. Deike. Axisymmetric simulation of viscoelastic filament thinning with the Oldroyd-B model. *Journal of Fluid Mechanics*, 851:R2, 2018.
- [56] R. A. Figueiredo, C. M. Oishi, A. M. Afonso, and M. A. Alves. Numerical study on micro-scale extensional viscoelastic flows. *Journal of Non-Newtonian Fluid Mechanics*, 276:104219, 2020.
- [57] L. J. Amoreira and P. J. Oliveira. Comparison of different formulations for the numerical calculation of unsteady incompressible viscoelastic fluid flow. *Advances in Applied Mathematics and Mechanics*, 2(4):483–502, 2010.

- [58] G. Brenn and G. Plohl. The oscillating drop method for measuring the deformation retardation time of viscoelastic liquids. *Journal of Non-Newtonian Fluid Mechanics*, 223:88 – 97, 2015.
- [59] R. B. Bird, P. J. Dotson, and N. L. Johnson. Polymer solution rheology based on a finitely extensible bead—spring chain model. *Journal of Non-Newtonian Fluid Mechanics*, 7(2-3):213–235, 1980.
- [60] M. Herrchen and H. C. Öttinger. A detailed comparison of various fene dumbbell models. *Journal of non-newtonian fluid mechanics*, 68(1):17–42, 1997.
- [61] A. Gaillard. *Flow and stability of a viscoelastic liquid curtain*. PhD thesis, Université Paris Diderot, 2018.
- [62] C. Clasen, J. P. Plog, W.-M. Kulicke, M. Owens, C. Macosko, L. E. Scriven, M. Verani, and G. H. McKinley. How dilute are dilute solutions in extensional flows? *Journal of Rheology*, 50(6):849–881, 2006.
- [63] L. Campo-Deaño and C. Clasen. The slow retraction method (SRM) for the determination of ultra-short relaxation times in capillary breakup extensional rheometry experiments. *Journal of Non-Newtonian Fluid Mechanics*, 165(23):1688–1699, 2010.
- [64] W. H. Hager. Wilfrid noel bond and the bond number. *Journal of Hydraulic Research*, 50(1):3–9, 2012.
- [65] L. A. Slobozhanin and J. M. Perales. Stability of liquid bridges between equal disks in an axial gravity field. *Physics of Fluids*, 5(6):1305–1314, 1993.
- [66] N. A. Bezdenejnykh, J. Meseguer, and J. M. Perales. Experimental analysis of stability limits of capillary liquid bridges. *Physics of Fluids*, 4(4):677–680, 1992.
- [67] H. Hencky. Welche umstände bedingen die verfestigung bei der bildsamen verformung von festen isotropen körpern? *Zeitschrift für Physik*, 55(3-4):145–155, 1929.
- [68] R. I. Tanner and E. Tanner. Heinrich hencky: A rheological pioneer. *Rheologica acta*, 42(1-2):93–101, 2003.
- [69] V. Tirtaatmadja, G. H. McKinley, and J. J. Cooper-White. Drop formation and breakup of low viscosity elastic fluids: Effects of molecular weight and concentration. *Physics of Fluids*, 18(4):043101, 2006.
- [70] W. V. Ohnesorge. The formation of drops at nozzles and the dissolution of liquid jets. *ZAMM - Journal of Applied Mathematics and Mechanics / Journal for Applied Mathematics and Mechanics*, 16(6):355–358, 1936.
- [71] G. McKinley and M. Renardy. Wolfgang von Ohnesorge. *Physics of Fluids*, 23:127101, 2011.
- [72] C. Clasen, P. M. Phillips, L. Palangetic, and J. Vermant. Dispensing of rheologically complex fluids: the map of misery. *American Institute of Chemical Engineers Journal*, 58(10):3242–3255, 2012.

- [73] A. U. Chen, P. K. Notz, and O. A. Basaran. Computational and experimental analysis of pinch-off and scaling. *Physical review letters*, 88(17):174501, 2002.
- [74] C. Wagner, Y. Amarouchene, D. Bonn, and J. Eggers. Droplet detachment and satellite bead formation in viscoelastic fluids. *Physical Review Letters*, 95(16):7–10, 2005.
- [75] J. Dinic and V. Sharma. Computational analysis of self-similar capillary-driven thinning and pinch-off dynamics during dripping using the volume-of-fluid method. *Physics of Fluids*, 31(2):021211, 2019.
- [76] M. Stelter, G. Brenn, A. L. Yarin, R. P. Singh, and F. Durst. Validation and application of a novel elongational device for polymer solutions. *Journal of Rheology*, 44(3):595–616, 2000.
- [77] V. M. Entov and A. L. Yarin. Influence of elastic stresses on the capillary breakup of jets of dilute polymer solutions. *Fluid Dynamics*, 19(1):21–29, 1984.
- [78] A. Gaillard, M. Roché, S. Lerouge, C. Gay, L. Lebon, and L. Limat. Viscoelastic liquid curtains: experimental results on the flow of a falling sheet of polymer solution. *Journal of Fluid Mechanics*, 873:358–409, 2019.
- [79] T. Sridhar, V. Tirtaatmadja, D. A. Nguyen, and R. K. Gupta. Measurement of extensional viscosity of polymer solutions. *Journal of Non-Newtonian Fluid Mechanics*, 40(3):271–280, 1991.
- [80] S. Berg, R. Kröger, and H.J. Rath. Measurement of extensional viscosity by stretching large liquid bridges in microgravity. *Journal of Non-Newtonian Fluid Mechanics*, 55(3):307 – 319, 1994.
- [81] J. Dinic, Y. Zhang, L. N. Jimenez, and V. Sharma. Extensional relaxation times of dilute, aqueous polymer solutions. *ACS Macro Letters*, 4(7):804–808, 2015.
- [82] P. Schümmer and K. H. Tebel. A new elongational rheometer for polymer solutions. *Journal of Non-Newtonian Fluid Mechanics*, 12(3):331–347, 1983.
- [83] E. Miller, Ch. Clasen, and J. P Rothstein. The effect of step-stretch parameters on capillary breakup extensional rheology (caber) measurements. *Rheologica Acta*, 48(6):625–639, 2009.
- [84] N. J. Kim, C. J. Pipe, K. H. Ahn, S. J. Lee, and G. H. McKinley. Capillary breakup extensional rheometry of a wormlike micellar solution. *Korea-Australia Rheology Journal*, 22(1):31–41, 2010.
- [85] H. C. Chang, E. A. Demekhin, and E. Kalaidin. Iterated stretching of viscoelastic jets. *Physics of Fluids*, 11(7):1717–1737, 1999.
- [86] R. Sattler, S. Gier, J. Eggers, and C. Wagner. The final stages of capillary break-up of polymer solutions. *Physics of Fluids*, 24(2):023101, 2012.
- [87] B. M. Baumert and S. J. Muller. Flow visualization of the elastic taylor-couette instability in boger fluids. *Rheologica Acta*, 34(2):147–159, 1995.

- [88] M. Stelter, G. Brenn, A. L. Yarin, R. P. Singh, and F. Durst. Investigation of the elongational behavior of polymer solutions by means of an elongational rheometer. *Journal of Rheology*, 46(2002):507, 2002.
- [89] V. Sharma, S. J. Haward, J. Serdy, B. Keshavarz, A. Soderlund, P. Threlfall-Holmes, and G. H. McKinley. The rheology of aqueous solutions of ethyl hydroxy-ethyl cellulose (EHEC) and its hydrophobically modified analogue (hmeEHEC): extensional flow response in capillary break-up, jetting (ROJER) and in a cross-slot extensional rheometer. *Soft Matter*, 11(16):3251–3270, 2015.
- [90] R. Keunings. An algorithm for the simulation of transient viscoelastic flows with free surfaces. *Journal of Computational Physics*, 62(1):199–220, 1986.
- [91] P. Moin. *Fundamentals of engineering numerical analysis*. Cambridge University Press, 2nd edition, 2010.
- [92] S. Popinet. A quadtree-adaptive multigrid solver for the Serre–Green–Naghdi equations. *Journal of Computational Physics*, 302:336 – 358, 2015.
- [93] S. Popinet. Numerical models of surface tension. *Annual Review of Fluid Mechanics*, 50(1):49–75, 2018.
- [94] C. W. Hirt and B. D. Nichols. Volume of fluid (VOF) method for the dynamics of free boundaries. *Journal of Computational Physics*, 39(1):201 – 225, 1981.
- [95] P. C. Sousa, E. J. Vega, R. G. Sousa, J. M. Montanero, and M. A. Alves. Measurement of relaxation times in extensional flow of weakly viscoelastic polymer solutions. *Rheologica Acta*, 56(1):11–20, 2017.
- [96] M. I. Kolte and P. Szabo. Capillary thinning of polymeric filaments. *Journal of Rheology*, 43(3):609–625, 1999.
- [97] M. Aytouna, J. Paredes, N. Shahidzadeh-Bonn, S. Moulinet, C. Wagner, Y. Amarouchene, J. Eggers, and D. Bonn. Drop formation in non-Newtonian fluids. *Physical Review Letters*, 110(3):1–5, 2013.
- [98] Y. Amarouchene, D. Bonn, J. Meunier, and H. Kellay. Inhibition of the finite-time singularity during droplet fission of a polymeric fluid. *Physical Review Letters*, 86(16):3558, 2001.
- [99] A. V. Bazilevsky, V. M. Entov, and A. N. Rozhkov. Liquid filament microrheometer and some of its applications. In *Third European Rheology Conference and Golden Jubilee Meeting of the British Society of Rheology*, pages 41–43. Springer, 1990.
- [100] X. Zhang, R. S. Padgett, and O. A. Basaran. Nonlinear deformation and breakup of stretching liquid bridges. *Journal of Fluid Mechanics*, 329:207–245, 1996.
- [101] B. Martínez-Arias and J. Peixinho. Torque in Taylor–Couette flow of viscoelastic polymer solutions. *Journal of Non-Newtonian Fluid Mechanics*, 247:221–228, 2017.
- [102] A. V. Chadov and E. D. Yakhnin. Investigation of the transfer of a liquid from one solid-surface to another. 1. Slow transfer-method of approximate calculation. *Colloid Journal of the USSR*, 41(4):700–703, 1979.

- [103] E. D. Yakhnin and A. V. Chadov. Investigation of the transfer of a liquid from one solid-surface to another. 2. Dynamic transfer. *Colloid Journal of the USSR*, 45(6): 1034–1039, 1983.
- [104] S. Dodds, M. S. Carvalho, and S. Kumar. Stretching and slipping of liquid bridges near plates and cavities. *Physics of Fluids*, 21(9):092103, 2009.
- [105] S. Dodds, M. S. Carvalho, and S. Kumar. Stretching liquid bridges with moving contact lines: The role of inertia. *Physics of Fluids*, 23(9):092101, 2011.
- [106] C.-H. Huang, M. S. Carvalho, and S. Kumar. Stretching liquid bridges with moving contact lines: Comparison of liquid-transfer predictions and experiments. *Soft Matter*, 12:7457–7469, 2016.
- [107] J.-T. Wu, M. S. Carvalho, and S. Kumar. Effects of shear and extensional rheology on liquid transfer between two flat surfaces. *Journal of Non-Newtonian Fluid Mechanics*, page 104173, 2019.
- [108] H. Kipphan. *Handbook of print media: Technologies and production methods*. Springer, 2001.
- [109] A Lorenz, A Senne, J Rohde, S Kroh, M Wittenberg, K Krüger, F Clement, and D Biro. Evaluation of flexographic printing technology for multi-busbar solar cells. *Energy Procedia*, 67:126–137, 2015.
- [110] A. Carlson, A. M. Bowen, Y. Huang, R. G. Nuzzo, and J. A. Rogers. Transfer printing techniques for materials assembly and micro/nanodevice fabrication. *Advanced Materials*, 24(39):5284–5318, 2012.
- [111] W.-X. Huang, S.-H. Lee, H. J. Sung, T.-M. Lee, and D.-S. Kim. Simulation of liquid transfer between separating walls for modeling micro-gravure-offset printing. *International Journal of Heat and Fluid Flow*, 29(5):1436–1446, 2008.
- [112] H. W. Kang, H. J. Sung, T. M. Lee, D. S. Kim, and C. J. Kim. Liquid transfer between two separating plates for micro-gravure-offset printing. *Journal of Micromechanics and Microengineering*, 19(1):015025, 2008.
- [113] H. Chen, T. Tang, and A. Amirfazli. Effects of surface wettability on fast liquid transfer. *Physics of Fluids*, 27(11):112102, 2015.
- [114] J. H. Snoeijer and B. Andreotti. Moving contact lines: scales, regimes, and dynamical transitions. *Annual review of fluid mechanics*, 45, 2013.
- [115] B. Qian and K. S. Breuer. The motion, stability and breakup of a stretching liquid bridge with a receding contact line. *Journal of Fluid Mechanics*, 666:554–572, 2011.
- [116] J. A. F. Plateau. Experimental and theoretical researches on the figures of equilibrium of a liquid mass withdrawn from the action of gravity. *Annual Reports of the Smithsonian Institution*, 1863.
- [117] L. Rayleigh. On the instability of jets. *Proceedings of the London mathematical society*, 1(1):4–13, 1878.

- [118] D. H. Ahmed, H. J. Sung, and D. S. Kim. Simulation of non-newtonian ink transfer between two separating plates for gravure-offset printing. *International Journal of Heat and Fluid Flow*, 32(1):298–307, 2011.
- [119] V. M. Entov and E. J. Hinch. Effect of a spectrum of relaxation times on the capillary thinning of a filament of elastic liquid. *Journal of Non-Newtonian Fluid Mechanics*, 72(1):31–53, 1997.
- [120] M. A. Fontelos and J. Li. On the evolution and rupture of filaments in giesekus and fene models. *Journal of non-newtonian fluid mechanics*, 118(1):1–16, 2004.
- [121] W. Mathues, S. Formenti, C. McIlroy, O. G. Harlen, and C. Clasen. Caber vs rojer—different time scales for the thinning of a weakly elastic jet. *Journal of Rheology*, 62(5):1135–1153, 2018.
- [122] G. Chen, Q. Xiong, P. J Morris, E. G. Paterson, A. Sergeev, and Y. Wang. OpenFOAM for computational fluid dynamics. *Notices of the AMS*, 61(4):354–363, 2014.
- [123] J. L. Favero, A. R. Secchi, N. S. M. Cardozo, and H. Jasak. Viscoelastic fluid analysis in internal and in free surface flows using the software OpenFOAM. *Computers & Chemical Engineering*, 34(12):1984–1993, 2010.
- [124] F. Pimenta and M. A. Alves. Stabilization of an open-source finite-volume solver for viscoelastic fluid flows. *Journal of Non-Newtonian Fluid Mechanics*, 239:85–104, 2017.
- [125] F. Pimenta and M. A. Alves. RheoTool, 2016. URL <https://github.com/fppimenta/rheoTool>.
- [126] F. Pimenta and M. A. Alves. Numerical simulation of electrically-driven flows using OpenFOAM, 2018. URL <https://arxiv.org/abs/1802.02843>.
- [127] F. Pimenta, R. G. Sousa, and M. A. Alves. Optimization of flow-focusing devices for homogeneous extensional flow. *Biomicrofluidics*, 12(5):054103, 2018.
- [128] F. Pimenta and M. A. Alves. A coupled finite-volume solver for numerical simulation of electrically-driven flows. *Computers & Fluids*, 193:104279, 2019.
- [129] M. A. Hulsen, R. Fattal, and R. Kupferman. Flow of viscoelastic fluids past a cylinder at high weissenberg number: stabilized simulations using matrix logarithms. *Journal of Non-Newtonian Fluid Mechanics*, 127(1):27–39, 2005.
- [130] R. Fattal and R. Kupferman. Time-dependent simulation of viscoelastic flows at high weissenberg number using the log-conformation representation. *Journal of Non-Newtonian Fluid Mechanics*, 126(1):23–37, 2005.
- [131] N. Latrache, O. Crumeyrolle, and I. Mutabazi. Transition to turbulence in a flow of a shear-thinning viscoelastic solution in a taylor-couette cell. *Physical Review E*, 86(5):056305, 2012.
- [132] Y. Layec and M.-N. Layec-Raphalen. Instability of dilute poly(ethylene-oxide) solutions. *Journal de Physique Lettres*, 44(3):121–128, 1983.

- [133] B. Song and J. Springer. Determination of interfacial tension from the profile of a pendant drop using computer-aided image processing: 1. Theoretical. *Journal of Colloid and Interface Science*, 184(1):64–76, 1996.
- [134] B. Song and J. Springer. Determination of interfacial tension from the profile of a pendant drop using computer-aided image processing: 2. Experimental. *Journal of Colloid and Interface Science*, 184(1):77–91, 1996.
- [135] R. G. Larson. Instabilities in viscoelastic flows. *Rheologica Acta*, 31(3):213–263, 1992.
- [136] P. J. Carreau. *Rheological equations of state from molecular network theories*. PhD thesis, PhD thesis, University of Wisconsin, Madison, 1968.
- [137] K. Y. Yasuda, R. C. Armstrong, and R. E. Cohen. Shear flow properties of concentrated solutions of linear and star branched polystyrenes. *Rheologica Acta*, 20(2):163–178, 1981.
- [138] J. H. Yu, S. V. Fridrikh, and G. C. Rutledge. The role of elasticity in the formation of electrospun fibers. *Polymer*, 47(13):4789–4797, 2006.
- [139] C. Tirel, M.-C. Renoult, and C. Dumouchel. Measurement of extensional properties during free jet breakup. *Experiments in Fluids*, 61(2):1–14, 2020.
- [140] A. D. Polyaniin and A. V. Manzhirov. *Handbook of mathematics for engineers and scientists*. CRC Press, 2006.
- [141] B. E. Larsen, D. R. Fuhrman, and J. Roenby. Performance of interfoam on the simulation of progressive waves. *Coastal Engineering Journal*, 61(3):380–400, 2019.
- [142] R. Valette, E. Hachem, M. Khalloufi, A. S. Pereira, M. R. Mackley, and S. A. Butler. The effect of viscosity, yield stress, and surface tension on the deformation and breakup profiles of fluid filaments stretched at very high velocities. *Journal of Non-Newtonian Fluid Mechanics*, 263:130–139, 2019.
- [143] M. S. N. Oliveira and G. H. McKinley. Iterated stretching and multiple beads-on-a-string phenomena in dilute solutions of highly extensible flexible polymers. *Physics of Fluids*, 17(7):071704, 2005.
- [144] O. Arnolds, H. Buggisch, D. Sachsenheimer, and N. Willenbacher. Capillary breakup extensional rheometry (caber) on semi-dilute and concentrated polyethyleneoxide (PEO) solutions. *Rheologica Acta*, 49(11):1207–1217, 2010.
- [145] P.-G. De Gennes. Wetting: statics and dynamics. *Reviews of modern physics*, 57(3):827, 1985.
- [146] A. L. Yarin, G. Brenn, O. Kastner, D. Rensink, and C. Tropea. Evaporation of acoustically levitated droplets. *Journal of Fluid Mechanics*, 399:151–204, 1999.
- [147] G. Brenn and S. Teichtmeister. Linear shape oscillations and polymeric time scales of viscoelastic drops. *Journal of Fluid Mechanics*, 733:504–527, 2013.

# **Appendix A**

## **Published article**

## Drop dynamics of viscoelastic filaments

Hrishikesh Pingulkar,<sup>1</sup> Jorge Peixinho ,<sup>1,2</sup> and Olivier Crumeyrolle<sup>1</sup>

<sup>1</sup>Laboratoire Ondes et Milieux Complexes, CNRS and Université Le Havre Normandie,  
76600 Le Havre, France

<sup>2</sup>Laboratoire PIMM, CNRS, Arts et Métiers Institute of Technology,  
Cnam, HESAM Université, 75013 Paris, France



(Received 14 September 2019; published 13 January 2020)

The stretching of viscoelastic polymer solutions close to breakup can create attached drops on a filament, whose properties and dynamics are little understood. The stretching of capillary bridges and the consecutive filament, until its breakup, can be quantified using diameter-space-time diagrams, which demonstrate hierarchy, as well as asymmetry of satellite drops around a big central drop. All drops experience migration, oscillation, and merging. In addition, the position of the minimum diameter on the filament is determined, along with the number of drops, their positions, the diameters of drops and the filament breakup time. The maximum number of drops on the filament can be predicted using the Deborah number. The diagrams also quantify the large Hencky strains in the filaments before pinch-off. The obtained minimum diameter is used to measure the extensional viscosity, which indicates the effect of polymer concentration and direction of filament thinning.

DOI: [10.1103/PhysRevFluids.5.011301](https://doi.org/10.1103/PhysRevFluids.5.011301)

*Introduction.* Understanding the extensional flow properties of polymer solutions is of practical and physical importance for many commercial applications such as spraying, coating, inkjet printing, food processing, atomization, etc. Most of these processes undergo filament breakup of solutions containing dissolved polymers and the extensional viscosity of these solutions plays an important role in the thinning and the drop dynamics. In contrast to Newtonian fluids, which have their extensional viscosity directly proportional to the shear viscosity, the extensional viscosity of viscoelastic fluids is more complex. Macromolecular solutions exhibit large extensional viscosity [1–10] because extensional flows are irrotational and presumably more efficient at disentangling or orienting flexible polymer molecules. It has been known for 50 years [11,12] that capillary jets of viscoelastic polymer solutions exhibit the peculiar morphology called beads on a string (BOAS). The instability and the initial sinusoidal growth has been reported [13–15] and has also been observed in the stretching of capillary bridges using extensional rheometers such as Capillary Breakup Extensional Rheometer (CaBER) [7,16–21]. These studies have consistently evidenced the linear viscous-capillary thinning, the exponential polymeric thinning [22], and the existence of drops attached to a thin filament [2,23–28], depending on the fluid properties.

A remarkable feature of the thinning of viscoelastic solution is the ability to form long and persistent filaments. Scanning electron microscopy observations [29] suggest the extensional flow is heterogeneous, with local variation of polymer concentration and localized pinching [30]. Yet, the BOAS morphology appears from the initial wavelength of capillary instability modified by the central fiber, which behaves as a solid core. The annular film becomes unstable, resulting in drops along the filament. Inside a drop, the polymers are in relaxed state but in the fluid necks, they are in stretched state [29].

# **Appendix B**

## **OpenFOAM *rheoTool* scripts**

This chapter is dedicated to guide future researchers for the numerical study of beads-on-a-string (BOAS) and liquid transfer using the *rheoTool* code.

## B.1 Newtonian solution: PEG20

### B.1.1 Initial conditions

#### B.1.1.1 `alpha.water`

```
{dimensions [0 0 0 0 0 0 0];
internalField uniform 0;
boundaryField
{
  atmosphere
  {type zeroGradient;}
  topWall
  {type dynamicAlphaContactAngle;
  theta0 23;
  thetaA 45;
  thetaR 22;
  uTheta 0.00;
  limit gradient;
  value uniform 1;}
  bottomWall
  {
  type dynamicAlphaContactAngle;
  theta0 65.77;
  thetaA 86.5;
  thetaR 65;
  uTheta 0.00;
  limit gradient;
  value uniform 1;
  }
  wFront
  {
  type wedge;
  }
  wBack
  {
  type wedge;
  }
  axis
  {type empty;
  }}}}
```

**B.1.1.2 Pressure, p**

```
dimensions [1 -1 -2 0 0 0 0];
internalField uniform 0;
boundaryField
{
  atmosphere
  {type fixedValue;
   value uniform 0;
  }
  topWall
  {
    type fixedFluxExtrapolatedPressure;
  }
  bottomWall
  {
    type fixedFluxExtrapolatedPressure;
  }
  wFront
  {
    type wedge;
  }
  wBack
  {
    type wedge;
  }
  axis
  {
    type empty;
  }
}
```

**B.1.1.3 Velocity,  $\mathbf{U}$** 

```
dimensions [0 1 -1 0 0 0 0];
internalField uniform (0 0 0);
boundaryField
{
  atmosphere
  {
    type zeroGradient;
  }
  topWall
  {
    type fixedValue;
    value uniform (0 0 0);
  }
  bottomWall
  {
    type fixedValue;
    value uniform (0 0 0);
  }
  wFront
  {
    type wedge;
  }
  wBack
  {
    type wedge;
  }
  axis
  {
    type empty;
  }
}
```

**B.1.1.4 Constitutive properties**

```
phases (water air);
water // PEG20
{
  parameters
  {
    type Newtonian;
    rho rho [ 1 -3 0 0 0 0 0 ] 1032.5;
    eta eta [1 -1 -1 0 0 0 0] 0.034;
    stabilization coupling;
  }
}
air
{
  parameters
  {
    type Newtonian;
    rho rho [1 -3 0 0 0 0 0] 1.2;
    eta eta [1 -1 -1 0 0 0 0] 1.8e-5;
  }
}
passiveScalarProperties
{
  solvePassiveScalar off;
  D D [ 0 2 -1 0 0 0 0 ] 1e-9;
}
sigma sigma [ 1 0 -2 0 0 0 0 ] 0.057;
```

**B.1.1.5 Gravity, g**

```
dimensions [0 1 -2 0 0 0 0];
value (0 -9.81 0);
```

## B.1.2 Mesh generation: blockMeshDict

```
convertToMeters 0.001;
vertices
(
  ( 0 6 0)
    ( 0 0 0)
    ( 4 0 -0.1)
    ( 4 6 -0.1)
    ( 4 0 0.1)
    ( 4 6 0.1));
blocks
(
  hex (0 2 5 3 0 1 4 3) (200 400 1) simpleGrading (1 1 1)
  hex (2 13 11 5 1 12 10 4) (20 400 1) simpleGrading (1 1 1)
  hex (9 8 13 2 6 7 12 1) (20 20 1) simpleGrading (1 1 1)
  hex (5 11 17 16 4 10 15 14) (20 20 1) simpleGrading (1 1 1)
);
edges
(
);
boundary
(
  topWall
  {type wall;
    faces ((0 3 5 0));}
  bottomWall
  {type wall;
    faces ((1 2 4 1));}
  atmosphere
  {type patch;
    faces ((3 2 4 5));}
  axis
  {type empty;
    faces ((0 1 1 0));}
  wFront
  {type wedge;
    faces ((0 1 4 5));}
  wBack
  {type wedge;
    faces ((0 1 2 3));}
);
mergePatchPairs
(
);
```

### B.1.3 Time step control: `controlDict`

```
application rheoInterFoam;
startFrom latestTime;
startTime 0.00;
stopAt endTime;
endTime 0.90;
deltaT 0.000001;
writeControl adjustableRunTime;
writeInterval 0.001;
purgeWrite 0;
writeFormat ascii;
writePrecision 6;
writeCompression compressed;
timeFormat general;
timePrecision 6;
runTimeModifiable yes;
adjustTimeStep yes;
maxCo 0.05;
maxAlphaCo 0.05;
maxDeltaT 0.001;
```

## B.1.4 Convection schemes settings: `fvSchemes`

```
ddtSchemes
{
    default Euler;
}
gradSchemes
{
    default Gauss linear;
    grad(p) Gauss linear;
    grad(U) Gauss linear;
    linExtrapGrad Gauss linear;
}
divSchemes
{
    default none;
    div(Sum(tau)) Gauss linear;
    div(grad(U)) Gauss linear;

    div(rhoPhi,U) Gauss limitedLinearV 1;

    div(phi,alpha) Gauss Gamma 0.2;
    div(phirb,alpha) Gauss interfaceCompression;

    div(eta*alpha*dev2(T(gradU))) Gauss linear;

    div(phi,theta.water) GaussDefCmpw cubista;
    div(phi,theta.air) GaussDefCmpw cubista;
    div(phi,tau.water) GaussDefCmpw cubista;
    div(phi,tau.air) GaussDefCmpw cubista;
}
```

```
laplacianSchemes
{
  default
}
interpolationSchemes
{
  default linear;
}
snGradSchemes
{
  default orthogonal;
}
fluxRequired
{
  default no;
  p_rgh;
  pcorr;
  alpha1;
}
```

### B.1.5 Solver control: `fvsolution`

```
solvers
{
  "alpha.water.*"
  {
    nAlphaCorr 1;
    nAlphaSubCycles 1;
    cAlpha 1;

    MULESCorr yes;
    nLimiterIter 3;
    solver smoothSolver;
    smoother symGaussSeidel;
    tolerance 1e-7;
    relTol 0.0;
  }
  "pcorr.*"
  {
    solver PCG;
    preconditioner DIC;
    tolerance 1e-10;
    relTol 0;
  }
  p_rgh
  {
    solver PCG;
    preconditioner DIC;
    tolerance 1e-10;
    relTol 0.0;
  }
  p_rghFinal
  {
    $p_rgh;
    relTol 0;
  }
}
```

```
"(theta.*|tau.*|U)"
{
  solver PBiCG;
  preconditioner
  {
    preconditioner DILU;
  }
  tolerance 1e-10;
  relTol 0;
  minIter 0;
  maxIter 1000;
}
}
PIMPLE
{
  nInIter 1;
  SIMPLEC true;

  nCorrectors 3;
  nNonOrthogonalCorrectors 1;
}
relaxationFactors
{
  equations
  {
    ".*" 1;
  }
}
}
```

### B.1.6 Setting initial field: `setFieldsDict`

```
defaultFieldValues
(
  volScalarFieldValue alpha.water 0
);
regions
(
  surfaceToCell
  {
    file "PEG20mm.stl";
    outsidePoints ((0.003 0.003 0.00));
    includeCut true;
    includeInside yes;
    includeOutside no;
    nearDistance 0.000;
    curvature 0.00;
    fieldValues
    (
      volScalarFieldValue alpha.water 1
    );
  }
);
```

## B.2 Viscoelastic solution: PEG20PEO1000

### B.2.1 Initial conditions

#### B.2.1.1 `alpha.water`

```
dimensions [0 0 0 0 0 0 0];
internalField uniform 0;
boundaryField
{
  atmosphere
  {
    type zeroGradient;
  }
  topWall
  {
    type dynamicAlphaContactAngle;
    theta0 32;
    thetaA 33;
    thetaR 30;
    uTheta 0.00;
    limit gradient;
    value uniform 1;
  }
  bottomWall
  {
    type dynamicAlphaContactAngle;
    theta0 65;
    thetaA 90;
    thetaR 64;
    uTheta 0.00;
    limit gradient;
    value uniform 1;
  }
}
```

```
wFront
{
  type wedge;
}
wBack
{
  type wedge;
}
axis
{
  type empty;
}
```

**B.2.1.2 Constitutive properties**

```
phases (water air);
water
{
  parameters
  {
    type Oldroyd-BLog;
    rho rho [ 1 -3 0 0 0 0 0 ] 1033.6;
    etaS etaS [1 -1 -1 0 0 0 0] 0.034;
    etaP etaP [1 -1 -1 0 0 0 0] 0.737;
    lambda lambda [0 0 1 0 0 0 0] 2.95;

    stabilization coupling;
  }
}
air
{
  parameters
  {
    type Newtonian;
    rho rho [1 -3 0 0 0 0 0] 1.2;
    eta eta [1 -1 -1 0 0 0 0] 1.8e-5;
  }
}
passiveScalarProperties
{
  solvePassiveScalar off;
  D D [ 0 2 -1 0 0 0 0 ] 1e-9;
}
sigma sigma [ 1 0 -2 0 0 0 0 ] 0.0565;
```

### B.2.1.3 Polymeric extra-stress: Tau

```
dimensions [1 -1 -2 0 0 0 0];
internalField uniform (0 0 0 0 0 0);
boundaryField
{
    atmosphere
    {
        type fixedValue;
        value uniform (0 0 0 0 0 0);
    }
    topWall
    {
        type linearExtrapolation;
        value uniform (0 0 0 0 0 0);
    }
    bottomWall
    {
        type linearExtrapolation;
        value uniform (0 0 0 0 0 0);
    }
    wFront
    {
        type wedge;
    }
    wBack
    {
        type wedge;
    }
}
axis
{
    type empty;
}
}
```

## B.2.2 Setting initial field: `setFieldsDict`

```
defaultFieldValues
(
  volScalarFieldValue alpha.water 0
);

regions
(
  surfaceToCell
  {
    file "PEG20PEO1000.stl";
    outsidePoints ((0.003 0.000 0.00));
    includeCut true;
    includeInside yes;
    includeOutside no;
    nearDistance 0.000;
    curvature 0.00;
    fieldValues
    (
      volScalarFieldValue alpha.water 1
    );
  }
);
```



## **Appendix C**

### **Measurements of the retardation time**

The retardation time,  $\lambda_2$ , is the characteristic time required for a material to respond when deformation is caused by the application of a force or stress. This delayed response is a characteristic creep property of the material. The experiments to measure the retardation time are carried out using the oscillating drop method and theoretical details are given in Yarin et al. [146], Brenn and Plohl [58] and Plohl [48]. The experiments are performed by following the protocols mentioned by Brenn and Plohl [58] and Plohl [48]. The aqueous solutions of PEO, PEG and PEG+PEO are prepared with a wide range of mass fractions, as shown in Tab. 2.3. For all the PEO solutions in this study, iso-propyl alcohol (IPA) is not used. Additionally, aqueous solutions of Polyacrylamide (PAM) are prepared with and without glycerol.

To experimentally investigate the retardation time, the technique of acoustic levitation is used [58, 147]. The acoustic levitation of drops is achieved using an ultrasonic levitator. A drop of the polymer solution is introduced close to a pressure node of the acoustic levitator and levitated into the acoustic field. The maximum sample diameter of the drop that can be levitated with the frequency of 58 kHz is around 2.5 mm, whereas the smallest drop diameter is about 15  $\mu\text{m}$ . Oscillations of the levitated drop are excited by amplitude-modulating ultrasound. Then the amplitude modulation is switched off within seconds after injecting the drop in the acoustic levitator. A series of pictures of the levitated drop are acquired to obtain its initial shape. The drop is then excited near its resonance frequency. Then, at some time during the steady excitation, the modulation is switched off and the drop exhibits damped oscillations. The oscillations and the damping of the drop are recorded using a camera and analysed using the Mathematica software (version 12.0), to calculate the retardation time. Different droplet sizes and different mass fractions of polymers are tested. The ratio of the retardation time to the relaxation time,  $\lambda_2/\lambda$ , is calculated and plotted against polymer mass fraction,  $w_{\text{Polymer}}$ , of PEO, PEG+PEO, PAM and Praestol 2500, as shown in Fig. C.1.

The data is further analysed to calculate the retardation time using the Elasto-Viscous Stress Splitting (EVSS) method, refer to section 1.4.2, details of which are given in Plohl [48]. The retardation time is calculated as  $\lambda_2 = \lambda(\eta_s/\eta_0)$ , where  $\eta_s$  is the solvent viscosity and  $\eta_0$  is the zero shear viscosity. These results are compared with the data obtained for Praestol 2500 by Plohl [48]. The results seem to agree only for PEO solutions with the PEO mass fraction up to 1000 wppm. However, for the higher mass fractions of PEO in PEG+PEO solutions and PAM solutions, the results are not reliable, as the solutions are too viscous, leading to very small or no oscillations. The results obtained for PAM solutions are not satisfactory and are irrelevant to the work.

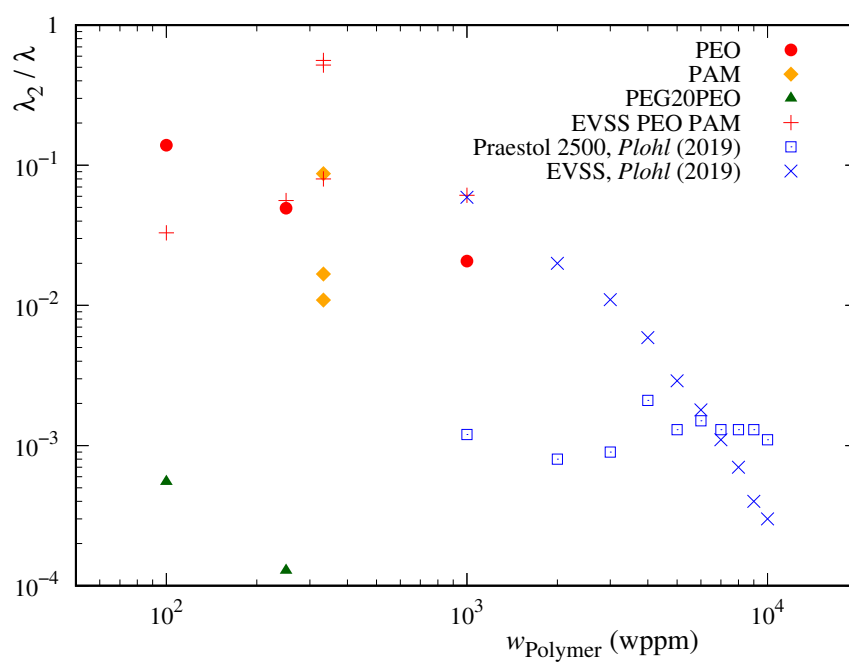


Fig. C.1 Ratio of the retardation time to the relaxation time,  $\lambda_2/\lambda$ , vs polymer mass fraction,  $w_{\text{polymer}}$ , of PEO, PEG+PEO, PAM and Praestol 2500.



## **Appendix D**

### **Polarised Light Microscopy**

A Polarised Light Microscopy is carried out for the PEG20PEO1000 viscoelastic solution, to further investigate the observation by [86] about the presence of the polymers in the beads, as well as, in the filaments. The polarised microscopy is carried out using Olympus XC30 Digital Camera. The basic principle of different optical properties, of isotropic and anisotropic crystallographic materials, is used to observe their presence. Here, to study beads-on-a-string (BOAS) structure of PEG20PEO1000, the BOAS structure, created by stretching liquid bridge, is placed on a clean glass slide. Then, the structure is observed under the microscope, and results are shown in Fig. D.1. The size of the big drop, for Fig. D.1(a), is  $\approx 220 \mu\text{m}$  and the size of the pinching point is  $\approx 14 \mu\text{m}$ . The multi-coloured regions indicate the presence of the polymer crystals, suggesting the polymers are present in the bead, see Fig. D.1(a), as well as, in the filament, see D.1(b), after pinching. More detailed study needs to be done, by using higher resolution of camera, along with the different viscoelastic solutions. Additionally, the presence of the polymer can be confirmed by drying the BOAS structure.



Fig. D.1 Beads-on-a-string (BOAS) microscopy for PEG20PEO1000, obtained from the Polarised Light Microscopy. (a) The view around the neck. The size of the big drop is  $\approx 220 \mu\text{m}$  and the size of the pinching point is  $\approx 14 \mu\text{m}$ . (b) The view of the filament, connecting different beads, and the average diameter  $\approx 20 \mu\text{m}$  can be observed.

## **Appendix E**

### **Effect of stretching direction on liquid transfer**

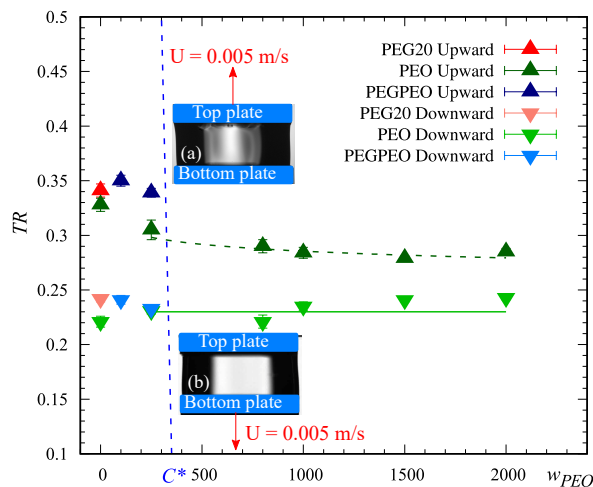


Fig. E.1 Effect of stretching direction on liquid transfer. The insets are photographs depicting the stretching of the capillary bridge with (a) the top plate moving in the upward direction, and (b) the bottom plate moving in the downward direction. The liquid bridge, formed in-between the two plates having  $D_P = 6$  mm and volume  $56 \mu\text{l}$  is stretched from  $IAR = 0.66$  to  $FAR = 2$ , with  $U = 0.005$  m/s. The red arrows denote the stretching direction. The vertical blue line indicates the critical mass fraction,  $w^*$ , of PEO. The error bars represent the dispersion over five experiments. The dashed green line is a trend line for the PEO solutions with the upward stretching direction.

The influence of the stretching direction on the liquid transfer is investigated. A liquid bridge, formed in-between the two plates having  $D_P = 6$  mm and volume  $56 \mu\text{l}$  is stretched from  $IAR = 0.66$  to  $FAR = 2$ . Two sets of experiments are performed by stretching either the top plate in the upward direction or the bottom plate in the downward direction, at  $U = 0.005$  m/s. For the downwards stretching, the experiments are performed at the CORIA laboratory (Université de Rouen Normandie) using a downward stretching apparatus. Water, PEG20, PEO solutions and PEG+PEO solutions are tested.

The obtained results for  $TR$  are plotted against  $w_{PEO}$  as shown Fig. E.1. For PEG20, PEO solutions and PEG+PEO solutions, shades of red, green and blue colours are used, respectively. For the upward stretching, the triangle symbols are used, whereas, for downward stretching, the inverted triangle symbols are used. Each symbol represents the average of five experiments. For all solutions,  $TR$  is higher for upward stretching than the downward stretching. Additionally, for the upward stretching,  $TR$  decreases with the increase in  $w_{PEO}$ . But for the downward stretching, there is no variation in  $TR$  is observed. In the downward stretching, the liquid bridge is stretched in the same direction as gravity. Therefore, more liquid is pulled from the top solution pool, that explains the lower values of  $TR$ .

# **Appendix F**

## **Résumé en langue française**

## Résumé en langue française :

Cette thèse traite de l'étirement uniaxial de ponts capillaires de solutions polymères. Elle se compose de deux parties expérimentales examinant la dynamique des gouttes et le taux de transfert de liquide de la surface inférieure à la surface supérieure. La thèse présente également quelques résultats numériques visant à reproduire les phénomènes quantifiés expérimentalement.

Les étirements uniaxiaux ou les jets de solutions de polymères viscoélastiques se caractérisent par la formation de filaments. Pour des concentrations et des masses molaires suffisantes, des structures particulières de type perles-sur-ficelle apparaissent avant la rupture. Cette instabilité est due à une interaction complexe entre les forces de viscosité, d'élasticité, de capillarité et d'inertie. Les propriétés dynamiques des gouttes du motif perle-sur-ficelle ne sont pas encore complètement comprises. Dans la thèse, des solutions aqueuses newtoniennes et viscoélastiques sont préparées à l'aide d'oxyde de polyéthylène (PEO) et de polyéthylène glycol (PEG) sur une large gamme de concentrations. Ce polymère a été choisi car il est constitué de macromolécules linéaires et est disponible sur une large gamme de masse molaire. De plus, il est transparent et non-toxique. Les propriétés des solutions ont été mesurées : la densité, la tension de surface et la viscosité de cisaillement à l'aide d'un rhéomètre rotatif et d'une géométrie type double cylindres coaxiaux. En outre, le temps de retardation des solutions a été déterminé par la technique de lévitation acoustique.

Les expériences sont réalisées à l'aide d'un instrument CaBER (*Capillary Breakup Extensional Rheometer*), d'un laser et d'une caméra rapide munie d'une lentille macro. L'utilisation du CaBER permet un contrôle de la vitesse d'étirement du pont capillaire positionné entre deux disques horizontaux coaxiaux. Initialement, le pont capillaire a la forme d'un cylindre avec les lignes de contact (liquide/air/solide) accrochée aux bords des disques. Les hauteurs initiales des disques sont contrôlées à l'aide de vises micrométriques. Les images sont obtenues par ombroscopie. L'évolution des ponts capillaires est analysée à l'aide de diagrammes spatio-temporels, qui quantifient le diamètre et la déformation sur la hauteur du filament et au cours du temps.

D'abord, l'évolution du diamètre au cours du temps est caractérisée par un amincissement exponentiel dont l'exposant représente le temps de relaxation. Les résultats obtenus pour les solutions de polymères préparés sont en bon accord quantitatifs avec les résultats de la littérature. En particulier, il y a une augmentation du temps de relaxation avec la concentration du polymère et également avec la viscosité des solutions.

Concernant le motif perle-sur-ficelle, les diagrammes démontrent la hiérarchie, ainsi que l'asymétrie des petites gouttes satellites autour d'une grosse goutte centrale. Toutes les gouttes subissent des translations le long du filament, des oscillations et des coalescences. Le nombre de gouttes, leurs positions, les diamètres des gouttes et le temps de rupture du filament sont représentés. De plus, la position et le diamètre minimum le long du filament sont déterminés. En particulier, il est montré que le nombre maximum de gouttes sur le filament peut être prédit à l'aide d'une loi puissance en fonction du nombre de Deborah, qui est le rapport entre les temps de relaxation de la solution de polymère et le temps de Rayleigh (inertio-capillaire). Les diagrammes quantifient également les grandes déformations de Hencky dans les filaments. L'évolution temporelle du diamètre minimum est utilisée pour calculer la viscosité élongationnelle. Cette viscosité élongationnelle augmente rapidement avec la déformation indiquant la résistance du filament aux grandes déformations.

L'effet de l'écartement initial et final sur l'instabilité du motif perle-sur-ficelle se manifeste principalement sur le nombre de gouttes, qui semble dépendre de la longueur du filament. Le nombre de gouttes diminue avec la hauteur initiale du pont capillaire et augmente pour les grands écartements. La vitesse d'étirement n'affecte pas le diamètre de la goutte centrale. Par contre, ce diamètre est sensible à l'écartement.

Après la rupture du filament, qui se produit au niveau du pincement supérieur, le système atteint un équilibre avec deux réservoirs de solution attachés aux plateaux inférieur et supérieur. Le taux de transfert de liquide viscoélastique d'une surface à une autre est une quantité importante dans de nombreuses technologies, et notamment dans les procédés d'impression. Les expériences considèrent le transfert de liquides viscoélastiques au travers de ponts capillaires de forme cylindrique entre deux disques parallèles circulaires. Les effets de la concentration de polymère, de la viscosité du solvant, du diamètre des supports, du rapport d'aspect initial (rapport hauteur initial sur diamètre), du rapport d'aspect final, de la vitesse d'étirement et de l'angle de contact sont étudiés expérimentalement. Les résultats montrent qu'avec l'augmentation de la concentration de polymère et de la viscosité du solvant, le transfert de liquide vers la plaque supérieure diminue systématiquement. On observe également que les hauteurs initiales et finales du pont capillaire ont des effets opposés sur le taux de transfert de liquide. La forme du pont capillaire initial est également étudiée en faisant varier le volume de liquide introduit entre les deux disques. Cette augmentation de volume a pour effet de modifier l'angle de contact au niveau du plateau support. Pour les solutions newtoniennes, le taux de transfert de liquide augmente alors que pour des solutions viscoélastiques, le taux diminue.

